Adjoint-based optimization for inkjet printing

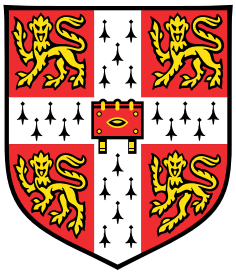

Petr Kungurtsev

Department of Engineering
University of Cambridge

This dissertation is submitted for the degree of
Doctor of Philosophy

St Edmund's College

December 2020

Declaration

This thesis is the result of my own work and includes nothing which is the outcome of work done in collaboration except as declared in the Preface and specified in the text. I further state that no substantial part of my thesis has already been submitted, or, is being concurrently submitted for any such degree, diploma or other qualification at the University of Cambridge or any other University or similar institution except as declared in the Preface and specified in the text. It does not exceed the prescribed word limit for the relevant Degree Committee.

Petr Kungurtsev
December 2020

Adjoint-based optimization for inkjet printing

Petr Kungurtsev

In this thesis the flow inside inkjet printhead microchannels is analysed using a two-parameter low Mach number expansion of the compressible Navier–Stokes equations and a reduced order model for the free surface flow inside the inkjet nozzle. The channel flow is separated into equations for an incompressible flow with no acoustic oscillations and equations for thermoviscous acoustic oscillations with no mean flow.

This thesis concerns two types of optimal control problems. The optimal control problem of the first type is finding a velocity profile of the piezo-electric actuator that eliminates residual oscillations after a droplet is ejected. The cost function is the sum of the acoustic energy in the channel and the surface energy of the spherical cap of ink at the end of the nozzle at a given time. This problem is approached by obtaining the sensitivity of the total energy inside an inkjet microchannel with respect to boundary forcing using the adjoint method. Using gradient-based optimization algorithms, optimal waveforms are found that minimize the objective value at various final times and for geometries with increasing complexity. Physical interpretation to the optimal waveforms profiles is provided, and the exploited mechanisms are revealed.

The optimal control problem of the second type is finding a shape of the inkjet printhead channel that maximises dissipation of the acoustic oscillations, without increasing the pressure drop required to drive the steady flow. Similarly, the adjoint approach is used to obtain the sensitivity of the acoustic flow eigenvalues with respect to boundary deformations in Hadamard form. Knowing the shape sensitivity of the incompressible flow viscous dissipation, the constrained optimization problem is solved to find a design that has the same viscous dissipation for the steady flow but a 40% larger decay rate for the oscillating flow. The final shape is not straightforward and would have been difficult to achieve through physical insight or trial and error. It could be improved further by adapting the parameters that describe the shape, but in this case the improvement would be small. The method is general and could be applied to many different applications in microfluidics.

In summary, the methods in this thesis are promising techniques in the design and optimization of inkjet printheads. The discussed numerical techniques and the gained physical understanding can be used to automatically find the optimal design parameters, or, at a minimum, accelerate the experimental trial and error processes.

To my grandfather.

Acknowledgements

I desire to record my thanks to Professor Matthew Juniper for constant support and boundless patience. I would have never made it so far without his guidance. Thank you for teaching me to take small steps when it seems to be no way forward.

All my Hopkinson lab friends: Jack, Hans, Filip, José, Stefano and Francesco, Ubaid, Maxim and Max, thank you all for these wonderful years. It was an honour to work together, and great pleasure to learn from you. ISO–40 will always be in my heart.

I would like to thank Dr Peter Boltryk for many fruitful discussions and lectures about the inkjet world.

I am very grateful to my family for granting me the opportunity to pursue my dreams. Everything I am, I am because of you and your love. I would like to thank my dearest Svetlana, my guiding star. It is always sunny when you are around.

I gratefully acknowledge the European Union's Framework Programme for Research and Innovation "Horizon 2020" under the Marie Skłodowska-Curie Innovative Training Programme, H2020-MSCA-ITN-2015, for funding this project. I would like to thank the whole SSeMID team for all the fantastic meetups, conferences, and dinners we shared.

Table of contents

List of figures

List of tables

Nomenclature

Roman Symbols

L_c	total length of an inkjet printhead channel
L	characteristic length scale
c_s	speed of sound
s	entropy variable
s	$= \sigma + \mathrm{i}\omega$, complex eigenvalue
$\mathcal{F}_.$	boundary energy flux
$\mathcal{M}_.$	boundary mass flux
$\mathcal{J}$	objective function
$\mathcal{T}$	temporal domain
$\mathcal{E}$	total flow energy
$\mathcal{R}$	volume acoustic dissipation
e	static internal energy
P	pressure variable
T	temperature variable
$\mathbf{q}$	generic state vector
$\mathbf{u}$	velocity variable
$\mathbf{x}$	spatial coordinate vector

Z boundary impedance

Greek Symbols

ϵ oscillating flow Mach number

γ_{th} the heat capacity ratio, c_p/c_v

Γ domain boundary

$\gamma_{\text{dim}}, \gamma$ dimensional and nondimensional surface tension coefficients

$\kappa, \hat{\kappa}$ curvature and effective curvature variables

κ_{th} thermal conductivity coefficient

μ throughflow Mach number

μ_{vis} viscosity

Ω spatial domain

ρ density variable

Σ time-space domain

σ_{ij} stress tensor

τ_{ij} viscous stress tensor

Superscripts

$\dagger$ adjoint variable

$\hat{\cdot}$ quantity related to the oscillating flow eigenmode

$\widetilde{\cdot}$ quantity related to the oscillating acoustic flow

$\bar{\cdot}$ quantity related to the throughflow

b ambient state quantity

(k) k-th order perturbation quantity

Subscripts

c quantity related to the printhead channel domain

h discrete quantity

i, j, k component of a vector

$u_i v_i$ $\equiv \sum_i u_i v_i$, summation over a set of indexed terms (Einstein notation)

n quantity related to the printhead nozzle domain

Other Symbols

$\overline{\partial_t}$ discrete time derivative

Δt time step

Pe Peclet number

Re Reynolds number

∇ $= \frac{\partial}{\partial \mathbf{x}}$, spatial derivative

Δ $= \nabla^2$, the Laplace operator

Chapter 1

Introduction

1.1 Inkjet printing

Piezoelectric inkjet drop-on-demand printing (Basaran et al., 2013; Li et al., 2019; Wijshoff, 2010) is a modern widely used technology and a promising tool for many future applications and research. Inkjet printers are used extensively in industry to print pictures, patterns and labels onto textiles, ceramics, and packaging (Hoath, 2016). Increasingly they are used for advanced manufacturing: 3D printing (Wang et al., 2016), chemical (Tamura et al., 2014) and biomedical applications (Herran, 2013; Spears et al., 2016), production of microelectronics and MEMS devices (Marinis, 2009; Parashkov et al., 2005). Polymeric inks, such as PEDOT (Groenendaal et al., 2000), are becoming increasingly popular (Gan et al., 2009) in emerging areas such as printed wiring and even bioelectronics (Donahue et al., 2020).

This study concerns inkjet drop-on-demand printheads. These contain several hundred ink-filled parallel channels, each of which has a piezo-electric actuator on one side and a 20-50 micron nozzle on the opposite side. There is a free surface at the end of each nozzle, where the ink meets the air. When a drop is demanded, an electric signal is applied to the actuator. The actuator moves the boundary of the channel by a few hundred nanometers, forcing an ink droplet out of the nozzle and onto a moving substrate below. After this droplet formation stage, acoustic oscillations reverberate within the channel, decaying through viscous and thermal dissipation (Beltman, 1999b; Dijksman, 2019; Tijdeman, 1975).

Challenges and objectives

The main objectives in engineering an inkjet printhead system are characteristics of individual droplets, such as volume and shape, ability to jet at high frequencies, and consistency and reproducibility of jetting behaviour under varying operating conditions (degradation of fluid, nozzle surface wetting, temperature variation (Shin et al., 2011)). Manufacturers would like to increase the printing resolution, and therefore decrease droplet size. Recent studies report that picolitre resolution jetting can be achieved (Chen and Basaran, 2002; Gan et al., 2009; Snyder et al., 2019). It is also required to control the droplet velocity in order to avoid merging of consecutive droplets before they reach the printing substrate (Khalate et al., 2011).

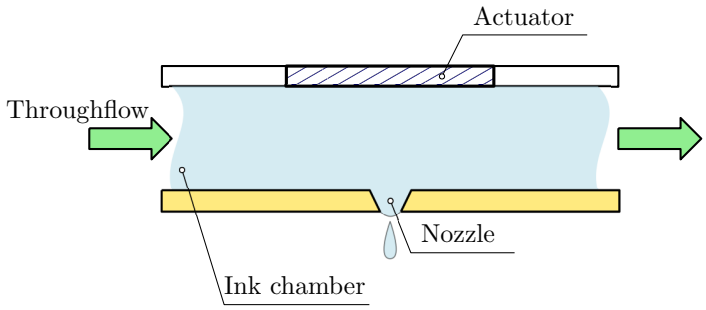

Fig. 1.1 A schematic of an inkjet microchannel cross section, showing the piezo actuator, the nozzle, and the ink throughflow (green arrows). Diagram from Strevens et al. (2020).

Manufacturers would like to increase the droplet ejection frequency, while retaining or improving the reproducibility of the droplets. There is, however, a trade-off between the droplet ejection frequency and the droplet reproducibility. If the characteristics of one droplet depend on the time since the previous droplet, sharp edges of the print become fuzzy. This occurs if the acoustic reverberations from the previous droplet have not died away sufficiently when the next droplet is demanded. As the time between ejections decreases, each droplet becomes increasingly affected by the residual oscillations from the previous ejection. This limits the rate at which droplets can be printed to around 100,000 per second (Basaran et al., 2013; Miers and Zhou, 2017). Manufacturers would like to increase this rate but, to do so, need the reverberations to decay more quickly. This can be done, for example, by designing print head shapes that passively damp residual oscillations (Kungurtsev and Juniper, 2019). Manufacturers also alter the electrical waveforms sent to the print heads microchannels in order to damp residual oscillations with open loop control (Khalate et al., 2011). These waveforms are currently adjusted by trial and error in extensive experimental campaigns.

In inkjet printers, it is crucial that every nozzle functions identically and that all drops are the same. If a single nozzle stops working, it leaves a straight unprinted line on the substrate. For this reason, ink is flushed continually through the channels (Crankshaw et al., 2016). This flushes away any air bubbles and also reduces the chance that any solid impurities become lodged in the nozzle. This, however, comes at a cost: a pump is required to push the ink through the narrow channels. A faster flow rate or more constricted channels require more power, which is dissipated by viscosity in the printhead.

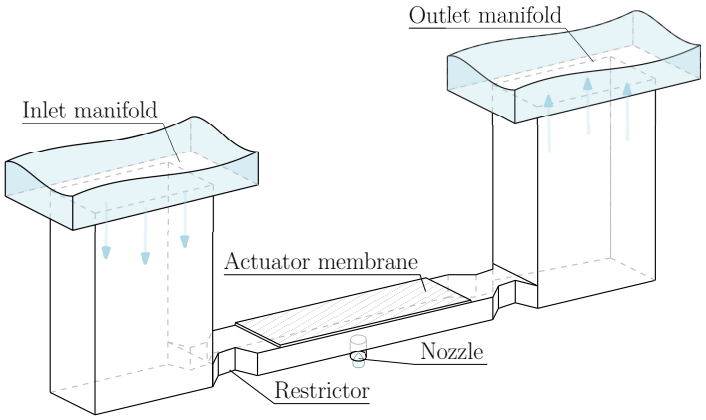

Fig. 1.2 A schematic of a U-shaped inkjet microchannel, showing the piezo actuator membrane, the nozzle, and the ink throughflow from the inlet to the outlet manifold.

Boundary deformations and propagation of pressure waves inside a single channel inevitably leads to cross-talk (Voit et al., 2011). When several channels are firing simultaneously, the drop velocity reduces, which results in dot placement errors. In some applications, this means that only every third nozzle can be active at the same time (Beurer and Kretschmer, 1997), which effectively reduces the droplet ejection frequency.

Modelling flow inside inkjet microchannels

The motion of a fluid inside an inkjet printhead microchannel can be described as a compressible flow with viscous and thermal effects, and is governed by the compressible Navier—Stokes equations. These equations can be simplified when the Mach number of the flow is small. The asymptotic analysis (Hunter, 2004) of compressible low Mach number flow is presented in Müller (1998) and (Alazard, 2008); the incompressible limit of the full system of compressible Navier–Stokes equations is discussed in Lin (1995); Rehm et al. (1978) presents the low Mach number approximation of thermally driven,

buoyant flows. A particularly interesting case is the two-parameter expansion of a reacting flow by Culick et al. (2012): the mean and the fluctuating flow components are shown to be independent to first order in low mean and fluctuating flow Mach numbers, and can be modelled separately. The low Mach number expansion of the compressible flow in microchannels yields the thermoviscous acoustic system of equations (Chu, 1965).

Although some earlier studies suggested that the inkjet microchannel flow can be described as incompressible (Beasley, 1977), experimental and theoretical analysis of flows inside one-dimensional inkjet transducers driven by piezoelectric sleeve contraction by Bogy and Talke (1984); Dijksman (1984) show that the flow inside an inkjet microchannel is governed by acoustic equations with viscous effects. Shield et al. (1987) used a linear acoustic model with Darcy-Weisbach type viscous drag to simulate pressure wave propagation and droplet formation inside a long glass tube, and found good agreement with experimental observations. This one-dimensional analysis can be extended to account for more complex physical effects relevant to inkjet dynamics, for example modelling entrapped air bubbles (de Jong et al., 2006; Jeurissen, 2009).

More advanced models of the acoustic motion are based on the linearized Navier–Stokes equations. Tijdeman (1975) investigated a compressible flow with viscosity and thermal conductivity inside a long tube with constant cross-section and proposed the low reduced frequency model. This model assumes constant pressure gradient along the domain, and presents an analytical solution that depends on the nondimensional (reduced) frequency of the harmonic flow oscillations and the Reynolds number. The analytical solutions of the low reduced frequency model are available for particularly simple geometries (Moser, 1980), and can be obtained for more general geometries (Beltman, 1999a,b), or solved numerically (Kampinga et al., 2010). Christensen (2011) compared the solution of the low reduced frequency model and the numerical solution of the full Navier–Stokes equations inside channels with different cross-sections, and confirmed good agreement.

Another approach is a class of boundary layer models that approximate the boundary layer effects by a special thermo-viscous impedance boundary condition. Bossart et al. (2003) proposed an iterative boundary element method that decouples the isentropic flow in the inner part of the computational domain from the thermal and viscous waves in the domain regions close to the boundaries. The analytical solution in the viscous and thermal boundary layers is transformed into an admittance boundary condition. Alternatively, viscous and thermal dissipation can be accounted for by a Wentzell boundary condition that is derived using asymptotic boundary-layer analysis (Berggren

et al., 2018; Rienstra and Hirschberg, 2013; Schmidt and Thöns-Zueva, 2019; Schmidt et al., 2014). The sequential linearized Navier–Stokes model (SLNS) (Kampinga et al., 2011) is derived using techniques from both low reduced frequency models (slowly varying pressure gradient), and boundary layer models (decoupling of the isentropic and thermo-viscous waves). The SLNS model is applicable to arbitrary geometries, when the thickness of the narrow parts of the domain is comparable to the boundary layer thickness. The results of these models, however, are not valid when the thickness of the boundary layer is of order of the radii of the surface curvature. While these models are computationally cheap and useful for initial designs, they fail to predict performance of printhead microchannels with complex geometries.

Obtaining a solution to the full linearized Navier–Stokes system of equations is more computationally demanding in comparison to the reduced order models: all unknowns (pressure, temperature, and velocity fields) are calculated directly, and careful meshing of the boundary layer regions is required (Joly, 2010). Modelling linear acoustic wave propagation that interacts with a mean flow is even more challenging because the mean flow field needs to be known in advance, for example, from a DNS solution of the nonlinear compressible Navier–Stokes equations (Kierkegaard et al., 2010). This is, however, impractical for most applications since the oscillating flow to mean flow interaction scales as the second order of small Mach number. A generic way to solve the thermoviscous acoustic problem is to use the finite element method (Alnæs et al., 2015) with an appropriate choice of spatial discretization (Kampinga et al., 2010). In this case, a sensible way to improve the accuracy of the numerical solution and construct a refined mesh is to use goal-oriented mesh adaptation (Fraysse et al., 2012; Rognes and Logg, 2013).

The frequency domain models of the acoustic flow inside the inkjet microchannel assume linear interaction between the flow and the multiphase interface at the end of the nozzle (Khalate et al., 2011; Wijshoff, 2010). The nonlinear interaction can be accurately captured by unsteady simulations (Wassink, 2007). Since some form of the energy norm is usually the quantity of interest (for example, energy transfer between the acoustic flow and the surface energy of the forming droplet, or the energy of the residual oscillations after a droplet ejection cycle), finite difference discretization (Trefethen, 1996) of the unsteady thermoviscous equations has to be free from numerical dissipation (Thomas and Roe, 1993). The second order accurate Crank–Nicolson scheme satisfies this criterion (Apel and Flaig, 2012; Thomas, 2013).

Modelling nozzle flow and droplet formation

Understanding the physics of jet instabilities (Eggers and Villermaux, 2008; Rayleigh, 1879) and drop formation (Driessen and Jeurissen, 2016) is the second ingredient of modelling inkjet drop-on-demand printing. Considering separate models for the nozzle and the channel flows allows the two domains to be considered separately and, if analysed numerically, to be discretized independently (Wijshoff, 2004). In turn this allows the analysis in the nozzle to be focused on droplet formation.

The formation of droplets can be investigated either experimentally or numerically. Experimental imaging-based techniques vary from simple measurement of the drop volume (Furbank and Morris, 2004) and observation of meniscus motion (Kwon, 2009) to more advanced image processing to determine the velocity profile inside the droplet (Snyder et al., 2019; van der Bos et al., 2014). Earlier studies of drop formation in liquid jets (Bogy, 1979) and emitting devices (Badie and Dirk Frits, 1997; Dijksman, 1984) show that these phenomena depend on the ink viscosity and surface tension, and the mass and energy transfer towards the multiphase interface in the nozzle. The flow in the short nozzle near the free surface (in contrast to the rest of the printhead microchannel) is typically modelled as incompressible and axisymmetric (Chen and Basaran, 2002; Shield et al., 1987; Wu et al., 2004), driven by the pressure (Fumagalli et al., 2018) or velocity inflow (McIlroy et al., 2013; Miers and Zhou, 2017) from the channel.

Various numerical methods have been proposed to model the free surface development, droplet formation, and pinch-off in inkjet print heads. One-dimensional models of droplet formation (Adams and Roy, 1986; Eggers and Dupont, 1994; Jiang and Tan, 2018) and jet break-up (Bogy, 1979) have shown good agreement with experiments. A particularly interesting method has been proposed by Driessen and Jeurissen (2011): for a fixed one-dimensional grid, small modifications to the surface tension can regularize pinch-off and coalescence singularities. Womersley (1955) analysed an axisymmetric incompressible arterial flow driven by a periodic pressure gradient, and derived an analytical solution for the velocity profile as a function of the oscillation frequency (a Womersley velocity profile). Brereton and Jiang (2005) took this idea one step further, and presented exact solutions for the unsteady laminar pipe flows under the assumption of constant pressure gradient along the pipe. They provided analytical relationships between various quantities of interest as functions of time. For example, it is possible to calculate the flow rate as a function of the time-varying pressure gradient, local velocity (and consequently kinetic energy) as a function of flow rate, and vice versa. Finally, Wassink (2007) extended this approach to study the drop initiation and

thinning of the drop tail processes. The proposed two-port modeling approach assumes a Poiseuille velocity profile of the flow inside a nozzle with a slowly varying cross section, and couples the flow rate at the free surface to the free surface deformation. This results in a fast, accurate, and experimentally validated numerical technique to simulate the ink channel dynamics.

Explicit interface tracking methods: the volume of fluid (Hirt and Nichols, 1981; Wu et al., 2004; Yang et al., 2005) and level-set methods (Galusinski and Vigneaux, 2008a; Miers and Zhou, 2017) have been successfully applied to compute the position of free surface boundary and droplet formation. In the above papers, the nozzle is assumed always to be filled with fluid. This assumption can be relaxed and the dynamics of the contact line between liquid, solid, and gas (Snoeijer and Andreotti, 2013) can be simulated using a variational approach (Fumagalli et al., 2018; Manservisi and Scardovelli, 2009).

Overall, development and verification of droplet formation modelling tools is a non-trivial task, and such simulations are computationally expensive and often require ad hoc improvements in the context of optimization (Hinze, 2000). If the nozzle flow is studied from the point of view of free surface relaxation after a droplet has already been formed, reduced order models: control volume approach (Wassink, 2007) or lumped element modelling (He et al., 2015; Shah et al., 2019) can be applied, if other free surface modelling tools are not available.

1.2 Optimization

1.2.1 Optimization of drop-on-demand inkjet systems

The main optimization objectives in inkjet printing are consistent droplet velocity and volume (Gan et al., 2009) and increasing the jetting frequency (Miers and Zhou, 2017). There are three groups of inkjet system parameters that can be altered to improve the inkjet performance: ink type or composition, the shape of the inkjet printhead microchannels, and the shape of the actuating waveform.

Experimental studies (Chen and Basaran, 2002; Jo et al., 2009) and computational analysis (Xu and Basaran, 2007) show that the drop formation regime and drop characteristics are determined by nondimensional characteristic numbers: the Weber number (ratio of fluid inertia to surface tension), and the Ohnesorge number (importance of the viscous force relative to the surface tension). The jetting behaviour can be

passively optimized by changing the fluid composition (Liu and Derby, 2019), or by adding small amounts of polymers (Hoath et al., 2015; Shore and Harrison, 2005).

Shape optimization

Changing the shape of the printhead microchannels is another promising approach to passively improve the performance of an inkjet system (Kungurtsev and Juniper, 2019). Kim et al. (2018) analysed the effect of the nozzle diameter and length and the length of the acoustic channel on the maximum jetting frequency. Reducing the nozzle diameter allows jetting at megahertz frequency and smaller droplet size (Miers and Zhou, 2017). However, no systematic approach to estimate the sensitivity of inkjet performance metrics with respect to the generic shape parameters has been reported.

Waveform optimization

Active control of the printing process is done by applying a fine-tuned actuating waveform to the piezo element that drives the ink drop formation (Gan et al., 2009) and damps residual oscillations and the cross-talk effects (Khalate et al., 2011, 2012). Waveform optimization does not require any hardware changes and is regularly applied to existing print heads, for example when a new ink is being used.

A common approach is to tune the pulse amplitude and duration of a fixed shape waveform (Shin et al., 2011). The most basic waveform is the unipolar (trapezoidal push in) waveform. Bogy and Talke (1984) concluded that the optimal pulse width is L/c_s, i.e., proportional to the length of the jetting device L_c, and the inverse of the speed of sound c_s (for a standard inkjet microchannel (Dijksman, 2019), the length L_c is the distance between the ink supply manifold and the nozzle, and the distance from the inflow to the outflow boundary for a through flow (Strevens et al., 2020) inkjet, see figure 1.2). This waveform has a number of drawbacks: the volume of the ejected droplets is large, the amplitude of residual reverberations is high, and satellite droplets are formed in addition to the main droplet (Kwon, 2009). Bipolar (trapezoidal push in then trapezoidal pull out) waveforms are used to eliminate satellite droplets (Gan et al., 2009). The W-shaped waveform type can significantly reduce the volume of ejected droplet, compared with unipolar and bipolar waveforms (Chen and Basaran, 2002), and eliminate the residual acoustic waves from the last ejection cycle (Gan et al., 2009). Droplets formed from complex waveforms are, however, more sensitive to changes in the waveform shape. This means that optimal waveforms become harder to find as the waveform type becomes more complex. Given that waveforms are usually found by trial and error during extensive experiments, this leads to considerable experimental cost as

the waveforms become more complex and motivates the more systematic approach in this thesis.

Systematic waveform optimization can be approached in several ways. A feed-forward control method (Khalate et al., 2011) can be used to eliminate residual reverberations by flattening the response of the meniscus velocity to the pulse frequency. If numerical models are not accurate enough, or are too computationally expensive to predict the droplet characteristics, then the waveform parameter space can be explored with model-free methods by combining an automated experimental rig with an optimization algorithm (Ezzeldin et al., 2010). The waveform shape is the experimental input and the droplet characteristics are the experimental output. This method has been used with a genetic algorithm (Snyder et al., 2019) and a swarm-intelligence based technique (He et al., 2015). Alternatively, a highly efficient adjoint-based approach of instantaneous control applied to unsteady incompressible flow has been developed by Gunzburger and Manservisi (2000); Hinze (2000), and extended by Fumagalli et al. (2018) to the free surface problem inside the inkjet nozzle. The approach developed in this study (also, Kungurtsev and Juniper (2020)) is similar, in that it considers a systematic approach to waveform optimization by using adjoint-based optimization, but it includes the acoustics in the channel as well as the flow in the nozzle.

1.2.2 Adjoint-based sensitivity analysis

Many problems in mathematical physics can be formulated as follows: find an optimal input $\mathbf{f}$ to a complex system that minimizes (or maximizes) some objective value $\mathcal{J}$. The state of the system $\mathbf{q}$ (a scalar or a vector of numbers or functions) usually explicitly defines the objective value: the objective is a function of the state $\mathcal{J} = \mathcal{J}(\mathbf{q})$. It is cheap to evaluate the objective given the state of the system. There is a matrix or a differential operator $\mathcal{A}$ that relates the input $\mathbf{f}$ to the state $\mathbf{q}$. Calculating the state of the system is quite often computationally expensive.

Gradient-based optimization algorithms are used to find a local minimum of the objective functions with respect to input parameters. Adjoint-based optimization is much faster than non-gradient-based or tangent-linear gradient-based methods when the number of control parameters greatly exceeds the number of objective functions, which is usually the case. If gradient vectors are calculated directly using the finite-difference approach, $N + 1$ (expensive) primal state evaluations are required, where N is the number of input parameters. The adjoint methods provide, in a single calculation, the gradient of an objective function with respect to all of the control parameters (Cossu, 2014; Luchini and Bottaro, 2014; Schmid and Brandt, 2014). This

requires only one (expensive) primal state evaluation, and M (cheap) linear adjoint computations, where M is the number of the objective functions. This gradient is then used within a gradient-based optimization algorithm in order to converge to a local optimum, and greatly speeds up optimization. It has been used in aerodynamics optimization (Nadarajah and Jameson, 2000), triggering in thermoacoustics (Juniper, 2011), hydrodynamic stability (Brewster and Juniper, 2020), and finding the minimal seed in transition to turbulence (Kerswell, 2018). Kast (2016) discussed the application of the adjoint method to error estimation and mesh adaptation.

A comprehensive introduction to the theory of adjoint operators, duality, and the underlying functional analysis is presented in Estep (2004). Here we briefly discuss the main ideas and the beauty of the adjoint method. We start by considering a linear operator $\mathcal{A}$ and a linear objective $\mathcal{J}$ function. In this case, the optimization problem is

$$\begin{aligned} &\text{Minimize } \mathcal{J} \equiv (\mathbf{v}, \mathbf{q}) \\ &\text{subject to } \mathcal{A}\mathbf{q} = \mathbf{f}, \end{aligned} \tag{1.1}$$

where $(\cdot\ , \cdot)$ is an appropriately defined scalar product, and $(\mathbf{v}, \cdot)$ is the linear objective function operator. The scalar product of the state equation residual $\mathbf{r} \equiv \mathcal{A}\mathbf{q} - \mathbf{f} = 0$ with an arbitrary function (vector) λ is always zero,

$$(\lambda, \mathbf{r}) = (\lambda, \mathcal{A}\mathbf{q} - \mathbf{f}) \equiv 0.$$

Let us define the *adjoint* operator $\mathcal{A}^\dagger$:

$$(u, \mathcal{A}v) = \left(\mathcal{A}^\dagger u, v\right) \quad \forall u, v. \tag{1.2}$$

The residual scalar product becomes

$$(\lambda, \mathcal{A}\mathbf{q}) - (\lambda, \mathbf{f}) = \left(\mathcal{A}^\dagger \lambda, \mathbf{q}\right) - (\lambda, \mathbf{f}) = 0.$$

Since the above expression is true for all λ, we can choose this variable to satisfy the following equation:

$$\mathcal{A}^\dagger \lambda = \mathbf{v}, \tag{1.3}$$

and therefore the objective function that previously implicitly depended on the input parameters $\mathbf{f}$ can be rewritten as an explicit expression $\mathcal{J} = (\mathbf{v}, \mathbf{q}) = \left(\mathcal{A}^\dagger \lambda, \mathbf{q}\right) = (\lambda, \mathbf{f})$. The *adjoint* state variable λ expresses the sensitivity of the objective function $\mathcal{J}$ with respect to the input parameters $\mathbf{f}$. In this linear case, a single calculation of the adjoint

equation (1.3) is required to get the objective value, while the state equation from (1.1) is never used.

The linear case can be generalized to nonlinear differential operators, commonly arising in CFD. Let $\mathcal{A}$ be a nonlinear differential operator, such that $\mathcal{A}\mathbf{q} = \mathbf{f}$ is a nonlinear state equation. The objective function is also a nonlinear function of $\mathbf{q}$. We can linearize the state equation and the objective around a *base* state $(\mathbf{f}_0, \mathbf{q}_0)$, given an arbitrary admissible variation of the state $\delta\mathbf{q}$:

$$\begin{aligned} \delta\mathcal{J}\left[\delta\mathbf{q}\right] &= \left(\mathcal{J}'_{\mathbf{q}}\left(\mathbf{q}_0\right), \delta\mathbf{q}\right), \\ \mathcal{A}'\left(\mathbf{q}_0\right)\delta\mathbf{q} - \delta\mathbf{f} &= 0. \end{aligned} \tag{1.4}$$

The variation of the objective function $\delta\mathcal{J}\left[\delta\mathbf{q}\right]$ equals the scalar product of the state variation $\delta\mathbf{q}$ and the objective function's sensitivity $\mathcal{J}'_{\mathbf{q}}$ with respect to the state variation. As for the previous case, this is a linear form, and the derivative of the objective function can be calculated using the adjoint approach: given the base state $\mathbf{q}_0$, the linear adjoint operator $\mathcal{A}^\dagger$ can be defined. By solving the adjoint state equation and finding λ, the sensitivity of the objective function with respect to the variation of the input parameters $\delta\mathbf{f}$ is available immediately.

$$\begin{aligned} \mathcal{A}\mathbf{q}_0 &= \mathbf{f}_0, \\ \mathcal{A}^\dagger: \quad \left(u, \mathcal{A}'\left(\mathbf{q}_0\right)v\right) &= \left(\mathcal{A}^\dagger u, v\right), \\ \mathcal{A}^\dagger\lambda &= \mathcal{J}'_{\mathbf{q}}\left(\mathbf{q}_0\right), \\ \delta\mathcal{J} &= \left(\lambda, \delta\mathbf{f}\right). \end{aligned} \tag{1.5}$$

The adjoint method can be applied to calculate the objective sensitivity not only to explicit input parameters, such as external forcing, initial or boundary conditions, spatial distribution of material properties, but also to the shape of the physical domain. In combination with gradient-based optimization algorithms, adjoint-based shape sensitivity analysis is a powerful tool that has been applied to the design of airfoils (Jameson and Martinelli, 2000), mixing of fluids (Eggl and Schmid, 2020), hydrodynamic instability (Brewster and Juniper, 2020) and thermoacoustic stability (Aguilar and Juniper, 2020).

1.3 Thesis scope and structure

The scope of the thesis is to: (i) develop accurate and computationally efficient models of the inkjet printhead microchannel flow, and implement a high level programming interface that automates the solution of such problems; (ii) define the optimization objectives and control parameters of the drop-on-demand inkjet systems; and (iii) develop an interpretable optimal control approach, and apply it to the inkjet flow.

Chapter 2 discusses the inkjet flow models. We split the inkjet printhead microchannel into the channel and the nozzle domain with different governing equations for each. For the channel domain, we use the low Mach number asymptotic analysis to separate the compressible Navier–Stokes equations into equations for an incompressible flow with no acoustic oscillations and equations for acoustic oscillations with no mean flow. We derive the weak forms of the unsteady and frequency domain oscillating thermoviscous acoustic flow, and use the finite element method to discretize and solve the problem numerically. For the nozzle domain, we use the mass and energy conservation equations to construct a reduced order model of an axisymmetric free surface flow. We develop a general approach to couple the channel to the nozzle through the boundary conditions on the surface between the channel and the nozzle. Finally, we study the spectrum and the frequency response of the coupled channel–nozzle inkjet system.

Chapters 3 and 4 contain the main results and the original contributions. Chapter 3 contains the derivation of the adjoint-based sensitivity analysis to external forcing applied at the actuator boundary. We define a cost function to be the sum of the acoustic energy in the channel and the surface energy of the spherical cap of ink at the end of the nozzle. We use a gradient-based optimization algorithm to find the optimal boundary condition that minimizes the cost function at various final times and for geometries with increasing complexity. We discuss the physical interpretation of the optimal waveform shape that eliminates residual oscillations after a droplet is ejected. Chapter 4 contains the derivation of the adjoint-based sensitivity analysis of the systems presented in chapter 2 to shape modifications of the channel. We obtain expressions for the gradient of two objective functions: the viscous dissipation of the steady flow and the dissipation of the oscillations with respect to boundary deformations in Hadamard form. We combine these with a gradient-based optimization algorithm, which quickly converges to a design that has the same viscous dissipation for the steady flow but a 50% larger decay rate for the oscillating flow. We show that this design is nearly optimal.

Chapter 5 contains the summary of the thesis results and suggestions of future work.

Chapter 2

Inkjet printhead flow models

In this chapter we develop an accurate and computationally feasible approach to model flows inside microscale devices, in particular inkjet printhead microchannels. The characteristic timescale of the processes of interest is tenths of microseconds, and the characteristic size of the microchannels is from several micrometers to a few millimeters. The flow disturbances propagate at the speed of sound. For a typical speed of sound of 1000 ms^{-1}, there are only a few wave reflections in the relevant observation time, so the flow compressibility cannot be neglected. Additionally, dissipation due to viscous and thermal effects in the boundary layers cannot be ignored.

This study focuses on one particular type of drop-on-demand inkjet printhead: a U-shaped microchannel connected to the ink supply manifolds, with a small conic nozzle and a flat piezoelectric actuator located on the channel's top boundary opposite the nozzle (figure 2.1). There are several sources of fluid motion inside a microchannel. The steady mean flow of ink is continually pumped through the microchannels and flushes away any air bubbles (de Jong et al., 2006; Fraters et al., 2019) and also reduces the chance that any solid impurities become lodged in the nozzle. An electric signal is applied to a piezoelectric actuator that moves the boundary by a few hundred nanometers at a frequency of up to several megahertz, forcing an ink droplet out of the nozzle (Bogy and Talke, 1984). This generates acoustic waves that travel along the channel and decay through viscous and thermal effects. The fluid–air interface in the inkjet nozzle deforms when the acoustic waves reflect off the interface, and ultimately ink droplets are forced out of the nozzle.

In section 2.2, we discuss how to reduce the complexity of the problem by splitting the full compressible Navier–Stokes equations into equations for a steady mean flow with no oscillation and equations for an oscillation with no mean flow. This is done by a two-parameter low Mach number asymptotic expansion of the equations of motion

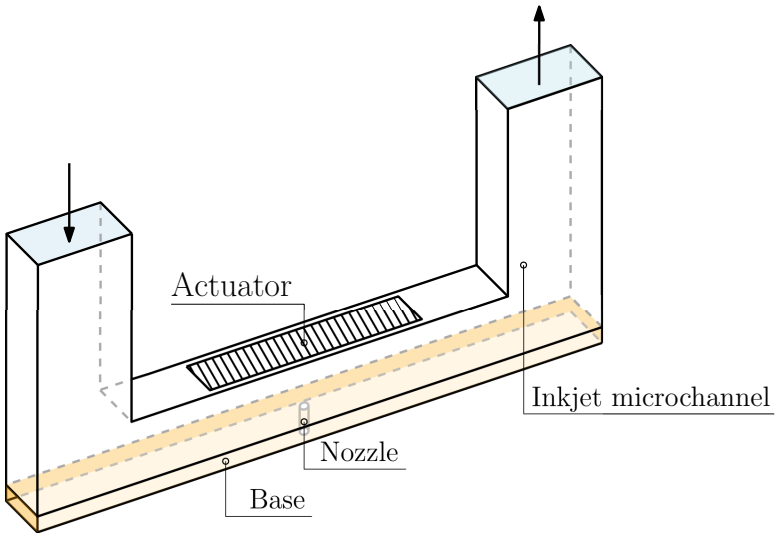

Fig. 2.1 Schematic representation of a 3D inkjet microchannel. The arrows indicate the inflow and the outflow of the recirculating ink throughflow.

(Culick et al., 2012; Müller, 1998). The steady flow is governed by the incompressible Navier–Stokes equations. The oscillating flow is governed by the thermoviscous acoustic equations.

The fluid inside a printhead microchannel is bounded by the channel's solid walls, inlet and outlet boundaries between the channel and the ink supply manifolds, and a free surface in the nozzle: a multiphase interface between the fluid and the outside gaseous phase (air). The physical domain occupied by the fluid moves: the position of the free surface and the three-phase contact line between the nozzle walls, fluid, and air changes over time. We split the printhead microchannel into two nonoverlapping parts: the static channel domain Ω_c, and the moving nozzle domain Ω_n (figure 2.2). The boundary between the Ω_c and Ω_n subdomains is static and splits the inkjet nozzle into two parts. It is chosen such that the fluid–air interface never intersects with the boundaries between the subdomains. The nozzle subdomain includes the bottom part of the inkjet nozzle with the moving fluid–air interface. The channel subdomain covers the rest of the printhead microchannel and the top part of the inkjet nozzle. This allows us to address modelling of the free surface movement separately from the fluid motion inside the channel. In section 2.3, we focus on the oscillating flow equations inside the channel domain: acoustics with thermal and viscous effects. We define the unsteady, frequency domain, and eigenvalue thermoviscous acoustic problems. We discuss the corresponding weak formulation of these problems, and time and FEM discretization. Section 2.4 is devoted to modelling the flow inside the nozzle domain and the moving

free surface. The nozzle flow is described by a reduced order model of an axisymmetric flow, with an explicitly parameterized shape of the fluid–gas interface. The resulting ODE system is linked to the acoustic channel flow via a boundary condition. This approach allows us to modify and adapt the nozzle flow model for a particular nozzle design, while the the flow model inside the rest of the microchannel remains the same. In this thesis, modelling is performed in a 2D domain. Extension to 3D is possible and conceptually straightforward.

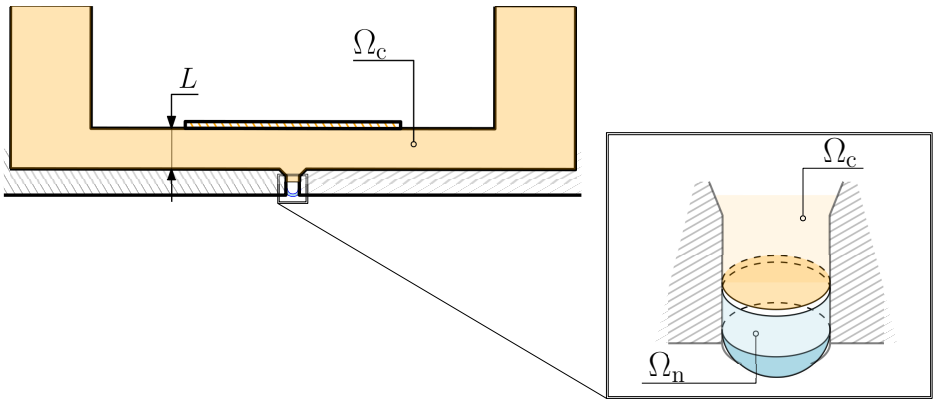

Fig. 2.2 Inkjet printhead microchannel consists of a channel Ω_c (oragne) and nozzle Ω_n (blue) subdomains.

Summing up, we propose a modular approach to describe how different phenomena contribute to the physics of the flow inside the printhead microchannel: we start with adding the most important flow models (thermoviscous acoustic flow, nozzle flow reduced order model) independently of each other (figure 2.3). Then, we work towards coupling the flow models via boundary conditions. We can add more physical effects or substitute the existing models with more advanced ones while keeping other parts unchanged. This accelerates development and testing, and allows finer control over the whole system, especially for industrial scale projects. In section 2.7.1 we discuss which physical effects are not considered in the system in figure 2.3, and what the requirements are to formulate the corresponding models.

2.1 Notation

We denote the spatial domain by $\Omega \subset \mathbb{R}^d$, $d = 1, 2, 3$, and the boundary of the domain by $\partial\Omega = \bigcup \Gamma_i \subset \mathbb{R}^{d-1}$. We denote the temporal domain of an unsteady problem by $\mathcal{T} = \{t : t_0 < t < t_f\}$, where t_0 and t_f are the initial and the final times, respectively.

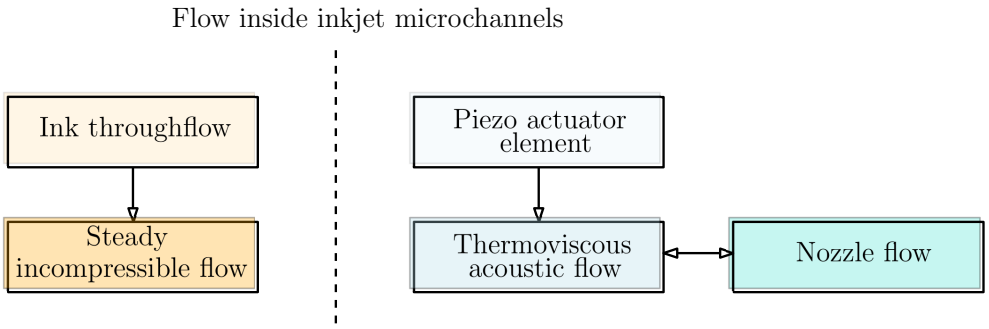

Fig. 2.3 Example model components diagram of the flow inside an inkjet printhead microchannel. Arrows denote interactions between models; a connection with one arrow means that there is no feedback from the receiving model, and a connection with a forward and a reverse arrow means that the models are two-way coupled.

We denote the joint time-space mixed domain of the problem by $\Sigma = (\Omega \times \mathcal{T})$, and $\partial\Sigma = (\partial\Omega \times \mathcal{T})$. A problem can be independent of time or a spatial coordinate.

We define the following scalar products in the spatial, temporal, and mixed domains:

$$[a,b]_\Sigma \equiv \int_{\mathcal{T}}\int_{\Omega} a^* \; b \; \mathrm{d}t\mathrm{d}\mathbf{x}, \quad \{a,b\}_{\partial\Sigma} \equiv \int_{\mathcal{T}}\int_{\partial\Omega} a^* \; b \; \mathrm{d}t\mathrm{d}\mathbf{s}, \tag{2.1a}$$

$$\langle a,b\rangle_\Omega \equiv \int_{\Omega} a^* \; b \; \mathrm{d}\mathbf{x}, \quad \{a,b\}_{\Gamma_i} \equiv \int_{\Gamma_i} a^* \; b \; \mathrm{d}\mathbf{s}, \tag{2.1b}$$

$$(a,b)_{\mathcal{T}} = \int_{\mathcal{T}} a^* \; b \; \mathrm{d}t. \tag{2.1c}$$

Here * denotes complex conjugation. An integral of a single variable over a domain is equivalent to the corresponding scalar product with $a \equiv 1$, $\langle b\rangle_\Omega \equiv \langle 1, b\rangle_\Omega$.

2.2 Equations of motion in the low Mach number limit

The motion of a fluid with viscosity, heat conductivity and compressibility is governed by the compressible Navier–Stokes equations, which, in conservative form, are given by:

$$\frac{\partial}{\partial t}\mathbf{q} + \nabla_j \left(\mathbf{f}_j^c(\mathbf{q}) - \mathbf{f}_j^v(\mathbf{q}, \nabla\mathbf{q})\right) = 0 \quad \text{in } \Omega, \tag{2.2}$$

where ∇_j is the j-th component of the spatial derivative $\nabla_j \equiv \frac{\partial}{\partial x_j}$, $\mathbf{f}^c$ and $\mathbf{f}^v$ refer to convective and viscous components of the equations. The vector of conservative

variables, $\mathbf{q}$, and the fluxes, $\mathbf{f}^c(\mathbf{q}), \mathbf{f}^v(\mathbf{q})$, are defined by

$$\mathbf{q} \equiv \begin{bmatrix} \rho \\ \rho u_i \\ \rho E \end{bmatrix}, \quad \mathbf{f}^c_j(\mathbf{q}) = \begin{bmatrix} \rho u_k \\ \rho u_i u_j + P\delta_{ik} \\ u_j\left(\rho E + P\right) \end{bmatrix}, \quad \mathbf{f}^v_j(\mathbf{q}) = \begin{bmatrix} 0 \\ \tau_{ji} \\ \tau_{ji}u_i + \kappa_{\text{th}}\nabla_j T \end{bmatrix} \tag{2.3}$$

The variables $\rho, \mathbf{u}, P, T$ denote the flow density, velocity vector, pressure and temperature; τ_{ij} is the viscous stress tensor, which is proportional to the dynamic viscosity coefficient μ_{vis}

$$\tau_{ij} = \mu_{vis}\left(\nabla_i u_j + \nabla_j u_i - \frac{2}{3}\delta_{ij}\nabla_k u_k\right). \tag{2.4}$$

Most of the standard inks used in printing are Newtonian (Basaran et al., 2013; Derby, 2010; Dijksman, 2019), so here the viscosity μ_{vis} is held constant. The total energy of the flow E is a sum of the kinetic energy and the static internal energy $e = e(T, P)$:

$$\rho E = \rho e + \frac{\rho u_i u_i}{2}, \tag{2.5}$$

and κ_{th} is the thermal conductivity coefficient. We also introduce an equation of state, which relates the pressure, density and temperature:

$$\rho = \rho(P, T) \tag{2.6}$$

Without loss of generality, we will use the flow velocity, pressure, and temperature as the primary variables.

2.2.1 Low Mach number expansion

Equation (2.2) can describe a range of physical phenomena, which is excessive in this case because the system's behaviour is governed to first order by only two phenomena. The first is steady flow in a channel with rigid boundaries, with the inlet velocity of order $\bar{U} = 1$ m/s and $Re \approx 10$. The second is periodic acoustic oscillation, with a small displacement amplitude at the boundary $\Delta \leq 0.1\mu$m and a high oscillation frequency $\omega \approx 100$ kHz. The characteristic oscillation velocity is of order $\tilde{U} = \omega\Delta \approx 0.01$ m/s.

We choose the ambient state density ρ^b and the speed of sound $\left(c_s^b\right)^2 = \left(\partial P/\partial\rho\right)_s$ (Landau and Lifschitz, 1986; Wang and Millero, 1973) as the reference dimensional density and velocity, and the characteristic domain size L as the reference length.

The reference pressure P^b is chosen as a function of density and the speed of sound: $P^b = \rho^b \left(c_s^b\right)^2$, and the reference temperature T^b is the ambient temperature.

In this problem, we assume that the local Mach number is small:

$$M \equiv \frac{\|\mathbf{u}\|}{c_s^b} \ll 1 \tag{2.7}$$

The characteristic velocity amplitudes of the steady flow, $\bar{U}$, and the oscillating flow, $\tilde{U}$, are also small in comparison to the speed of sound, which allows us to introduce two small parameters: the steady flow Mach number, μ, and the oscillating flow Mach number, ϵ:

$$\mu \equiv \frac{\bar{U}}{c_s^b} \simeq \frac{1.0}{1000} \ll 1, \tag{2.8a}$$

$$\epsilon \equiv \frac{\tilde{U}}{c_s^b} \simeq \frac{0.1}{1000} \ll 1 \tag{2.8b}$$

The oscillating flow time scale differs greatly from the steady flow time scale. The oscillating time scale is $t_{\text{ac}} \sim L/c_s^b$, and the steady flow time scale is $t_{\text{hyd}} \sim L/\bar{U} = \mu^{-1} t_{\text{ac}} \gg t_{\text{ac}}$. This allows us to decouple two phenomena and study them independently. We consider a generic state variable $\psi(\mathbf{x}, t) = (\mathbf{u}, P, T)$. We denote a zero-order state variable by $\psi_0(\mathbf{x}, t)$, as if the steady flow and the oscillating flow were absent: $\psi_0(\mathbf{x}, t) \equiv \psi(\mathbf{x}, t, \epsilon = 0, \mu = 0)$. If there is no external energy and momentum production (by imposed temperature gradients, heat release or body forces), then ψ_0 is uniform in space and constant in time. The perturbation $\phi(\mathbf{x}, t)$ of ψ is proportional to μ and ϵ, such that:

$$\psi(\mathbf{x}, t) = \psi_0 + \phi(\mathbf{x}, t, \mu, \epsilon) \tag{2.9}$$

We assume that a flow state perturbation related to a particular phenomenon depends solely on the phenomenon's temporal scale, such that $\phi(\mathbf{x}, t)$ becomes a sum of the slow hydrodynamic perturbation $\bar{\phi}(\mathbf{x}, t, \mu)$, labelled the steady flow, and the fast acoustic perturbation $\tilde{\phi}(\mathbf{x}, t, \epsilon)$, labelled the oscillating flow:

$$\phi(\mathbf{x}, t, \mu, \epsilon) = \bar{\phi}(\mathbf{x}, t, \mu) + \tilde{\phi}(\mathbf{x}, t, \epsilon), \tag{2.10a}$$

$$\bar{\phi}(\mathbf{x}, t, \mu) = \frac{1}{t_{\text{ac}}} \int_{t_{\text{ac}}} \phi(\mathbf{x}, t, \mu, \epsilon) \mathrm{d}t. \tag{2.10b}$$

In summary, the generic flow variable $\psi(\mathbf{x}, t)$ consists of the zero-frequency ambient state, ψ_0, the low-frequency hydrodynamic perturbation $\bar{\phi}(\mathbf{x}, t_{\text{hyd}}, \mu)$, and the high-

frequency acoustic perturbation $\tilde{\phi}(\mathbf{x}, t_{\text{ac}}, \epsilon)$:

$$\psi(\mathbf{x}, t) = \psi_0 + \bar{\phi}(\mathbf{x}, t_{\text{hyd}}, \mu) + \tilde{\phi}(\mathbf{x}, t_{\text{ac}}, \epsilon) \tag{2.11}$$

We can perform a low Mach number expansion in terms of μ and ϵ because they are both small. The state perturbations $\bar{\phi}(\mathbf{x}, t_{\text{hyd}})$ and $\tilde{\phi}(\mathbf{x}, t_{\text{ac}})$ independently tend to zero as $\mu \to 0$ and $\epsilon \to 0$, so we assume low Mach-number decompositions of the form

$$\bar{\phi}(\mathbf{x}, t_{\text{hyd}}) = \left\|\bar{\phi}\right\| \sum \mu^k \bar{\phi}^{(k)}(\mathbf{x}, t_{\text{hyd}}),$$

and

$$\tilde{\phi}(\mathbf{x}, t_{\text{ac}}) = \left\|\tilde{\phi}\right\| \sum \epsilon^k \tilde{\phi}^{(k)}(\mathbf{x}, t_{\text{ac}}),$$

where $\bar{\phi}^{(k)}, \tilde{\phi}^{(k)}$ are the k-th order non-dimensional perturbation shapes, and $\left\|\bar{\phi}\right\|, \left\|\tilde{\phi}\right\|$ are the characteristic dimensional magnitudes of the variables: $\|\bar{\mathbf{u}}\| = \bar{U}, \|\tilde{\mathbf{u}}\| = \tilde{U}, \left\|\bar{P}\right\| = \left\|\tilde{P}\right\| = P^b, \left\|\bar{T}\right\| = \left\|\tilde{T}\right\| = T^b$.

We neglect the interaction between the steady flow and the oscillating flow given by the higher order mixed terms $\sum \mu^n \epsilon^m \phi^{(m+n)}(\mathbf{x}, t_{\text{ac}}, t_{\text{hyd}})$; $m, n \geq 1$ because ϵ and μ are both small. The expansion of the primal variables is therefore:

$$\mathbf{u}(\mathbf{x}, t) = c_s^b \left(\mu \bar{\mathbf{u}}^{(1)} + \epsilon \tilde{\mathbf{u}}^{(1)}\right) + O(\mu^2, \epsilon^2, \mu\epsilon), \tag{2.12a}$$

$$P(\mathbf{x}, t) = P^b P^{(0)} + P^b \left(\mu \bar{P}^{(1)} + \mu^2 \bar{P}^{(2)} + \epsilon \tilde{P}^{(1)}\right) + O(\mu^3, \epsilon^2, \mu\epsilon), \tag{2.12b}$$

$$T(\mathbf{x}, t) = T^b T^{(0)} + T^b \left(\mu \bar{T}^{(1)} + \epsilon \tilde{T}^{(1)}\right) + O(\mu^2, \epsilon^2, \mu\epsilon) \tag{2.12c}$$

The highest order velocity components are proportional to μ, ϵ to first order. We keep both the first and second order pressure terms $\mu \bar{P}^{(1)} + \mu^2 \bar{P}^{(2)}$ here because the first order steady flow pressure perturbation $\mu \bar{P}^{(1)}$ does not contribute to the steady flow, because it is a part of the ambient state (Müller, 1998).

The expansion of the derivative flow variables, such as density, energy, and entropy can be achieved by substituting the primal variables expansion into the respective thermodynamics expansions, for example,

$$\rho = \rho^{(0)} + \left(\frac{\partial \rho}{\partial P}\right)_T \left(P - P^{(0)}\right) + \left(\frac{\partial \rho}{\partial T}\right)_P \left(T - T^{(0)}\right) + \mathcal{O}\left(\mu^2, \epsilon^2, \mu\epsilon\right)$$

The pressure gradient due to the gravity force is small $\Delta P = gL = 10^{-3}$ Pa in comparison to the ambient pressure $P^b P^{(0)} = 10^5$ Pa, and is therefore neglected. The

nondimensional gravity term $gL/\left(c_s^b\right)^2 = 10^{-9} \ll \epsilon$ is also neglected in the low Mach number oscillating flow equations.

2.2.2 Zero Mach number limit

Substituting the primal variables expansion (2.12) into (2.2) and (2.6), and collecting the zero-order terms, we obtain:

$$\nabla_i P^{(0)}(\mathbf{x}) = 0, \tag{2.13a}$$

$$\nabla_k \left(\kappa_{\text{th}} \nabla_k T^{(0)}(\mathbf{x})\right) = 0, \tag{2.13b}$$

$$\rho^{(0)}(\mathbf{x}) = \rho(P^{(0)}, T^{(0)}). \tag{2.13c}$$

The zeroth-order equations describe the ambient state, $\epsilon = \mu = 0$. Equation (2.13a) shows that the ambient pressure $P^{(0)}$ is spatially uniform, and (2.13b) describes the temperature distribution of the ambient state. If all the boundaries have uniform and constant temperature, then the ambient temperature and density are uniform and non-dimensionalized as $T^{(0)}(\mathbf{x}) = 1, \rho^{(0)}(\mathbf{x}) = 1$.

2.2.3 Low Mach number incompressible flow

We substitute the flow variable expansion (2.12) into (2.3) and collect the first order terms of μ in the continuity equation and the second order terms of μ^2 in the momentum equations. Assuming a Newtonian fluid results in the incompressible Navier–Stokes equation:

$$\nabla_i \bar{u}_i^{(1)} = 0, \tag{2.14a}$$

$$\frac{\partial}{\partial t_{hyd}} \bar{u}_i^{(1)} + \left(\bar{u}_j^{(1)} \nabla_j\right) \bar{u}_i^{(1)} + \nabla_i \bar{P}^{(2)} - \frac{1}{\overline{Re}} \nabla_k^2 \bar{u}_i^{(1)} = 0, \tag{2.14b}$$

where $\overline{Re} \equiv \rho^b L \bar{U}/\mu_{vis}$ is the steady flow Reynolds number. The steady flow pressure perturbation, $\bar{P}$, balances the nonlinear convective term in the momentum equation, so $\bar{P} = \mu^2 \bar{P}^{(2)} + O(\mu^3)$.

We supplement the incompressible flow equations with a prescribed velocity boundary condition at the inlet, Γ_{in}, a no slip boundary condition on the walls, Γ_{w}, and a

zero stress boundary condition at the outlet, Γ_{out}:

$$\bar{\mathbf{u}}^{(1)} = \mathbf{U}_{\text{in}} \quad \text{on } \Gamma_{\text{in}}, \tag{2.15a}$$

$$\bar{\mathbf{u}}^{(1)} = 0 \quad \text{on } \Gamma_{\text{w}}, \tag{2.15b}$$

$$-\bar{P}^{(2)}\mathbf{n} + \frac{1}{Re}\frac{\partial \bar{\mathbf{u}}^{(1)}}{\partial \mathbf{n}} = 0 \quad \text{on } \Gamma_{\text{out}} \tag{2.15c}$$

2.2.4 Low Mach number oscillating flow

We substitute the flow variable expansion (2.12) into (2.3) and collect the first order terms of ϵ. Using the internal energy expansion to first order in ϵ (the first law of thermodynamics),

$$\tilde{e}^{(1)} = T^{(0)}\tilde{\mathrm{S}}^{(1)} + \frac{P^{(0)}}{\left(\rho^{(0)}\right)^2}\tilde{\rho}^{(1)}$$

we obtain the nondimensional continuity, momentum and energy equations for the oscillating acoustic flow:

$$\frac{\partial}{\partial t_{\text{ac}}}\tilde{\rho}^{(1)} + \nabla_i \tilde{u}_i^{(1)} = 0, \tag{2.16a}$$

$$\frac{\partial}{\partial t_{\text{ac}}}\tilde{u}_i^{(1)} + \nabla_i \tilde{P}^{(1)} = \frac{1}{\tilde{Re}}\nabla_j \tilde{\tau}_{ij}^{(1)}, \tag{2.16b}$$

$$\frac{\left(c_s^b\right)^2}{T^b}\frac{\partial}{\partial t_{\text{ac}}}\tilde{\mathrm{S}}^{(1)} = \frac{c_p}{\tilde{Pe}}\Delta\tilde{T}^{(1)} \tag{2.16c}$$

The Reynolds and Peclet numbers based on the speed of sound are $\tilde{Re} \equiv \rho^b L c_s^b/\mu_{vis}$ and $\tilde{Pe} \equiv \rho^b L c_s^b c_p/\kappa_{\text{th}}$. The heat capacity ratio is $\gamma_{\text{th}} \equiv c_p/c_v$, where c_p and c_v are the specific heats at constant pressure and constant volume. In this study, the speed of sound is one of the most crucial parameters. The speed of sound is therefore imposed directly, rather than calculated from an equation of state. The value of the speed of sound used in inkjet studies varies from 800 to 1600 ms^{-1} (Beltman, 1998; Dijksman, 2019; Kim et al., 2014). We use a value of 1000 ms^{-1}. The ratio of specific heats, which describes how much a fluid expands when heated, is slightly greater than 1 for liquids. If taken to be exactly 1, as in Beltman (1998), there is no thermal expansion and the thermal field becomes decoupled from the mechanical field and can be neglected. In this thesis, we wish to consider the more general and accurate case in which this coupling is retained. We therefore use $\gamma_{\text{th}} = 1.017$, which is charactersitic of water at 25°C (Kell, 1970). In any case, for values of gamma just greater than 1, the thermal field has little influence on the problem, meaning that gamma has little influence on the

problem. The viscous contribution to the mechanical energy dissipation $\nabla_k \left(\tilde{\tau}_{kj}^{(1)} \tilde{u}_j^{(1)}\right)$, and the time derivative of the kinetic energy $\frac{\partial}{\partial t_{\mathrm{ac}}} \left(\rho^{(0)} \tilde{u}_i \tilde{u}_i^{(1)}/2\right)$ are absent in (2.16c) because they are second order in ϵ and therefore negligible.

We aim to formulate the acoustic flow equations in terms of the acoustic pressure $\tilde{P}^{(1)}$, velocity $\tilde{\mathbf{u}}^{(1)}$ and temperature $\tilde{T}^{(1)}$. The flow density and entropy are functions of the pressure and temperature variables. Using the classical thermodynamics differentials, they can be explicitly expressed as $\tilde{\mathrm{s}}^{(1)} = \tilde{\mathrm{s}}(\tilde{P}^{(1)}, \tilde{T}^{(1)})$, and $\tilde{\rho}^{(1)} = \tilde{\rho}(\tilde{P}^{(1)}, \tilde{T}^{(1)})$:

$$\mathrm{s}^b \tilde{\mathrm{s}}^{(1)} = \left(\frac{\partial S}{\partial P}\right)_T P^b \tilde{P}^{(1)} + \left(\frac{\partial S}{\partial T}\right)_P T^b \tilde{T}^{(1)} = -\frac{\alpha_p}{\rho_b} P^b \tilde{P}^{(1)} + \frac{c_p}{T_b} T^b \tilde{T}^{(1)}, \tag{2.17a}$$

$$\rho^b \tilde{\rho}^{(1)} = \left(\frac{\partial \rho}{\partial P}\right)_T P^b \tilde{P}^{(1)} + \left(\frac{\partial \rho}{\partial T}\right)_P T^b \tilde{T}^{(1)} = \frac{\gamma_{\mathrm{th}}}{\left(c_s^b\right)^2} P^b \tilde{P}^{(1)} - \rho^b \alpha_p T^b \tilde{T}^{(1)}, \tag{2.17b}$$

where $\alpha_p \equiv \rho^b \left(\frac{\partial V}{\partial T}\right)_P$ is the volumetric coefficient of thermal expansion, and has dimension of temperature. These expressions are substituted into (2.16). For convenience, we redefine the acoustic flow temperature as $\alpha_p T^b \tilde{T}^{(1)} \to \tilde{T}^{(1)}$. We also note that $c_p - c_v = T^b \left(c_s^b\right)^2 \alpha_p^2 / \gamma_{\mathrm{th}}$. The density and entropy variables are expressed as:

$$\tilde{\rho}^{(1)} \equiv \gamma_{\mathrm{th}} \tilde{P}^{(1)} - \tilde{T}^{(1)}, \quad \tilde{\mathrm{s}}^{(1)} \equiv \frac{\tilde{T}^{(1)}}{\gamma_{\mathrm{th}} - 1} - \tilde{P}^{(1)} \tag{2.18}$$

These explicit expressions for the density and entropy variables allow us to express the continuity (2.16ba), momentum (2.16b) and energy (2.16c) equations in terms of the primal acoustic variables:

$$\frac{\partial}{\partial t_{ac}} \left(\gamma_{\mathrm{th}} \tilde{P}^{(1)} - \tilde{T}^{(1)}\right) + \nabla_i \tilde{u}_i^{(1)} = 0, \tag{2.19a}$$

$$\frac{\partial}{\partial t_{\mathrm{ac}}} \tilde{u}_i^{(1)} + \nabla_i \tilde{P}^{(1)} = \frac{1}{\tilde{Re}} \nabla_j \tilde{\tau}_{ij}^{(1)}, \tag{2.19b}$$

$$\frac{\partial}{\partial t_{ac}} \left(\frac{\tilde{T}^{(1)}}{\gamma_{\mathrm{th}} - 1} - \tilde{P}^{(1)}\right) = \frac{1}{\left(\gamma_{\mathrm{th}} - 1\right) \tilde{Pe}} \Delta \tilde{T}^{(1)} \tag{2.19c}$$

Here $\Delta \equiv \nabla^2$ is the Laplace operator. This is a system of linear thermoviscous acoustic equations. No-slip $\tilde{\mathbf{u}}^{(1)} = 0$ and isothermal $\tilde{T}^{(1)} = 0$ walls induce viscous and thermal boundary layers, which damp the acoustic waves. The thickness of the viscous boundary layer δ_ν and the thermal boundary layer δ_T depends on the oscillation frequency (Beltman, 1999b): $\delta_\nu(\omega) = \sqrt{\mu_{vis}/(\rho^b \omega)} = \delta_T \sqrt{Pr}$. The non-dimensional

viscous and thermal boundary layers thicknesses, $\tilde{\delta}_\nu(\omega), \tilde{\delta}_T(\omega)$, are:

$$\tilde{\delta}_\nu^2(\omega) = \frac{\delta_\nu^2(\omega)}{L^2} = \frac{1}{\tilde{R}e}\frac{\omega_{ac}}{\omega}, \quad \tilde{\delta}_T^2(\omega) = \frac{\delta_T^2(\omega)}{L^2} = \frac{1}{\tilde{P}e}\frac{\omega_{ac}}{\omega}, \tag{2.20}$$

where $\omega_{ac} = t_{ac}^{-1}$ is the characteristic acoustic frequency. If the oscillation frequency, ω, is similar to or smaller than the acoustic frequency, ω_{ac}, then the viscothermal effects cannot be ignored for general $\tilde{R}e, \tilde{P}e$. This is true for inkjet printhead microchannels: the fluid viscosity is of order 10^{-2} Pa·s, the speed of sound is 10^3 ms^{-1}, and the channel width is of order 100μm, which results in $\omega_{ac} = 10$ MHz. For inks used in inkjet printers, with $10 < Pr < 30$ (Seccombe, 1997), $\tilde{\delta}_T \sim 0.025$. At the typical operational frequency of $\omega = 100$kHz the viscous boundary layer thickness is then $\tilde{\delta}_\nu \sim 0.1$. The thermal boundary layer thickness is smaller by a factor of $\sqrt{Pr}$.

In the absense of inhomogeneous initial or boundary condition on $\tilde{T}^{(1)}$, thermal dissipation becomes less influential as γ_{th} decreases towards 1. The energy equation (2.19c) can be rewritten as a heat equation with a source term:

$$\frac{\partial}{\partial t_{ac}}\tilde{T}^{(1)} - \frac{1}{\tilde{P}e}\Delta\tilde{T}^{(1)} = (\gamma_{\text{th}} - 1)\,\tilde{P}^{(1)}.$$

If $\gamma_{\text{th}} \to 1$, the magnitude of the temperature variable is small: $\tilde{T}^{(1)} \sim (\gamma_{\text{th}} - 1)\,\tilde{P}^{(1)} \ll \tilde{P}^{(1)}$, and $\tilde{T}^{(1)}$ can be ignored in the continuity equation (2.19a):

$$\frac{\partial}{\partial t_{ac}}\tilde{P}^{(1)} + \nabla_i\tilde{u}_i^{(1)} = \frac{\partial}{\partial t_{ac}}\left(\tilde{T}^{(1)} - (\gamma_{\text{th}} - 1)\,\tilde{P}^{(1)}\right) = \mathcal{O}\left(\gamma_{\text{th}} - 1\right).$$

In this case, the continuity and the momentum equations become independent of the temperature component, and the oscillating flow is governed by the viscous acoustic equations. We retain the energy equation such that further analysis is applicable for all possible values of γ_{th}. The thermal contribution can be omitted in numerical simulations of a flow in inkjet microchannels, unless the flow is driven by thermal effects.

2.3 Thermoviscous acoustic flow

2.3.1 General formulation

The thermoviscous acoustic flow is formulated in terms of the pressure, velocity, and temperature acoustic variables that constitute the acoustic state vector, $\mathbf{q}(\mathbf{x}, t) \equiv (\mathbf{u}, P, T)$.

The acoustic flow is defined in a one-, two-, or three-dimensional nondeforming domain $\Omega \subset \mathbb{R}^d$, $d = 1, 2, 3$, where $\partial\Omega = \bigcup \Gamma_i \subset \mathbb{R}^{d-1}$ is the boundary. The temporal domain of the problem is $\mathcal{T} = \{t : 0 < t < t_f\}$, where t_f is the final time. The joint time-space domain is $\Sigma = (\Omega \times \mathcal{T})$. We write the governing equation (2.19) in matrix form:

$$\frac{\partial}{\partial t}\mathrm{A}\mathbf{q}(\mathbf{x}, t) + \mathrm{B}\mathbf{q}(\mathbf{x}, t) = 0 \quad \text{in } \Sigma, \tag{2.21a}$$

$$\mathrm{A} \equiv \begin{bmatrix} 1 & 0 & 0 \\ 0 & \gamma_{\mathrm{th}} & -1 \\ 0 & -1 & \frac{1}{\gamma_{\mathrm{th}}-1} \end{bmatrix}, \quad \mathrm{B} \equiv \begin{bmatrix} -\frac{1}{\tilde{R}e}\nabla_j \boldsymbol{\tau}_{ij} & \nabla_i & 0 \\ \nabla_i & 0 & 0 \\ 0 & 0 & -\frac{\Delta}{(\gamma_{\mathrm{th}}-1)\tilde{P}e} \end{bmatrix}. \tag{2.21b}$$

Here $\boldsymbol{\tau}_{ij}$ is a viscous stress tensor operator: $\boldsymbol{\tau}_{ij} u_i \equiv \tau_{ij}$. We introduce the symmetric stress tensor, σ_{ij}:

$$\sigma_{ij} \equiv -P\delta_{ij} + \frac{1}{\tilde{R}e}\tau_{ij}. \tag{2.22}$$

The thermoviscous acoustic problem initial condition at $t = 0$ is

$$\mathbf{q}(\mathbf{x}, t = 0) = \mathbf{q}_0(\mathbf{x}). \tag{2.23}$$

For the domain boundaries $\partial\Omega = \bigcup \Gamma_i$, either the velocity $\mathcal{U}$ or force $\mathbf{f}$ is prescribed at the boundary. We apply homogeneous no slip and stress-free boundary conditions by setting $\mathcal{U} = 0$ on no slip boundaries, and $\mathbf{f} = 0$ on stress-free (outlet) boundaries:

$$\mathbf{u} = \mathcal{U} \quad \text{on } \Gamma_{\mathrm{in}}, \quad \mathbf{u} = 0 \quad \text{on } \Gamma_{\mathrm{w}}, \tag{2.24a}$$

$$\sigma_{ij} n_j = f_i \quad \text{on } \Gamma_{\mathrm{force}}, \quad \sigma_{ij} n_j = 0 \quad \text{on } \Gamma_{\mathrm{out}}. \tag{2.24b}$$

The same applies to the temperature and heat flux boundary conditions, and the homogeneous isothermal and adiabatic boundary conditions:

$$T = T_0 \quad \text{on } \Gamma_{\mathrm{th}}, \quad \frac{\partial T}{\partial \mathbf{n}} = \kappa_{\mathrm{th}} Q_{\mathrm{heat}} \quad \text{on } \Gamma_{\mathrm{heat}}, \tag{2.25a}$$

$$T = 0 \quad \text{on } \Gamma_{\mathrm{isoth}}, \quad \frac{\partial T}{\partial \mathbf{n}} = 0 \quad \text{on } \Gamma_{\mathrm{adiab}}. \tag{2.25b}$$

It is possible for a boundary condition to represent a particular physical phenomenon, in which case the boundary velocity (or stress) is a function of the acoustic state, $\mathbf{u}(\mathbf{x}, t) = \mathbf{u}\left(\mathbf{q}(\mathbf{x}', t')\right)$ on Γ. If $\mathbf{x} \neq \mathbf{x}'$ or $t > t'$, the boundary condition is non-local in space or time.

2.3.2 Frequency domain and the eigenvalue problems

The unsteady thermoviscous acoustic problem can be analysed in the frequency domain. The thermoviscous acoustic problem (2.21) is linear in $\mathbf{q}$, and we perform a Fourier transform $\mathbf{q}(\mathbf{x},t) \xrightarrow{\mathscr{F}} \hat{\mathbf{q}}_\omega(\mathbf{x})$ for a real-valued frequency $\omega \in \mathbb{R}$ and a complex frequency mode $\hat{\mathbf{q}}_\omega$. If any of the boundary conditions are nonlinear in $\mathbf{q}$, we would also need to linearize them. The time-harmonic equation for a given frequency ω is

$$\begin{aligned} &\text{Find } \hat{\mathbf{q}}_\omega(\mathbf{x}) \text{ such that} \\ &\quad i\omega \mathrm{A}\hat{\mathbf{q}}_\omega + \mathrm{B}\hat{\mathbf{q}}_\omega = 0 \quad \text{in } \Omega. \end{aligned} \tag{2.26}$$

For the thermoviscous acoustic eigenvalue problem, we linearize the acoustic state $\mathbf{q} = \mathbf{q}_0 + \delta\mathbf{q}$ and the boundary conditions, and perform a modal decomposition of the acoustic flow perturbation $\delta\mathbf{q}(\mathbf{x},t) = \hat{\mathbf{q}}(\mathbf{x})e^{st}$. The time derivative operator acts as $\frac{\partial}{\partial t} \to s$. We solve the eigenvalue problem and find the complex eigenfunctions $\hat{\mathbf{q}} = (\hat{\mathbf{u}}, \hat{P}, \hat{T})$ and the corresponding complex eigenvalues $s = \sigma + i\omega$, where $-\sigma$ is the decay rate and ω is the angular frequency of the mode:

$$\begin{aligned} &\text{Find } s, \hat{\mathbf{q}}(\mathbf{x}) \text{ such that} \\ &\quad s\mathrm{A}\hat{\mathbf{q}} + \mathrm{B}\hat{\mathbf{q}} = 0 \quad \text{in } \Omega, \\ &\quad s = \sigma + i\omega. \end{aligned} \tag{2.27}$$

The time-harmonic inhomogeneous velocity and force boundary conditions, and the homogeneous no slip and stress-free boundary conditions are equivalent to the unsteady boundary conditions (2.24). All boundary conditions of the eigenvalue problem (2.27) have to be homogeneous: a no slip condition is applied on both the no slip walls and the inflow boundaries, and a stress-free condition is applied on the both outlet and forced boundaries:

$$\hat{\mathbf{u}} = 0 \quad \text{on } \Gamma_{\mathrm{w}} \bigcup \Gamma_{\mathrm{in}}, \quad \hat{\sigma}_{ij} n_j = 0 \quad \text{on } \Gamma_{\mathrm{free}} \bigcup \Gamma_{\mathrm{force}}. \tag{2.28}$$

Similarly, the isothermal and adiabatic boundary conditions are:

$$\hat{T} = 0 \text{ on } \Gamma_{\mathrm{isoth}}, \quad \frac{\partial \hat{T}}{\partial \mathbf{n}} = 0 \text{ on } \Gamma_{\mathrm{adiab}}. \tag{2.29}$$

If the domain Ω is a symmetric domain, let yz (for 3D problems) or y (for 2D problems) be the symmetry plane located at $x = 0$, and Ω_{s1}, Ω_{s2} be the symmetric subdomains: $\Omega = \Omega_{s1} \bigcup \Omega_{s2}$ and $\Gamma_{\mathrm{sym}} \equiv \Omega_{s1} \bigcap \Omega_{s2}$. We might want to employ the

symmetry of the eigenmodes $\hat{\mathbf{q}}$ in Ω, and solve a smaller eigenvalue problem in a subdomain Ω_{s1} (or Ω_{s2}). The spectrum and the eigenmodes of the original problem can be found by solving the eigenvalue problem in Ω_{s1} with the additional boundary conditions on the symmetry boundary Γ_{sym}. From (2.19b) we notice that the parity of the velocity x-component $\hat{u}_x = \hat{\mathbf{u}} \cdot \mathbf{e}_{\text{x}}$ is different from the velocity y, z-components $\hat{u}_y, \hat{u}_z$ and pressure $\hat{P}$:

$$\frac{\hat{u}_x(-x,y,z)}{\hat{u}_x(x,y,z)} = -\frac{\hat{u}_y(-x,y,z)}{\hat{u}_y(x,y,z)} = -\frac{\hat{u}_z(-x,y,z)}{\hat{u}_z(x,y,z)} = -\frac{\hat{P}(-x,y,z)}{\hat{P}(x,y,z)}.$$

From (2.19c), the parity of the pressure $\hat{P}$ and the temperature $\hat{T}$ functions are the same: $\hat{P}(-x,y,z)/\hat{P}(x,y,z) = \hat{T}(-x,y,z)/\hat{T}(x,y,z)$. Due to the symmetry of the original problem, the components of the eigenmodes can be either even or odd, and therefore there are two possible solutions in the subdomain Ω_{s1} depending on the choice of the symmetry boundary type. The first type of symmetry boundary conditions

$$\hat{\sigma}_{ij} n_j = 0, \ \hat{T} = 0 \quad \text{on } \Gamma_{\text{sym}} \tag{2.30}$$

results in $\hat{u}_x$ being an even function and $\hat{u}_y, \hat{u}_z, \hat{P}, \hat{T}$ being odd functions. The second type of symmetry boundary conditions

$$\hat{\mathbf{u}} \cdot \mathbf{e}_{\text{x}} = \hat{\mathbf{u}} \cdot \mathbf{n} = 0, \ \frac{\partial \hat{T}}{\partial \mathbf{n}} = 0 \quad \text{on } \Gamma_{\text{sym}} \tag{2.31}$$

results in $\hat{u}_x$ being an odd function and $\hat{u}_y, \hat{u}_z, \hat{P}, \hat{T}$ being even functions. The set of eigenvalues and eigenmodes of (2.27) is a union of the eigenvalues and eigenmodes of the smaller eigenvalue problems in Ω_{s1} with the symmetry boundary conditions of the first and second type.

Robin boundary conditions

The inkjet microchannel walls are not fully rigid, and displace in reaction to the flow on the boundary. A typical wall displacement is $10 - 20$ nm (Wijshoff, 2010) and is small in comparison to the channel width. Modelling this phenomenon as a full fluid structure interaction problem is excessive. The boundary reaction to the acoustic perturbations can be modelled via the impedance boundary condition that links the acoustic pressure and velocity on the boundary (Myers, 1980). The compliance of the walls against a stress from the flow can be computed from the wall thickness, Young's

modulus of elasticity, and Poisson's ratio (Timoshenko and Woinowsky-Krieger, 1959). For viscous flow, the force applied to a surface is a sum of the pressure and viscous stress. The impedance boundary condition is

$$Z\hat{u}_i = \hat{\sigma}_{ij} n_j \quad \text{on } \Gamma_{\text{imped}}. \tag{2.32}$$

Here we neither restrict the tangential velocity to be zero nor forbid tangential displacements of the compliant boundary. As the boundary impedance tends to zero, $Z \to 0$, the boundary becomes a stress-free surface, $\hat{\sigma}_{ij} n_j \to 0$. For large values, $Z \to \infty$, the boundary becomes a no slip rigid wall, $\hat{\mathbf{u}} \to 0$.

Similarly, the thermal accommodation coefficient $\alpha_w : \mathrm{Re}(\alpha_w) \geq 0$ can be introduced to describe the temperature boundary condition (Beltman, 1999b; Carslaw and Jaeger, 1986),

$$\hat{T} = -\alpha_w \frac{\partial \hat{T}}{\partial \mathbf{n}} \quad \text{on } \Gamma_{\text{accom}}. \tag{2.33}$$

As $|\alpha_w| \to 0$, the boundary becomes isothermal. As $|\alpha_w| \to \infty$, the boundary becomes adiabatic.

The domain boundaries can have non-uniform compliance and thermal properties. The boundary impedance and thermal accommodation coefficients are non-uniform frequency dependent functions, $Z = Z(\mathbf{x}, s)$, $\alpha_w = \alpha_w(\mathbf{x}, s)$ on $\partial\Omega$.

In summary, the velocity and temperature boundary conditions can be generalized to Robin boundary conditions (2.32, 2.33), with special cases for rigid and stress-free boundaries:

$$Z = 0 \text{ on } \Gamma_{\text{w}}, \quad Z^{-1} = 0 \text{ on } \Gamma_{\text{out}}, \tag{2.34a}$$

$$\alpha_w = 0 \text{ on } \Gamma_{\text{isoth}}, \quad \alpha_w^{-1} = 0 \text{ on } \Gamma_{\text{adiab}}. \tag{2.34b}$$

Using the universal parameters, Z and α_w, to describe all boundary types is convenient for formulation of the boundary value problem and further analysis.

2.3.3 Weak formulation and energy norms

To construct the weak formulation of the acoustic problem (2.21), we choose a Hilbert function space W of test functions on a non-deforming domain Ω. We introduce the

pressure P, velocity V, and temperature T spaces,

$$\mathrm{W} = \mathrm{P} \times \mathrm{V} \times \mathrm{T}, \tag{2.35a}$$

$$\mathrm{V} = \left\{ \mathbf{v} \in \left(H^1(\Omega) \right)^d : \mathbf{v} = 0 \text{ on } \Gamma_{\mathrm{w}} \bigcup \Gamma_{\mathrm{in}} \right\}, \tag{2.35b}$$

$$\mathrm{P} = \left\{ w \in L^2(\Omega) \right\}, \tag{2.35c}$$

$$\mathrm{T} = \left\{ q \in H^1(\Omega) : q = 0 \text{ on } \Gamma_{\mathrm{isoth}} \bigcup \Gamma_{\mathrm{th}} \right\}. \tag{2.35d}$$

Weak formulation of the unsteady thermoviscous acoustic problem

We start by introducing the weak form of the unsteady thermoviscous problem. We multiply the state equations by a vector of test functions $\mathbf{p} \equiv (\mathbf{v}, w, q) \in \mathrm{W}$ and integrate over the volume, $\left\langle \mathbf{p}, \frac{\partial}{\partial t}\mathrm{A}\mathbf{q} + \mathrm{B}\mathbf{q} \right\rangle_\Omega = 0$. After integration by parts the terms with the highest (second) order spatial derivatives once, we obtain the weak formulation of the problem:

$$a\left(\mathbf{p}, \frac{\partial}{\partial t}\mathbf{q}\right) + b\left(\mathbf{p}, \mathbf{q}\right) + b_\Gamma\left(\mathbf{p}, \mathbf{q}\right) = 0 \quad \forall \mathbf{p} \in \mathrm{W}, \tag{2.36}$$

where the bilinear form $b\left(\mathbf{p}, \mathbf{q}\right)$ represents the volume terms that appear after the integration by parts, and $b_\Gamma\left(\mathbf{p}, \mathbf{q}\right)$ represents the boundary components of the weak form:

$$a\left(\mathbf{p}, \mathbf{q}\right) \equiv \langle \mathbf{p}, \mathrm{A}\mathbf{q} \rangle_\Omega = \langle w, \rho \rangle_\Omega + \langle \mathbf{v}, \mathbf{u} \rangle_\Omega + \langle q, \mathrm{s} \rangle_\Omega, \tag{2.37a}$$

$$b\left(\mathbf{p}, \mathbf{q}\right) \equiv \langle q, \nabla_i u_i \rangle_\Omega - \langle \nabla_i v_i, P \rangle_\Omega + \left\langle \nabla_j v_i, \frac{1}{\tilde{Re}} \tau_{ij} \right\rangle_\Omega + \left\langle \nabla_j q, \frac{1}{(\gamma_{\mathrm{th}} - 1)\tilde{Pe}} \nabla_j T \right\rangle_\Omega, \tag{2.37b}$$

$$b_\Gamma\left(\mathbf{p}, \mathbf{q}\right) \equiv -\left\{ v_i, \sigma_{ij} n_j \right\}_{\partial\Omega} - \left\{ q, \frac{1}{(\gamma_{\mathrm{th}} - 1)\tilde{Pe}} \frac{\partial T}{\partial \mathbf{n}} \right\}_{\partial\Omega}. \tag{2.37c}$$

The term $b_\Gamma\left(\mathbf{p}, \mathbf{q}\right)$ is a linear form on the boundaries with Dirichlet and Neumann type of boundary conditions (2.24, 2.25), $b_\Gamma = b_\Gamma\left(\mathbf{q}\right)$. On the boundaries with homogeneous boundary conditions it is zero, $b_\Gamma = 0$.

We define total acoustic energy $\mathcal{E}_{\mathrm{ac}}$ (Chu, 1965), volume dissipation $\mathcal{R}_{\mathrm{ac}}$, and boundary energy flux $\mathcal{F}$ corresponding to the thermoviscous acoustic problem (2.21)

as

$$\mathcal{E}_{\text{ac}} = \frac{1}{2} a\left(\mathbf{q},\mathbf{q}\right) = \frac{1}{2}\left(\langle P,\rho\rangle_{\Omega} + \langle \mathbf{u},\mathbf{u}\rangle_{\Omega} + \langle T,\text{s}\rangle_{\Omega}\right), \tag{2.38a}$$

$$\mathcal{R}_{\text{ac}} = b\left(\mathbf{q},\mathbf{q}\right) = \left\langle \frac{1}{\tilde{Re}}\tau_{ij}, \nabla_j^s u_i \right\rangle_{\Omega} + \left\langle \nabla_j T, \frac{1}{(\gamma_{\text{th}}-1)\tilde{Pe}} \nabla_j T \right\rangle_{\Omega}, \tag{2.38b}$$

$$\mathcal{F} = -b_{\Gamma}\left(\mathbf{q},\mathbf{q}\right) = \left\{u_i, \sigma_{ij} n_j\right\}_{\partial\Omega} + \left\{ T, \frac{1}{(\gamma_{\text{th}}-1)\tilde{Pe}} \frac{\partial T}{\partial \mathbf{n}} \right\}_{\partial\Omega}, \tag{2.38c}$$

where $\nabla_j^s u_i$ is a symmetric gradient $\nabla_j^s u_i = \frac{1}{2}\left(\nabla_j u_i + \nabla_i u_j\right)$. Using the definitions of the acoustic density and entropy (2.18), the acoustic energy is non-negative for $\gamma_{\text{th}} > 1$:

$$\mathbf{u}^2 \geq 0, \quad \rho P + \text{s}T = \gamma_{\text{th}} P^2 - 2PT + \frac{T^2}{\gamma_{\text{th}} - 1} \geq 0,$$

and, therefore, the total acoustic energy $\mathcal{E}_{\text{ac}}$ is non-negative.

The volume-averaged energy balance equation is obtained by choosing the state vector $\mathbf{q}$ as the test function in (2.36):

$$\frac{d}{dt}\mathcal{E}_{\text{ac}} + \mathcal{R}_{\text{ac}} = \mathcal{F}. \tag{2.39}$$

The energy changes due to the viscous and thermal effects inside the domain, and the energy flux through the domain boundaries. The total boundary energy flux is a sum of the energy fluxes through all domain boundaries: $\mathcal{F} = \sum\limits_{k} \mathcal{F}_{\Gamma_{\text{k}}}$. The kinetic component of the energy flux $\{u_i, \sigma_{ij} n_j\}$ is naturally zero on the no slip and stress-free boundaries, and the thermal component $\left\{ T, \frac{1}{(\gamma_{\text{th}}-1)\tilde{Pe}} \frac{\partial T}{\partial \mathbf{n}} \right\}$ is zero on the adiabatic and isothermal boundaries.

Weak formulation of the thermoviscous acoustic eigenvalue problem

We proceed with the analysis of the thermoviscous acoustic eigenvalue problem (2.27). The natural frequency s is a complex value $s = \sigma + \text{i}\omega$, and the state vector $\hat{\mathbf{q}}$ is a complex function, $\hat{\mathbf{q}} \equiv \text{Re}(\hat{\mathbf{q}}) + \text{iIm}(\hat{\mathbf{q}}) = \hat{\mathbf{q}}^R + \text{i}\hat{\mathbf{q}}^I$. The operator A is symmetric and real (2.21b), and the operator B can be complex, $\text{B} = \text{B}^R + i\text{B}^I$ (for instance, due to the azimuthal components of the flow state in cylindrical domains). For computational convenience, we construct the eigenvalue problem in weak form in terms of real operators and functions. We split the eigenvalue problem into real and imaginary components,

and write it in matrix form:

$$\begin{bmatrix} \sigma & -\omega \\ \omega & \sigma \end{bmatrix} \begin{bmatrix} \mathrm{A} & 0 \\ 0 & \mathrm{A} \end{bmatrix} \begin{bmatrix} \hat{\mathbf{q}}^R \\ \hat{\mathbf{q}}^I \end{bmatrix} + \begin{bmatrix} \mathrm{B}^R & -\mathrm{B}^I \\ \mathrm{B}^I & \mathrm{B}^R \end{bmatrix} \begin{bmatrix} \hat{\mathbf{q}}^R \\ \hat{\mathbf{q}}^I \end{bmatrix} = 0. \tag{2.40}$$

We introduce two test functions $\mathbf{p}^R$ and $\mathbf{p}^I$ that belong to the space W: $\mathbf{p}^R, \mathbf{p}^I \in \mathrm{W}$. By testing the matrix equation (2.40) against the vector $\left(\mathbf{p}^R, \mathbf{p}^I\right)$, integrating over the volume and applying the boundary conditions, we obtain the following weak formulation:

$$\begin{aligned} &\sigma\left(\alpha^R(\hat{\mathbf{q}}^R) + \alpha^I\left(\hat{\mathbf{q}}^I\right)\right) + \omega\left(-\alpha^R\left(\hat{\mathbf{q}}^I\right) + \alpha^I\left(\hat{\mathbf{q}}^R\right)\right) \\ &+ \beta^{RR}\left(\hat{\mathbf{q}}^R\right) - \beta^{RI}\left(\hat{\mathbf{q}}^I\right) + \beta^{IR}\left(\hat{\mathbf{q}}^I\right) + \beta^{II}\left(\hat{\mathbf{q}}^R\right) = 0 \quad \forall \mathbf{p}^R \in \mathrm{W},\ \forall \mathbf{p}^I \in \mathrm{W}, \end{aligned} \tag{2.41}$$

where α^j, β^{jk} are useful real-valued operators defined by

$$\begin{aligned} \alpha^j(\cdot) &= a\left(\mathbf{p}^j, \cdot\right), \quad j = R, I, \\ \beta^{jk}(\cdot) &= b^k\left(\mathbf{p}^j, \cdot\right) + b^k_\Gamma\left(\mathbf{p}^j, \cdot\right), \quad j = R, I,\ k = R, I. \end{aligned}$$

Since the test functions $\mathbf{p}^R, \mathbf{p}^I$ are independent, we can fix $\mathbf{p}^R = 0$ and test the problem against $\mathbf{p}^I$, and vice versa. This is equivalent to writing the weak formulation (2.41) in matrix form:

$$\begin{bmatrix} \sigma & -\omega \\ \omega & \sigma \end{bmatrix} \begin{bmatrix} \alpha^R & 0 \\ 0 & \alpha^I \end{bmatrix} \begin{bmatrix} \hat{\mathbf{q}}^R \\ \hat{\mathbf{q}}^I \end{bmatrix} + \begin{bmatrix} \beta^{RR} & -\beta^{RI} \\ \beta^{II} & \beta^{IR} \end{bmatrix} \begin{bmatrix} \hat{\mathbf{q}}^R \\ \hat{\mathbf{q}}^I \end{bmatrix} = 0. \tag{2.43}$$

The equation (2.43) represents the weak form of the eigenvalue problem (2.27), where all operators (α^j, β^{jk}) and state functions $(\hat{\mathbf{q}}^R, \hat{\mathbf{q}}^I)$ are real.

The problem (2.43), however, is not in the form of an eigenvalue problem; to find $s \equiv \sigma + \mathrm{i}\omega$ and $\hat{\mathbf{q}}^R, \hat{\mathbf{q}}^I$ we will work with an auxiliary problem. We introduce two complex functions ϕ, ψ defined in the same function space as $\hat{\mathbf{q}}$. The auxiliary eigenvalue problem is: find $\iota, (\phi, \psi)$ such that

$$\iota \begin{bmatrix} \alpha^R & 0 \\ 0 & \alpha^I \end{bmatrix} \begin{bmatrix} \phi \\ \psi \end{bmatrix} + \begin{bmatrix} \beta^{RR} & -\beta^{RI} \\ \beta^{II} & \beta^{IR} \end{bmatrix} \begin{bmatrix} \phi \\ \psi \end{bmatrix} = 0. \tag{2.44}$$

As discussed by Brewster (2020), the weak solution of the original eigenvalue problem (2.27) can be recovered from the eigenvalue ι and the eigenmode (ϕ, ψ) of the problem (2.44) as

$$\begin{aligned} s &= \iota, \\ \hat{\mathbf{q}}^R &= \mathrm{Re}(\phi) - \mathrm{Im}(\psi), \\ \hat{\mathbf{q}}^I &= \mathrm{Im}(\phi) + \mathrm{Re}(\psi). \end{aligned} \tag{2.45}$$

We introduce the spectral energy norm, $\hat{\mathcal{E}}_{\mathrm{ac}}$:

$$\hat{\mathcal{E}}_{\mathrm{ac}} = a\left(\hat{\mathbf{q}}, \hat{\mathbf{q}}\right) = \langle \hat{\mathbf{u}}, \hat{\mathbf{u}} \rangle_\Omega + \left\langle \hat{P}, \hat{\rho} \right\rangle_\Omega + \left\langle \hat{T}, \hat{s} \right\rangle_\Omega . \tag{2.46}$$

The total energy $\mathcal{E}_{\mathrm{ac}} = \hat{\mathcal{E}}_{\mathrm{ac}} e^{2st}$ decays in time as $e^{2\sigma t}$. We substitute the real and imaginary components of the eigenmode $\hat{\mathbf{q}}$ into the bilinear forms (2.41) instead of $\mathbf{p}^R, \mathbf{p}^I$, and express the the decay rate σ of the mode:

$$\begin{aligned} \sigma = &\frac{b^R(\hat{\mathbf{q}}^R, \hat{\mathbf{q}}^R) + b^R_\Gamma(\hat{\mathbf{q}}^R, \hat{\mathbf{q}}^R) + b^R(\hat{\mathbf{q}}^I, \hat{\mathbf{q}}^I) + b^R_\Gamma(\hat{\mathbf{q}}^I, \hat{\mathbf{q}}^I)}{a(\hat{\mathbf{q}}^R, \hat{\mathbf{q}}^R) + a(\hat{\mathbf{q}}^I, \hat{\mathbf{q}}^I)} \\ &+ \frac{b^I(\hat{\mathbf{q}}^I, \hat{\mathbf{q}}^R) + b^I_\Gamma(\hat{\mathbf{q}}^I, \hat{\mathbf{q}}^R) - b^I(\hat{\mathbf{q}}^R, \hat{\mathbf{q}}^I) - b^I_\Gamma(\hat{\mathbf{q}}^R, \hat{\mathbf{q}}^I)}{a(\hat{\mathbf{q}}^R, \hat{\mathbf{q}}^R) + a(\hat{\mathbf{q}}^I, \hat{\mathbf{q}}^I)} \end{aligned} \tag{2.47}$$

In the absence of the imaginary component B^I (no azimuthal component, i.e. no swirl) the operator $\beta^{j,I}$ is identically zero, and the decay rate expression simplifies to

$$\begin{aligned} \sigma \equiv \mathrm{Re}(s) = &\frac{1}{\hat{\mathcal{E}}_{\mathrm{ac}}} \left\langle -\frac{1}{2\tilde{Re}} \tau_{ij} \nabla^s_j \hat{u}^*_i - \frac{1}{(\gamma_{\mathrm{th}} - 1)\tilde{Pe}} \left| \nabla_i \hat{T} \right|^2 \right\rangle_\Omega \\ &+ \frac{1}{\hat{\mathcal{E}}_{\mathrm{ac}}} \left\{ -\frac{\mathrm{Re}(\alpha_w)}{(\gamma_{\mathrm{th}} - 1)\tilde{Pe}} \left| \frac{\partial \hat{T}}{\partial \mathbf{n}} \right|^2 + \mathrm{Re}(Z) \left| \hat{\mathbf{u}} \right|^2 \right\}_{\partial\Omega} \\ \equiv &\frac{1}{\hat{\mathcal{E}}_{\mathrm{ac}}} \left(\int_\Omega \sigma_\Omega \mathrm{d}\mathbf{x} + \int_{\partial\Omega} \sigma_{\partial\Omega} \mathrm{d}s \right). \end{aligned} \tag{2.48}$$

The decay rate σ is a sum of volumetric energy dissipation σ_Ω and the surface energy transfer $\sigma_{\partial\Omega}$: $\sigma = \sigma_\Omega + \sigma_{\partial\Omega}$. The volumetric energy dissipation of the acoustic perturbation consists of viscous and thermal dissipation and is always negative, $\sigma_\Omega \leq 0$, while the surface energy transfer of the acoustic perturbation depends on the heat losses through the boundary and the work done by or on the fluid at the boundary. The surface energy transfer vanishes on the rigid and stress free boundaries (2.34a) and adiabatic and isothermal boundaries (2.34b), and therefore their contribution to $\sigma_{\partial\Omega}$ is zero.

Similarly to (2.48), the expression for ω can be obtained by substituting $(-\hat{\mathbf{q}}^I, \hat{\mathbf{q}}^R)$ instead of $\mathbf{p}^R, \mathbf{p}^I$ in (2.41):

$$\begin{aligned}\omega = &\frac{b^R(\hat{\mathbf{q}}^I, \hat{\mathbf{q}}^R) + b^R_\Gamma(\hat{\mathbf{q}}^I, \hat{\mathbf{q}}^R) - b^R(\hat{\mathbf{q}}^R, \hat{\mathbf{q}}^I) - b^R_\Gamma(\hat{\mathbf{q}}^R, \hat{\mathbf{q}}^I)}{a(\hat{\mathbf{q}}^R, \hat{\mathbf{q}}^R) + a(\hat{\mathbf{q}}^I, \hat{\mathbf{q}}^I)} \\ &+ \frac{b^I(\hat{\mathbf{q}}^R, \hat{\mathbf{q}}^R) + b^I_\Gamma(\hat{\mathbf{q}}^R, \hat{\mathbf{q}}^R) + b^I(\hat{\mathbf{q}}^I, \hat{\mathbf{q}}^I) + b^I_\Gamma(\hat{\mathbf{q}}^I, \hat{\mathbf{q}}^I)}{a(\hat{\mathbf{q}}^R, \hat{\mathbf{q}}^R) + a(\hat{\mathbf{q}}^I, \hat{\mathbf{q}}^I)}\end{aligned} \tag{2.49}$$

In the absence of the imaginary component B^I the operator $\beta^{j,I}$ is identically zero, and the frequency expression simplifies to

$$\begin{aligned}\omega \equiv \mathrm{Im}(s) = &\frac{2}{\hat{\mathcal{E}}_{\mathrm{ac}}} \left\langle P^I \mathrm{div}\mathbf{u}^R - P^R \mathrm{div}\mathbf{u}^I \right\rangle_\Omega \\ &+ \frac{1}{\hat{\mathcal{E}}_{\mathrm{ac}}} \left\{ -\frac{\mathrm{Im}(\alpha_w)}{(\gamma_{\mathrm{th}} - 1)\tilde{Pe}} \left| \frac{\partial \hat{T}}{\partial \mathbf{n}} \right|^2 + \mathrm{Im}(Z) \left| \hat{\mathbf{u}} \right|^2 \right\}_{\partial\Omega} \\ \equiv &\frac{1}{\hat{\mathcal{E}}_{\mathrm{ac}}} \left(\int_\Omega \omega_\Omega \mathrm{d}\mathbf{x} + \int_{\partial\Omega} \omega_{\partial\Omega} \mathrm{d}s \right).\end{aligned} \tag{2.50}$$

The oscillation frequency ω is a sum of volumetric ω_Ω and surface $\omega_{\partial\Omega}$ components.

2.3.4 Time discretization

To discretize the unsteady problem (2.36) in time, we divide the time domain $\mathcal{T}$ into N intervals of length Δt. The discrete time domain is $\mathcal{T}_h = \{t^n \equiv n\Delta t, n = 0 \dots N\}$. A function of time $f(t)$ evaluated on $\mathcal{T}_h$ at t^n is denoted as $f^n \equiv f(t^n)$. A value of the time-discrete function at an intermediate time $t^{n+\theta} = (1-\theta)t^n + \theta t^{n+1}, 0 \leq \theta < 1$ is approximated by a weighted linear combination of the closest discrete values, $f(t^{n+\theta}) \equiv f^{n+\theta} = (1-\theta)f^n + \theta f^{n+1}$. We approximate the discrete time derivative of the first order as $\overline{\partial_t} f^{n+\theta} = \frac{f^{n+\theta+\frac{1}{2}} - f^{n+\theta-\frac{1}{2}}}{\Delta t}$.

Following Bangerth et al. (2010), the mid-point rule $\theta = \frac{1}{2}$ is chosen to discretize the unsteady thermoviscous acoustic equations by a finite difference scheme. This choice of θ is equivalent to the non-dissipative, dispersive, second order accurate Crank-Nicolson scheme (Thomas, 2013). We choose a non-dissipative scheme because we want to minimize the error in the acoustic energy due to the numerical effects.

The time discrete form of the unsteady thermoviscous acoustic problem is: given the initial acoustic state $\mathbf{q}^0 = \mathbf{q}_0$, for each $n = 0, \dots, N-1$ find $\mathbf{q}^{n+1}$ such that

$$a\left(\mathbf{p}, \overline{\partial_t}\mathbf{q}^{n+\frac{1}{2}}\right) + b\left(\mathbf{p}, \mathbf{q}^{n+\frac{1}{2}}\right) + b^{n+\frac{1}{2}}_\Gamma\left(\mathbf{p}, \mathbf{q}^{n+\frac{1}{2}}\right) = 0 \quad \forall \mathbf{p} \in \mathrm{W}, \tag{2.51}$$

where $\mathbf{q}^{n+\frac{1}{2}} \equiv (\mathbf{u}^{n+\frac{1}{2}}, P^{n+\frac{1}{2}}, T^{n+\frac{1}{2}})$, and the boundary operator $b_\Gamma^{n+\frac{1}{2}}$ is defined at $t^{n+\frac{1}{2}}$. For example, the stress component of b_Γ on a boundary Γ_{force} with prescribed force boundary condition $\mathbf{f}(t)$ is $\left\{\mathbf{v}, \mathbf{f}^{n+\frac{1}{2}}\right\}_{\Gamma_{\text{force}}}$. For each time step, we solve the following linear variational problem: find $\mathbf{q}^{n+1}$ such that

$$\frac{1}{\Delta t} a\left(\mathbf{p}, \mathbf{q}^{n+1}\right) + \frac{1}{2}\left(b\left(\mathbf{p}, \mathbf{q}^{n+1}\right) + b_\Gamma^{n+1}\left(\mathbf{p}, \mathbf{q}^{n+1}\right)\right) = L^n(\mathbf{p}) \quad \forall \mathbf{p} \in \mathrm{W}. \tag{2.52}$$

Here $L^n : \mathrm{W} \to \mathbb{R}$ is a linear form that includes data from the previous time step and inhomogeneous boundary conditions:

$$L^n(\mathbf{p}) = \frac{1}{\Delta t} a\left(\mathbf{p}, \mathbf{q}^n\right) - \frac{1}{2}\left(b\left(\mathbf{p}, \mathbf{q}^n\right) + b_\Gamma^n\left(\mathbf{p}, \mathbf{q}^n\right) + b_\Gamma^{n+1}\left(\mathbf{p}\right)\right). \tag{2.53}$$

2.3.5 Spatial discretization

We derive the FEM approximation of the thermoviscous acoustic problem and the weak components (2.37). We divide the acoustic domain Ω into triangular elements with local discretization size h (Geuzaine and Remacle, 2009); the discrete spatial domain is Ω_h. The test $\mathbf{p}_h$ and trial $\mathbf{q}_h$ functions are continuous polynomial functions of degree $(r_P, r_\mathbf{u}, r_T)$ defined on a corresponding discrete space $\mathrm{W}_h = (\mathrm{P}_h \times \mathrm{V}_h \times \mathrm{T}_h) \subset \mathrm{W}$ in Ω_h. The discrete spatial scalar products $\mathrm{W}_h \times \mathrm{W}_h \to \mathbb{R}$ are denoted $\langle \cdot, \cdot \rangle_{\Omega_h}$ and $\{\cdot, \cdot\}_{\partial\Omega_h}$. In this study, we use a second order polynomial approximation of the velocity and temperature components $r_\mathbf{u} = r_T = 2$, so $\mathrm{V}_h, \mathrm{T}_h = \{\psi \in C^0(\Omega) : \ \psi|_K \in \mathbb{P}_2(K)\ \forall K \in \Omega_h\}$, and a first order polynomial approximation of the pressure component $r_P = 1$, so that $\mathrm{P}_h = \{\psi \in C^0(\Omega) : \ \psi|_K \in \mathbb{P}_1(K)\ \forall K \in \Omega_h\}$ (Kampinga et al., 2010).

We construct the FEM approximation of the weak form components (2.37): $a\left(\mathbf{p}_h, \mathbf{q}_h\right)$, $b\left(\mathbf{p}_h, \mathbf{q}_h\right)$ and $b_\Gamma\left(\mathbf{p}_h, \mathbf{q}_h\right)$ using the UFL form language (Alnæs et al., 2014) and the FEniCS form compiler FFC (Alnæs et al., 2015; Kirby and Logg, 2006). For the unsteady problem, we define the initial discrete state vector $\mathbf{q}_h^0$ as a FEM interpolation of the original initial condition $\mathbf{q}(t = 0)$. For each of the problems of interest (unsteady acoustics (2.51), frequency domain and eignevalue problems (2.44)) we use the discrete components in the respective weak formulations. A python package `firecrest` (Kungurtsev, 2020a) was developed to automate the initialization and solution of 2D thermoviscous acoustic problems using finite element (detailed in appendix A.2).

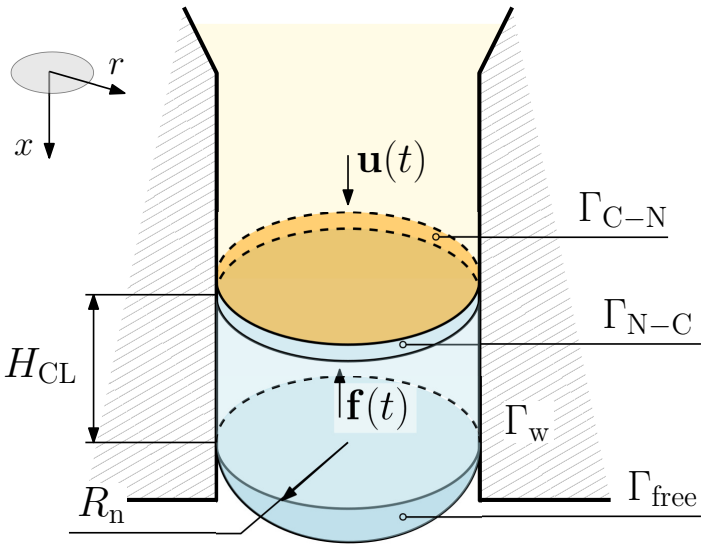

Fig. 2.4 Fluid inside a cylindrical nozzle domain Ω_{n} is bounded by the solid walls Γ_{w} and the free surface Γ_{free}, and connects to the channel domain Ω_{c} through $\Gamma_{\mathrm{N-C}}$. R_{n} is the nozzle radius, and H_{CL} is the distance from the boundary between the nozzle and channel domains and the free surface at rest.

2.4 Nozzle flow reduced order models

A nozzle is an integral part of any inkjet system. It is an axisymmetric cylindrical tube or an orifice in a solid base of a microchannel. Nozzle dimensions and shapes are determined by many parameters, such as the manufacturing technology, type of ink, and printing conditions. We assume that the volume of the nozzle part of the microchannel is much smaller than the total volume of the microchannel, which is true for most inkjet drop on demand printheads. A typical radius R_{n} of a nozzle of a modern inkjet printer is $10 - 50\mu$m (Chen and Basaran, 2002), and the length of the nozzle (the base plate thickness or the length of the nozzle tube) is approximately $20 - 100\mu$m. Depending on the application, nozzles can have cylindrical, conical, barrel, or bell mouth (Knol, 2017) shapes. We envisage that custom nozzle shapes that are optimized for particular microchannels, ink properties, and operational conditions will be necessary to print at ultrahigh speed (more than MHz droplet ejection frequency).

For the fluid density $\rho = 10^3$ kg m^{-3} and surface tension coefficient $\gamma_{\mathrm{dim}} = 50 \cdot 10^{-3}$ N m^{-2}, the capillary time scale is $t_\gamma = \sqrt{\rho R_{\mathrm{n}}^3/\gamma_{\mathrm{dim}}} = 10^{-5}$ s (Popinet, 2018; Rayleigh, 1879). The ratio of fluid inertia to surface tension is given by the Weber number. For a characteristic velocity of the flow $|\mathbf{u}| = 0.1$ ms^{-1} and large deformations of the free surface (the curvature radius of the free surface equals the nozzle radius), the ratio of

fluid inertia to surface tension is small:

$$We = \frac{\rho \left|\mathbf{u}\right|^2 R_n}{\gamma_{\text{dim}}} = 2.0 \cdot 10^{-3}.$$

The ratio of viscous forces to surface tension is also small:

$$Ca = \frac{\mu_{vis} \left|\mathbf{u}\right|}{\gamma_{\text{dim}}} = 2.0 \cdot 10^{-2},$$

where $\mu_{vis} = 10^{-2}$ Pa·s is the dynamic viscosity. In section 2.4.1, we show that the fluid inertial and viscous forces cannot be ignored for small amplitude deformations of the free surface.

The fluid inside the nozzle is enclosed between rigid walls Γ_{w} and a free surface Γ_{free} which is a multiphase interface between the fluid and the outside gas. Direct simulation of the free boundary problem, namely formation and pinch-off of an ink droplet and subsequent relaxation of the free surface, and sensitivity analysis of such a system are computationally expensive. In order to avoid explicit modelling of the acoustic flow boundary conditions on the moving free surface, we decompose the original domain into two non-overlapping subdomains. We separate a small part of the physical domain that encloses the multiphase interface from the rest of the microchannel by a (virtual) flat shared boundary, and call this part of the printhead domain a nozzle subdomain.

Let Ω_{n} denote the nozzle subdomain, and Ω_{c} denote the remaining static part of the microchannel. The shared boundary is denoted by $\Gamma_{\text{C–N}} \subset \partial\Omega_{\text{c}}$ and $\Gamma_{\text{N–C}} \subset \partial\Omega_{\text{n}}$, such that $\mathbf{n}|_{\Gamma_{\text{C–N}}} = -\mathbf{n}|_{\Gamma_{\text{N–C}}}$. The position of the shared boundary does not change over time. We assume that Ω_{n} is entirely inside the microchannel's nozzle, or equivalently that the free surface and the shared boundary never intersect. Figure 2.4 shows the decomposition of the nozzle part of the original physical domain into the channel subdomain (orange) and the nozzle subdomain (blue). We consider that the radius of the cylindrical nozzle domain equals $R_{\text{n}} = 10\mu$m, and the distance between the shared boundary and the free boundary at rest (the fluid-solid-air contact line at rest) is $H_{\text{CL}} = 10\mu$m.

We need to define a set of boundary conditions on $\Gamma_{\text{C–N}}, \Gamma_{\text{N–C}}$ for the flow fields inside Ω_{c} and Ω_{n} that are consistent with the original problem. Some numerical studies of the free boundary problem allow mass exchange between the domain with a free surface (Ω_{n}) and the rest of the channel (Ω_{c}), and suggest using a force boundary condition on $\Gamma_{\text{N–C}}$ (Fumagalli et al., 2018). The shared boundary $\Gamma_{\text{N–C}}$ can also be treated as an inflow boundary with the flow velocity prescribed on it (Miers and Zhou,

2017; Wu et al., 2004). In both formulations, the boundary condition on $\Gamma_{\mathrm{N-C}}$ is provided by the state of the acoustic channel flow on $\Gamma_{\mathrm{C-N}} \subset \Omega_{\mathrm{c}}$. Here we choose the velocity Dirichlet boundary condition on $\Gamma_{\mathrm{N-C}}$, and therefore the flow inside Ω_{c} has the Neumann stress boundary condition prescribed on $\Gamma_{\mathrm{C-N}}$. Let $\mathbf{q}_{\mathrm{c}}$ denote the flow state in Ω_{c}, and $\mathbf{q}_{\mathrm{n}}$ denote the flow state in Ω_{n}. A generic form of the boundary conditions is

$$\mathbf{q}_{\mathrm{c}} \ : \ \sigma_{ij} n_j = f_i(\mathbf{q}_{\mathrm{n}}) \quad \text{on } \Gamma_{\mathrm{C-N}}, \tag{2.54a}$$

$$\mathbf{q}_{\mathrm{n}} \ : \ \mathbf{u} = \mathbf{u}(\mathbf{q}_{\mathrm{c}}) \quad \text{on } \Gamma_{\mathrm{N-C}}. \tag{2.54b}$$

It is possible to apply existing simulation techniques to solve the free boundary problem inside the nozzle subdomain given the inflow boundary condition, calculate the force applied to the shared boundary $\Gamma_{\mathrm{N-C}}$, and couple the nozzle flow to the channel flow via (2.54). This can be done using a one-dimensional approximation of the axisymmetric incompressible flow (Eggers and Dupont, 1994; Jiang and Tan, 2018), interface capturing methods (Galusinski and Vigneaux, 2008b; Wu et al., 2004; Zahedi et al., 2009), or explicit computation of the domain motion (Donea et al., 2017; Fumagalli et al., 2018; Gerbeau et al., 2003). In this study we do not focus on accurate tracking of the exact position of the multiphase interface and the exact solution of the flow field in Ω_{n}. Instead, we introduce several approximations on the nozzle domain flow field and the shape of the free surface, and discuss a reduced order model based on conservation of mass and energy in Ω_{n}. We calculate the force field on $\Gamma_{\mathrm{C-N}}$ acting on the acoustic channel flow from the nozzle using the reduced order model.

2.4.1 Conservation laws in the nozzle subdomain

We start by deriving volume and mass conservation equations in the moving nozzle domain $\Omega_{\mathrm{n}} = \Omega_{\mathrm{n}}(t)$. A vector field $\mathbf{w}$ defines the domain deformation due to the movement of the free boundary Γ_{free}. The relationship between $\mathbf{w}$ and $\mathbf{u}$ depends on the type of boundary. On Γ_{w} both the domain and the fluid velocities have zero normal component (2.55a). On Γ_{free} the flow velocity and the domain velocity are equal in the normal direction (2.55b). On $\Gamma_{\mathrm{N-C}}$ there is no deformation although there is mass flow through this boundary (2.55c).

$$\mathbf{w} \cdot \mathbf{n} = \mathbf{u} \cdot \mathbf{n} = 0 \quad \text{on} \quad \Gamma_{\mathrm{w}}. \tag{2.55a}$$

$$\mathbf{w} \cdot \mathbf{n} = \mathbf{u} \cdot \mathbf{n} \quad \text{on} \quad \Gamma_{\mathrm{free}}. \tag{2.55b}$$

$$\mathbf{w} \cdot \mathbf{n} = 0 \quad \text{on} \quad \Gamma_{\mathrm{N-C}}. \tag{2.55c}$$

The algebraic relation between the time derivative of the nozzle volume $|\Omega_\mathrm{n}(t)|$ and the velocity of the free surface, although obvious, can be derived rigorously with the Reynolds transport theorem by considering the time derivative of a volume functional $\mathcal{J} = \langle\phi\rangle_\Omega$:

$$\frac{d}{dt}\mathcal{J} = \left\langle \frac{\partial}{\partial t}\phi + div(\phi\mathbf{w}) \right\rangle_\Omega = \left\langle \frac{\partial}{\partial t}\phi \right\rangle_\Omega + \{\phi\mathbf{w}\cdot\mathbf{n}\}_{\partial\Omega}\,. \tag{2.56}$$

By choosing $\phi \equiv 1, \Omega = \Omega_\mathrm{n}$, the functional is the domain volume $\mathcal{J} = \langle 1\rangle_{\Omega_\mathrm{n}} \equiv |\Omega_\mathrm{n}|$. After applying the boundary condition (2.55), the time derivative of the nozzle volume equals the normal flow at the free surface.

$$\frac{d}{dt}\left|\Omega_\mathrm{n}\right| = \{\mathbf{w}\cdot\mathbf{n}\}_{\Gamma_\mathrm{free}} = \{\mathbf{u}\cdot\mathbf{n}\}_{\Gamma_\mathrm{free}}\,.$$

By choosing $\phi \equiv \rho$, and considering the continuity equation $\partial_t\rho + div(\rho\mathbf{u}) = 0$ in Ω_n, the time derivative of the total mass inside the nozzle domain is

$$\frac{d}{dt}\langle\rho\rangle_{\Omega_\mathrm{n}} = \{\rho\,(\mathbf{w}-\mathbf{u})\cdot\mathbf{n}\}_{\partial\Omega_\mathrm{n}} = -\{\rho\mathbf{u}\cdot\mathbf{n}\}_{\Gamma_{\mathrm{N-C}}}\,.$$

The flow inside the nozzle (and therefore the free surface) is driven by the acoustic inflow from the channel domain Ω_c. The nozzle velocity on $\Gamma_{\mathrm{N-C}}$, $\mathbf{u} = c_s^b\epsilon\mathcal{U}$, is determined by the acoustic velocity on $\Gamma_{\mathrm{C-N}}$: $\mathbf{u} = \mathcal{U}$. For a flow coming from the axisymmetric nozzle part of the channel domain, we can neglect the velocity components that are tangent to $\Gamma_{\mathrm{C-N}}$. Following the same strategy as in section 2.2.4, we expand the density and velocity variables in terms of the oscillating flow Mach number, $\rho \simeq \rho^b\left(\rho^{(0)} + \epsilon\rho^{(1)}\right) + \mathcal{O}\left(\epsilon^2\right)$ and $\mathbf{u} \simeq c_s^b\epsilon\mathbf{u}^{(1)} + \mathcal{O}\left(\epsilon^2\right)$. We use the characteristic size L of the channel domain Ω_c as the reference length. The nondimensional volume and mass conservation equations integrated over Ω_n are:

$$\frac{d}{dt_\mathrm{ac}}\left|\Omega_\mathrm{n}\right| = \epsilon\left\{\mathbf{u}^{(1)}\cdot\mathbf{n}\right\}_{\Gamma_\mathrm{free}} + \mathcal{O}\left(\epsilon^2\right), \tag{2.57a}$$

$$\frac{d}{dt_\mathrm{ac}}\left|\Omega_\mathrm{n}\right| + \epsilon\frac{d}{dt_\mathrm{ac}}\left\langle\rho^{(1)}\right\rangle_{\Omega_\mathrm{n}} = -\epsilon\left\{\mathcal{U}\cdot\mathbf{n}\right\}_{\Gamma_{\mathrm{N-C}}} + \mathcal{O}\left(\epsilon^2\right). \tag{2.57b}$$

The fluid possesses a kinetic energy $\mathcal{K}_\mathrm{n} \equiv \langle\rho\mathbf{u}^2\rangle_{\Omega_\mathrm{n}}/2$ and a potential energy $\mathcal{P}_\mathrm{n} \equiv \langle\rho e\rangle_{\Omega_\mathrm{n}}$. The amount of energy transferred through the shared boundary $\Gamma_{\mathrm{N-C}}$ and the free boundary Γ_free is defined by the energy fluxes $\mathcal{F}_{\mathrm{N-C}}$ and $\mathcal{F}_\mathrm{free}$, respectively. The energy dissipates through viscous and thermal effects inside the fluid $\mathcal{R}_{\Omega_\mathrm{n}} \equiv \left\langle\tau_{ij}\nabla_j u_i + \kappa_\mathrm{th}\left(\nabla_k T\right)^2\right\rangle_{\Omega_\mathrm{n}}$ and on the nozzle walls $\mathcal{R}_{\partial\Omega_\mathrm{n}} \equiv \{-u_i\sigma_{ij}n_j - \kappa_\mathrm{th}T\partial_\mathbf{n}T\}_{\Gamma_\mathrm{w}}$ via wall friction and heat flux. The stress component of $\mathcal{R}_{\partial\Omega_\mathrm{n}}$ is identically zero if the

nozzle walls are modelled as no slip boundaries $\mathbf{u} = 0$ on Γ_{w}. Next to the contact line $\Gamma_{\mathrm{w}} \bigcap \Gamma_{\mathrm{free}}$ no slip has to be replaced with the Navier boundary condition (Qian et al., 2006; Ren and Weinan, 2007) that relates velocity to the tangential stress via the wall friction coefficient: $-\beta_s \mathbf{u}_\tau = (\sigma_{ij} n_j)_\tau$ on Γ_{w}, where $(\cdot)_\tau$ is the tangential projection defined as $\mathbf{a}_\tau \equiv \mathbf{a} - (\mathbf{a} \cdot \mathbf{n})\,\mathbf{n}$. The stress component of the wall dissipation function then becomes $\{-u_i \sigma_{ij} n_j\}_{\Gamma_{\mathrm{w}}} = \{\beta_s \mathbf{u}_\tau^2\}_{\Gamma_{\mathrm{w}}} \geq 0$. The volume-averaged energy conservation equation is

$$\frac{d}{dt}\left(\mathcal{K}_{\mathrm{n}} + \mathcal{P}_{\mathrm{n}}\right) + \mathcal{R}_{\Omega_{\mathrm{n}}} + \mathcal{R}_{\partial\Omega_{\mathrm{n}}} = \mathcal{F}_{\mathrm{N-C}} + \mathcal{F}_{\mathrm{free}}.$$

The energy flux on Γ_{free} by construction equals the change of the free surface energy E_{free}, and therefore the energy conservation equation can be rewritten as

$$\frac{d}{dt}\left(\mathcal{K}_{\mathrm{n}} + \mathcal{P}_{\mathrm{n}} + E_{\mathrm{free}}\right) + \mathcal{R}_{\Omega_{\mathrm{n}}} + \mathcal{R}_{\partial\Omega_{\mathrm{n}}} = \mathcal{F}_{\mathrm{N-C}}.$$

The free surface energy is a sum of the potential energies of the fluid-gas interface, fluid-solid interface, and solid-gas interface. Here the contact line is assumed static: the distance between the shared boundary $\Gamma_{\mathrm{N-C}}$ and the contact line is static $\frac{d}{dt} H_{\mathrm{CL}} = 0$. This implies that that contribution to the capillary force acting on the fluid in the nozzle that arises due to the difference between the the fluid-solid and the gas-solid surface coefficients (called the uncompensated Young stress on the contact line (Batchelor, 2000; Qian et al., 2003)) is neglected. Equivalently, the free surface energy is given only by the potential energy of the fluid-gas interface $E_{\mathrm{free}} = \{\gamma_{\mathrm{dim}}\}_{\Gamma_{\mathrm{free}}}$.

We divide all terms of the energy conservation equation by $\rho^b L^2 \left(c_s^b\right)^3$ and expand the nondimensional variables in terms of the oscillating flow Mach number ϵ. The first order terms cancel out due to (2.19), and the second order terms give

$$\frac{d}{dt_{\mathrm{ac}}}\left(\epsilon^2 \mathcal{K}_{\mathrm{n}}^{(2)} + \epsilon^2 \mathcal{P}_{\mathrm{n}}^{(2)}\right) + \epsilon^2 \mathcal{R}_{\Omega_{\mathrm{n}}}^{(2)} + \epsilon^2 \mathcal{R}_{\partial\Omega_{\mathrm{n}}}^{(2)} = \mathcal{F}_{\mathrm{N-C}} + \mathcal{F}_{\mathrm{free}} + \mathcal{O}\left(\epsilon^3\right). \tag{2.58}$$

For simplicity the flow in Ω_{n} is assumed to be adiabatic: the entropy variation is zero $\epsilon s^{(1)} \equiv 0$, and therefore the potential energy $\mathcal{P}_{\mathrm{n}}^{(2)}$ equals $\left\langle P^{(1)} \cdot P^{(1)} \right\rangle_{\Omega_{\mathrm{n}}} / 2$. The nondimensional energy flux through $\Gamma_{\mathrm{N-C}}$ is

$$\mathcal{F}_{\mathrm{N-C}} = \epsilon^2 \left\{ \mathcal{U}_i \sigma_{ij}^{(1)} n_j \right\}_{\Gamma_{\mathrm{N-C}}}.$$

The force applied to the nozzle flow from the free surface is $\sigma_{ij} n_j = -\gamma_{\mathrm{dim}} \kappa n_i$ on Γ_{free}, where γ_{dim} is the surface tension coefficient of the liquid-gas interface, and κ is

the curvature of the free surface. The nondimensional energy flux through Γ_{free} is

$$\mathcal{F}_{\text{free}} = \epsilon^2 \left\{ -\gamma \kappa_{\text{n.d.}} \mathbf{u}^{(1)} \cdot \mathbf{n} \right\}_{\Gamma_{\text{free}}},$$

where $\gamma \equiv 2\gamma_{\text{dim}} / \left(\epsilon \rho^b \left(c_s^b \right)^2 R_n \right)$ is the nondimensional surface tension coefficient, and $\kappa_{\text{n.d.}} \equiv \kappa R_n / 2$ is the nondimensional curvature of the free surface.

The nondimensional energy of the free surface (divided by ϵ^2) is $E_{\text{free}} = \epsilon^{-1} \frac{r_n}{2} \gamma \left| \Gamma_{\text{free}} \right|$. We define the total energy of the nozzle system as

$$\mathcal{E}_{\text{n}} \equiv E_{\text{free}} + \mathcal{K}_{\text{n}}^{(2)} + \mathcal{P}_{\text{n}}^{(2)}. \tag{2.59}$$

We normalize the geometric quantities in the nondimensional conservation equations (2.57b, 2.58) using the channel characteristic size L as the reference length. The nondimensional radius of the nozzle domain is $r_n \equiv R_n / L$. We introduce an effective nondimensional height of the channel defined as the ratio between the nondimensional volume of the nozzle domain and the area of the shared boundary:

$$h_n \equiv \left| \Omega_{\text{n}} \right| / \left| \Gamma_{\text{N-C}} \right| = \left| \Omega_{\text{n}} \right| / \left(\pi r_n^2 \right). \tag{2.60}$$

Volume integrals scale as $\langle \cdot \rangle_{\Omega_{\text{n}}} \sim h_n r_n^2$, and surface integrals scale as $\{ \cdot \}_{\Gamma_{\text{w}}} \sim h_n r_n$ and $\{ \cdot \}_{\Gamma_{\text{N-C}}}, \{ \cdot \}_{\Gamma_{\text{free}}} \sim r_n^2$. In this study we consider that the nozzle height is considerably shorter than the reference length, and expand the conservation equations in terms of $h_n \ll 1$. If $h_n L \simeq L$, however, then the terms proportional to h_n cannot be ignored and the flow should be directly modelled in the nozzle as well as in the channel.

Zero-order approximation, $h_n = 0$

By setting h_n to zero in (2.57b) and (2.58) we effectively neglect the flow energy and the energy dissipation inside the nozzle domain. Mass and energy propagates directly from the static shared boundary $\Gamma_{\text{N-C}}$ to the free surface Γ_{free}. The zero-order mass and energy conservation equations are:

$$-\left\{ \mathcal{U} \cdot \mathbf{n} \right\}_{\Gamma_{\text{N-C}}} = \left\{ \mathbf{u}^{(1)} \cdot \mathbf{n} \right\}_{\Gamma_{\text{free}}}, \tag{2.61a}$$

$$\left\{ \mathcal{U}_i \sigma_{ij}^{(1)} n_j \right\}_{\Gamma_{\text{N-C}}} = \left\{ \gamma \kappa_{\text{n.d.}} \mathbf{u}^{(1)} \cdot \mathbf{n} \right\}_{\Gamma_{\text{free}}}. \tag{2.61b}$$

From (2.61a), the zero-order nozzle volume conservation equation is expressed in terms of the acoustic variables

$$\frac{d}{dt_{\mathrm{ac}}}\left|\Omega_{\mathrm{n}}\right| = \epsilon\left\{\mathbf{u}\cdot\mathbf{n}\right\}_{\Gamma_{\mathrm{C-N}}}. \tag{2.62}$$

Let $\gamma\hat{\kappa}$ be an effective pressure of the free surface, $\gamma\hat{\kappa}\left\{\mathbf{u}^{(1)}\cdot\mathbf{n}\right\}_{\Gamma_{\mathrm{free}}} = \left\{\gamma\kappa_{\mathrm{n.d.}}\mathbf{u}^{(1)}\cdot\mathbf{n}\right\}_{\Gamma_{\mathrm{free}}}$. We substitute this into (2.61b) and use (2.61a) to obtain

$$\left\{\mathcal{U}_i\left(\sigma_{ij}^{(1)}n_j + \gamma\hat{\kappa}n_i\right)\right\}_{\Gamma_{\mathrm{N-C}}} = 0,$$

thereby the force acting on the shared boundary can be consistently approximated by $\sigma_{ij}^{(1)}n_j = -\gamma\hat{\kappa}n_i$ on $\Gamma_{\mathrm{N-C}}$. Equivalently, the zero-order approximation to the force boundary condition for the acoustic channel flow on $\Gamma_{\mathrm{C-N}}$ is

$$\sigma_{ij}n_j = -\gamma\hat{\kappa}n_i \quad \text{on } \Gamma_{\mathrm{C-N}}. \tag{2.63}$$

First-order approximation, $0 < h_n \ll 1$

The next step is to retain the terms that are linear in h_n to account for the fluid compressibility, energy and dissipation in Ω_{n}. We can estimate the magnitude of the inertial term as $\rho^b H_{\mathrm{CL}}\omega\left|\mathbf{u}\right| \simeq 10^3$ Pa for a characteristic flow velocity of $\left|\mathbf{u}\right| \simeq 0.1$ ms^{-1} and a typical oscillation frequency $\omega \simeq 10^6$ s^{-1}. This is equivalent to pressure generated by a free surface with a radius of curvature 100μm. Considering that the radius of the nozzle is $R_{\mathrm{n}} = 10\mu$m, the pressure drop due to the inertial and viscous effects can be safely neglected when the free surface curvature is high ($0.1 \leq \hat{\kappa} \leq 1$), but may not be negligible otherwise.

We start by expanding the flow velocity and pressure:

$$\mathbf{u}^{(1)} \simeq \mathcal{U}|_{\Gamma_{\mathrm{N-C}}} + \mathcal{O}\left(h_n\right), \quad P^{(1)} \simeq P^{(1)}\Big|_{\Gamma_{\mathrm{N-C}}} + \mathcal{O}\left(h_n\right) \quad \text{in } \Omega_{\mathrm{n}}.$$

The expansion of the continuity equation (2.57b) reads

$$\begin{aligned}
-\left\{\mathcal{U}\cdot\mathbf{n}\right\}_{\Gamma_{\mathrm{N-C}}} &= \left\{\mathbf{u}^{(1)}\cdot\mathbf{n}\right\}_{\Gamma_{\mathrm{free}}} + \frac{d}{dt_{\mathrm{ac}}}\left\langle P^{(1)}\right\rangle_{\Omega_{\mathrm{n}}} \\
&\simeq \left\{\mathbf{u}^{(1)}\cdot\mathbf{n}\right\}_{\Gamma_{\mathrm{free}}} + \frac{d}{dt_{\mathrm{ac}}}\left\{h_n P^{(1)}\right\}_{\Gamma_{\mathrm{N-C}}} + \mathcal{O}\left(h_n^2\right) \\
&= \left\{\mathbf{u}^{(1)}\cdot\mathbf{n}\right\}_{\Gamma_{\mathrm{free}}} + \frac{d}{dt_{\mathrm{ac}}}\left(\gamma\hat{\kappa}\left|\Omega_{\mathrm{n}}\right|\right) + \mathcal{O}\left(h_n^2\right),
\end{aligned}$$

and consequently the first-order nozzle volume conservation equation in terms of the acoustic variables is

$$\frac{d}{dt_{\mathrm{ac}}}\left|\Omega_{\mathrm{n}}\right| = \epsilon\left\{\mathbf{u}\cdot\mathbf{n}\right\}_{\Gamma_{\mathrm{C-N}}} - \epsilon\frac{d}{dt_{\mathrm{ac}}}\left(\gamma\hat{\kappa}\left|\Omega_{\mathrm{n}}\right|\right). \tag{2.64}$$

In comparison to the zero-order approximation (2.62), the extra term on the right hand side is proportional to h_n and accounts for compressibility effects. Although $\epsilon\frac{d}{dt_{\mathrm{ac}}}\left|\Omega_{\mathrm{n}}\right|\hat{\kappa}$ in (2.64) is of order ϵ^2 and therefore small, we retain this term to be consistent with the change of the potential energy of the nozzle flow.

Kinetic and potential energy of the nozzle flow $\mathcal{K}_{\mathrm{n}}^{(2)}, \mathcal{P}_{\mathrm{n}}^{(2)}$ and energy dissipation $\mathcal{R}_{\Omega_{\mathrm{n}}}^{(2)}$ and $\mathcal{R}_{\partial\Omega_{\mathrm{n}}}^{(2)}$ are approximated by the value of the integrand on $\Gamma_{\mathrm{N-C}}$:

$$\begin{aligned}
2\mathcal{K}_{\mathrm{n}}^{(2)} &= \left\langle \mathbf{u}^{(1)}\cdot\mathbf{u}^{(1)}\right\rangle_{\Omega_{\mathrm{n}}} \simeq h_n\left\{\mathbf{u}^{(1)}\cdot\mathbf{u}^{(1)}\right\}_{\Gamma_{\mathrm{N-C}}} + \mathcal{O}\left(h_n^2\right) = h_n\left\{\mathcal{U}\cdot\mathcal{U}\right\}_{\Gamma_{\mathrm{N-C}}} + \mathcal{O}\left(h_n^2\right),\\
2\mathcal{P}_{\mathrm{n}}^{(2)} &= \left\langle P^{(1)}\cdot P^{(1)}\right\rangle_{\Omega_{\mathrm{n}}} = \left|\Omega_{\mathrm{n}}\right|\left(\gamma\hat{\kappa}\right)^2 + \mathcal{O}\left(h_n^2\right),
\end{aligned}$$

and

$$\begin{aligned}
\mathcal{R}_{\Omega_{\mathrm{n}}}^{(2)} + \mathcal{R}_{\partial\Omega_{\mathrm{n}}}^{(2)} &= \frac{1}{\tilde{Re}}\left(\left\langle\tau_{ij}^{(1)}\nabla_j u_i^{(1)}\right\rangle_{\Omega_{\mathrm{n}}} + \left\{\tau_{ij}^{(1)}n_j u_i^{(1)}\right\}_{\Gamma_{\mathrm{w}}}\right)\\
&\simeq -\frac{h_n}{\tilde{Re}}\left\{\mathbf{u}^{(1)}\cdot\Delta_\Gamma\mathbf{u}^{(1)}\right\}_{\Gamma_{\mathrm{N-C}}} + \mathcal{O}\left(h_n^2\right) = -\frac{h_n}{\tilde{Re}}\left\{\mathcal{U}\cdot\Delta_\Gamma\mathcal{U}\right\}_{\Gamma_{\mathrm{N-C}}} + \mathcal{O}\left(h_n^2\right).
\end{aligned}$$

We substitute these approximations into the energy conservation equation, and apply (2.57b). Up to first order in h_n, the energy equation becomes

$$\begin{aligned}
&\frac{1}{2}\frac{d}{dt_{\mathrm{ac}}}h_n\left\{\mathcal{U}\cdot\mathcal{U}\right\}_{\Gamma_{\mathrm{N-C}}} + \frac{1}{2}\frac{d}{dt_{\mathrm{ac}}}\left\langle P^{(1)}\cdot P^{(1)}\right\rangle_{\Omega_{\mathrm{n}}} - \frac{h_n}{\tilde{Re}}\left\{\mathcal{U}\cdot\Delta_\Gamma\mathcal{U}\right\}_{\Gamma_{\mathrm{N-C}}}\\
&= \left\{\mathcal{U}_i\sigma_{ij}^{(1)}n_j\right\}_{\Gamma_{\mathrm{N-C}}} + \gamma\hat{\kappa}\left(\left\{\mathcal{U}\cdot\mathbf{n}\right\}_{\Gamma_{\mathrm{N-C}}} + \frac{d}{dt_{\mathrm{ac}}}\left\langle P^{(1)}\right\rangle_{\Omega_{\mathrm{n}}}\right) + \mathcal{O}\left(h_n^2\right).
\end{aligned}$$

The pressure terms cancel out:

$$\frac{1}{2}\frac{d}{dt_{\mathrm{ac}}}\left\langle P^{(1)}\cdot P^{(1)}\right\rangle_{\Omega_{\mathrm{n}}} - \gamma\hat{\kappa}\frac{d}{dt_{\mathrm{ac}}}\left\langle P^{(1)}\right\rangle_{\Omega_{\mathrm{n}}} \simeq \mathcal{O}\left(h_n^2\right),$$

and the remaining expression can be rewritten as

$$\left\{\mathcal{U}_i\left(\sigma_{ij}^{(1)}n_j + \gamma\hat{\kappa}n_i - h_n\frac{d}{dt_{\mathrm{ac}}}\mathcal{U}_i + \frac{h_n}{\tilde{Re}}\Delta_\Gamma\mathcal{U}_i\right)\right\}_{\Gamma_{\mathrm{N-C}}} = \mathcal{O}\left(h_n^2\right).$$

(Here the terms proportional to $\frac{d}{dt_{\mathrm{ac}}} h_n \sim \epsilon$ are neglected.) Similarly to the zero-order case, we use the above expression to derive an approximation to the force acting on the shared boundary that is consistent with the energy transfer through $\Gamma_{\mathrm{N-C}}$. Hence the acoustic force boundary condition on $\Gamma_{\mathrm{C-N}}$ is given up to first order in h_n by

$$\sigma_{ij} n_j = -\gamma \hat{\kappa} n_i - h_n \left(\frac{d}{dt_{\mathrm{ac}}} u_i - \frac{1}{\tilde{Re}} \Delta_\Gamma u_i \right) \quad \text{on } \Gamma_{\mathrm{C-N}}. \tag{2.65}$$

In comparison to the zero-order approximation (2.63), the new terms on the right hand side are proportional to h_n and account for the kinetic energy of the flow and viscous dissipation inside the nozzle domain.

Summing up, we derive a force boundary condition for the acoustic flow in Ω_{c} that accounts for the potential and kinetic energy of the flow in the nozzle subdomain Ω_{n}, viscous dissipation, and the free surface energy. This boundary condition is a function of the acoustic velocity on $\Gamma_{\mathrm{C-N}}$ and the effective curvature of the free surface $\hat{\kappa}$. While the acoustic velocity field is given by the solution of the acoustic flow in the channel domain itself, the curvature is calculated from a nozzle volume conservation equation (2.62) or (2.64). In the next section we discuss the relationship between the nozzle volume $|\Omega_{\mathrm{n}}|$ and the effective curvature $\hat{\kappa}$.

2.4.2 Free surface parametrization

In this section we aim to develop a parametric reduced order model of the free surface boundary Γ_{free}. Inspired by experimental observations (Hsiao et al., 2011; van der Meulen et al., 2016; Yang et al., 2014) and existing numerical models (Dijksman, 2019; Kim et al., 2014), we approximate the free surface as a spherical cap, $\Gamma_{\mathrm{free}} \simeq \hat{\Gamma}_{\mathrm{free}}$, neglecting the presence of large wavenumber capillary waves $k \gg \pi / R_{\mathrm{n}}$. Van Der Meulen et al. (2020) studies the effects of higher wave number disturbance shapes, and shows that a much higher free surface acceleration magnitude is required for those shapes to appear, in comparison to the smallest wavenumber mode. The axisymmetric surface with the smallest energy - *i.e.* a spherical cap - is chosen as the starting point for the present simulations.

Naturally, the uniform curvature of the approximate free surface coincides with the effective curvature $\kappa|_{\hat{\Gamma}_{\mathrm{free}}} = \hat{\kappa}$, and this notation will be used to denote the uniform curvature of $\hat{\Gamma}_{\mathrm{free}}$. The uniform curvature of the surface $\hat{\Gamma}_{\mathrm{free}}$ is nondimensionalized by the nozzle radius $\hat{\kappa} = \kappa R_{\mathrm{n}} / 2$, such that the free surface is a hemisphere when $\hat{\kappa} = 1$.

The surface area $\left|\hat{\Gamma}_{\text{free}}(\hat{\kappa})\right|$ nondimensionalized by L^2 equals

$$\left|\hat{\Gamma}_{\text{free}}(\hat{\kappa})\right| = \frac{r_n^2}{4}\frac{8\pi}{\hat{\kappa}^2}\left(1-\cos\theta(\hat{\kappa})\right), \tag{2.66}$$

where $\cos\theta(\hat{\kappa}) \equiv \sqrt{1-\hat{\kappa}^2}$. The nondimensional energy of the free boundary with uniform curvature (divided by ϵ^2) equals $\hat{E}_{\text{free}} = \epsilon^{-1}\gamma\frac{r_n}{2}\left|\hat{\Gamma}_{\text{free}}\right|$.

The nozzle volume $|\Omega_{\text{n}}|$ consists of the volume between the shared boundary $\Gamma_{\text{N-C}}$ and the plane of the free surface contact line, and the volume $\left|\hat{\Omega}_{\text{n}}\right|$ enclosed between the plane of the free surface contact line and the free surface:

$$|\Omega_{\text{n}}| = \pi r_n^2\frac{H_{\text{CL}}}{L} + \left|\hat{\Omega}_{\text{n}}\right| = \pi r_n^2 h_{\text{CL}} + \frac{r_n^3}{8}\frac{8\pi}{3}\frac{1}{\hat{\kappa}^3}\left(2+\cos\theta(\hat{\kappa})\right)\left(1-\cos\theta(\hat{\kappa})\right)^2.$$

The effective height of the channel h_n (2.60) and the derivatives of the surface area and enclosed volume are functions of $\hat{\kappa}$:

$$h_n = h_n(\hat{\kappa}) = h_{\text{CL}} + \frac{r_n}{3}\frac{1}{\hat{\kappa}^3}\left(2+\cos\theta(\hat{\kappa})\right)\left(1-\cos\theta(\hat{\kappa})\right)^2, \tag{2.67a}$$

$$\frac{8}{r_n^3}\frac{d\left|\hat{\Omega}_{\text{n}}(\hat{\kappa})\right|}{d\hat{\kappa}} = \frac{4}{r_n^2}\frac{1}{\hat{\kappa}}\frac{d\left|\hat{\Gamma}_{\text{free}}(\hat{\kappa})\right|}{d\hat{\kappa}} = \frac{8\pi}{\hat{\kappa}^4}\frac{\left(1-\cos\theta(\hat{\kappa})\right)^2}{\cos\theta(\hat{\kappa})} \tag{2.67b}$$

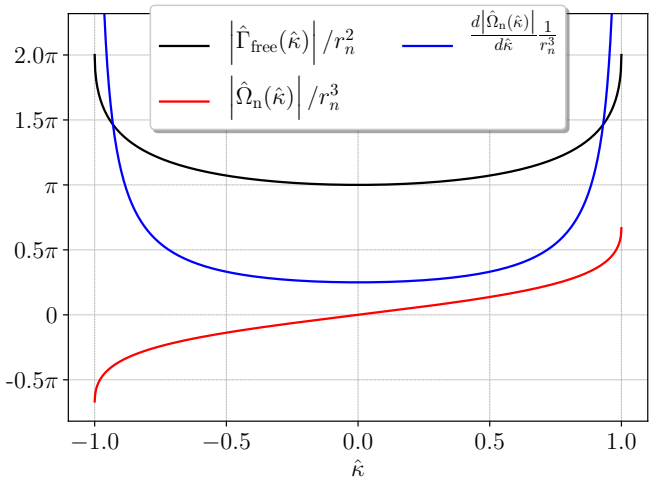

Fig. 2.5 Nondimensional area and volume of a spherical cap as functions of the uniform curvature variable $\hat{\kappa}$.

As discussed before, we assume that the position of the contact line does not change over time $\frac{d}{dt}H_{\text{CL}} = L\frac{d}{dt}h_{\text{CL}} = 0$, and therefore $\frac{d}{dt_{\text{ac}}}|\Omega_{\text{n}}| = \frac{d}{dt_{\text{ac}}}\left|\hat{\Omega}_{\text{n}}(\hat{\kappa})\right|$. The nozzle

volume conservation equation (2.64) then becomes an ODE on the uniform curvature $\hat{\kappa}$:

$$\left(\frac{d\left|\hat{\Omega}_{\mathrm{n}}(\hat{\kappa})\right|}{d\hat{\kappa}}\right)\frac{d}{dt_{\mathrm{ac}}}\hat{\kappa} = \epsilon\left\{\mathbf{u}\cdot\mathbf{n}\right\}_{\Gamma_{\mathrm{C-N}}} - \epsilon\left|\Omega_{\mathrm{n}}(\hat{\kappa})\right|\frac{d}{dt_{\mathrm{ac}}}\gamma\hat{\kappa}.$$

Given an initial condition $\hat{\kappa}(t=0)=\hat{\kappa}_0$, we can integrate this equation to calculate the uniform curvature at any time t:

$$\hat{\kappa}(t) = \hat{\kappa}_0 + \int_0^t \mathrm{d}t\left(\frac{d\left|\hat{\Omega}_{\mathrm{n}}(\hat{\kappa})\right|}{d\hat{\kappa}} + \epsilon\gamma\left|\Omega_{\mathrm{n}}(\hat{\kappa})\right|\right)^{-1}\epsilon\left\{\mathbf{u}\cdot\mathbf{n}\right\}_{\Gamma_{\mathrm{C-N}}}. \tag{2.68}$$

The term $\epsilon\gamma\left|\Omega_{\mathrm{n}}(\hat{\kappa})\right|$ is the sum of the static $\epsilon\gamma h_{\mathrm{CL}}\left|\Gamma_{\mathrm{C-N}}\right|$ and dynamic $\epsilon\gamma\left|\hat{\Omega}_{\mathrm{n}}(\hat{\kappa})\right|$ components. The contribution of the dynamic component $\epsilon\gamma\left|\hat{\Omega}_{\mathrm{n}}(\hat{\kappa})\right| \ll \frac{d\left|\hat{\Omega}_{\mathrm{n}}(\hat{\kappa})\right|}{d\hat{\kappa}}$ is of order ϵ^2, and can be neglected. This means that we consider the compressibility effects and potential energy of the nozzle flow only between the shared boundary and the static contact line. Under this assumption, the curvature state equation is

$$\frac{d}{dt_{\mathrm{ac}}}\left|\hat{\Omega}_{\mathrm{n}}(\hat{\kappa})\right| = \epsilon\left\{\mathbf{u}\cdot\mathbf{n}\right\}_{\Gamma_{\mathrm{C-N}}} - \epsilon h_{\mathrm{CL}}\left|\Gamma_{\mathrm{C-N}}\right|\frac{d}{dt_{\mathrm{ac}}}\gamma\hat{\kappa}, \tag{2.69a}$$

$$\hat{\kappa}(t) = \hat{\kappa}_0 + \int_0^t \mathrm{d}t\left(\frac{d\left|\hat{\Omega}_{\mathrm{n}}(\hat{\kappa})\right|}{d\hat{\kappa}} + \epsilon\gamma h_{\mathrm{CL}}\left|\Gamma_{\mathrm{C-N}}\right|\right)^{-1}\epsilon\left\{\mathbf{u}\cdot\mathbf{n}\right\}_{\Gamma_{\mathrm{C-N}}}. \tag{2.69b}$$

Finally, we substitute (2.67a) and (2.69b) into the acoustic stress boundary condition (2.65) which becomes a nonlinear (through the curvature term $\hat{\kappa}$) impedance boundary condition that depends only on the acoustic variables.

The proposed model is well-defined for $-1 \leq \hat{\kappa} \leq 1$. If the absolute value of the volume $\left|\hat{\Omega}_{\mathrm{n}}\right|$ exceeds $\frac{2}{3}\pi r_n^3$ the surface can no longer be parameterized only by the uniform curvature $\hat{\kappa}$. Thus we would need to extend the free surface reduced order model, for example by taking into account the motion of the contact line. The generalized Navier boundary condition is a promising candidate for the moving contact line model, as discussed by Fumagalli et al. (2018); Gerbeau et al. (2003); Qian et al. (2003).

2.5 Nozzle boundary conditions for the acoustic flow problems

We combine the acoustic stress boundary condition (2.65) and the uniform curvature free surface parametrization (2.67a) and (2.69b). The acoustic stress boundary condition then depends only on the acoustic velocity at the target boundary, explicitly via the inertial and viscous term, and implicitly via the curvature term. The nonlinear (through the curvature term $\hat{\kappa}$) impedance boundary condition approximates the flow field and the free surface inside the nozzle domain Ω_{n}. We simplify the nonlinear term $h_n\left(\frac{d}{dt_{\mathrm{ac}}}u_i - \frac{1}{\tilde{Re}}\Delta_\Gamma u_i\right)$ in the stress boundary condition (2.65) by considering the inertial and viscous effects only in the static part of the nozzle domain, and replace h_n with h_{CL}.

$$\sigma_{ij}n_j = -\gamma\hat{\kappa}n_i - h_{\mathrm{CL}}\left(\frac{d}{dt_{\mathrm{ac}}}u_i - \frac{1}{\tilde{Re}}\Delta_\Gamma u_i\right) \quad \text{on } \Gamma_{\mathrm{C-N}}, \tag{2.70a}$$

$$\left(\frac{d\left|\hat{\Omega}_{\mathrm{n}}(\hat{\kappa})\right|}{d\hat{\kappa}}\right)\frac{d}{dt_{\mathrm{ac}}}\hat{\kappa} = \epsilon\left\{\mathbf{u}\cdot\mathbf{n}\right\}_{\Gamma_{\mathrm{C-N}}} - \epsilon h_{\mathrm{CL}}\left|\Gamma_{\mathrm{C-N}}\right|\frac{d}{dt_{\mathrm{ac}}}\gamma\hat{\kappa}, \tag{2.70b}$$

$$\hat{\kappa}(t=0) = \hat{\kappa}_0, \tag{2.70c}$$

$$\left|\Omega_{\mathrm{n}}(\hat{\kappa})\right| = \pi r_n^2 h_{\mathrm{CL}} + \left|\hat{\Omega}_{\mathrm{n}}(\hat{\kappa})\right|. \tag{2.70d}$$

The boundary condition (2.70a) represents a system that possesses non-zero energy, and the acoustic energy conservation equation (2.39) can be rewritten as

$$\frac{d}{dt}\left(\mathcal{E}_{\mathrm{ac}} + \mathcal{E}_{\mathrm{n}}\right) + \mathcal{R}_{\mathrm{ac}} = \mathcal{F}_{\partial\Omega_{\mathrm{c}}/\Gamma_{\mathrm{C-N}}}, \tag{2.71a}$$

$$\mathcal{E}_{\mathrm{n}} = \epsilon^{-1}\frac{r_n}{2}\gamma\left|\hat{\Gamma}_{\mathrm{free}}\right| + \frac{h_{\mathrm{CL}}}{2}\left(\left\{(\mathbf{u}\cdot\mathbf{n})^2\right\}_{\Gamma_{\mathrm{C-N}}} + \left|\Gamma_{\mathrm{C-N}}\right|(\gamma\hat{\kappa})^2\right). \tag{2.71b}$$

Similarly to the simplified stress boundary condition, the kinetic and potential energy of the nozzle flow are accounted for only inside the static part of the nozzle domain.

The proposed impedance-type boundary condition (2.70) can be compared to existing models. In Kim et al. (2014); Stachewicz et al. (2009), the movement of the ink in the nozzle is described using a linear damping system. Similarly to the model in this thesis, those studies approximate the free surface by a spherical cap, but the equivalent of the curvature equation (2.70b) is linearized around $\hat{\kappa} = 0$. The fluid inertia is taken to be proportional to the ink column height, which corresponds exactly to the term $h_{\mathrm{CL}}\frac{d}{dt_{\mathrm{ac}}}u_i$ in (2.70a). The aforementioned studies approximate the

viscous flow resistance of the nozzle using the Poiseuille law, while in this study the viscous resistance $h_{\mathrm{CL}}\tilde{Re}^{-1}\Delta_\Gamma u_i$ is explicitly calculated from the acoustic state. Some studies (Kim et al., 2014; Shah et al., 2019) that use a linear damping model suggest estimating the viscous effects from numerical flow simulations with an actual nozzle shape geometry. Overall, the model used in this thesis is conceptually close to the existing models, but does not rely on the assumption of small magnitude perturbations of the free surface curvature, and can be more easily coupled with the acoustic flow model inside the channel.

2.5.1 Time discretization of the boundary condition

We derive the time discrete acoustic boundary condition on $\Gamma_{\mathrm{N-C}}$ for the unsteady thermoviscous acoustic equations (2.3.1). Using the Crank–Nicolson scheme, the discrete in time stress boundary condition (2.70a) becomes

$$\sigma_{ij}^{n+\frac{1}{2}} n_j = -\gamma\hat{\kappa}^{n+\frac{1}{2}} n_i - h_{\mathrm{CL}}\left(\overline{\partial_t} u_i^{n+\frac{1}{2}} - \frac{1}{\tilde{Re}}\Delta_\Gamma u_i^{n+\frac{1}{2}}\right) \quad \text{on } \Gamma_{\mathrm{C-N}}. \tag{2.72}$$

We substitute the stress term into the boundary term of the time discrete weak form (2.52), and collect the acoustic state variables $\mathbf{q}^{n+1}$ in the bilinear form.

The second order accurate discretization of the curvature equation (2.70b) is

$$\overline{\partial_t}\left|\hat{\Omega}_{\mathrm{n}}(\hat{\kappa})\right|^{n+\frac{1}{2}} = \epsilon\left\{\mathbf{u}^{n+\frac{1}{2}}\cdot\mathbf{n}\right\}_{\Gamma_{\mathrm{C-N}}} - \epsilon h_{\mathrm{CL}}\left|\Gamma_{\mathrm{C-N}}\right|\overline{\partial_t}\gamma\hat{\kappa}^{n+\frac{1}{2}} + \mathcal{O}\left(\Delta t^2\right), \tag{2.73}$$

or, in terms of the curvature variable $\hat{\kappa}^n$

$$\begin{aligned}\left(\frac{d\left|\hat{\Omega}_{\mathrm{n}}(\hat{\kappa})\right|}{d\hat{\kappa}}\right)^n \overline{\partial_t}\hat{\kappa}^{n+\frac{1}{2}} + \frac{\Delta t}{2}\left(\overline{\partial_t}\hat{\kappa}^{n-\frac{1}{2}}\right)^2\left(\frac{d^2\left|\hat{\Omega}_{\mathrm{n}}(\hat{\kappa})\right|}{d\hat{\kappa}^2}\right)^n = \\ = \epsilon\left\{\mathbf{u}^{n+\frac{1}{2}}\cdot\mathbf{n}\right\}_{\Gamma_{\mathrm{C-N}}} - \epsilon h_{\mathrm{CL}}\left|\Gamma_{\mathrm{C-N}}\right|\overline{\partial_t}\gamma\hat{\kappa}^{n+\frac{1}{2}} + \mathcal{O}\left(\Delta t^2\right),\end{aligned} \tag{2.74}$$

which allows us to express the unknown curvature at the $n+1$ time step as a function of $\mathbf{u}^{n+1}$ and variables from the previous time step.

The volume terms $a\left(\mathbf{p},\mathbf{q}^{n+1}\right), b\left(\mathbf{p},\mathbf{q}^{n+1}\right)$ in the time-discrete bilinear form (2.52) are independent of time. We notice that by using the implicit expression (2.74) in the stress boundary condition (2.72), the boundary term $b^{n+1}_{\Gamma_{\mathrm{C-N}}}\left(\mathbf{p},\mathbf{q}^{n+1}\right)$ becomes time

dependent,

$$b^{n+1}_{\Gamma_{\mathrm{C-N}}}\left(\mathbf{p},\mathbf{q}^{n+1}\right)=\left\{\gamma\hat{\kappa}^{n+1}\mathbf{v}\cdot\mathbf{n}\right\}_{\Gamma_{\mathrm{C-N}}}+\ldots$$
$$=\frac{\gamma\Delta t}{\left(\frac{d\left|\hat{\Omega}_{\mathrm{n}}(\hat{\kappa})\right|}{d\hat{\kappa}}\right)^{n}+\epsilon\gamma h_{\mathrm{CL}}\left|\Gamma_{\mathrm{C-N}}\right|}\frac{\epsilon}{2}\left\{\mathbf{u}^{n+1}\cdot\mathbf{n}\right\}_{\Gamma_{\mathrm{C-N}}}\left\{\mathbf{v}\cdot\mathbf{n}\right\}_{\Gamma_{\mathrm{C-N}}}+\ldots$$

In this case, after spatial discretization of the boundary component, a different matrix has to be inverted every time. If the discrete bilinear form is independent of time, the matrix factorization can be stored and re-used each time step. This greatly reduces the computational time required to run a direct solver, and, as shown later, the adjoint solver backwards in time. In order to reduce the cost of the unsteady computations, we use explicit approximation of the weak form boundary components that depend on time. We use explicit approximation of the term $\left\{\mathbf{u}^{n+\frac{1}{2}}\cdot\mathbf{n}\right\}_{\Gamma_{\mathrm{C-N}}}$ in (2.73) and (2.74), $\mathbf{u}^{n+\frac{1}{2}}\approx\left(1+\Delta t\overline{\partial_t}\right)\mathbf{u}^{n-\frac{1}{2}}+\mathcal{O}\left(\Delta t^2\right)=\frac{1}{2}\left(3\mathbf{u}^{n}-\mathbf{u}^{n-1}\right)\cdot\mathbf{n}+\mathcal{O}\left(\Delta t^2\right)$:

$$\overline{\partial_t}\left|\hat{\Omega}_{\mathrm{n}}(\hat{\kappa})\right|^{n+\frac{1}{2}}=\epsilon\left\{\left(1+\Delta t\overline{\partial_t}\right)\mathbf{u}^{n-\frac{1}{2}}\cdot\mathbf{n}\right\}_{\Gamma_{\mathrm{C-N}}}-\epsilon h_{\mathrm{CL}}\left|\Gamma_{\mathrm{C-N}}\right|\overline{\partial_t}\gamma\hat{\kappa}^{n+\frac{1}{2}}+\mathcal{O}\left(\Delta t^2\right),\tag{2.75}$$

and

$$\begin{aligned}&\left(\frac{d\left|\hat{\Omega}_{\mathrm{n}}(\hat{\kappa})\right|}{d\hat{\kappa}}\right)^{n}\overline{\partial_t}\hat{\kappa}^{n+\frac{1}{2}}+\frac{\Delta t}{2}\left(\overline{\partial_t}\hat{\kappa}^{n-\frac{1}{2}}\right)^{2}\left(\frac{d^2\left|\hat{\Omega}_{\mathrm{n}}(\hat{\kappa})\right|}{d\hat{\kappa}^2}\right)^{n}=\\&=\epsilon\left\{\left(1+\Delta t\overline{\partial_t}\right)\mathbf{u}^{n-\frac{1}{2}}\cdot\mathbf{n}\right\}_{\Gamma_{\mathrm{C-N}}}-\epsilon h_{\mathrm{CL}}\left|\Gamma_{\mathrm{C-N}}\right|\overline{\partial_t}\gamma\hat{\kappa}^{n+\frac{1}{2}}+\mathcal{O}\left(\Delta t^2\right).\end{aligned}\tag{2.76}$$

The time discrete boundary terms $b^{n+1}_{\Gamma_{\mathrm{C-N}}}\left(\mathbf{p},\mathbf{q}^{n+1}\right), b^{n}_{\Gamma_{\mathrm{C-N}}}\left(\mathbf{p},\mathbf{q}^{n}\right)$ are therefore given by

$$b^{n+\frac{1}{2}}_{\Gamma_{\mathrm{C-N}}}\left(\mathbf{p},\mathbf{q}^{n+\frac{1}{2}}\right)\equiv\frac{1}{2}\left(b^{n+1}_{\Gamma_{\mathrm{C-N}}}\left(\mathbf{p},\mathbf{q}^{n+1}\right)+b^{n}_{\Gamma_{\mathrm{C-N}}}\left(\mathbf{p},\mathbf{q}^{n}\right)\right),\tag{2.77a}$$

$$b^{n+1}_{\Gamma_{\mathrm{C-N}}}\left(\mathbf{p},\mathbf{q}^{n+1}\right)=h_{\mathrm{CL}}\left\{\left(\frac{2}{\Delta t}-\frac{1}{\tilde{R}e}\Delta_{\Gamma}\right)\mathbf{u}^{n+1},\mathbf{v}\right\}_{\Gamma_{\mathrm{C-N}}},\tag{2.77b}$$

$$\begin{aligned}b^{n}_{\Gamma_{\mathrm{C-N}}}\left(\mathbf{p},\mathbf{q}^{n}\right)=&\,h_{\mathrm{CL}}\left\{\left(\frac{2}{\Delta t}+\frac{1}{\tilde{R}e}\Delta_{\Gamma}\right)\mathbf{u}^{n},\mathbf{v}\right\}_{\Gamma_{\mathrm{C-N}}}+2\gamma\hat{\kappa}^{n}\left\{\mathbf{v}\cdot\mathbf{n}\right\}_{\Gamma_{\mathrm{C-N}}}\\&+\frac{2\epsilon\Delta t\gamma\left\{\left(1+\Delta t\overline{\partial_t}\right)\mathbf{u}^{n-\frac{1}{2}}\cdot\mathbf{n}\right\}_{\Gamma_{\mathrm{C-N}}}}{\left(\frac{d\left|\hat{\Omega}_{\mathrm{n}}(\hat{\kappa})\right|}{d\hat{\kappa}}\right)^{n}+\epsilon\gamma h_{\mathrm{CL}}\left|\Gamma_{\mathrm{C-N}}\right|}\left\{\mathbf{v}\cdot\mathbf{n}\right\}_{\Gamma_{\mathrm{C-N}}}.\end{aligned}\tag{2.77c}$$

The term (2.77b), and the first and the third terms in (2.77c) represent the change of the nozzle flow kinetic energy and viscous dissipation inside the nozzle Ω_{n}. The second term in (2.77c) approximates the change of the free surface energy.

Together with the volume components of the weak form (2.52), the discussed time discretization of the boundary components on the shared boundary $\Gamma_{\mathrm{C-N}}$ (2.77) results in a second-order accurate approximation of the original unsteady problem. Although the weak formulation contains explicit terms in $b^{n+\frac{1}{2}}_{\Gamma_{\mathrm{C-N}}}\left(\mathbf{p}, \mathbf{q}^{n+\frac{1}{2}}\right)$, the spatial discretization of the resulting bilinear form is independent of time, and has to be factorized only once for each unsteady problem. The same inverted matrix is then applied to the vector representation of the linear form (2.53) at each time step.

To verify the implementation of the time integration scheme, an unsteady thermoviscous acoustic problem was solved in a unit square domain with the nondimensional final time $t_f = 1$. The nozzle boundary condition (2.72) with $\hat{\kappa}(t = 0) = 0.25$ is prescribed on one wall, and the other boundaries are no slip. The initial acoustic state is zero everywhere. The total energy $\mathcal{E} = \mathcal{E}_{\mathrm{ac}} + \mathcal{E}_{\mathrm{n}}$ is calculated at $t = t_f$, and the convergence of this value with respect to the time step size Δt is shown in figure 2.6. For all examined mesh sizes h, the second order convergence in Δt is observed, as expected.

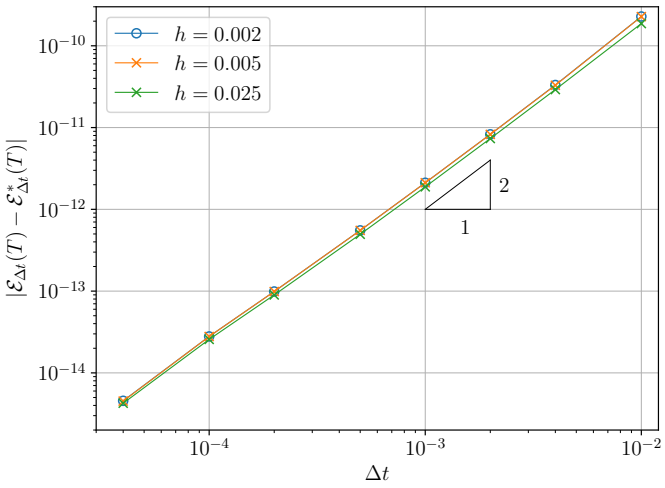

Fig. 2.6 Convergence of the total energy $\mathcal{E}(t_f)$ with time step refinement for an unsteady thermoviscous flow with a nozzle boundary condition.

2.5.2 Eigenvalue problem boundary conditions

We derive the boundary conditions for the acoustic eigenvalue problem discussed in section 2.3.2. The acoustic stress boundary condition on the surface between the channel and nozzle domains $\Gamma_{\mathrm{C-N}}$ (2.70) is given by a nonlinear system of equations. We linearize the nozzle state equation (2.70b) around the base state,

$$\hat{\kappa} = \hat{\kappa}^{(0)} + \delta\hat{\kappa}, \quad |\Omega_{\mathrm{n}}(\hat{\kappa})| \simeq \left|\Omega_{\mathrm{n}}(\hat{\kappa}^{(0)})\right|, \quad h_n^{(0)} \equiv h_n(\hat{\kappa}^{(0)}) = h_{\mathrm{CL}} + \frac{\left|\hat{\Omega}_{\mathrm{n}}(\hat{\kappa}^{(0)})\right|}{|\Gamma_{\mathrm{C-N}}|}.$$

We perform a Fourier transform and replace the time derivative operator with the complex oscillation frequency of the mode $\frac{\partial}{\partial t} \to s$. The linearized nozzle state equation becomes

$$s\left(\frac{d\left|\hat{\Omega}_{\mathrm{n}}(\hat{\kappa})\right|}{d\hat{\kappa}} + \epsilon\gamma h_n\left|\Gamma_{\mathrm{C-N}}\right|\right)\Bigg|_{\hat{\kappa}^{(0)}} \delta\hat{\kappa} = \epsilon\left\{\hat{\mathbf{u}}\cdot\mathbf{n}\right\}_{\Gamma_{\mathrm{C-N}}}.$$

The linearized acoustic stress boundary condition on $\Gamma_{\mathrm{C-N}}$ is an impedance type boundary condition. It is a sum of the capacitive reactance, inductive reactance, and resistance terms:

$$\begin{aligned}\hat{\sigma}_{ij}n_j =& -\gamma\delta\hat{\kappa}n_i - h_n^{(0)}\left(s - \frac{1}{Re}\Delta_\Gamma\right)\hat{u}_i \\ =& -\frac{1}{s}\underbrace{\frac{\epsilon\gamma}{\left(\frac{d\left|\hat{\Omega}_{\mathrm{n}}(\hat{\kappa})\right|}{d\hat{\kappa}} + \epsilon\gamma h_n\left|\Gamma_{\mathrm{C-N}}\right|\right)\Big|_{\hat{\kappa}^{(0)}}}}_{\text{Capacitance}}\left\{\hat{\mathbf{u}}\cdot\mathbf{n}\right\}_{\Gamma_{\mathrm{C-N}}} n_i \\ & - s\underbrace{h_n^{(0)}}_{\text{Inductance}}\hat{u}_i + \underbrace{\frac{h_n^{(0)}}{Re}\Delta_\Gamma}_{\text{Resistance}}\hat{u}_i.\end{aligned} \tag{2.78}$$

The first term, $-\frac{1}{sC}$, is a high-pass filter, as the the free surface contribution to the acoustic stress boundary condition is proportional to the cumulative (integrated over time) mass flow through the shared boundary $\{\mathbf{u}\cdot\mathbf{n}\}_{\Gamma_{\mathrm{C-N}}}$ (see 2.70b), and high frequency oscillations on average do not contribute to the change in $\hat{\kappa}$. The second term, $-sL$, is a low-pass filter, as the nozzle flow inertia attenuates high frequency oscillations.

The inductance and resistance terms of the acoustic stress $\hat{\sigma}_{ij}n_j$ depend on the local velocity value $\hat{u}_i$, and the capacitance term contains a nonlocal term $\{\hat{\mathbf{u}}\cdot\mathbf{n}\}_{\Gamma_{\mathrm{C-N}}}$. We use different strategies to find a solution of the frequency domain problem (2.26)

and the eigenvalue problem (2.27) subject to the impedance boundary condition on $\Gamma_{\mathrm{C-N}}$.

The eigenvalue problem boundary condition

Finite element approximation of the eigenpairs of second order eigenvalue problems with nonlocal Dirichlet, Neumann and Robin boundary conditions is discussed in Ta-Tsien (1989), De Schepper and Van Keer (1997), Andreev and Racheva (2007). The key point of solving such problems is to introduce a suitable finite element space V and a finite dimensional subspace $V_h \subset V$,

$$V = \left\{ v \in H^1(\Omega) \,\middle|\, \int_{\Gamma_0} v \, \mathrm{d}s = 0 \right\},$$

where Γ_0 is the boundary with a nonlocal boundary condition. However, the finite element framework FEniCS used in this study does not implement automated generation of such discrete spaces. Instead, we propose to replace the nonlocal term with a local approximation,

$$\{\hat{\mathbf{u}} \cdot \mathbf{n}\}_{\Gamma_{\mathrm{C-N}}} n_i \to |\Gamma_{\mathrm{C-N}}| \, \hat{u}_i,$$

such that the stress boundary condition for the eigenvalue problem becomes a local impedance boundary condition:

$$\hat{\sigma}_{ij} n_j = Z_{\mathrm{loc}}(s) \hat{u}_i \quad \text{on } \Gamma_{\mathrm{C-N}}, \tag{2.79a}$$

$$Z_{\mathrm{loc}}(s) = -\frac{1}{s} \frac{\epsilon\gamma \, |\Gamma_{\mathrm{C-N}}|}{\left(\frac{d\left|\hat{\Omega}_{\mathrm{n}}(\hat{\kappa})\right|}{d\hat{\kappa}} + \epsilon\gamma h_n \, |\Gamma_{\mathrm{C-N}}| \right)\Big|_{\hat{\kappa}^{(0)}}} - s h_n^{(0)} + \frac{h_n^{(0)}}{Re} \Delta_\Gamma. \tag{2.79b}$$

$Z_{\mathrm{loc}}(s)$ is a differential impedance operator. We substitute the boundary condition into the weak form (2.41) and obtain a nonlinear (through the capacitance term) eigenvalue problem.

The discrete eigenproblem: find $s, \hat{\mathbf{q}}_h$ such that

$$sa(\mathbf{p}_h, \hat{\mathbf{q}}_h) + b(\mathbf{p}_h, \hat{\mathbf{q}}_h) + b_{\partial\Omega_{\mathrm{c}}/\Gamma_{\mathrm{C-N}}}(\mathbf{p}_h, \hat{\mathbf{q}}_h) + b_{\Gamma_{\mathrm{C-N}}}(s; \mathbf{p}_h, \hat{\mathbf{q}}_h) = 0 \tag{2.80}$$

is solved using a fixed-point iterative algorithm (Nicoud et al., 2007) with relaxation (Ni, 2017).

1. We set $\hat{\sigma}_{ij} n_j = 0$ on $\Gamma_{\mathrm{C-N}}$ and therefore $b_{\Gamma_{\mathrm{C-N}}}(s; \mathbf{p}_h, \hat{\mathbf{q}}_h) = 0$, and identify the eigenvalues $s_i^{[0]}$, $i = 1, 2, \ldots$ of the acoustic eigenvalue problem with a stress-free

boundary condition on $\Gamma_{\mathrm{C-N}}$. We select one frequency of interest $s^{[0]}$ and use it as an initial guess for the algorithm.

2. We use $s^{[0]}$ as the first iteration guess, and solve

$$sa\left(\mathbf{p}_h, \hat{\mathbf{q}}_h\right) + b\left(\mathbf{p}_h, \hat{\mathbf{q}}_h\right) + b_{\partial\Omega_{\mathrm{c}}/\Gamma_{\mathrm{C-N}}}\left(\mathbf{p}_h, \hat{\mathbf{q}}_h\right) + b_{\Gamma_{\mathrm{C-N}}}\left(s^{[0]}; \mathbf{p}_h, \hat{\mathbf{q}}_h\right) = 0.$$

The first iteration approximation of the eigenvalue is $s^{[1]} = s$.

3. We define the algorithm tolerance criteria, $\varepsilon > 0$. For $k \geq 2$, we set $b_{\Gamma_{\mathrm{C-N}}} = b_{\Gamma_{\mathrm{C-N}}}\left(s^{[k-1]}; \mathbf{p}_h, \hat{\mathbf{q}}_h\right)$ in (2.80), and find the eigenvalue s of the corresponding problem that is closest to the previous step solution $s^{[k-1]}$. The k-th iteration value $s^{[k]}$ is calculated using relaxation

$$s^{[k]} = \alpha s + (1-\alpha) s^{[k-1]},$$

where the value of the relaxation coefficient α is chosen in order to optimize the convergence of the algorithm (Ni, 2017):

$$\alpha = \frac{1}{1 - \frac{\partial s}{\partial s^{[k-1]}}}, \qquad \frac{\partial s}{\partial s^{[k-1]}} \approx \frac{s - s^{[k-1]}}{s^{[k-1]} - s^{[k-2]}}. \tag{2.81}$$

The iterative algorithm is stopped if the difference falls below the convergence threshold $\left|s^{[k]} - s^{[k-1]}\right| < \varepsilon$. Otherwise, we proceed to the next iteration $k \to k+1$.

This iterative fixed-point algorithm effectively minimizes the difference $\left|s - s^{[k]}\right|$ using Newton's method with the function gradient given by the backwards difference approximation.

2.6 Numerical examples

In this section, we study the eigenvalue problem corresponding to the thermoviscous acoustic flow inside an inkjet printhead microchannel (figure 2.7). The physical domain is a symmetric U-shaped channel, and we perform the analysis in the left subdomain and provide an appropriate set of boundary conditions on the symmetry plane Γ_{sym}. We apply standard no slip, adiabatic boundary conditions on the channel walls Γ_{w}, and stress-free, isothermal conditions on the outlet boundaries Γ_{out}. A typical depth of the channel in 3D is 100μm. We examine a 2D domain now, but extension to 3D is

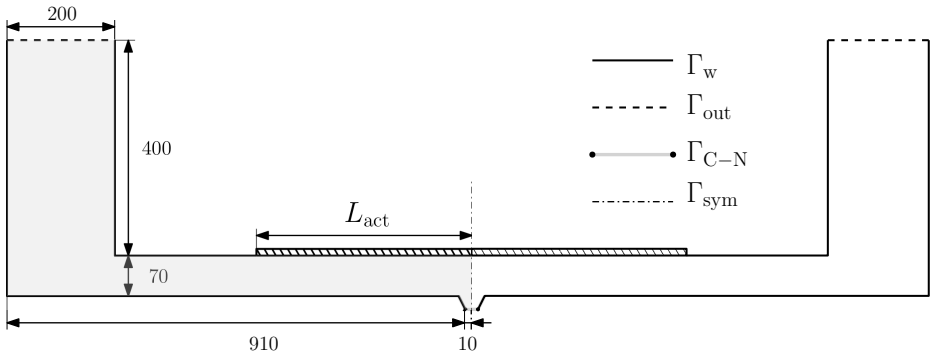

Fig. 2.7 Symmetric printhead microchannel domain (sizes in μm). The right boundary is a symmetry plane.

possible and conceptually straight-forward. The parameters of the experiments are provided in table 2.1.

	dimensional value
speed of sound, c_s, m $\cdot$ s^{-1}	10^3
Mach number, ϵ	10^{-5}
viscosity, μ_{vis}, kg (m $\cdot$ s)$^{-1}$	$1.6 \cdot 10^{-2}$
Prandtl number, Pr	10
surface tension, γ_{dim}, N $\cdot$ m^{-1}	$50 \cdot 10^{-3}$
nozzle radius, R_n, m	$10 \cdot 10^{-6}$
nozzle height, H_{CL}, m	$10 \cdot 10^{-6}$
characteristic length, L, m	$100 \cdot 10^{-6}$
actuator length, L_{act}, m	$400 \cdot 10^{-6}$

Table 2.1 Dimensional parameters of the inkjet microchannels numerical experiments.

2.6.1 Spectrum of a 2D printhead microchannel

The thermoviscous acoustic flow (§2.3.3) is dissipative $\frac{d}{dt}\mathcal{E}_{\text{ac}} < 0$, and therefore the real part of the spectrum is always negative $\text{Re}(s) \equiv \sigma < 0$. We solve the discretized eigenvalue problem (2.44) using the SLEPc toolkit (Hernandez et al., 2005) and its `python` interface `SLEPc4py` (Dalcin et al., 2011). To speed up the convergence of the eigenvalue solver, we apply the shift-invert strategy and target the lowest magnitude eigenvalues.

Since the printhead microchannel domain is symmetric, we can solve the eigenvalue problem in the left half of the domain subject to the symmetric (2.31) or antisymmetric

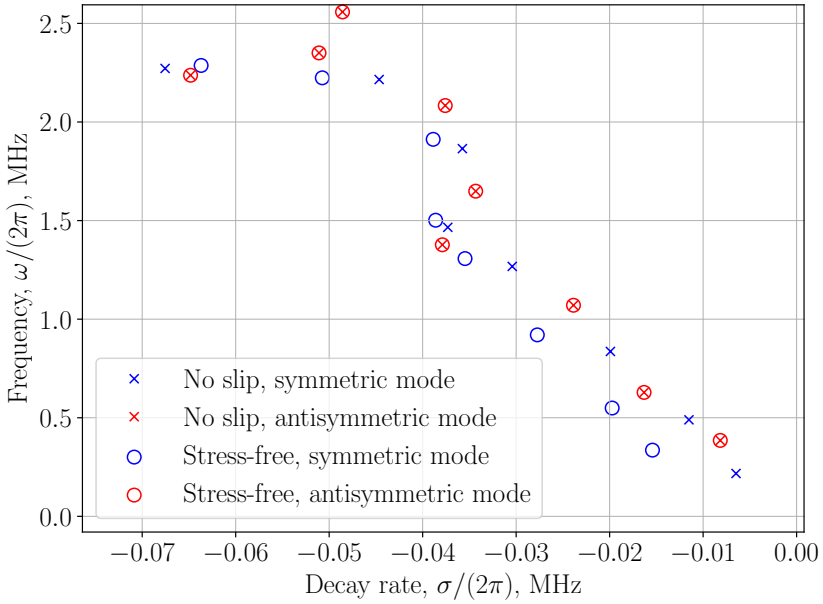

Fig. 2.8 Spectrum of the thermoviscous acoustic flow inside a printhead microchannel with the stress-free boundary condition (∘), and no slip boundary condition (×) on $\Gamma_{\mathrm{C-N}}$. Blue markers denote symmetric modes, red markers denote antisymmetric modes.

(2.30) boundary conditions on Γ_{sym} (the symmetry is presumed with respect to the pressure modes):

$$\begin{aligned} \text{symmetric modes}: \quad & \hat{\mathbf{u}} \cdot \mathbf{n} = 0, \ \frac{\partial \hat{T}}{\partial \mathbf{n}} = 0 \quad \text{on } \Gamma_{\mathrm{sym}}, \\ \text{antisymmetric modes}: \quad & \hat{\sigma}_{ij} n_j = 0, \ \hat{T} = 0 \quad \text{on } \Gamma_{\mathrm{sym}}. \end{aligned} \tag{2.82}$$

The spectrum of the acoustic flow in the original domain is the sum of the symmetric and antisymmetric eigenvalues. Figure (2.8) shows the spectrum of the thermoviscous acoustic flow inside the printhead microchannel when the channel-nozzle boundary $\Gamma_{\mathrm{C-N}}$ is modelled as a stress free, adiabatic boundary (empty circles ∘), and the flow spectrum when the no slip boundary condition is applied on $\Gamma_{\mathrm{C-N}}$ (× markers). Blue symbols denote symmetric modes, and red symbols denote antisymmetric modes.

For the modes with frequency ω below 1.2 MHz and stress-free boundary condition on $\Gamma_{\mathrm{C-N}}$, symmetric modes have a lower decay rate σ (the magnitude of the negative decay rate is larger) than the antisymmetric modes. The symmetric acoustic oscillations decay faster due to the high velocity of the flow inside the nozzle part of the channel

(figure 2.9b), while the velocity magnitude in the nozzle of the antisymmetric modes (figure 2.10b) is almost zero.

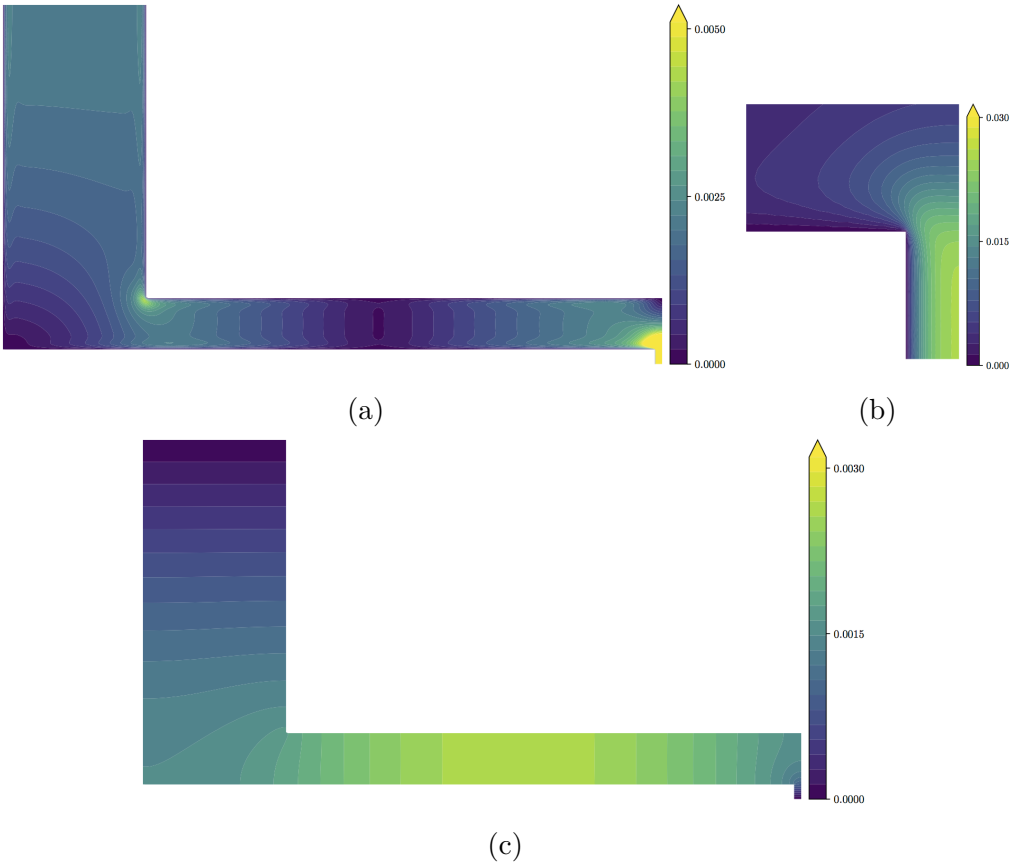

Fig. 2.9 The first symmetric mode with the stress-free boundary condition on $\Gamma_{\mathrm{C-N}}$. (a) Velocity component magnitude $|\hat{\mathbf{u}}|$ inside the printhead microchannel, (b) inside the nozzle part of the microchannel. (c) Pressure component magnitude $\left|\hat{P}\right|$.

The eigenvalues of the antisymmetric modes with no slip and stress-free boundary conditions on $\Gamma_{\mathrm{C-N}}$ are almost equal (compare the red markers in figure 2.8) because the effective impedance of the nozzle part of the domain is high. The mode shapes are very similar (compare the velocity fields in figures 2.10a and 2.11a, and the pressure fields in figures 2.10c and 2.11c), and differ only in the nozzle part of the channel, where different boundary conditions are applied on $\Gamma_{\mathrm{C-N}}$ (figures 2.10b and 2.11b).

Figure 2.13 shows the volumetric decay rate σ_Ω (2.48) for the lowest frequency symmetric modes with stress-free and no slip $\Gamma_{\mathrm{C-N}}$. In both cases, acoustic oscillations mostly dissipate in the boundary layers near the no slip walls Γ_{w}, and there is almost no dissipation along the centreline of the channel. The high velocity amplitude near the nozzle in the stress-free case (figure 2.13a) greatly contributes to the decay rate

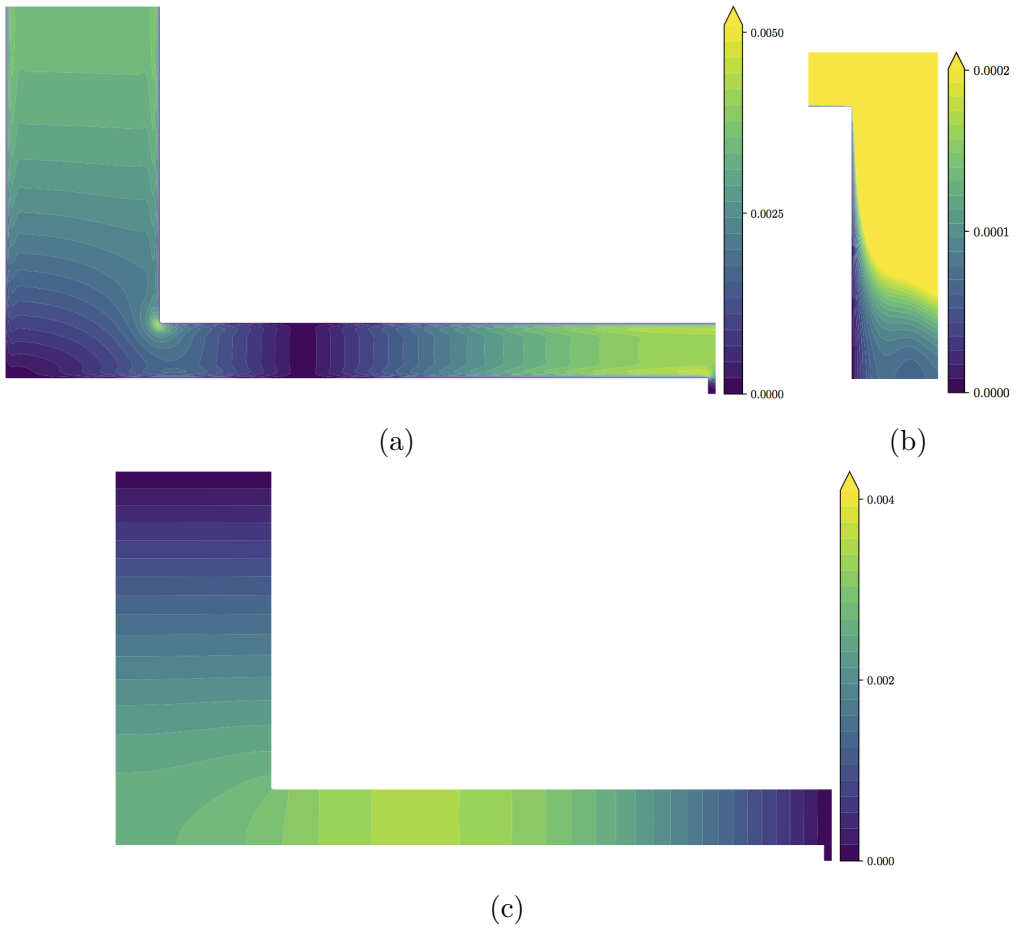

(a) (b)

(c)

Fig. 2.10 The first antisymmetric mode with the stress-free boundary condition on $\Gamma_{\mathrm{C-N}}$. (a) Velocity component magnitude $|\hat{\mathbf{u}}|$ inside the printhead microchannel, (b) inside the nozzle part of the microchannel. (c) Pressure component magnitude $\left|\hat{P}\right|$.

of the mode, which is the expected behaviour for typical inkjet systems (Smith and Shin, 2012). In the no slip case (figure 2.13b), the velocity amplitude near the nozzle is almost zero, and contributes very little to the decay rate of the mode.

2.6.2 Printhead spectrum with the nozzle model boundary condition

So far we have discussed the spectrum of a printhead microchannel with the stress-free and no slip boundary conditions on the nozzle boundary $\Gamma_{\mathrm{C-N}}$. We continue this analysis by applying the impedance boundary condition (2.79) that represents the reduced order model of the nozzle flow with the moving free surface. We use the same values of the nozzle radius and height, fluid viscosity and Mach number as in table

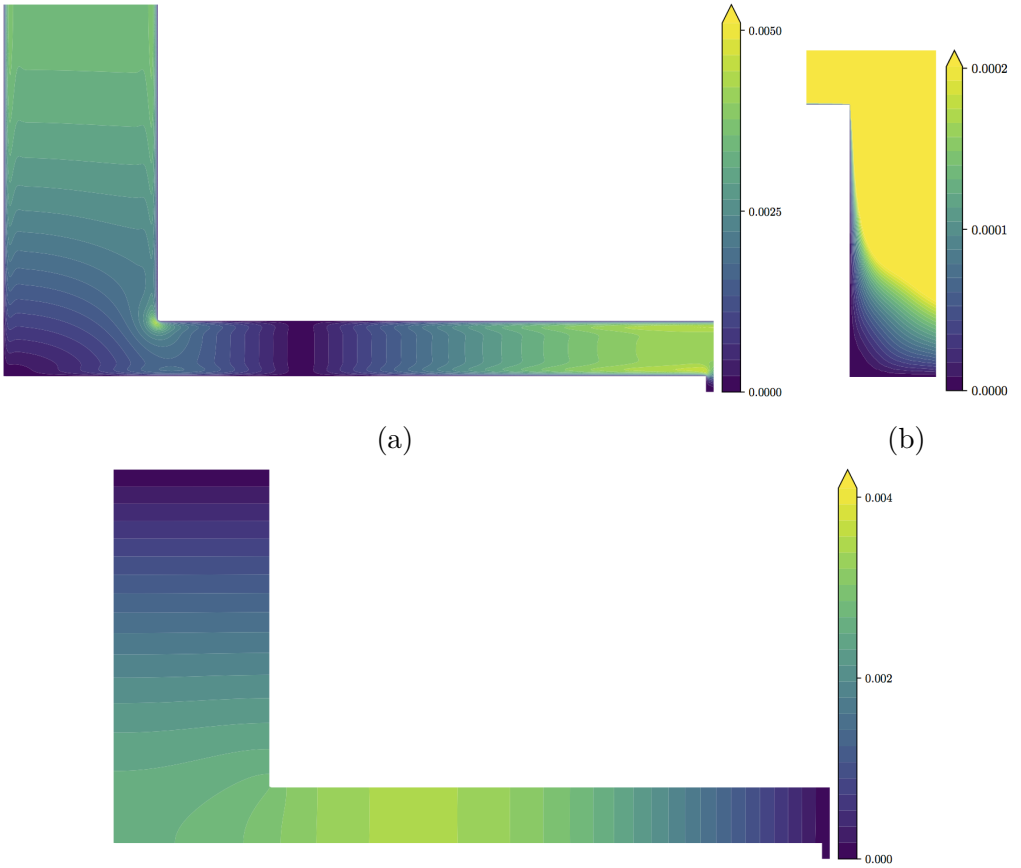

Fig. 2.11 The first antisymmetric mode with the no slip boundary condition on $\Gamma_{\mathrm{C-N}}$. (a) Velocity component magnitude $|\hat{\mathbf{u}}|$ inside the printhead microchannel, (b) inside the nozzle part of the microchannel. (c) Pressure component magnitude $\left|\hat{P}\right|$.

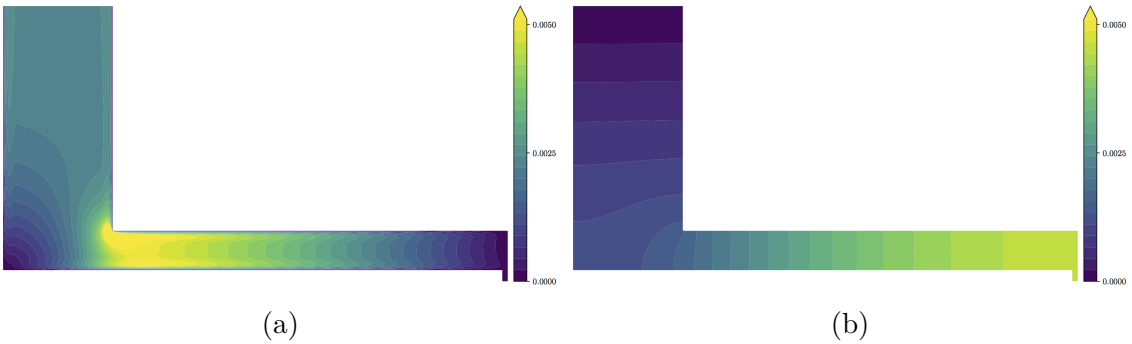

Fig. 2.12 The first symmetric mode with the no slip boundary condition on $\Gamma_{\mathrm{C-N}}$. (a) Velocity component magnitude $|\hat{\mathbf{u}}|$. (b) Pressure component magnitude $\left|\hat{P}\right|$.

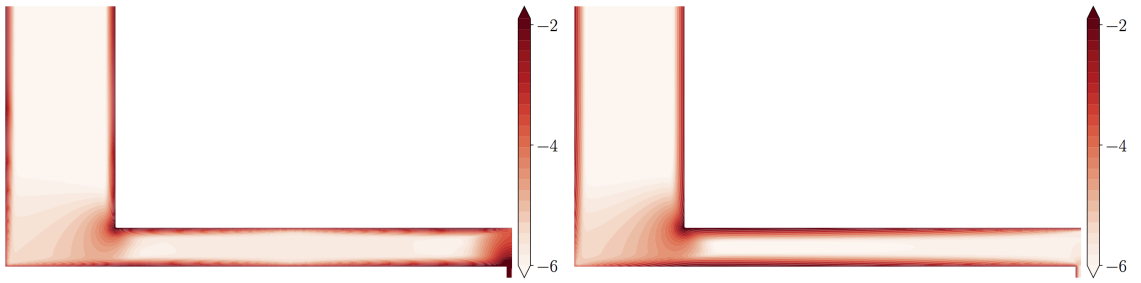

(a) (b)

Fig. 2.13 Spatial distribution of the absolute value of the volumetric decay rate in the printhead channel (on a logarithmic scale), $\log_{10}(-\sigma_\Omega)$, of the first symmetric mode with (a) the stress-free, (b) no slip boundary on $\Gamma_{\mathrm{C-N}}$.

2.1. The effective height of the nozzle is always positive $h_n^{(0)} > 0$. The value of the capacitance term is defined by the nondimensional surface tension coefficient, and the base state curvature $\hat{\kappa}^{(0)}$ around which the linearisation is done. The value of $\hat{\kappa}^{(0)}$ determines the value of the nozzle volume derivative with respect to the curvature $\frac{d\left|\hat{\Omega}_{\mathrm{n}}(\hat{\kappa})\right|}{d\hat{\kappa}}$ (2.5). The capacitance term is positive and bounded from above:

$$0 < \frac{\epsilon\gamma\left|\Gamma_{\mathrm{C-N}}\right|}{\left(\frac{d\left|\hat{\Omega}_{\mathrm{n}}(\hat{\kappa})\right|}{d\hat{\kappa}} + \epsilon\gamma h_n\left|\Gamma_{\mathrm{C-N}}\right|\right)\Big|_{\hat{\kappa}^{(0)}}} \leq \frac{4\epsilon\gamma}{r_n}, \tag{2.83}$$

and reaches its maximum value at $\hat{\kappa}^{(0)} = 0$. We use the flat free surface $\hat{\kappa}^{(0)} = 0$ as the base state. When the surface tension coefficient γ is large, the capacitance term dominates and the nozzle boundary $\Gamma_{\mathrm{C-N}}$ becomes no slip in the limiting case. When $\gamma \to 0$, however, the nozzle boundary does not become a stress-free boundary because of the non-zero inductance and resistance.

The motion of the actuator boundary creates symmetric acoustic oscillations, and we choose the lowest frequency symmetric modes to be the main target for our analysis. We analyse the spectrum of the symmetric acoustic oscillations and the drift of the eigenvalues for different values of γ. For a range of nondimensional surface tension values $\gamma \in [0, 10]$ we solve the corresponding eigenvalue problems using the iterative technique discussed in section 2.5.2. We start by setting $\gamma = 0$ and use one of the low frequency eigenvalues of the stress-free modes ($\hat{\sigma}_{ij}n_j = 0$ on $\Gamma_{\mathrm{C-N}}$) as the initial guess. Figure 2.14 shows that the natural frequencies of these modes ($\gamma = 0$, red dots) are close to the stress-free eigenvalues (empty blue circles), as expected. We gradually increase γ and use the previous converged eigenvalue as the new initial guess; the eigenvalues approach the no slip solution with a lower frequency and decay rate. Figure

2.14 shows the trajectories of the eigenvalues from $\gamma = 0$ to $\gamma \to \infty$ (solid red lines). For a typical surface tension of ink $\gamma_{\text{dim}} = 20 \cdot 10^{-3}$ Nm^{-1} to $70 \cdot 10^{-3}$ Nm^{-1} (Dijksman, 2019), the nondimensional value is $\gamma = 0.2$ to 1.4, and the respective eigenvalues lie between the stress-free and the no slip modes. If a free surface with a non-zero curvature is chosen as the base state $\hat{\kappa}^{(0)} \neq 0$, or the acoustic flow Mach number ϵ is low, the magnitude of the capacitance term decreases and the $\gamma = 1$ eigenvalues shifts towards the $\gamma = 0$ solution. In this case, the stress-free boundary condition on $\Gamma_{\text{C-N}}$ is a better approximation than the no slip boundary condition.

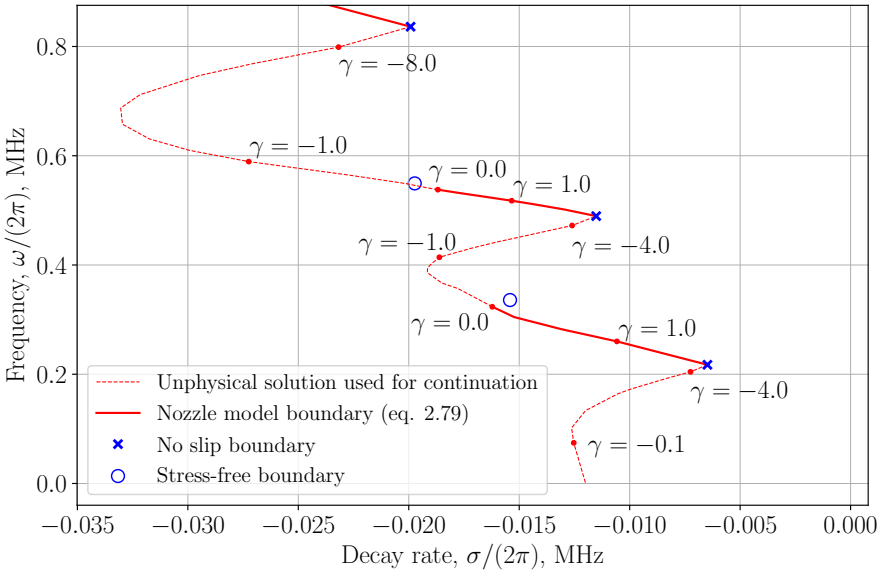

Fig. 2.14 Eigenvalues of the symmetric modes of the acoustic flow inside the printhead microchannel with the no slip (×) and stress-free (○) boundary conditions on $\Gamma_{\text{C-N}}$. The solid red lines show the eigenvalues corresponding to a range of positive surface tension coefficients γ used in the reduced order model of the nozzle flow (2.79) as the boundary condition on $\Gamma_{\text{C-N}}$. The dashed red lines are the continuation of the eigenvalue trajectories to the negative capacitance of the nozzle boundary condition.

We can find a continuation of the positive γ eigenvalues trajectories if we allow the capacitance term to be negative, or, equivalently, allow negative surface tension $\gamma < 0$. Figure 2.14 shows that the negative trajectories (dashed red lines) connect the $\gamma = 0$ modes to higher frequency, no slip modes as γ decreases to $\gamma \to -\infty$. The trajectory of the eigenvalues shift becomes a continuous line parameterized by the value of the capacitance term $\frac{\epsilon\gamma|\Gamma_{\text{C-N}}|}{\left(\frac{d|\hat{\Omega}_{\text{n}}(\hat{\kappa})|}{d\hat{\kappa}} + \epsilon\gamma h_n|\Gamma_{\text{C-N}}|\right)\Big|_{\hat{\kappa}(0)}}$.

2.7 Conclusions

In this chapter the physics and modelling of the flow inside an inkjet printhead microchannel is discussed. We use low Mach number asymptotic analysis to separate the compressible Navier–Stokes equations into equations for a steady flow with no oscillations (incompressible flow) and equations for oscillations with no steady flow (thermoviscous acoustic flow). The main requirements of this method are that the steady flow Mach number and oscillating flow Mach number are small, which are often satisfied in microfluidics, so the methods in this chapter could be applied to many other applications.

We focus on the acoustic flow phenomena. We separate the free surface flow inside the nozzle part of the channel Ω_{n} from the acoustic flow inside the rest of the printhead microchannel Ω_{c}. We approximate the free interface between the fluid (ink) and the outside gas by a spherical cap with uniform curvature, and account for the kinetic and potential energy and viscous dissipation of the flow inside the nozzle subdomain Ω_{n}. We develop a reduced order model for the nozzle flow that is an ordinary differential equation of the free surface effective curvature, and a nonlinear acoustic impedance boundary condition on the shared boundary $\Gamma_{\mathrm{C-N}} = \Omega_{\mathrm{c}} \bigcap \Omega_{\mathrm{n}}$.

We analyse the spectrum of the thermoviscous acoustic flow inside a 2D inkjet printhead microchannel. We show that the natural frequencies of the flow with the nozzle model boundary condition on $\Gamma_{\mathrm{C-N}}$ are enclosed between natural frequencies corresponding to the flow with stress-free and no slip boundary conditions on $\Gamma_{\mathrm{C-N}}$. We discuss how the surface tension coefficient and the deformation amplitude (curvature) of the base unperturbed state of the free surface affects the natural modes of the system. The reduced order nozzle model boundary condition behaves more as an open end (stress-free) boundary rather than a no slip boundary for typical values of the surface tension coefficient.

2.7.1 Advanced models

So far we have introduced several assumptions about fluid and structural dynamics of an inkjet printhead. First, we ignored any interaction between the incompressible and the acoustic flows: the low Mach number flows discussed in sections 2.2.3 and 2.2.4 are independent. Bubbles and solid impurities carried by the incompressible mean flow will impact the natural oscillation frequencies and the acoustic wave propagation inside the microchannels (de Jong et al., 2006). Second, we assumed that the piezo actuator boundary velocity can be prescribed directly. However, the transfer function between

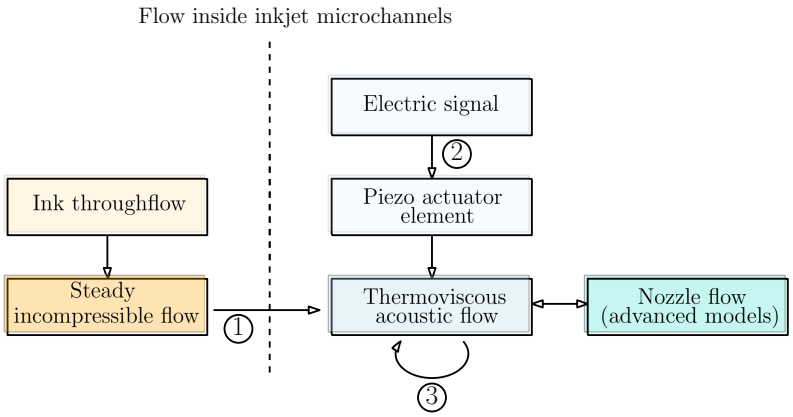

Fig. 2.15 Advanced model components diagram of the flow inside an inkjet printhead microchannel: (1) interaction between the steady incompressible through flow and the acoustic oscillations, (2) dependency between the applied voltage and the piezo actuator displacement, and (3) cross-talk effects.

the applied driving voltage V_{piezo} and the piezo element displacement d, $\mathcal{H} : V_{\text{piezo}} \to d$ depends on frequency, the piezo layer thickness and operating conditions (Brünahl and Grishin, 2002; Gautschi, 2002; Wijshoff, 2010). It is important to investigate the effect of the implicit control model: voltage to actuator velocity, on the feasible waveforms. Third, we ignored the interactions between adjacent microchannels, as if they were separated by an impermeable solid plate that damps all fluid and channel walls vibration. The cross-talk effect generated by neighboring channels deformation and travelling acoustic pressure waves reduces the performance of inkjet printheads: it is not possible to maintain desired jetting behaviour in two neighboring channels at the same time (Kretschmer and Beurer, 1997; Smith and Shin, 2012). Incorporating a model to measure cross-talk is a first step towards optimal cross-talk control (Khalate et al., 2012; Voit et al., 2011) and the multichannel waveform design. These are left for future work.

Chapter 3

Actuator velocity profile optimization

Piezo actuator waveforms consist of two phases: the *ejection* phase and the *residual control* phase. The purpose of the *ejection* phase is to push the flow through the nozzle and form a droplet with the desired characteristics. The purpose of the *residual control* phase is to prepare the flow inside the microchannel for the next printing cycle, by active damping of residual acoustic waves and elimination of satellite droplets. We aim to reduce the residual oscillations by optimizing the deformation at the channel wall caused by the piezo-electric actuator. In practice, this deformation is caused by a voltage waveform, which is applied across the actuator. The relationship between voltage and deformation depends on the actuator so, rather than focus on a specific actuator, here we focus on the motion it induces at the boundary. In this chapter we use adjoint-based optimization to find an actuator velocity waveform that, within the *residual control* phase of a given time, both flattens the liquid/air interface at the nozzle and eliminates residual oscillations in the channel. In practice, this time would be the desired period between droplets and this process would prepare the channel for the subsequent ejection in order that each ejected drop is identical. We use the approach discussed in chapter 2 and separate the domain into the channel and the nozzle domain with different governing equations for each. The channel flow state is coupled to the nozzle state through the boundary conditions on the surface between the channel and the nozzle. We then derive the adjoint of this coupled channel–nozzle system (section 3.1.1) and discuss the time discretization of the adjoint problem (section 3.1.2). We optimize the velocity waveform at the actuator for a one-dimensional test case and various two dimensional channel shapes (section 3.2): a straight channel, a long straight print head channel and a generic printhead channel, and different optimization times.

We reveal the physical mechanisms that are exploited in order to reduce the residual oscillations and define the minimum residual control phase duration. In section 3.2.5, optimal waveforms with a uniform actuator velocity profile and a parabolic actuator velocity profile are compared. It is shown that the shape of the actuator velocity profile has little influence on the optimized waveform. The results in this chapter have been submitted for publication: Kungurtsev and Juniper (2020).

3.1 Optimal control of coupled domains

In this section a PDE-constrained optimization problem of channel and nozzle printhead domains is considered, and an optimization framework is derived using the method of Lagrange multipliers. The goal is to calculate the sensitivity of an energy-based objective functional with respect to boundary conditions. We demonstrate how to derive the adjoint problem and the functional in continuous forms, and obtain the time-discrete forms. This approach is useful for demonstrating and learning the adjoint method, but depends on the choice of governing equations and the discretization scheme. Future research might consider obtaining adjoint-based sensitivities of a generic objective function with respect to generic control automatically, for example, using `dolfin-adjoint` (Dokken et al., 2020; Mitusch et al., 2019), or `cashocs` (Blauth, 2021). Rapid development of algorithmic differentiation frameworks makes it easier to focus only on the primal problem, and automatically compute gradient information for a wide range of objective functionals and types of control. This requires, however, knowledge of how automatic differentiation works and how to structure a code so that its adjoint is realizable and quick to evaluate, for which this thesis will be valuable.

3.1.1 Governing equations for the adjoint problems

Here we derive the adjoint counterpart of the coupled acoustic and nozzle flow system. The acoustic state $\mathbf{q}_{\mathrm{ac}}$ is defined in $\Sigma_{\mathrm{c}} = (\Omega_{\mathrm{c}} \times \mathcal{T})$ and governed by the thermoviscous acoustic equations (2.21) and boundary conditions (2.24, 2.25). The nozzle flow state $\hat{\kappa}$ is characterized by the free surface curvature ODE (2.70b). The acoustic and nozzle flows are coupled via the boundary conditions (2.70a) and the flow through the shared boundary. The acoustic energy and the flow energy inside the nozzle are defined by (2.38) and (2.71b), respectively. We choose the total energy $\mathcal{E} \equiv \mathcal{E}_{\mathrm{ac}} + \mathcal{E}_{\mathrm{n}}$ at the final

time t_f as the objective function $\mathcal{J}$ at $t = t_f$:

$$\begin{aligned}\mathcal{J} &\equiv \mathcal{E}_{\text{ac}} + \mathcal{E}_{\text{n}} \\ &= \frac{1}{2} a \left\langle \mathbf{q}_{\text{ac}}, \mathbf{q}_{\text{ac}} \right\rangle_{\Omega_{\text{c}}} + \epsilon^{-1} \frac{r_n}{2} \gamma \left| \hat{\Gamma}_{\text{free}} \right| + \frac{h_{\text{CL}}}{2} \left(\left\{ (\mathbf{u} \cdot \mathbf{n})^2 \right\}_{\Gamma_{\text{C-N}}} + |\Gamma_{\text{C-N}}| \left(\gamma \hat{\kappa} \right)^2 \right).\end{aligned} \tag{3.1}$$

We account for the kinetic and potential energy of the nozzle flow only inside the static part of the nozzle domain. We multiply the acoustic state equations (2.21) by the adjoint acoustic variables $\Lambda_c^\dagger \equiv \left(\mathbf{u}^\dagger, P^\dagger, T^\dagger \right)$. We multiply the nozzle state equations (2.70b) by $\epsilon^{-1}\gamma\kappa^\dagger$, where $\kappa^\dagger$ is the adjoint curvature variable. The augmented objective function is:

$$\begin{aligned}\mathcal{L} = \mathcal{J} &- \left[\Lambda_c^\dagger, \frac{\partial}{\partial t} \mathrm{A} \mathbf{q}_{\text{ac}} \ + \mathrm{B} \mathbf{q}_{\text{ac}} \right]_{\Sigma_{\text{c}}} \\ &- \left[\epsilon^{-1} \gamma \kappa^\dagger, \frac{d}{dt} \left| \hat{\Omega}_{\text{n}}(\hat{\kappa}) \right| + \epsilon \left\{ \mathbf{u} \cdot \mathbf{n} \right\}_{\Gamma_{\text{N-C}}} + \epsilon h_{\text{CL}} \left| \Gamma_{\text{C-N}} \right| \frac{d}{dt} \gamma \hat{\kappa} \right]_{\Sigma_{\text{n}}}.\end{aligned} \tag{3.2}$$

We set the variation of the Lagrangian $\delta\mathcal{L}$ with respect to the primal state to zero:

$$\frac{\partial \mathcal{L}}{\partial \mathbf{q}_{\text{ac}}} \delta \mathbf{q}_{\text{ac}} = 0, \quad \frac{\partial \mathcal{L}}{\partial \hat{\kappa}} \delta \hat{\kappa} = 0 \quad \forall t \in \mathcal{T}. \tag{3.3}$$

Since the objective function contains only terms at $t = t_f$, the variation of the objective function $\delta\mathcal{J} = \frac{\partial \mathcal{J}}{\partial \mathbf{q}_{\text{ac}}} \delta \mathbf{q}_{\text{ac}}(t = t_f) + \frac{\partial \mathcal{J}}{\partial \hat{\kappa}} \delta \hat{\kappa}(t = t_f)$ determines the initial conditions for the adjoint acoustic $\Lambda_c^\dagger$ and curvature $\kappa^\dagger$ variables at $t = t_f$.

After successive integration by parts and applying the acoustic initial and boundary conditions, we obtain the adjoint acoustic equations (with the leftmost expression indicating the origin of the equation):

$$\left[\ \cdot \ , \delta \mathbf{q}_{\text{ac}} \right]_{\Sigma_{\text{c}}} : \quad - \frac{\partial}{\partial t} \mathrm{A} \Lambda_c^\dagger + \mathrm{B}^\dagger \Lambda_c^\dagger = 0 \quad \text{in} \quad \Sigma_{\text{c}}, \tag{3.4a}$$

$$\left[\ \cdot \ , \delta \mathbf{q}_{\text{ac}} \right]_{(\Gamma_{\text{C-N}} \times \mathcal{T})} : \quad \sigma_{ij}^\dagger n_j = -\gamma \kappa^\dagger n_i - h_{\text{CL}} \left(\frac{d}{dt} + \frac{1}{\tilde{Re}} \Delta_\Gamma \right) u_i^\dagger \text{ on } \quad \Gamma_{\text{C-N}}, \tag{3.4b}$$

$$\left\langle \ \cdot \ , \delta \mathbf{q}_{\text{ac}}(t_f) \right\rangle_{\Omega_{\text{c}}} : \quad \Lambda_c^\dagger(\mathbf{x}, t = t_f) = \mathbf{q}_{\text{ac}}(\mathbf{x}, t = t_f), \tag{3.4c}$$

and the adjoint nozzle flow equations, given by the $(\,\cdot\,, \delta\hat{\kappa})_{\mathcal{T}}$ and $(\,\cdot\,, \delta\hat{\kappa}(t_f))$ terms, respectively:

$$\left(\frac{d\left|\hat{\Omega}_{\mathrm{n}}(\hat{\kappa})\right|}{d\hat{\kappa}}\right)\frac{d}{dt}\kappa^{\dagger} = \epsilon\left\{\mathbf{u}^{\dagger}\cdot\mathbf{n}\right\}_{\Gamma_{\mathrm{N-C}}} - \epsilon\frac{\partial\left(\left|\hat{\Omega}_{\mathrm{n}}(\hat{\kappa})\right|\hat{\kappa}\right)}{\partial\hat{\kappa}}\frac{d}{dt}\gamma\kappa^{\dagger} = 0 \quad \text{in} \quad \Sigma_{\mathrm{n}}, \tag{3.5a}$$

$$\kappa^{\dagger}(t = t_f) = \hat{\kappa}(t = t_f). \tag{3.5b}$$

The adjoint acoustic operator $\mathrm{B}^{\dagger}$ is defined as

$$\mathrm{B}^{\dagger} = \begin{bmatrix} -\frac{1}{\tilde{R}e}\nabla_j\boldsymbol{\tau}_{ij} & -\nabla_i & 0 \\ -\nabla_i & 0 & 0 \\ 0 & 0 & -\frac{\Delta}{(\gamma_{\mathrm{th}}-1)\tilde{P}e} \end{bmatrix}. \tag{3.6}$$

The adjoint acoustic stress tensor is defined as $\sigma^{\dagger}_{ij} = -P^{\dagger}\delta_{ij} - \tilde{R}e^{-1}\tau^{\dagger}_{ij}$. The adjoint no slip velocity and stress free boundary conditions, as well as the isothermal and adiabatic temperature boundary conditions, are equal to the homogeneous boundary conditions of the primal problem.

3.1.2 Adjoint problem discretization

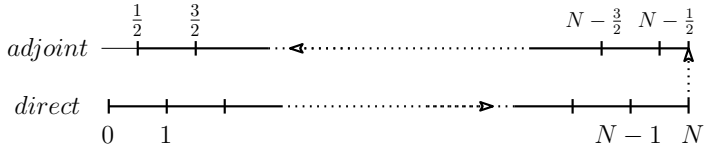

Fig. 3.1 Time discretization for the primal (bottom) and the adjoint (top) variables. The direct calculation runs forward in time, while the adjoint calculation runs backwards in time.

Figure (3.1) shows the grid used for the time discretization of the primal and adjoint problems. In sections 2.3.4 and 2.5.1, the channel and nozzle states were discretized on the gridpoints $t^n, n = 0, \ldots, N$. The solution is approximated in the midpoints $t^{n+\frac{1}{2}}$ using a second order accurate finite difference scheme. The adjoint states will be approximated in the midpoints using the same method. This results in a consistent time-discrete dual problem (Apel and Flaig, 2012). The discrete form of the integration rule (2.1c) consistent with the chosen time discretization is:

$$(a, b)_{\mathcal{T}_h} \equiv \sum_{n=0}^{N-1} \Delta t \; a^{n+\frac{1}{2}} \; b^{n+\frac{1}{2}}. \tag{3.7}$$

We start by constructing a time-discrete form of the Lagrangian (3.2). We retain the notation of section 3.1.1, with an additional index that indicates the timestep. We use time-discrete adjoint acoustic variables $\Lambda_c^{\dagger,n+\frac{1}{2}} \equiv \left(\mathbf{u}^{\dagger,n+\frac{1}{2}}, P^{\dagger,n+\frac{1}{2}}, T^{\dagger,n+\frac{1}{2}}\right)$ as a test function $\mathbf{p}$ in the semi-discrete acoustic state equation (2.52). The curvature equation (2.73) is multiplied by $\Lambda_d^{\dagger,n+\frac{1}{2}} \equiv \epsilon^{-1}\gamma\kappa^{\dagger,n+\frac{1}{2}}$, where $\kappa^{\dagger,n+\frac{1}{2}}$ is a time-discrete adjoint curvature. The objective function (the total energy of the acoustic channel flow and the nozzle flow) is evaluated at the final time $t_f = t^N$. The time-discrete Lagrangian is:

$$\begin{aligned}\mathcal{L} = \quad & \mathcal{E}_{\mathrm{ac}}^N + \mathcal{E}_{\mathrm{n}}^N \\ & - \left[\Lambda_c^\dagger, \overline{\partial}_t \mathrm{A}\mathbf{q}_{\mathrm{ac}} + \mathrm{B}\mathbf{q}_{\mathrm{ac}}\right]_{(\Omega_{\mathrm{c}}\times\mathcal{T}_h)} \\ & - \Big(\epsilon^{-1}\gamma\kappa^\dagger,\ \overline{\partial}_t \left|\hat{\Omega}_{\mathrm{n}}(\hat{\kappa})\right| + \epsilon \left\{\mathbf{u}\cdot\mathbf{n}\right\}_{\Gamma_{\mathrm{N-C}}} + \epsilon h_{\mathrm{CL}} \left|\Gamma_{\mathrm{C-N}}\right| \overline{\partial}_t \gamma\hat{\kappa}\Big)_{\mathcal{T}_h}.\end{aligned} \tag{3.8}$$

We obtain the time-discrete version of the adjoint system (3.4, 3.5) by setting to zero the Lagrangian variation with respect to the primal variables

$$\frac{\partial\mathcal{L}}{\partial\mathbf{q}_{\mathrm{ac}}^n}\delta\mathbf{q}_{\mathrm{ac}}^n = 0, \quad \frac{\partial\mathcal{L}}{\partial\hat{\kappa}^n}\delta\hat{\kappa}^n = 0 \quad \text{for all } n.$$

After successive integrations by parts, we collect the groups of the similar variation terms at each time step. The adjoint quantities $\Lambda_c^{\dagger,n}$ mean the same as in the primal problem, $\Lambda_c^{\dagger,n} = \frac{1}{2}\left(\Lambda_c^{\dagger,n+\frac{1}{2}} + \Lambda_c^{\dagger,n-\frac{1}{2}}\right)$. The same applies for the time derivatives. The strong form of the adjoint problem becomes (with the leftmost expression indicating the origin of the equation):

$$\begin{aligned}&\text{Find} \quad \Lambda_d^{\dagger,n+\frac{1}{2}}, \kappa^{\dagger,n+\frac{1}{2}}, \text{ for } n = N-2,\ldots,0, \text{ such that :} \\ \langle\cdot,\delta\mathbf{q}_{\mathrm{ac}}^n\rangle_{\Omega_{\mathrm{c}}} : \quad & -\overline{\partial}_t \mathrm{A}\Lambda_c^{\dagger,n} + \mathrm{B}^\dagger\Lambda_c^{\dagger,n} = 0, && \text{(3.9a)} \\ \{\cdot,\delta u_i^n\}_{\Gamma_{\mathrm{C-N}}} : \quad & \sigma_{ij}^{\dagger,n} n_j = -\gamma n_i \kappa^{\dagger,n} - h_{\mathrm{CL}}\left(\overline{\partial}_t + \frac{1}{\tilde{R}e}\Delta_\Gamma\right) u_i^{\dagger,n} \quad \text{on} \quad \Gamma_{\mathrm{C-N}}, && \text{(3.9b)} \\ \delta\hat{\kappa}^n : \quad & \left(\frac{d\left|\hat{\Omega}_{\mathrm{n}}(\hat{\kappa})\right|}{d\hat{\kappa}}\right)^n \overline{\partial}_t\kappa^{\dagger,n} = && \text{(3.9c)} \\ & = -\epsilon\left\{\mathbf{u}^{\dagger,n}\cdot\mathbf{n}\right\}_{\Gamma_{\mathrm{N-C}}} - \epsilon\left(\frac{\partial\left|\hat{\Omega}_{\mathrm{n}}(\hat{\kappa})\right|\hat{\kappa}}{\partial\hat{\kappa}}\right)^n \overline{\partial}_t\gamma\kappa^{\dagger,n}.\end{aligned}$$

In section 2.5.1, an alternative form of the curvature equation (2.75) was introduced. The explicit approximation of the term $\left\{\mathbf{u}^{n+\frac{1}{2}}\cdot\mathbf{n}\right\}_{\Gamma_{\mathrm{C-N}}}$ allowed us to reduce the computational cost due to the matrix inversion of the discrete bilinear form. If (2.75)

is used in the Lagrangian (3.8), the adjoint stress boundary condition (3.9b) on $\Gamma_{\mathrm{N-C}}$ becomes:

$$\sigma_{ij}^{\dagger,n} n_j = -\gamma n_i \left(1 - \Delta t \overline{\partial_t}\right) \kappa^{\dagger,n+1} - h_{\mathrm{CL}} \left(\overline{\partial}_t + \frac{1}{\tilde{Re}} \Delta_\Gamma\right) u_i^{\dagger,n}. \tag{3.9d}$$

If we use (2.75) for the primal problem and proceed with the spatial discretization of the adjoint problem, the matrix of the adjoint bilinear form will also be independent of time, and therefore the LU factorization of it can also be reused.

The adjoint initial conditions are defined at $t^{N-\frac{1}{2}}$, and we obtain them by setting the variation of the primal states at the final time to zero:

$$\left\langle \cdot, \delta \mathbf{q}_{\mathrm{ac}}^N \right\rangle_{\Omega_{\mathrm{c}}} \text{terms}: \quad \frac{\mathrm{A}\Lambda_c^{\dagger,N-\frac{1}{2}} - \mathrm{A}\mathbf{q}_{\mathrm{ac}}^N}{\Delta t/2} + \mathrm{B}^\dagger \Lambda_c^{\dagger,N-\frac{1}{2}} = 0, \tag{3.10a}$$

$$\left\{ \cdot, \delta u_i^N \right\}_{\Gamma_{\mathrm{C-N}}} \text{terms}: \quad \sigma_{ij}^{\dagger,N-\frac{1}{2}} n_j = -\gamma n_i \kappa^{\dagger,N-\frac{1}{2}} \tag{3.10b}$$

$$- \frac{h_{\mathrm{CL}}}{\Delta t/2} \left(u_i^N - u_i^{\dagger,N-\frac{1}{2}}\right) - \frac{h_{\mathrm{CL}}}{\tilde{Re}} \Delta_\Gamma u_i^{\dagger,N-\frac{1}{2}} \quad \text{on} \quad \Gamma_{\mathrm{C-N}},$$

$$\delta\hat{\kappa}^N \text{terms}: \quad \left(\frac{d\left|\hat{\Omega}_{\mathrm{n}}(\hat{\kappa})\right|}{d\hat{\kappa}}\right)^N \frac{\hat{\kappa}^N - \kappa^{\dagger,N-\frac{1}{2}}}{\Delta t/2} = -\epsilon \left\{ \mathbf{u}^{\dagger,N-\frac{1}{2}} \cdot \mathbf{n} \right\}_{\Gamma_{\mathrm{N-C}}} \tag{3.10c}$$

$$- \epsilon \left(\frac{\partial \left|\hat{\Omega}_{\mathrm{n}}(\hat{\kappa})\right| \hat{\kappa}}{\partial \hat{\kappa}}\right)^N \gamma \frac{\hat{\kappa}^N - \kappa^{\dagger,N-\frac{1}{2}}}{\Delta t/2}.$$

The initial condition equations can be read as a backwards half time step from the primal terminating condition to the adjoint initial condition.

3.1.3 The primal–adjoint problems symmetry

There is symmetry between the primal (2.21, 2.70b) and the adjoint problems (3.4, 3.5). In the frequency domain, performing complex conjugation and then inverting the sign of the velocity component makes the adjoint problem equivalent to the primal problem. Complex conjugation in the frequency domain translates to time inversion in the time domain: $t \to -t$. The velocity sign change has the same effect. We introduce a symmetry operator, $\mathbb{S}$:

$$\mathbb{S} : \Lambda_c^\dagger \to \check{\Lambda}_c^\dagger = \left(-\mathbf{u}^\dagger, P^\dagger, T^\dagger\right)(-t) \equiv \left(\check{\mathbf{u}}^\dagger, \check{P}^\dagger, \check{T}^\dagger\right)(\check{t}).$$

We apply the symmetry operator to the coupled adjoint problems (3.4, 3.5), which results in

$$\frac{\partial}{\partial \check{t}}\mathrm{A}\check{\Lambda}_c^\dagger + \mathrm{B}^\dagger\check{\Lambda}_c^\dagger = 0 \quad \text{in} \quad \check{\Sigma}_c, \tag{3.11a}$$

$$\check{\sigma}_{ij}^\dagger n_j = -\gamma\kappa^\dagger n_i - h_{\mathrm{CL}}\left(\frac{d}{d\check{t}} - \frac{1}{\tilde{Re}}\Delta_\Gamma\right)\check{u}_i^\dagger \quad \text{on} \quad \Gamma_{\mathrm{C-N}}, \tag{3.11b}$$

$$\check{\Lambda}_c^\dagger(\mathbf{x}, t = t_f) = \mathbb{S}\mathbf{q}_{\mathrm{ac}}(\mathbf{x}, t = t_f), \tag{3.11c}$$

and

$$\left(\frac{d\left|\hat{\Omega}_{\mathrm{n}}(\hat{\kappa})\right|}{d\hat{\kappa}}\right)\frac{d}{d\check{t}}\kappa^\dagger = -\epsilon\left\{\check{\mathbf{u}}^\dagger\cdot\mathbf{n}\right\}_{\Gamma_{\mathrm{N-C}}} - \epsilon\frac{d\left(\left|\hat{\Omega}_{\mathrm{n}}(\hat{\kappa})\right|\hat{\kappa}\right)}{d\hat{\kappa}}\frac{d}{d\check{t}}\gamma\kappa^\dagger = 0 \quad \text{in} \quad \check{\Sigma}_n, \tag{3.12a}$$

$$\kappa^\dagger(\check{t} = t_f) = \hat{\kappa}(t = t_f). \tag{3.12b}$$

After applying the symmetry operator, $\mathbb{S}$, to the adjoint problem, the temporal components of Σ_{c} and Σ_{n} change such that the adjoint flow propagates forward in time, in $\check{\mathcal{T}} = -\mathcal{T}$. The updated adjoint stress tensor is $\check{\sigma}_{ij}^\dagger = -\check{P}^\dagger\delta_{ij} + \tilde{Re}^{-1}\check{\tau}_{ij}^\dagger$. The initial condition for $\check{\Lambda}_c^\dagger$ (3.12b) implies that time integration of the adjoint problem should start from the state $\mathbf{q}_{\mathrm{ac}}(\mathbf{x}, t = t_f)$, but with the velocity vector pointing in the opposite direction. The adjoint system now has the same form as the primal systems (2.21, 2.70b), with the difference that the terms $\left(\frac{d\left|\hat{\Omega}_{\mathrm{n}}(\hat{\kappa})\right|}{d\hat{\kappa}}\right)$ and $\frac{d\left(\left|\hat{\Omega}_{\mathrm{n}}(\hat{\kappa})\right|\hat{\kappa}\right)}{d\hat{\kappa}}$ in (3.12a) come from the solution of the primal problem: the adjoint curvature follows the trajectory defined by the primal curvature $\hat{\kappa}$.

Finally, we discretize and apply the symmetry operator, $\mathbb{S}$, that was introduced in section 3.1.1. This changes the sign of the adjoint acoustic velocity and the direction of the time integration of the adjoint system of equations. The symmetry operator reflects the adjoint time grid with respect to the termination time of the primal problem:

$$\mathbb{S} : \Lambda^{\dagger,n} \rightarrow \check{\Lambda}^{\dagger,2N-n} \equiv \left(-\mathbf{u}^{\dagger,2N-n}, P^{\dagger,2N-n}, T^{\dagger,2N-n}\right).$$

The discrete time derivative changes to $\overline{\partial}_t f^n \overset{\mathbb{S}}{\rightarrow} -\overline{\partial}_t f^{2N-n}$. We update the time integration rule for a scalar product between a primal state and the reflected adjoint variables:

$$(\check{a}, b)_{\mathcal{T}_h} \equiv \sum_{n=0}^{N-1} \Delta t\ \check{a}^{2N-\left(n+\frac{1}{2}\right)}\ b^{n+\frac{1}{2}}. \tag{3.13}$$

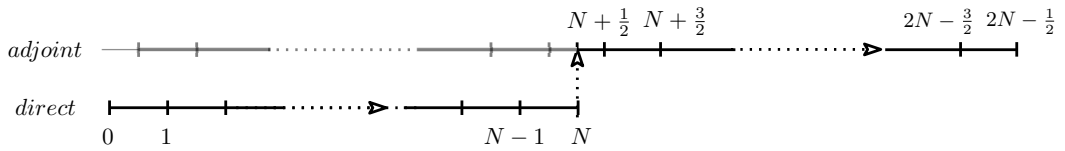

Fig. 3.2 Time discretization for the primal (bottom) and the adjoint (top) variables after the symmetry operator $\mathbb{S}$ has been applied to the adjoint variables. Both the primal and adjoint states run forwards in time.

The transformation of the time-discrete adjoint problem yields:

$$\begin{aligned}
&\text{Find} \quad \check{\Lambda}_d^{\dagger,n+\frac{1}{2}}, \kappa^{\dagger,n+\frac{1}{2}}, \text{ for } n = N+1,\dots,2N-1, \text{ such that :}\\
&\quad \overline{\partial}_t \mathrm{A}\ \check{\Lambda}_c^{\dagger,n} + \mathrm{B}^{\dagger}\check{\Lambda}_c^{\dagger,n} = 0, && \text{(3.14a)}\\
&\quad \sigma_{ij}^{\dagger,n} n_j = -\gamma n_i \kappa^{\dagger,n} - h_{\mathrm{CL}}\left(\overline{\partial}_t - \frac{1}{\tilde{Re}}\Delta_\Gamma\right)\check{u}_i^{\dagger,n} \quad \text{on} \quad \Gamma_{\mathrm{C-N}}, && \text{(3.14b)}\\
&\quad \left(\frac{d\left|\hat{\Omega}_{\mathrm{n}}(\hat{\kappa})\right|}{d\hat{\kappa}}\right)^n \overline{\partial}_t \kappa^{\dagger,n} = -\epsilon\left\{\check{\mathbf{u}}_i^{\dagger,n}\cdot\mathbf{n}\right\}_{\Gamma_{\mathrm{N-C}}} - \epsilon\left(\frac{\partial\left|\hat{\Omega}_{\mathrm{n}}(\hat{\kappa})\right|\hat{\kappa}}{\partial\hat{\kappa}}\right)^n \overline{\partial}_t \gamma\kappa^{\dagger,n}, && \text{(3.14c)}
\end{aligned}$$

or, if (3.9d) is set as a boundary condition, the stress on $\Gamma_{\mathrm{N-C}}$ equals:

$$\sigma_{ij}^{\dagger,n} n_j = -\gamma n_i\left(1-\Delta t\overline{\partial_t}\right)\kappa^{\dagger,n+1} - h_{\mathrm{CL}}\left(\overline{\partial}_t - \frac{1}{\tilde{Re}}\Delta_\Gamma\right)\check{u}_i^{\dagger,n}. \tag{3.14d}$$

We perform the spatial discretization of the adjoint problem (3.14) in the same way as that of the primal problem in section 2.5.1. By using (2.75) (and, consequently, (3.14d)), the bilinear forms of the discrete primal and adjoint problem coincide, while the linear forms naturally differ.

3.1.4 The augmented gradient

The top boundary of the channel contains a piezo-electric actuator, which we model as a prescribed velocity boundary condition $\mathcal{U}(t)$. We minimize the objective function $\mathcal{J}$ (3.1) by optimizing the velocity profile on the actuator boundary Γ_{act}. This control is described through a velocity Dirichlet boundary condition:

$$\mathbf{u} = \mathcal{U} \quad \text{on } \Gamma_{\mathrm{act}}.$$

The only non-zero term in the Lagrangian variation (3.2) is the adjoint stress boundary integral on Γ_{act}. This equals the objective variation with respect to the control, and

therefore the objective gradient is:

$$\mathcal{J}'[\delta\mathcal{U}] = \left\{\sigma^\dagger_{ij} n_j, \delta\mathcal{U}_i\right\}_{\partial\Sigma_{\text{act}}}. \tag{3.15}$$

In other words, the distribution of the adjoint stress along the control boundary is the sensitivity distribution.

The objective gradient with respect to the control velocity is zero only if the adjoint stress on the control boundary is zero, $\sigma^\dagger_{ij} n_j \equiv 0$. Since the adjoint initial condition is defined by the primal state at the final time, the optimality condition for the waveform shape $\mathcal{U}(t)$ yields that no adjoint acoustic disturbances reach the control boundary at any time.

Similarly to the velocity Dirichlet boundary condition, the control can be described through a boundary forcing (2.24b) and even the boundary temperature or the heat flux (2.25):

$$\sigma_{ij} n_j = f_i \quad \text{on } \Gamma_{\text{act}},$$
$$T = T_0 \quad \text{or} \quad \frac{\partial T}{\partial \mathbf{n}} = Q_{\text{heat}} \quad \text{on } \Gamma_{\text{act}}.$$

In these cases, the objective variations with respect to the control force is:

$$\mathcal{J}'[\delta\mathbf{f}] = \left\{\mathbf{u}^\dagger, \delta\mathbf{f}\right\}_{\partial\Sigma_{\text{act}}}, \tag{3.16}$$

and variations with respect to the actuator temperature and the heat flux are:

$$\begin{aligned} \mathcal{J}'[\delta T_0] &= \left\{\frac{1}{(\gamma_{\text{th}}-1)\tilde{Pe}} \frac{\partial T^\dagger}{\partial \mathbf{n}}, \delta T_0\right\}_{\partial\Sigma_{\text{act}}} \quad \text{or} \\ \mathcal{J}'[\delta Q_{\text{heat}}] &= \left\{T^\dagger, \frac{1}{(\gamma_{\text{th}}-1)\tilde{Pe}} \delta Q_{\text{heat}}\right\}_{\partial\Sigma_{\text{act}}}. \end{aligned} \tag{3.17}$$

Remark. The sensitivity of an objective to a control function can be used to evaluate the objective variation caused by a random fluctuation of the control. If the ensemble average of the fluctuations is zero (which is often the case), the ensemble average of the objective variation is also zero. Unfortunately, this means that it is impossible to infer any useful information about the average objective response to a zero mean noise, as this would require higher order sensitivity functionals.

3.1.5 Waveform parameterization

We solve primal and adjoint problems that are discrete in time and space to find the cost function sensitivity. The sensitivity functional $\left\{\sigma^{\dagger}_{ij} n_j,\ \cdot\ \right\}_{\partial\Sigma_{\text{act}}}$ is given by values of the adjoint stress vector for each boundary degree of freedom on Γ_{act} and for each time step in $\mathcal{T}_h$. For a typical 2D problem, the number of spatial degrees of freedom can reach several hundred points, and there are several thousand time steps. The value of the adjoint stress for each boundary degree of freedom and for each time step can be considered as an optimization parameter. The resulting optimization space contains millions of optimization parameters. We reduce the dimension of the optimization problem by projecting the original high dimensional spaces into lower dimensional spaces, defined by physical constraints of printhead systems. We iteratively solve the optimization problem on nested optimization spaces, and use the coarse solution as an initial guess for the next optimization round on a finer search space.

For each optimization problem: find the actuator velocity profile $\mathcal{U}(\mathbf{x}, t)$ that minimizes the final energy of the system, we define a set of basis functions in time and space that represent $\mathcal{U}$. The simplest case of the spatial basis is a uniform velocity profile: $\mathcal{U}(\mathbf{x}) = 1 \cdot \mathbf{n}(\mathbf{x})c(t)$. For a general actuator velocity profile $\mathbf{V}(\mathbf{x})$, the boundary velocity equals $\mathcal{U}(\mathbf{x}) = \mathbf{V}(\mathbf{x})c(t)$. We choose piecewise linear interpolation of the actuator velocity, so the temporal basis functions are the first order Lagrange polynomials. The boundary velocity belongs to a continuous piecewise linear function space $\mathbb{T}^1_w = \left\{u \in H^1_0(\mathcal{T}_h) \mid \forall K \in \mathcal{T}_w,\ u_{|K} \in P^1\right\}$, where $\mathcal{T}_w$ is a tessellation of the discrete space $\mathcal{T}_h$ into equal intervals of width w. For a natural number $n \geq 2$, the space $\mathbb{T}^1_w$ is embedded into $\mathbb{T}^1_{w/n}$, and functions $f \in \mathbb{T}^1_w$ can be projected on $\mathbb{T}^1_{w/n}$ exactly. Figure 3.3 shows an example signal (blue line) projected on two piecewise linear function spaces: $\mathbb{T}^1_w$ with $w = 1.0$ (solid black line), and $\mathbb{T}^1_w$ with $w = 0.2$ (dashed black line).

At each timestep of an optimization step, we project the adjoint stress onto the admissible spatial space. The objective gradient data at each timestep is then projected onto the $\mathbb{T}^1_w$ space. The latter is implemented in the `PiecewiseLinearBasis` class as part of the `firecrest` package. The class provides functionality to convert vectors that belong to $\mathcal{T}_h$ from and to $\mathbb{T}^1_w$, and to convert vectors between piecewise linear function spaces with different widths w.

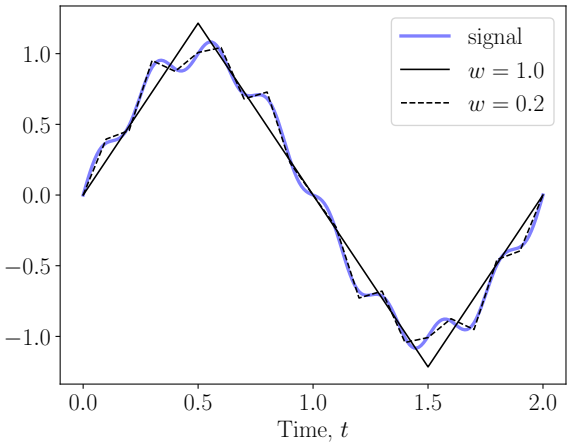

Fig. 3.3 An example projection of a signal on piecewise linear spaces with different basis widths.

3.2 Applications

3.2.1 One dimensional test case

In order to illustrate the method and to discuss the physical mechanisms it exploits, we first apply the optimization technique in section 3.1 to a one-dimensional test case. A thermoviscous acoustic flow inside a unit length domain $\Omega_c = \{x : 0 \leq x \leq 1\}$ is initially at rest $\mathbf{q}_{ac}(x, t = 0) = 0$. The boundary at $x = 1$ is set as a control boundary. We prescribe a velocity profile $u(x = 1) = \mathcal{U}(t)$ on this boundary. The boundary at $x = 0$ is a free surface (2.70b). This free surface is initially deformed $\hat{\kappa}(t = 0) = 0.05$, and therefore possesses non-zero initial energy $\mathcal{E}(t = 0) = \mathcal{E}_n(t = 0)$.

We define the nondimensional acoustic timescale t_{ac} to be the time taken for a wave to travel from $x = 0$ to $x = 1$. In these units the time taken for a wave to travel from one side to the other and back is $t_L = 2$. This is a key quantity that will be referred to later. We discretize the time domain $\mathcal{T}$ into equal intervals with time step $\Delta t = 10^{-4}$. The non-dimensional parameters of the experiment are provided in table 3.1. The optimization search space consists of control velocity values at each discrete time point $\mathcal{U}^n$ for $n = 1 \ldots N - 1$. The values of $\mathcal{U}^0, \mathcal{U}^N$ are fixed to zero. We use the `scipy.minimize(method='TNC')` (Jones et al., 2020) implementation of the truncated Newton method as the gradient-based algorithm to minimize the objective function (3.1).

We start with the case in which the final time is set to $t_f = 2.5$ and use the gradient-based method to find the optimal waveform (figure 3.4a). Figure 3.4b shows the time history of the free surface energy $\mathcal{E}_n$ (green line) and the acoustic energy $\mathcal{E}_{ac}$

	non-dimensional value
domain length, L_c	1
final time, t_f	2.5, 3
speed of sound, c_s^b	1
Mach number, ϵ	10^{-3}
Reynolds number, $\tilde{Re}$	$5 \cdot 10^3$
initial curvature, $\hat{\kappa}(t=0)$	0.05
surface tension, γ	0.01
nozzle radius, r_n	0.1
time step size, Δt	10^{-4}

Table 3.1 Parameters of the optimization test case 3.2.1

(blue line) in the optimally controlled case, normalized by the initial total energy value $\mathcal{E}(t=0)$. The final energy at $\mathcal{E}(t=t_f)$ is 10^5 time lower the initial value. In this simple case, the physical mechanism that it exploits can be clearly identified. The optimal waveform consist of three stages. The first stage is a pulse lasting $\tau_p = t_f - t_\mathrm{L} = 0.5$ that withdraws half the volume stored in the nozzle domain. In the second stage the actuator remains inactive while the front and back of the pulse reach the free surface at $t = 1$ and $t = 1 + \tau_p$ respectively. The pulse velocity amplitude doubles as it reflects from the free surface. The amount of fluid transferred through the free surface is therefore equal to the volume initially stored in the nozzle domain. Between these two times the free surface relaxes to zero curvature and, in doing so, reflects an acoustic pulse back towards the actuator. At $t = 2$ the front of the reflected pulse reaches the actuator. The third stage is a pulse lasting $\tau_p = t_f - t_\mathrm{L} = 0.5$ that withdraws more fluid such that the reflected pulse leaves the channel without further reflection and returns the fluid in the channel to its initial state at exactly $t = t_f$. The two pulses, when combined, withdraw exactly the amount of fluid initially stored in the nozzle domain.

For comparison we then examine the case in which the final time is set to $t_f = 3.0$ (figure 3.5). Figure 3.5b shows the time history of the free surface energy $\mathcal{E}_\mathrm{n}$ (green line) and the acoustic energy $\mathcal{E}_\mathrm{ac}$ (blue line) in the optimally controlled case, normalized by the initial total energy value $\mathcal{E}(t=0)$. The optimal waveform is qualitatively identical to that found when $t_f = 2.5$ but with pulses lasting $\tau_p = t_f - t_\mathrm{L} = 1.0$ rather than $\tau_p = 0.5$. As before, the actuator withdraws exactly the half mass of fluid between the initial and final positions of the surface, but this time with a longer pulse and, consequently, with a smaller actuator velocity. Consideration of the physical mechanism

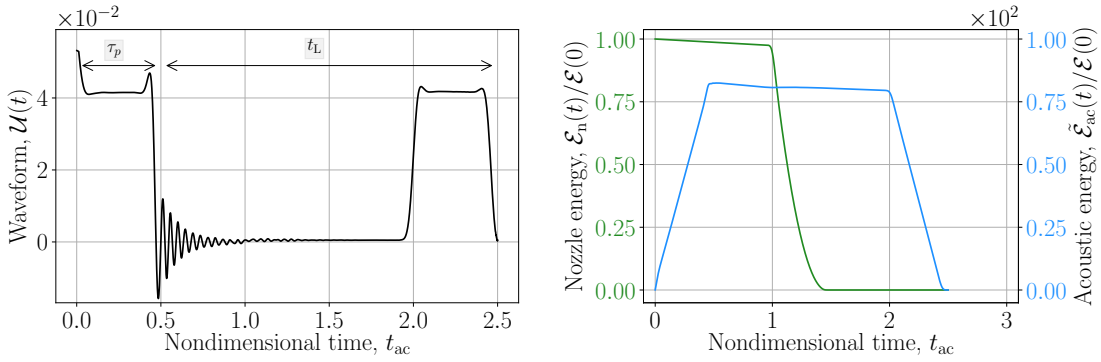

(a) (b)

Fig. 3.4 Optimally controlled case of one-dimensional unit-length domain, $t_f = 2.5$. (a) optimal velocity $\mathcal{U}$ of the control boundary, τ_p indicates the pulse duration, and t_L is the timescale of length of channel; (b) nozzle energy (green), and acoustic energy (blue), normalized by the initial total energy value $\mathcal{E}(t = 0)$.

shows that the optimization time has to be greater than $t_f = 2$ and that, beyond that, its lower limit will be determined by the maximum speed of the actuator. In both cases, the spurious oscillations in $\mathcal{U}$ appear due to the Crank-Nicholson time discretization scheme, which is dispersive.

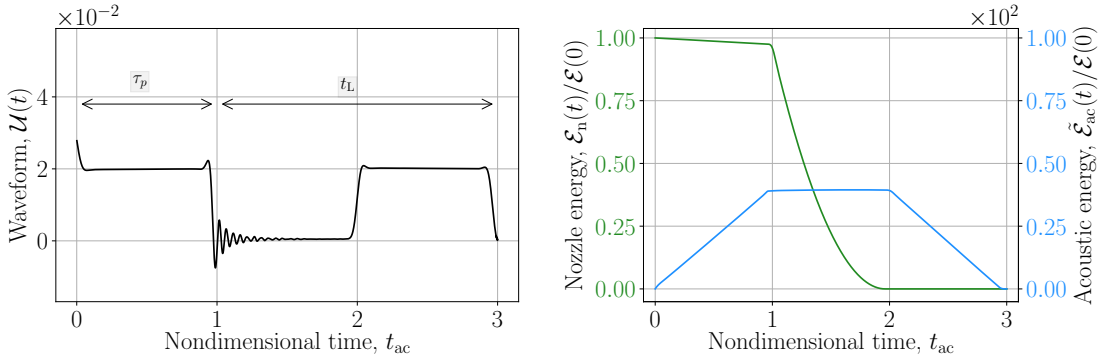

(a) (b)

Fig. 3.5 Optimally controlled case of one-dimensional unit-length domain, $t_f = 3$. (a) optimal velocity $\mathcal{U}$ of the control boundary, τ_p indicates the pulse duration, and t_L is the timescale of length of channel; (b) nozzle energy (green), and acoustic energy (blue), normalized by the initial total energy value $\mathcal{E}(t = 0)$.

	dimensional value
final time, t_f, s	$(1-5)\cdot 10^{-6}$
speed of sound, c_s^b, m/s	10^3
Mach number, ϵ	10^{-3}
viscosity, μ_{vis}, kg/(m · s)	$2\cdot 10^{-2}$
Prandtl number, Pr	10
initial curvature, $\kappa(t=0)$, m^{-1}	$0.05\cdot 10^6$
surface tension, γ_{dim}, N/m	$50\ \cdot 10^{-3}$
nozzle radius, R_n, m	$10\ \cdot 10^{-6}$
nozzle height, H_{CL}, m	$20\ \cdot 10^{-6}$
time step size, Δt, s	10^{-9}

Table 3.2 Inkjet microchannels setup parameters (section 3.2.2)

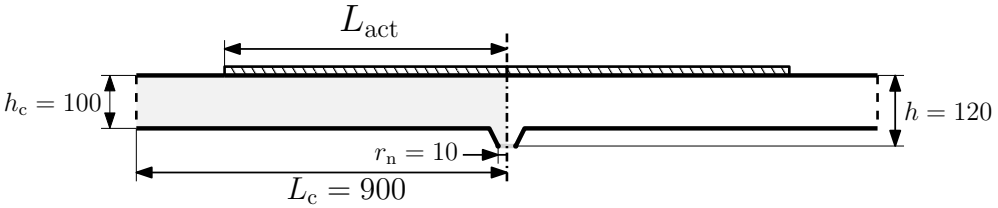

Fig. 3.6 Two dimensional straight channel domain (sizes in μm).

3.2.2 Two dimensional straight channel

Having shown that the optimization algorithm works for a simple 1D case, and having identified the physical mechanism in that case, we now examine a 2D straight channel with a nozzle placed at the centre of one wall, an actuator along the opposite wall, an outlet boundary at the left side, and a symmetry boundary at the right side (figure 3.6). The dimensional parameters of the nozzle domain and acoustic constants are given in table 3.2. In the remaining sections, we present the time and space scales in dimensional format because this enables easier comparison with the literature.

We assume that the nozzle state $\hat{\kappa}$ shortly after the droplet has been expelled is a free surface with uniform curvature. For ease of explanation, we assume that the acoustic energy in the channel has already decayed to zero. This assumption could easily be relaxed in practice. The simulation therefore starts from the zero acoustic state and non zero curvature:

$$\mathbf{q}_{\text{ac}}(t=0)=0, \quad \hat{\kappa}(t=0)=0.25. \tag{3.18}$$

The actuator is at rest at $t = 0$. The objective is to minimize the total energy at final time $\mathcal{J} = \mathcal{E}(t_f) = \mathcal{E}_{\text{ac}}(t_f) + \mathcal{E}_{\text{n}}(t_f)$ (3.1).

Typically the time between droplets is between 2 μs and 20 μs. Here, we will examine optimization times of 1 μs, 2 μs and 3 μs in order to investigate whether open loop control over these times could significantly reduce the the total energy, and therefore the time required between droplets. We discretize the time domain $\mathcal{T}$ into equal time intervals with the time step $\Delta t = 10^{-3}$ μs. The time step is chosen in order to have sufficient time resolution of the acoustic motion inside the narrowest part of the channel Ω_{c}, near the nozzle boundary.

The actuating waveforms in inkjet printing are constrained by the limitations of the driving electronics and response of the piezo-electric actuator. We assume that the piezo-electric actuator deforms as a solid plate in the direction normal to the channel's wall. We model this as a boundary velocity $\mathcal{U}$ that is spatially uniform along the control boundary Γ_{act}. In practical devices the electric signal that forces the piezo-electric actuator is piecewise linear with a temporal resolution, w, between 0.01 μs and 0.1 μs. We use a continuous piecewise linear function to describe the boundary velocity.

In our model, shown in figure 3.6, the length of the control element (actuator boundary) varies from $L_{\text{act}} = 20\mu$m to $L_{\text{act}} = 200\mu$m. The waveform time resolution is fixed at $w = 0.1\mu$s. The left boundary is stress-free. The right boundary is a symmetry plane.

Figure 3.7 shows the optimized total energy at final time $\mathcal{E}_{\text{n}}(t_f)$ normalized by the uncontrolled total energy at final time $\mathcal{E}^*(t_f)$. For 1μs optimization time there is almost no energy reduction because, as will be shown later, there is insufficient time to control the wave reflected by the left boundary. For 2μs optimization time the final energy reduces by one order of magnitude. For 3μs optimization time the final energy reduces by a further order of magnitude. The actuator size has little influence as long as it exceeds 100μm. The physical reasons for this are explored next.

Waveform optimization for $t_f = 2\mu$s.

For illustration, we will examine the results with final time $t_f = 2\mu$s and actuator length $L_{\text{act}} = 200\mu$m. Figure 3.8a shows the nozzle surface energy (green) and the total energy (blue) for the uncontrolled (dashed) and controlled (solid) cases. Figure 3.8c shows, for the uncontrolled case, the integrated acoustic energy dissipation (red dashed) and, for the controlled case, the total energy $\mathcal{E}(t)$ again (blue), the integrated energy flux through the actuator boundary $\int \mathcal{F}_{\text{act}}(\tau)\text{d}\tau$ (purple), the integrated acoustic energy dissipation $\int \mathcal{R}(\tau)\text{d}\tau$ (red solid). Due to the energy balance (2.71a), these are

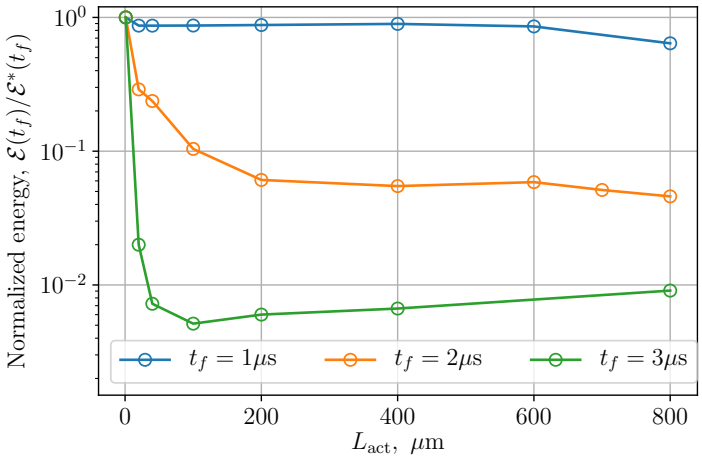

Fig. 3.7 Optimized objective values for eight actuator lengths, L_{act}, and three final times, t_f. The values are normalized by the total energy at final time in the uncontrolled case.

related by

$$\mathcal{E}(t) = \mathcal{E}(0) + \int_0^t \mathcal{F}_{\text{act}}(\tau)\mathrm{d}\tau - \int_0^t \mathcal{R}(\tau)\mathrm{d}\tau. \tag{3.19}$$

Figure 3.8b shows the mass flux through the actuator boundary (black) and the nozzle boundary (red). Figure 3.9 shows snapshots of the pressure field of the controlled case at times corresponding to the empty circles in figure 3.8.

For the uncontrolled case, the nozzle surface energy $\mathcal{E}^*_{\text{n}}$ (green dashed line in figure 3.8a) reduces smoothly as the free surface relaxes. As for the one-dimensional test case, this sends an acoustic wave down the channel, increasing the acoustic energy. The total energy $\mathcal{E}^*$ (blue dashed line, figure 3.8a), which comprises the nozzle surface energy and the acoustic energy, reduces gently as the wave dissipates due to thermo-viscous mechanisms.

At time $t = t_f = 2.0$ μs, the controlled case has almost 20 times lower energy than the uncontrolled case (compare the solid blue and dashed blue lines in figure 3.8a). The optimal waveform (black line in figure 3.8c) consists of three phases. During the first phase $\mathcal{A}^+ : 0 \leq t \leq 0.38$ μs the actuator pulls fluid upwards and creates a negative pressure wave (figure 3.9a). This wave moves down towards the nozzle and left along the channel. The wave reaches the nozzle boundary at $t = 0.12\mu$s, at which point mass starts to be pulled out of the nozzle (red solid line in 3.8b), and the nozzle surface energy starts to reduce (green solid line in 3.8a). The wave reflects back off the nozzle, reaching the actuator at $t = 0.24\mu$s. Reverberations at this timescale, which is that

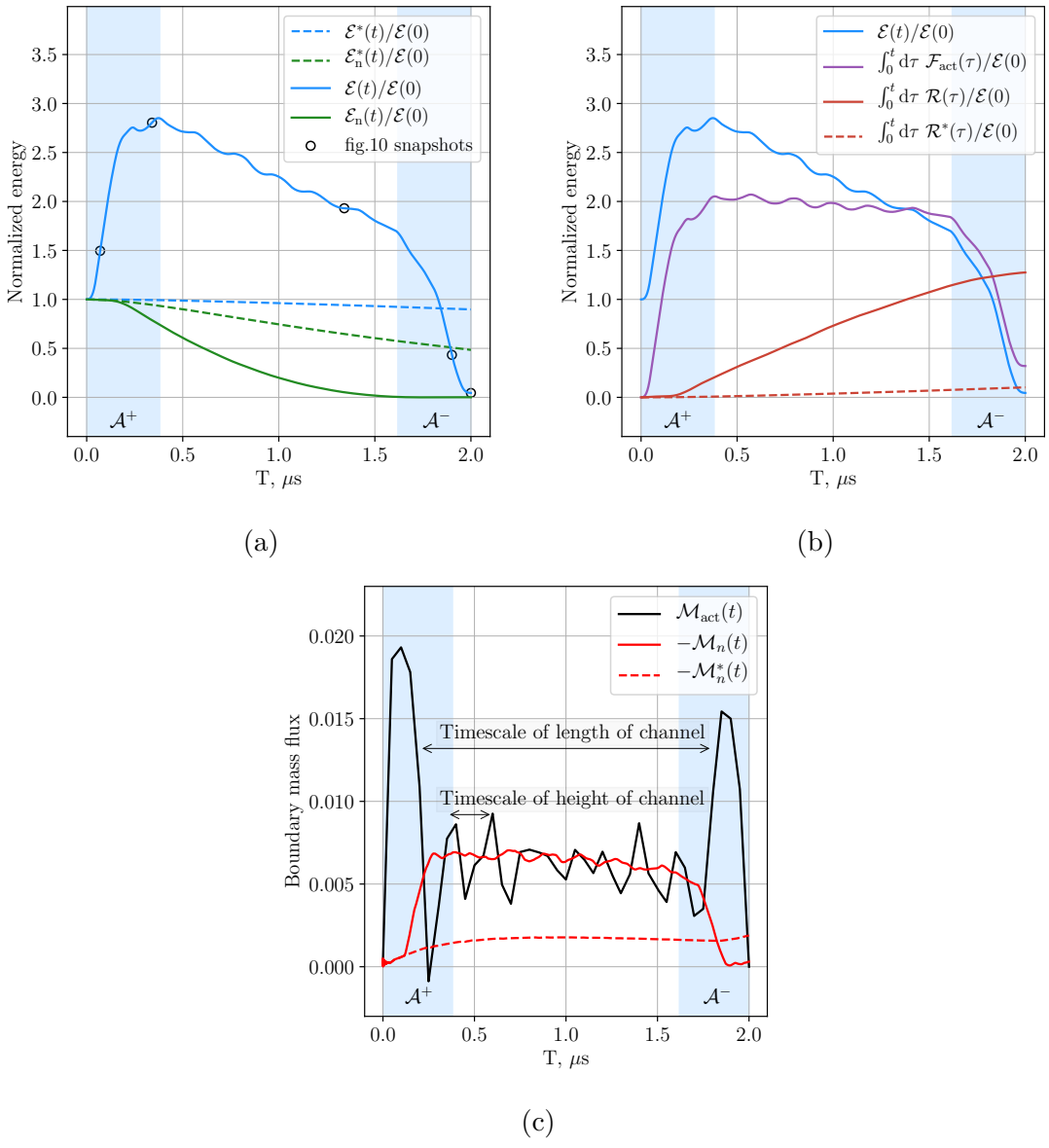

Fig. 3.8 Comparison between the uncontrolled case (dashed lines) and the optimally controlled case (solid lines) with $L_{\text{act}} = 200\mu$m and $t_f = 2\mu$s. (a) Total energy $\mathcal{E}_{\text{n}}(t)$ (blue) and nozzle energy $\mathcal{E}_{\text{n}}(t)$ (green), normalized by $\mathcal{E}(t=0)$. (b) Integrated energy flux through the actuator boundary $\int \mathcal{F}_{\text{act}}(\tau)\mathrm{d}\tau$ (purple line), integrated acoustic energy dissipation $\int \mathcal{R}(\tau)\mathrm{d}\tau$ (red solid line), and the integrated acoustic energy dissipation $\int \mathcal{R}^*(\tau)\mathrm{d}\tau$ in the uncontrolled case (red dashed line). (c) Boundary mass flux through the actuator boundary $\mathcal{M}_{\text{act}}$ (black) and the nozzle boundary $\mathcal{M}_{\text{n}}$ (red). The red dashed line is the mass flux $\mathcal{M}_{\text{n}}^*$ through the nozzle boundary in the uncontrolled case. The coloured patches denote the actuation phases, when the acoustic waves are formed ($\mathcal{A}^+$) and absorbed by the actuator ($\mathcal{A}^-$).

of the height of the channel, continue during the controlled period. This behaviour is similar to that of the 1D test case but is more complicated because the flow is 2D. This wave relaxes the free surface but, unavoidably, produces a large amplitude wave moving left along the channel (figure 3.9b). Indeed the energy flux through the control boundary during the first phase, $\mathcal{A}^+$, is large and the total energy rapidly increases to nearly three times that of the uncontrolled case.

During the second phase $0.38 \leq t \leq 1.62$ μs the integrated mass flux through the actuator, $\mathcal{M}_{\text{act}} \equiv \{\mathbf{u} \cdot \mathbf{n}\}_{\Gamma_{\text{act}}}$, is almost identical to the integrated mass flux away from the nozzle, $\mathcal{M}_{\text{n}}$ (black and red solid lines in figure 3.8c). Compared with the first pulse, this motion is relatively slow, shown by the fact that the energy flux through the actuator boundary is small $\partial_t \mathcal{E} \simeq 0$. The nozzle surface energy reduces to nearly zero during this phase (green solid line in 3.8a). Meanwhile, in the channel, the pressure wave generated during the first phase reflects off the stress-free boundary and a positive pressure wave travels back towards the nozzle and the actuator (figure 3.9c). The total energy $\mathcal{E}$ steadily decreases due to viscous and thermal dissipation of the acoustic wave (figure 3.8b, red line).

The third phase $\mathcal{A}^-$: $1.62 \leq t \leq 2.0$ μs is the counterpart of the first phase $\mathcal{A}^+$. When the positive pressure wave reaches the symmetry plane of the channel the actuator quickly moves upwards again (black line in figure 3.8b) and optimally absorbs the acoustic energy (blue line in figure 3.8c) by moving to make the wave do work on the actuator boundary (purple line in figure 3.8c). The acoustic pressure quickly reduces and remains small thereafter (fig. 3.9f). This acts on the timescale of the channel: $2L_{\text{c}}/c_s^b = 2 \times 900\mu\text{m}/\,(1000\text{m/s}) = 1.8\mu\text{s}$. If the optimization time is 1μs, the nozzle free surface energy could be reduced by the actuator but there would then be insufficient time to absorb the acoustic wave that is reflected off the stress-free boundary. The optimal solution is to do almost nothing.

We now investigate the effect of the actuator size L_{act} on the final energy and the optimal waveform. Figure 3.7 (orange line) shows the final total energy of the controlled cases, normalized by the final energy of the uncontrolled case. Figure 3.10 shows the optimal mass flux through the actuator boundary for different actuator sizes, L_{act}. All waveforms have the three-phase shape described above and exploit the same mechanism.

Waveform optimization for $t_f = 3\mu$s.

For illustration, we will examine the results with final time $t_f = 3\mu$s and actuator length $L_{\text{act}} = 100\mu$m. Figure 3.11 shows the time history of the energy and boundary

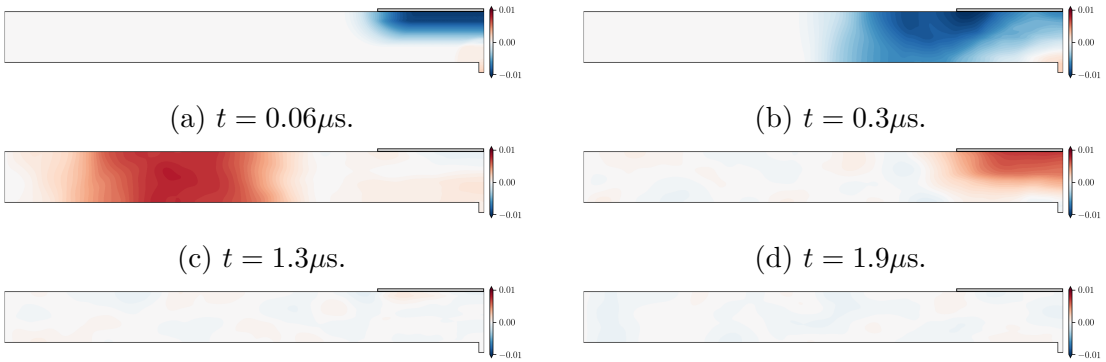

(a) $t = 0.06\mu$s. (b) $t = 0.3\mu$s.

(c) $t = 1.3\mu$s. (d) $t = 1.9\mu$s.

(e) $t = 2.0\mu$s. (f) $t = 2.5\mu$s.

Fig. 3.9 Snapshots of the pressure distribution inside an injector channel at different times, with the optimal control applied to the actuator boundary, $L_{\text{act}} = 200\mu$m, $t_f = 2\mu$s.

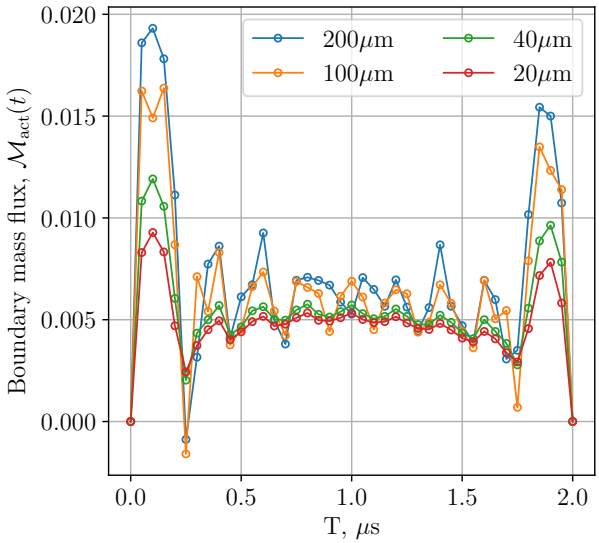

Fig. 3.10 Optimal mass flux through the control boundary as a function of time, for different actuator lengths. The control duration is 2 μs.

mass fluxes for the uncontrolled and optimally controlled cases. Figure 3.12 shows snapshots of the pressure field at the times shown as open circles in figure 3.11.

The first phase $\mathcal{A}^+ : 0 \leq t \leq 0.55$ μs is similar to the $\mathcal{A}^+$ phase of the $t_f = 2\mu$s case. The actuator pulls fluid upwards and generates a negative pressure wave (figure 3.12a). As before, the wave reaches the nozzle boundary at $t = 0.12\mu$s and mass starts to be pulled out of the nozzle. This wave reflects back off the nozzle. The reverberations in the fluid are as strong as in the previous case (which has a shorter actuator and

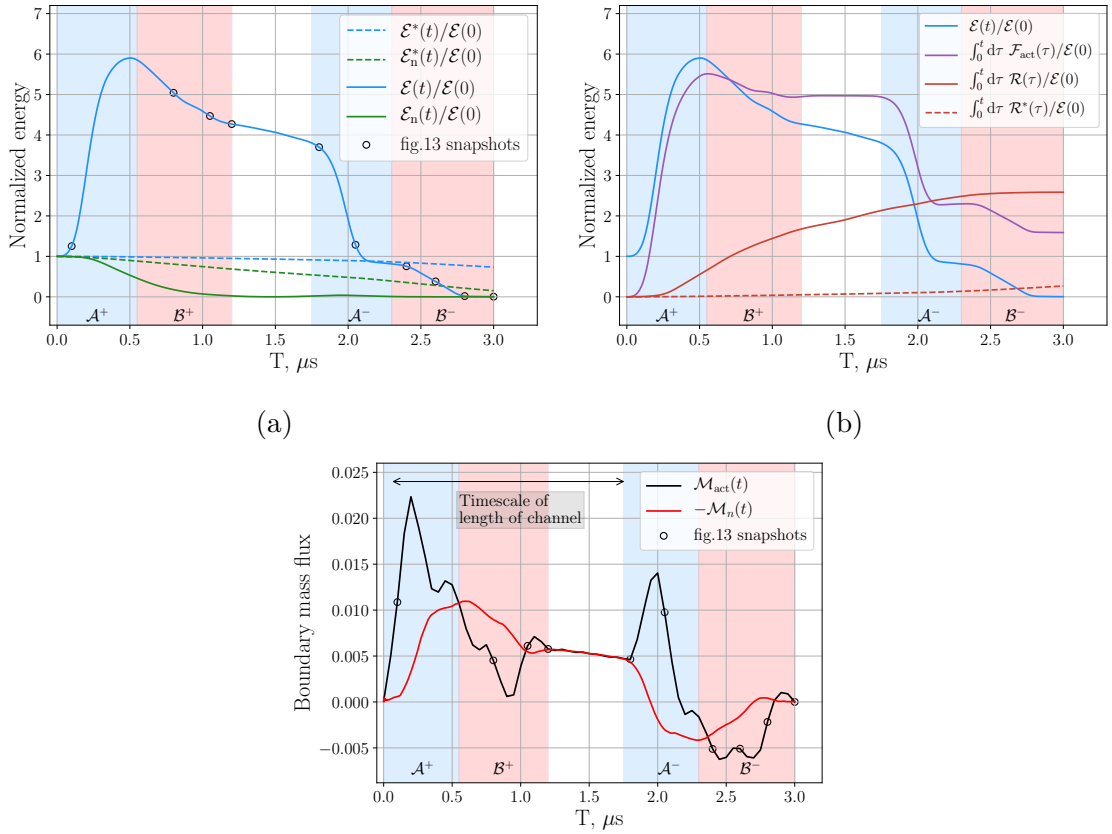

Fig. 3.11 Comparison between the uncontrolled case (dashed lines) and the optimally controlled case (solid lines) with $L_{\mathrm{act}} = 100\mu$m and $t_f = 3\mu$s. (a) Total energy $\mathcal{E}(t)$ (blue) and nozzle energy $\mathcal{E}_{\mathrm{n}}(t)$ (green), normalized by $\mathcal{E}(t=0)$. (b) Integrated energy flux through the actuator boundary $\int \mathcal{F}_{\mathrm{act}}(\tau)\mathrm{d}\tau$ (purple line), integrated acoustic energy dissipation $\int \mathcal{R}(\tau)\mathrm{d}\tau$ (red solid line), and the integrated acoustic energy dissipation $\int \mathcal{R}^*(\tau)\mathrm{d}\tau$ in the uncontrolled case (red dashed line). (c) Boundary mass flux through the actuator boundary $\mathcal{M}_{\mathrm{act}}$ (black) and the nozzle boundary $\mathcal{M}_{\mathrm{n}}$ (red). The coloured patches denote the actuation phases, when the acoustic waves are formed $(\mathcal{A}^+, \mathcal{B}^+)$ and absorbed by the actuator $(\mathcal{A}^-, \mathcal{B}^-)$.

a shorter channel) but the actuator is wider and would be unable to reduce their amplitude without simultaneously creating high amplitude waves elsewhere. Therefore the actuator moves less. As before, this motion produces a large amplitude wave moving left along the channel.

During the second phase $\mathcal{B}^+ : 0.55 \leq t \leq 1.2\mu$s the mass flux through the nozzle reaches a maximum. The actuator is still moving upwards, partially compensating for the flow from the nozzle and slowly absorbing the acoustic energy. A positive pressure

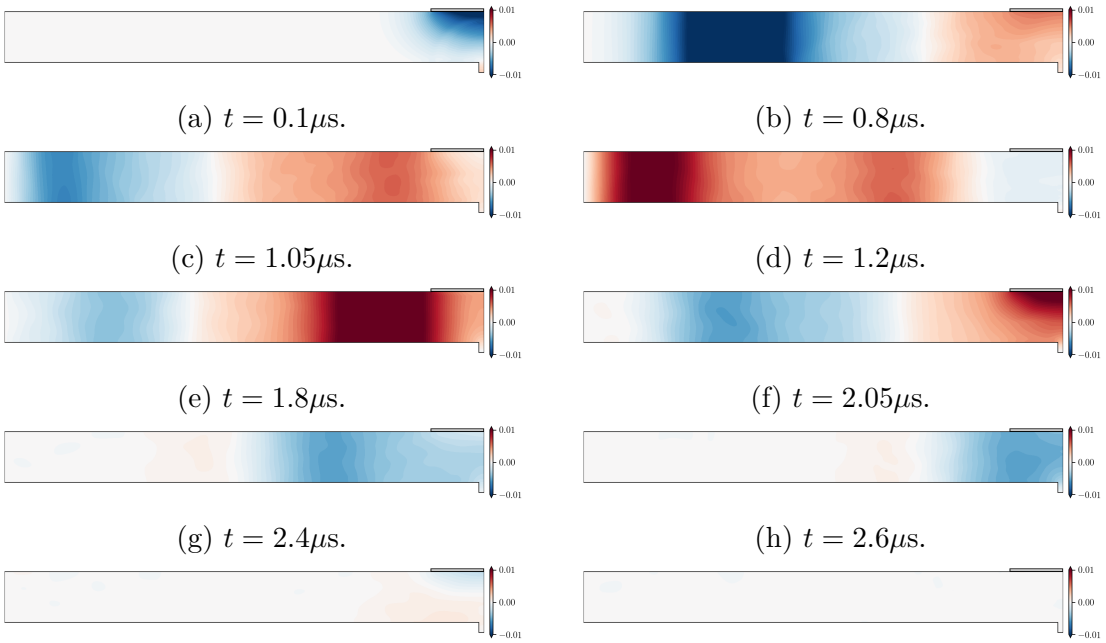

(a) $t = 0.1\mu$s. (b) $t = 0.8\mu$s.

(c) $t = 1.05\mu$s. (d) $t = 1.2\mu$s.

(e) $t = 1.8\mu$s. (f) $t = 2.05\mu$s.

(g) $t = 2.4\mu$s. (h) $t = 2.6\mu$s.

(i) $t = 2.8\mu$s. (j) $t = 3.0\mu$s.

Fig. 3.12 Snapshots of the pressure distribution inside an injector channel at different times, with the optimal control applied to the actuator boundary, $L_{\text{act}} = 100\mu$m, $t_f = 3\mu$s.

wave moves left along the channel (fig. 3.12b). (The optimization algorithm does not create this wave for the 2μs case because there is insufficient time to cancel it.) During this phase, almost all of the fluid is quickly transferred from the nozzle to the channel. By the end of the $\mathcal{B}^+$ phase, the free surface has nearly reached its final low energy state.

During the third phase $1.2 \leq t \leq 1.75\mu$s the mass flux from the actuator broadly cancels that from the nozzle. No new pressure waves form during this phase (fig.3.12c). The negative pressure left-running wave reflects from the open end (3.12d) and becomes a positive pressure right-running wave. This middle phase is similar to the middle phase of the $T = 2\mu$s case.

The fourth phase $\mathcal{A}^- : 1.8 \leq t \leq 2.3\mu$s is the same as the $\mathcal{A}^-$ phase in the $T = 2\mu$s case. The positive right-running wave is absorbed by the actuator (fig. 3.12e, 3.12f). This results in rapid decrease in total energy. Meanwhile the positive left-running wave has reflected from the open end and has become a negative right-running wave. During the fifth phase $\mathcal{B}^- : 2.3 \leq t \leq 3.0\mu$s, the negative left-running pressure wave reaches the actuator, and is optimally absorbed by doing work on the actuator boundary.

Figure 3.13 shows the mass flow at the actuator $\mathcal{M}_{\text{act}}$ as a function of time for different L_{act}. The shapes of the waveforms for $T = 3\mu$s with different actuator lengths are similar.

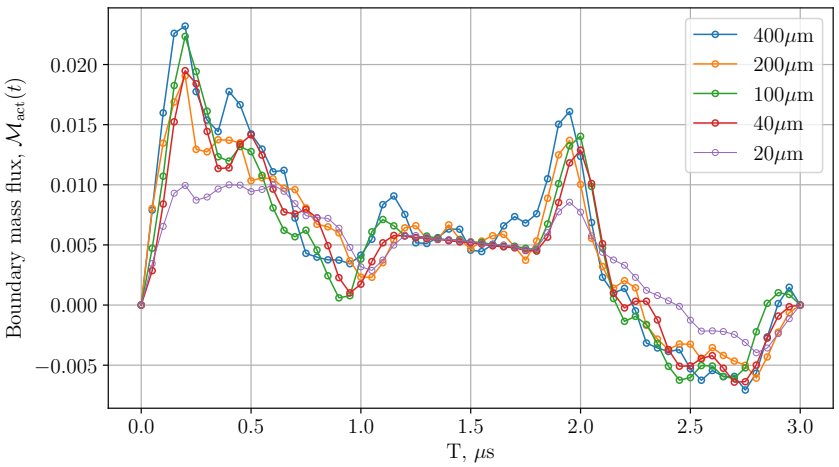

Fig. 3.13 Optimal mass flux through the control boundary as a function of time, for different actuator lengths. The control duration is 3 μs.

In summary, the most effective control is achieved when the actuator moves out of the domain and provides a negative pressure pulse to accelerate the flow at the nozzle, and then adapts to the large mass flux during the $\mathcal{B}^+$ phase. This combination efficiently transfers all fluid from the nozzle to the channel and leaves sufficient time for the actuator to absorb the reflected waves afterwards. At lower optimization times, reasonably effective control can be achieved with a short negative pulse, followed by a long middle period in which the channel slowly absorbs the fluid from the nozzle, leaving sufficient time to cancel its reverberation from the ends of the channel. If there is insufficient time to cancel the reverberation from the ends of the channel then any control is ineffective. This shows that the minimum optimization time (i.e. the minimum time between droplet ejections) is $2L_{\text{c}}/c_s^b$.

3.2.3 Two dimensional long straight print head channel

We now examine the case with a longer channel ($L_{\text{c}} = 1235\mu$m) and a longer optimization time ($t_f = 5\mu$s). This length is equal to the distance along the centreline of the U-shaped channel in section 3.2.4.

Figure 3.14 shows the time history of the energy and boundary mass fluxes for the uncontrolled and optimally controlled cases. Figure 3.15 shows snapshots of the

pressure field at the times shown as open circles on figure 3.14. By comparing figure 3.14 with figure 3.11, we see that the physical mechanisms are the same as those for the optimally controlled case with $L_{act} = 100\mu$m and $t_f = 3\mu$ s but that there is no gap between the $\mathcal{B}^+$ and $\mathcal{A}^-$ phases.

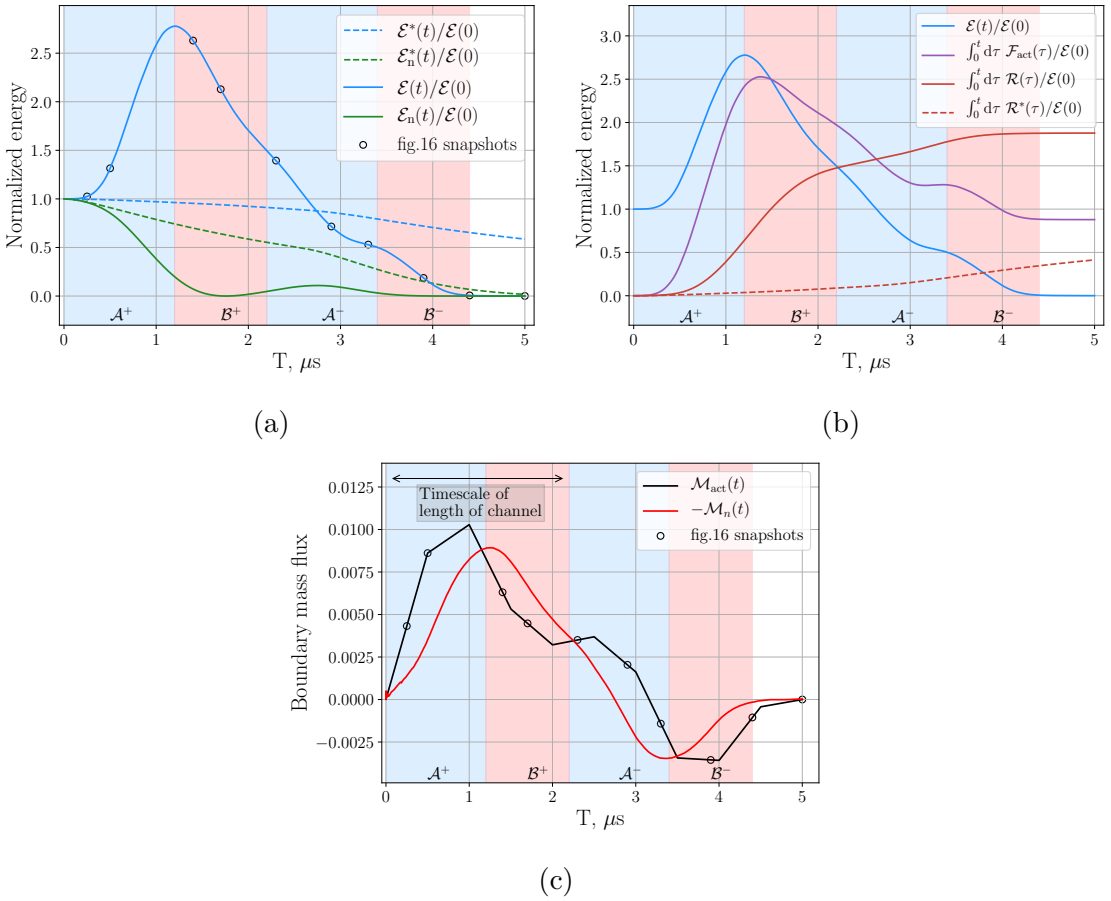

Fig. 3.14 Comparison between the uncontrolled case (dashed lines) and the optimally controlled case (solid lines) with $L_{\text{act}} = 400\mu$m and $t_f = 5\mu$s. (a) Total energy $\mathcal{E}(t)$ (blue) and nozzle energy $\mathcal{E}_{\text{n}}(t)$ (green), normalized by $\mathcal{E}(t = 0)$. (b) Integrated energy flux through the actuator boundary $\int \mathcal{F}_{\text{act}}(\tau)\mathrm{d}\tau$ (purple line), integrated acoustic energy dissipation $\int \mathcal{R}(\tau)\mathrm{d}\tau$ (red solid line), and the integrated acoustic energy dissipation $\int \mathcal{R}^*(\tau)\mathrm{d}\tau$ in the uncontrolled case (red dashed line). (c) Boundary mass flux through the actuator boundary $\mathcal{M}_{\text{act}}$ (black) and the nozzle boundary $\mathcal{M}_{\text{n}}$ (red). The coloured patches denote the actuation phases, when the acoustic waves are formed $(\mathcal{A}^+, \mathcal{B}^+)$ and absorbed by the actuator $(\mathcal{A}^-, \mathcal{B}^-)$.

In the first phase ($\mathcal{A}^+ : 0 \leq t \leq 1.2\mu$s) the actuator pulls fluid upwards and generates a negative pressure wave (figures 3.15a, 3.15b). Note that the total mass pulled upwards during the first phase is the same as for the previous, $T = 3\mu$s case.

Note also that, by moving more slowly, the actuator puts less energy into the system (compare maximum normalized energy of the $t_f = 5\mu$s case, $\mathcal{E}_{\max}/\mathcal{E}(0) \approx 2.8$ with that of the $t_f = 3\mu$s case, $\mathcal{E}_{\max}/\mathcal{E}(0) \approx 5.9$). This actuator motion creates a large amplitude negative pressure wave moving left along the channel. This reaches the end of the channel at 1.3μs and reflects off the stress-free boundary (figures 3.15c, 3.15d). During this $\mathcal{A}^+$ phase, the free surface contracts and fluid moves into the channel from the nozzle (red line in figure 3.14c). The mass flux from the nozzle reaches a maximum, and a positive pressure wave moves left along the channel (3.15d–3.15g), which then reflects as a negative pressure wave (phase $\mathcal{B}^+ : 1.2 \leq t \leq 2.2\mu$s). Meanwhile, the actuator has continued to move upwards in order to absorb the mass flux from the nozzle. From $t = 1.2$ to $t = 2.2\mu$s the actuator mass flux is returning to zero until, at 2.2μs the reflection of the first wave arrives back at the outer edge of the actuator, as a positive pressure wave. From 2.2 to 3.4 μs, the actuator moves upwards again to absorb the energy from this wave ($\mathcal{A}^-$). Then, around 3.4 μs, the reflection of the second wave arrives back at the actuator, as a negative pressure wave (figure 3.15h). The actuator moves downwards to absorb this wave ($\mathcal{B}^-$) and, by 4.5 μs has absorbed both waves.

In summary, in the 5 μs case we see the same waves ($\mathcal{A}^+$ and $\mathcal{B}^+$) as for the $t_f = 3\mu$s case but the actuator moves more slowly and for a longer period of time so that the maximum acoustic energy is less.

3.2.4 Two dimensional U-shaped print head channel

Having shown that the optimization algorithm works for a straight channel, and having highlighted the importance of wave reflections at the ends of the channel, we now examine a realistic case, in which the ends of the channel bend upwards to make a U-shape and the length along the centreline is the same as that in section 3.2.3 (figure 2.7). We set the actuator length to $L_{\text{act}} = 400\mu$m.

From the snapshots (figure 3.17) we see that the waves disperse slightly as they travel round the corner. By comparing figure 3.16 with figure 3.14, however, we see that the optimal profiles for the U-shaped channel are qualitatively identical to those for the long straight channel in section 3.2.3. From this, and the snapshots, we deduce that the optimization method is exploiting the same physical mechanism.

Figure 3.16 shows the comparison between the uncontrolled case (dashed lines) and optimally controlled case (solid lines) for the waveform with time resolution $w = 1.0\mu$s. In the uncontrolled case, the total energy (figure 3.16a, blue dashed line) decreases over time, and almost half of the total energy dissipates through viscous and thermal effects.

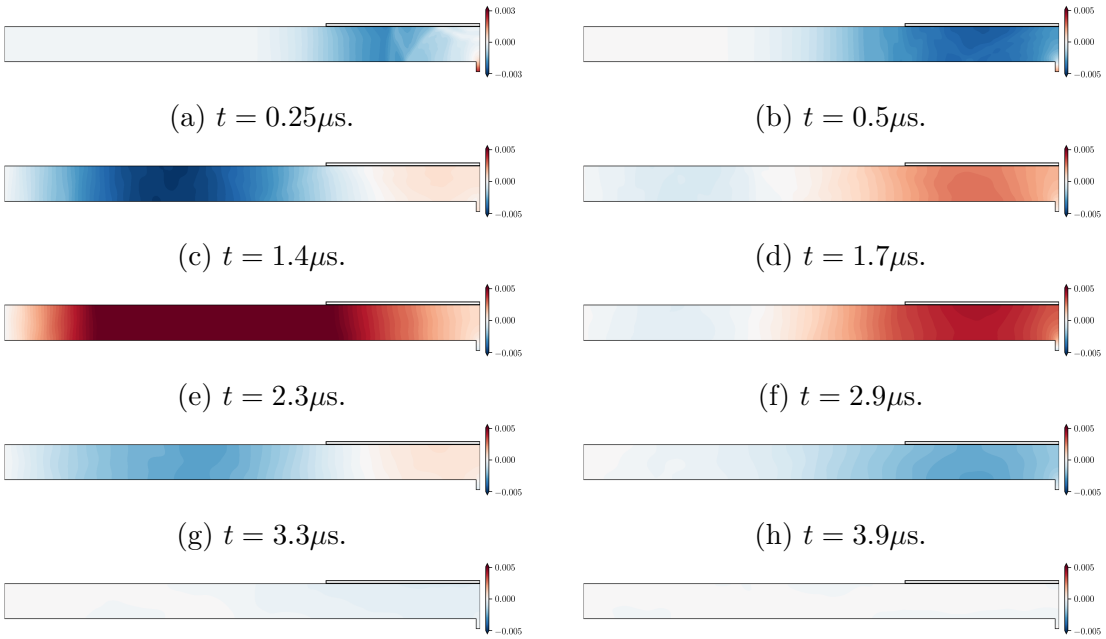

(a) $t = 0.25\mu$s. (b) $t = 0.5\mu$s.

(c) $t = 1.4\mu$s. (d) $t = 1.7\mu$s.

(e) $t = 2.3\mu$s. (f) $t = 2.9\mu$s.

(g) $t = 3.3\mu$s. (h) $t = 3.9\mu$s.

(i) $t = 4.4\mu$s. (j) $t = 5.0\mu$s.

Fig. 3.15 Snapshots of the pressure distribution inside a long straight printhead at different times, with the optimal control applied to the actuator boundary, $L_{\text{act}} = 400\mu\text{m}$, $t_f = 5\mu$s.

The mass flux through the nozzle surface $\mathcal{M}_{\text{n}}^*$ (red dashed line, figure 3.16c) oscillates due to the reflected acoustic waves approaching the nozzle surface at different times.

Figure 3.16c shows the optimal waveform (black line). The actuator moves out of the domain at $t \leq 1\mu$s, and accelerates the flow inside the nozzle $\mathcal{M}_{\text{n}}$ (red line). The energy flux through the actuator $\mathcal{F}_{\text{act}}$ is positive (figure 3.16b, purple line). For $t > 1.4\mu$, the energy flux $\mathcal{F}_{\text{act}}$ is negative (except for a short period $2.8 \leq t \leq 3.2\mu$s), and energy is actively removed from the system by the actuator (figure 3.16b, purple line). However, energy is mostly dissipated passively by viscous and thermal effects $\mathcal{R}$ (figure 3.16b, red line), similarly to the setups discussed in section 3.2.2. By the end of the simulation at $t = 5\mu$s, the work done by the actuator on the system is positive and approximately equal to the initial energy of the system. The dissipated energy $\int_0^T \mathrm{d}t\ \mathcal{R}(t)$ is therefore almost double the amount of initial energy in the system.

Finally we investigate how the objective value changes when we increase the waveform time resolution from $w = 1.0$ to $w = 0.5$, and 0.25μs. These correspond to the time resolution of state-of-the-art piezoelectric controllers. We project the optimal waveform with $w = 1.0\mu$s (figure 3.18b, solid line) to a higher dimensional space $\mathbb{T}_w^1$ with $w = 0.5\mu$s, and use the projected solution as the initial guess for a new

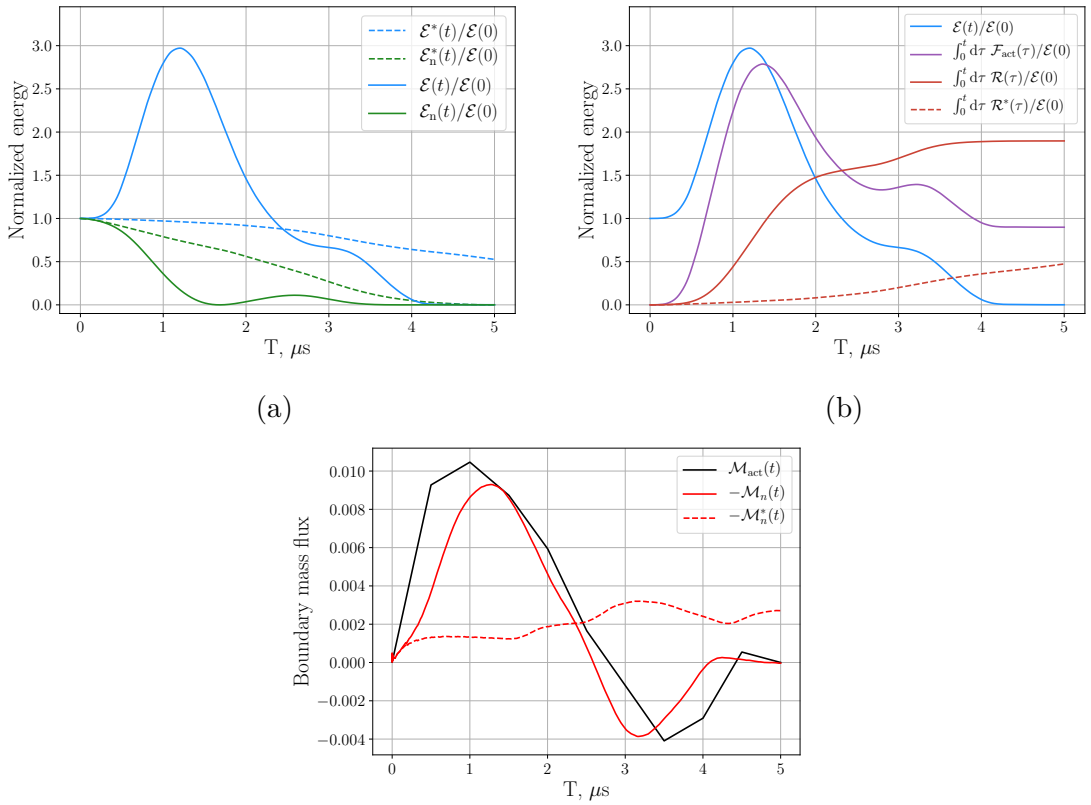

Fig. 3.16 Comparison between the printhead uncontrolled case (dashed lines) and the optimally controlled case (solid lines) with $L_{\mathrm{act}} = 400\mu$m and T = 5 μs. (a) Total energy $\mathcal{E}(t)$ (blue) and nozzle energy $\mathcal{E}_{\mathrm{n}}(t)$ (green), normalized by $\mathcal{E}(t = 0)$. (b) Integrated energy flux through the actuator boundary $\int_0^t \mathcal{F}_{\mathrm{act}}(\tau)\mathrm{d}\tau$ (purple line), integrated acoustic energy dissipation $\int \mathcal{R}(\tau)\mathrm{d}\tau$ (red solid line), and the integrated acoustic energy dissipation $\int \mathcal{R}^*(\tau)\mathrm{d}\tau$ in the uncontrolled case (red dashed line). (c) Boundary mass flux through the actuator boundary $\mathcal{M}_{\mathrm{act}}$ (black) and the nozzle boundary $\mathcal{M}_{\mathrm{n}}$ (red). The red dashed line is the mass flux $\mathcal{M}^*_{\mathrm{n}}$ through the nozzle boundary in the uncontrolled case.

optimization problem. We noticed that using the coarse solution as the initial guess for a more resolved waveform has considerably decreased the number of optimization iterations to converge. The optimal waveform for $w = 0.5\mu$s (figure 3.18b, dash-dotted line) results in 25% lower objective value (figure 3.18a). We use the optimal solution for $w = 0.5\mu$s as the initial guess for the $w = 0.25\mu$s case. The optimal waveform for $w = 0.25\mu$s (figure 3.18b, dotted line) results in further 4% reduction in the objective value. These improvements are quite small, showing that the rather basic sinusoid-type waveform for the $w = 1.0\mu$s case provides a good trade-off between efficiency and

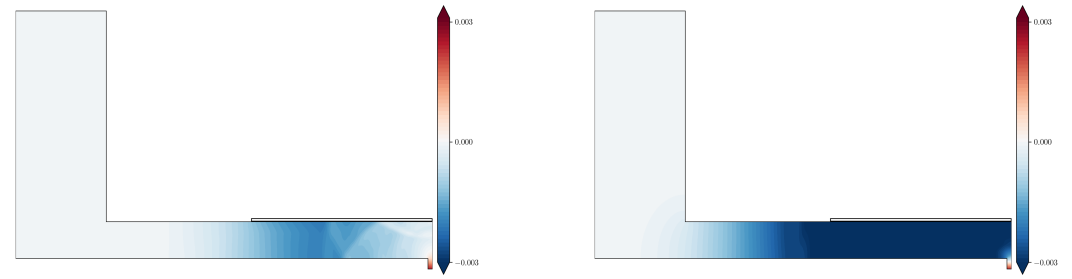

(a) $t = 0.25\mu$s. (b) $t = 0.5\mu$s.

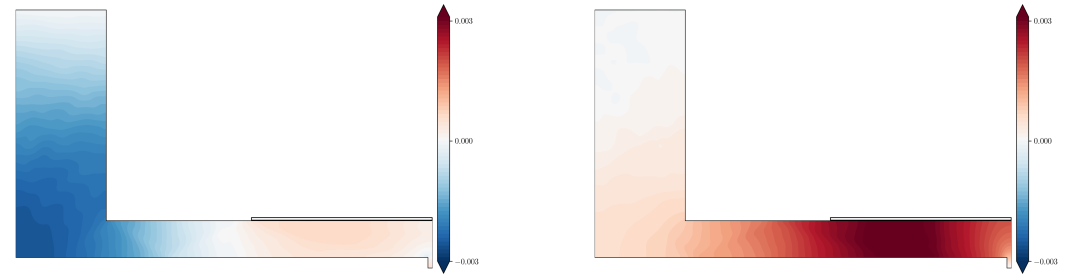

(c) $t = 1.4\mu$s. (d) $t = 1.7\mu$s.

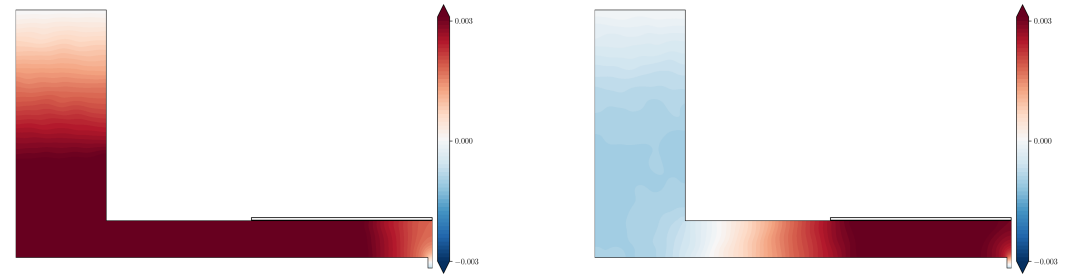

(e) $t = 2.3\mu$s. (f) $t = 2.9\mu$s.

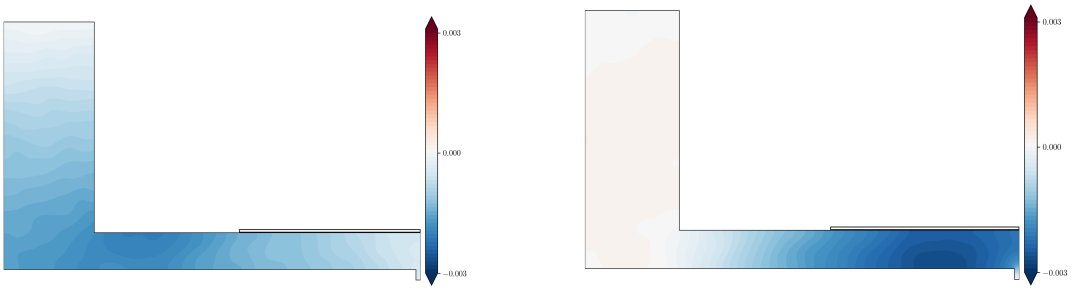

(g) $t = 3.3\mu$s. (h) $t = 3.9\mu$s.

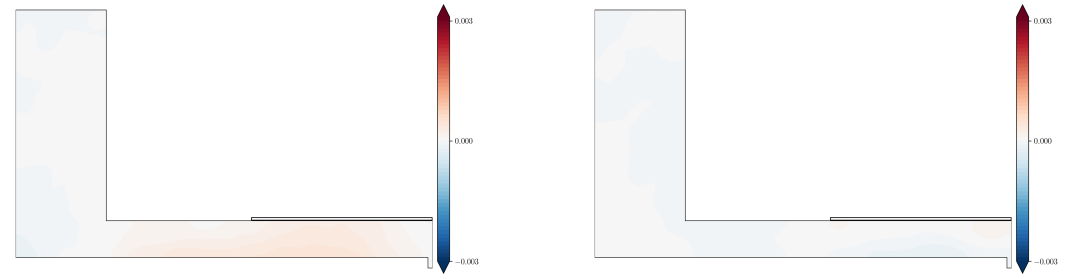

(i) $t = 4.4\mu$s. (j) $t = 5.0\mu$s.

Fig. 3.17 Snapshots of the pressure distribution inside a U-shaped printhead at different times, with the optimal control applied to the actuator boundary, $L_{\text{act}} = 400\mu$m, $t_f = 5\mu$s.

complexity. This waveform is an outward moving pulse lasting 2.7μs, and an inwards moving pulse lasting 2 μs. The outward pulse causes the free surface to relax but generates acoustic waves that travel down the channel. These reflect and first arrive back at the actuator at $t = 2.4\mu$s. The trailing edge of the outward pulse and then the inward pulse absorb these reflected waves optimally. Given that this waveform would be imposed just after ejection of the droplet, it is reassuringly similar to the W-shaped waveform that, by trial and error, has been shown to remove residual acoustic waves arising from the previous ejection cycle (Gan et al., 2009). The advance in this thesis is to show this rigorously with adjoint-based optimization in the time domain and to identify the physical mechanisms that this waveform exploits.

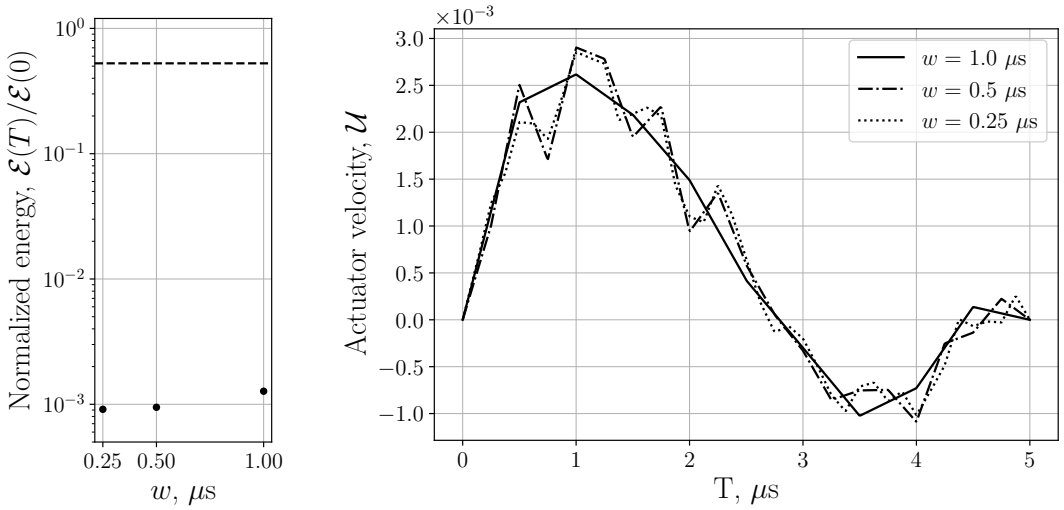

(a) (b)

Fig. 3.18 (a) Optimized objective values (total energy at final time $\mathcal{E}(T)$ normalized by initial value $\mathcal{E}(0)$) for different waveform resolution w, and (b) corresponding waveforms.

3.2.5 Optimization with a parabolic actuator velocity profile

In previous sections, the flow inside a straight and a U-shaped channels driven by an actuator with a uniform actuator velocity profile has been optimized. This section examines a system with a parabolic actuator velocity profile, and two cases are considered: a straight channel with $L_{\text{act}} = 200\mu$m, $t_f = 2\mu$s (similar to 3.2.2), and a U-shaped channel with $L_{\text{act}} = 400\mu$m, $t_f = 5\mu$s (similar to 3.2.4). The velocity boundary condition on Γ_{act} is $\mathbf{u} = c(t)\,(x - x_{\text{act}})\,(x - x_{\text{act}} - 2L_{\text{act}})\,\mathbf{n}$, where x is the

coordinate along the actuator boundary, and x_{act} is the position of the leftmost point on the actuator boundary.

The same optimization strategy as descried in section 3.2.1 is applied to find an optimal waveform. Figure 3.19 shows an optimal waveform, and a mass and energy fluxes for a straight channel (figure 3.6) and $t_f = 2\mu$s (dashed lines). Solid lines denote the optimized results for a flat actuator velocity profile (from section 3.2.2). The optimal waveforms (figure 3.19c) for parabolic and flat velocity profiles are very similar, and the energy transfer between the nozzle, channel, and the actuator follow the same pattern (figure 3.19b).

Figure 3.20 shows optimization results for a U-shaped printhead channel (the same as in section 3.2.4) with a parabolic actuator velocity profile. Again, the parabolic profile results (dashed lines) match very closely the optimization results for a uniform profile (solid lines). This means that the energy damping mechanism is independent of the exact shape of the actuator velocity profile, and is governed by the mass flow through the actuator boundary $\mathcal{M}_{\text{act}}$.

3.3 Concluding remarks

In this chapter we develop a gradient-based approach that uses adjoint methods in the time domain to optimize the motion of the piezo-electric actuator in an inkjet printhead microchannel. We seek to minimize the residual reverberations inside the microchannel after a droplet is ejected by defining the objective function to be the sum of the acoustic and free surface energy at a given final time (3.1). We derive the adjoint equations for the acoustic equations and the free surface model (3.11, 3.12), and thereby obtain the expression for the objective function derivative (3.15). With an optimization method we obtain the optimal deformation for a one-dimensional test case (3.2.1), a two-dimensional rectangular microchannel (3.2.2, 3.2.3), and a U-shaped printhead microchannel (3.2.4). We show that an optimally controlled actuator can reduce the total energy inside the printhead microchannel geometry by 1000 times, compared with the uncontrolled case. The physical mechanism for reducing the energy is qualitatively similar for all three microchannels, and does not depend on the exact shape of the actuator velocity profile. The actuator's initial deformation withdraws fluid from the nozzle. The liquid/gas surface relaxes towards the zero curvature state. This initial deformation sends an acoustic wave down the microchannel, which reflects off the open end and returns some time later. The actuator then deforms in order to perfectly absorb the reflected acoustic wave. The minimum time over which optimization can be

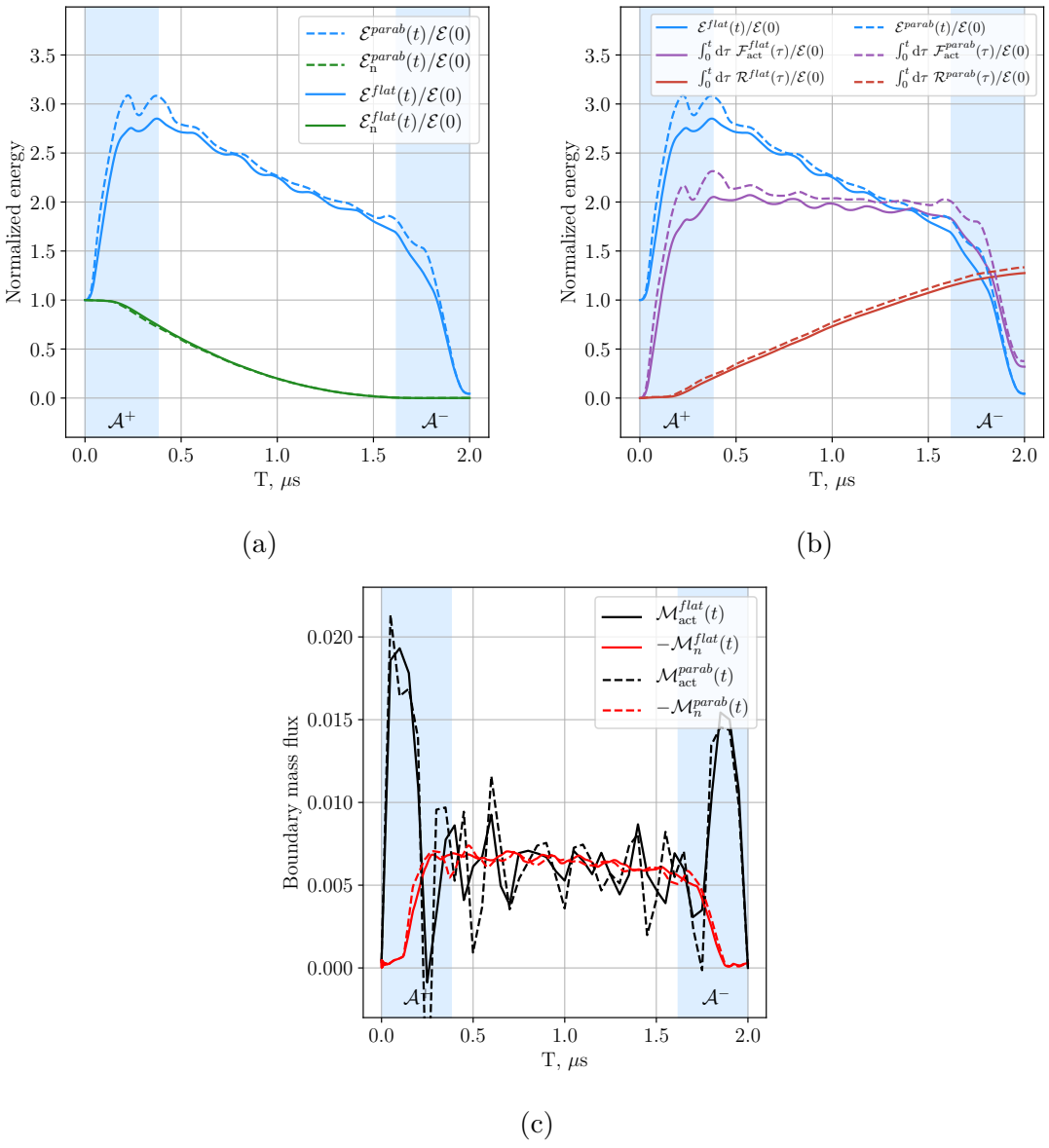

Fig. 3.19 Comparison between the optimally controlled straight channel flow with flat (solid lines) and parabolic (dahsed lines) actuator velocity profiles with $L_{\text{act}} = 200\mu$m and $t_f = 2\mu$s. (a) Total energy $\mathcal{E}_{\text{n}}(t)$ (blue) and nozzle energy $\mathcal{E}_{\text{n}}(t)$ (green), normalized by $\mathcal{E}(t=0)$. (b) Integrated energy fluxes through the actuator boundary $\int \mathcal{F}_{\text{act}}(\tau)\text{d}\tau$ (purple line), integrated acoustic energy dissipation $\int \mathcal{R}(\tau)\text{d}\tau$ (red solid line). (c) Boundary mass fluxes through the actuator boundary $\mathcal{M}_{\text{act}}$ (black) and the nozzle boundary $\mathcal{M}_{\text{n}}$ (red). The coloured patches denote the actuation phases, when the acoustic waves are formed ($\mathcal{A}^+$) and absorbed by the actuator ($\mathcal{A}^-$).

successful, which is therefore the minimum time between droplets, is the time taken for an acoustic wave to travel from the actuator to the open end and back. The duration of

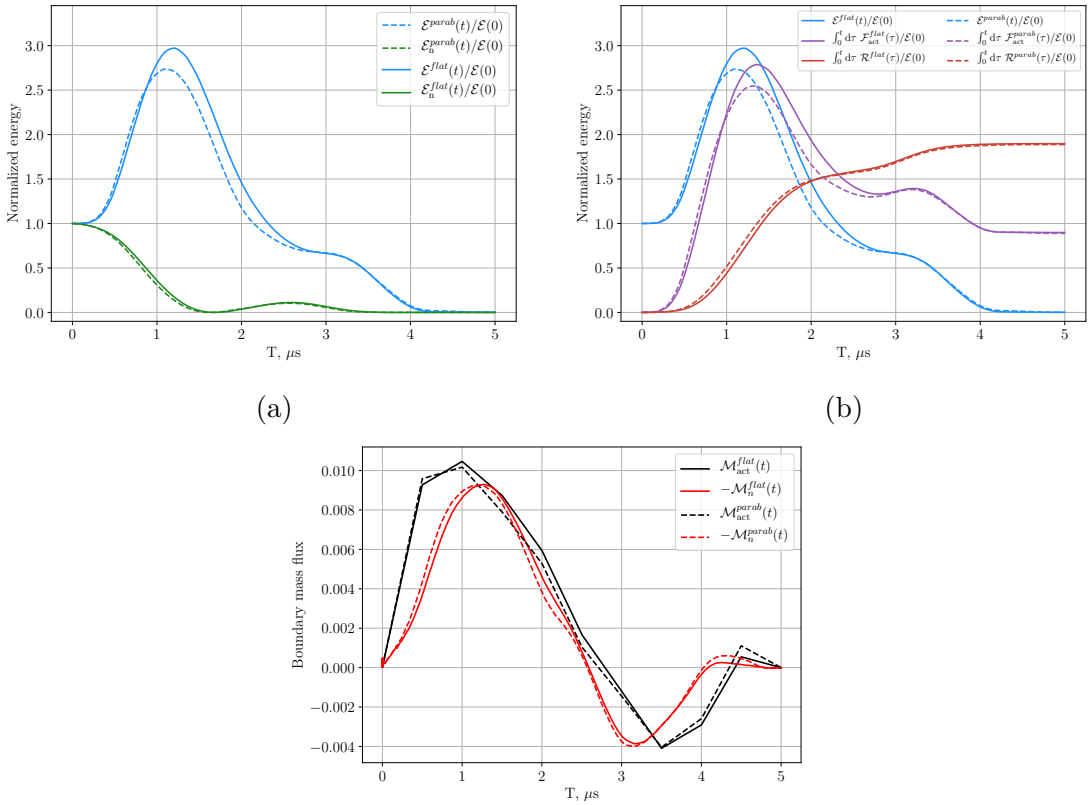

Fig. 3.20 Comparison between the optimally controlled printhead flow with flat (solid lines) and parabolic (dahsed lines) actuator velocity profiles with $L_{\text{act}} = 400\mu$m and T = 5 μs. (a) Total energy $\mathcal{E}(t)$ (blue) and nozzle energy $\mathcal{E}_{\text{n}}(t)$ (green), normalized by $\mathcal{E}(t=0)$. (b) Integrated energy fluxes through the actuator boundary $\int_0^t \mathcal{F}_{\text{act}}(\tau)\text{d}\tau$ (purple line), integrated acoustic energy dissipation $\int \mathcal{R}(\tau)\text{d}\tau$ (red solid line). (c) Boundary mass fluxes through the actuator boundary $\mathcal{M}_{\text{act}}$ (black) and the nozzle boundary $\mathcal{M}_{\text{n}}$ (red).

the waveform itself must be added to this time. Short waveforms (e.g. $\mathcal{A}^+$ in figure 3.8) are in one direction only and reduce the energy by just over one order of magnitude. Longer optimization times allow sufficient time for the deformation waveform to have two components in opposite directions (e.g. $\mathcal{A}^+$ and $\mathcal{B}^+$ in figures 3.11 and 3.14)). This waveform reduces the free surface energy more quickly and by over a further order of magnitude. Although these qualitative features are consistent, the exact optimal waveform and the final energy depend on the available optimization time, the actuator length, and the waveform resolution.

Chapter 4

Shape optimization of the inkjet microchannels

We consider the reverberation (residual control) stage of the drop-on-demand process, and ask whether it is possible to change the shape of the printhead's microchannels in order to increase the decay rate $\mathrm{Re}(s)$ of acoustic reverberations while decreasing (or at least maintaining) the pressure drop required to flush ink through the printhead. In both cases, viscous dissipation in the channel is the major damping mechanism. We define two objective functions: the steady flow viscous dissipation that serves as a proxy for the channel's pressure drop, and the oscillating flow decay rate. We then set the former one to be a constraint. We discover that it is possible to increase one while decreasing the other. The question then arises as to how to find the optimal channel shape. So many shape parameters can be changed that a particularly efficient approach is to use gradient-based optimization algorithms.

Using the adjoint approach, it is possible to obtain the sensitivity of the objective functions to shape modifications. The shape sensitivity of the steady flow viscous dissipation is calculated using results obtained by Schmidt and Schulz (2010). In this chapter we derive the adjoint counterpart of the thermoviscous acoustic eigenvalue problem and calculate the natural frequency and decay rate shape sensitivities (e.g. Luchini and Bottaro (2014)).

We choose the parameter-based approach to define the optimization boundaries, and describe the optimization domain in terms of B-spline boundaries. This approach provides smooth surfaces with analytic expressions of parametric sensitivities and surface properties. An alternative parameter-free approach requires additional surface smoothing (Jameson and Martinelli, 2000) to obtain shapes that can be reproduced by

CAD programs (Schmidt et al., 2016) and avoid being stuck at local optima (Bängtsson et al., 2003).

The main goal of this chapter is to describe the method and the physics that it exploits. The gradient-based optimization is then applied to a two-dimensional channel and a generic geometry of the printhead's microchannels. Constraining the channel to be two-dimensional considerably reduces the computational expense of the problem without altering the most influential aspects of the physics. This is because the longest-lasting residual oscillations are those of the lowest frequency mode, whose frequency is determined mainly by the length of the channel and whose dissipation is predominantly in the boundary layers at the sides of the channel. The results of this chapter have been published in Kungurtsev and Juniper (2019).

4.1 Shape optimization framework

4.1.1 Shape calculus formalism

We consider a governing equation $\mathcal{R}(q, \mathbf{a}) = 0$ satisfied over a domain Ω, with solution q for model parameters $\mathbf{a}$. In this particular case, the model parameters determine the domain shape: $\Omega = \Omega(\mathbf{a})$. We define an objective function $J(q, \Omega, \mathbf{a})$. The optimal control problem we aim to solve is

$$\begin{aligned} &\text{Find } \Omega^* = \arg\min J(q, \Omega, \mathbf{a}) \\ &\text{subject to } \mathcal{R}(q, \mathbf{a}) = 0, \\ &\mathbf{a} \in \mathcal{A}_{\text{adm}},\ \Omega \in \mathcal{O}_\Omega, \end{aligned} \tag{4.1}$$

where $\mathcal{A}_{\text{adm}}$ is a set of admissible model parameters, and $\mathcal{O}_\Omega$ is the set of admissible domains.

In 2D, a displacement field $V : \mathbb{R}^2 \to \mathbb{R}^2$ defined in Ω represents the domain deformation, and ξ is the displacement amplitude. Following Schmidt and Schulz (2010), we define a parametric family of mappings $T_\xi : \mathbf{x} \to \mathbf{x} + \xi V(\mathbf{x})$ for $\mathbf{x} \in \Omega$. The perturbed domain Ω_ξ and the perturbed boundary $\Gamma_\xi = \partial\Omega_\xi$ are given by

$$\Omega_\xi = T_\xi(\Omega), \quad \Gamma_\xi = \Gamma + \xi V(\mathbf{x}) \quad \text{for } \mathbf{x} \in \Gamma. \tag{4.2}$$

q_ξ denotes the corresponding perturbed flow state. The Fréchet derivative of J with respect to a domain perturbation, V, at $\Omega_0 = \Omega(\mathbf{a}_0)$, $q_0 = q(\Omega_0, \mathbf{a}_0)$, is denoted with a

square bracket $J'[V]$:

$$J'(q_0, \Omega_0, \mathbf{a}_0)[V] = \lim_{\xi \to 0^\dagger} \frac{J(q_\xi, \Omega_\xi) - J_0}{\xi}. \tag{4.3}$$

If the domain boundary Γ is sufficiently smooth, any tangential displacement only changes the boundary parametrization but not the actual shape. Therefore the boundary displacements in the direction of V and its normal component $(V \cdot \mathbf{n})\,\mathbf{n}$ are equivalent, where $\mathbf{n}$ is the boundary unit normal vector. A shape derivative $J'(\Omega)[V]$ can be written in Hadamard form (Delfour and Zolésio, 2011; Grinfeld, 2010) as a scalar product of a sensitivity functional $G(q, q^\dagger)$ and the normal component of the deformation field V, where $q^\dagger$ is the adjoint state:

$$J'[V] = \int_{\Gamma_0} (V \cdot \mathbf{n})\, G(q, q^\dagger) \mathrm{d}s. \tag{4.4}$$

The sensitivity functional naturally depends on the choice of the state equations and the objective function. We derive the sensitivity functionals of interest in section 4.2.

Shape derivatives of boundary conditions

The shape derivative of a general boundary condition independent of the geometry, in particular independent of the surface normal, can be calculated as follows. Given a boundary condition $\mathbf{g}(q_0) = g_0$ on the unperturbed boundary Γ_0, the perturbed boundary condition $\mathbf{g}(q_\xi) = g_\xi$ on Γ_ξ can be linearised around Γ_0 for a small shape deformation with magnitude $\xi \ll 1$. We expand the perturbed solution as

$$\begin{aligned} q_\xi(\Gamma_\xi) &= (1 + \xi(V \cdot \nabla))\, q_\xi(\Gamma_0) + \mathcal{O}\left(\xi^2\right) \\ &= (1 + \xi(V \cdot \nabla))\, (q_0(\Gamma_0) + \xi q_0'[V](\Gamma_0)) + \mathcal{O}\left(\xi^2\right) \\ &= q_0(\Gamma_0) + \xi q_0'[V](\Gamma_0) + \xi\, (V \cdot \nabla)\, q_0(\Gamma_0) + \mathcal{O}\left(\xi^2\right), \end{aligned} \tag{4.5}$$

such that the total (material) derivative of the solution with respect to the shape perturbation V is $\mathrm{d}q[V] \equiv q_0'[V](\Gamma_0) + (V \cdot \nabla) q_\xi(\Gamma_0)$ and $q_0'[V]$ is the local shape derivative. The linearisation of the boundary condition is

$$\mathbf{g}(q_\xi(\Gamma_\xi)) = \mathbf{g}(q_0 + \xi \mathrm{d}q[V]) = \mathbf{g}(q_0, \Gamma_0) + \xi \left(\left.\frac{\partial \mathbf{g}}{\partial q}\right|_0 (q_0'[V] + (V \cdot \nabla) q_0) \right) + \mathcal{O}\left(\xi^2\right), \tag{4.6}$$

where the subscript $|_0$ indicates the value at $q = q_0, \Gamma = \Gamma_0$. The term $\left.\frac{\partial \mathbf{g}}{\partial q}\right|_0 q'[V]$ represents the boundary condition of the first order solution's response to shape deformation on the unperturbed boundary. It can be expressed in terms of the initial solution q_0 as

$$\left.\frac{\partial \mathbf{g}}{\partial q}\right|_0 q'[V] = \lim_{\xi \to 0^\dagger} \frac{g_{b,\xi} - g_{b,0}}{\xi} - \left.\frac{\partial \mathbf{g}}{\partial q}\right|_0 (V \cdot \nabla) q_0 = (V \cdot \nabla) g_{b,0} - \left.\frac{\partial \mathbf{g}}{\partial q}\right|_0 (V \cdot \nabla) q_0. \quad (4.7)$$

4.1.2 Parameter-based shape optimization

We use the parameter-based shape optimization framework, and require that the model parameters belong to a discrete space $\mathbf{a} = \left\{a^k,\ k = 1, 2, \ldots\right\}$. The parameter-based approach restricts the number of possible boundary deformations to the number of control parameters. Essentially, a parametrization projects the function space of the admissible shape deformations onto a lower dimensional subspace, which allows us to operate with the vector representation of shape gradients instead of the continuous boundary sensitivities. We assume that there is a unique mapping between the original model parameters and a set of two (or three) dimensional *control points*. Each control point generates a boundary displacement field, V^k, which is, by definition, the boundary shape sensitivity to the control point's position:

$$V^k = \frac{\partial \Gamma}{\partial a^k}. \quad (4.8)$$

The objective function gradient with respect to the displacement field $J'[V^k]$ transforms to the sensitivity with respect to the control parameters, $J'[a^k]$.

For a sufficiently small perturbation $\delta\mathbf{a}$, the objective function can be locally approximated as $J(\mathbf{a}) = J(\mathbf{a}_0 + \delta\mathbf{a}) \simeq J(\mathbf{a}_0) + J'(\mathbf{a}_0)[\mathbf{a}]\delta\mathbf{a}$. The components of the vector $J'[\delta\mathbf{a}] \in \mathbb{R}^N$ are $J'[a^k] \equiv \left\{\left(V^k \cdot \mathbf{n}\right) G(q, q^\dagger)\right\}$. In general, the basis $\left\{V^k,\ k = 1, 2, \ldots\right\}$ is not orthonormal: $\left\{V^k, V^{k'}\right\}_\Gamma \neq \delta_{k,k'}$, and the metric corresponding to the scalar product is defined by a mass matrix $M_{k,k'}$: for two deformation fields $V_1 = \sum_k \alpha_1^k V^k$ and $V_2 = \sum_{k'} \alpha_2^{k'} V^{k'}$,

$$\{V_1, V_2\}_\Gamma = \sum_{k,k'} \alpha_1^k \alpha_2^{k'} \left\{V^k, V^{k'}\right\}_\Gamma \equiv \sum_{k,k'} \alpha_1^k \alpha_2^{k'} M_{k,k'}.$$

Therefore, the covariant gradient descent is given by

$$\delta a^k \sim -M^{-1}_{k,k'} J'(\mathbf{a}_0)[a^{k'}]. \quad (4.9)$$

This result is discussed in details by Kiendl et al. (2014), and has been visualized for a simple objective function $J = |\Omega|$ by Wang et al. (2017). Naive application of $\delta\mathbf{a} = J'(\mathbf{a}_0)$ as the gradient step in steepest descent minimization algorithms results in parameterization-dependent convergence, while the covariant gradient descent (4.9) is parameterization-agnostic.

We can estimate the optimality of a shape (but not the parametrization) by considering the scalar product of the objective shape sensitivity, G, with the constraint shape sensitivity, G'. The surface inner product $\{G, G'\}_\Gamma$ and the surface norm $\|G\|_\Gamma^2 = \{G, G\}_\Gamma$ form the optimality coefficient α:

$$\alpha = \frac{\{G, G'\}_\Gamma}{\|G\|_\Gamma \|G'\|_\Gamma} \geq -1. \tag{4.10}$$

The optimality coefficient indicates the cosine of the angle between the objective function shape sensitivity and the constraint shape sensitivity, such that $\alpha = -1$ implies that they point in opposite directions and the system has reached its local optimum. In the case of N optimization parameters, a sensitivity functional is realised on a shape deformation subspace, spanned by V^k, $k = 1 \dots N$. The parametric optimality coefficient α_p is:

$$\alpha_p = \frac{\mathbf{g}^T \mathbf{g}'}{\|\mathbf{g}\| \cdot \|\mathbf{g}'\|} \leq \alpha, \tag{4.11}$$

where $\mathbf{g}_i = \{G, V^i\}_\Gamma$ and $\mathbf{g}'_i = \{G', V^i\}_\Gamma$. In the parameter-based optimization, $\alpha_p = -1$ implies that the local optimum has been reached within the choice of parametrization.

4.1.3 Automatic shape generation using `PySplines`

The python package `PySplines` (Kungurtsev, 2020b) has been developed as a part of this work. It is based on a symbolic algebra package `sympy` (Meurer et al., 2017). The development of the tool is motivated by CAD-style parameter-based shapes generation and optimization. The tool aims to solve the following problems:

1. allow easy generation of B-splines with given control points and degree;
2. provide fast access to the surface properties in analytical and numerical forms (normals, curvature, displacement fields), especially when they are used multiple times;
3. implement fine control of the curve smoothness and uniformity of the points distribution along the curve.

The following example illustrates the B-spline generation and refinement features:

```
from pysplines.bsplines import Bspline

def generate_bsplines():
    # Create two `Bspline` objects: with and without refinement.
    control_points = [
        [[0.0, 0.0], [2.0, 0.0], [-1.0, 1.0], [1.0, 1.0]]
    ]
    bspline = Bspline(control_points, degree=3, refine=False)
    refined_bspline = Bspline(
        control_points, degree=3, refine=True, angle_tolerance=0.03
    )
    return bspline, refined_bspline


if __name__ == "__main__":
    bspline, refined_bspline = generate_bsplines()

    bspline.plot(color="blue", show=False)
    refined_bspline.plot(color="red")
```

Figure 4.1 shows the resulting curves. While both lines are a discrete representation of the same B-spline with an equal number of surface points, the refined spline (red line) approximates the regions with high curvature better than the spline without refinement (blue line). The majority of the refined curve surface points are located near the bend of the spline (figure 4.1b). As shown in the following sections, accurate representation of these boundary features is important for calculating viscous and thermal dissipation in the acoustic flow boundary layers during shape optimization.

The `BSpline` class implements several commonly used boundary properties: the surface normal, curvature, displacement fields (as defined by 4.8), and the mass matrix (4.9). These built-in methods are used for automatic estimation of shape sensitivities and re-building the optimization domain.

4.2 Shape sensitivities

In this section we discuss the choice of the objective functions for the steady and the oscillating flows, construct the adjoint states, and derive the corresponding sensitivity functionals. Detailed derivation of the objective function shape gradient in Hadamard form with respect to an arbitrary boundary displacement V is provided in Appendix B.

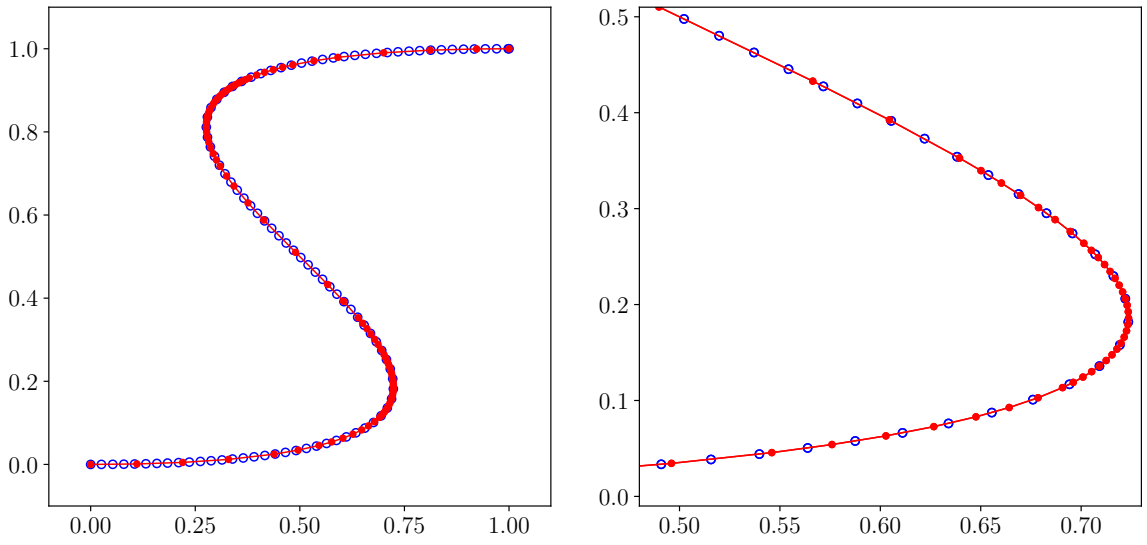

(a) (b)

Fig. 4.1 B-splines generated using the `PySplines` package. Two third-order splines with equal control points and number of discrete surface points are demonstrated: without (blue) and with (red) automatic refinement.

4.2.1 Incompressible flow shape sensitivity

For the unsteady incompressible flow, we wish to minimize the viscous dissipation, J_{vd}, in the domain Ω and averaged over time:

$$J_{vd}(\bar{\mathbf{u}}, \Omega) = \left[\frac{1}{Re} \left(\nabla_j \bar{u}_i \right)^2 w(t) \right], \tag{4.12}$$

where $\bar{\mathbf{u}}$ satisfies the momentum equation and the divergence-free condition given by (2.14, 2.15), and $w(t)$ is an optional weight function $w(t) : \mathcal{T} \rightarrow \mathbb{R}$. By choosing $w(t) \equiv 1$, the objective function is a simple time-averaged viscous dissipation. The unsteady incompressible flow viscous dissipation shape derivative with respect to shape displacements defined on no slip boundaries is:

$$J'[V] = \left[(V \cdot \mathbf{n}) \, G_{vd} \right]_{\Gamma_\mathrm{w} \times \mathcal{T}} + \left\langle \bar{u}_i^\dagger, \bar{u}_i'[V] \right\rangle_{\Omega, t=0}. \tag{4.13}$$

The term $\bar{u}_i'[V](t = 0)$ denotes the sensitivity of the initial condition with respect to shape modifications; the term is zero if the initial condition is homogeneous. As discussed by Schmidt and Schulz (2010), the viscous dissipation sensitivity functional

G_{vd} is

$$G_{vd}(\bar{u}_i, \bar{u}_i^\dagger) = \frac{1}{\overline{Re}} \frac{\partial \bar{u}_i}{\partial \mathbf{n}} \frac{\partial \left(\bar{u}_i^\dagger - \bar{u}_i \right)}{\partial \mathbf{n}}, \tag{4.14}$$

where $\bar{u}_i^\dagger$ and $\bar{u}_p^\dagger$ are the adjoint velocity and pressure states satisfying

$$\frac{\partial}{\partial t}\bar{u}_i^\dagger + \bar{u}_j \nabla_j \bar{u}_i^\dagger + \bar{u}_j \nabla_i \bar{u}_j^\dagger - \nabla_i \bar{u}_p^\dagger + \frac{1}{\overline{Re}} \Delta \bar{u}_i^\dagger = \frac{2w(t)}{\overline{Re}} \Delta \bar{u}_i, \tag{4.15a}$$

$$\nabla_i \bar{u}_i^\dagger = 0, \quad \text{in } \Omega, \tag{4.15b}$$

$$\bar{u}_i^\dagger = 0 \quad \text{on } \Gamma_{\text{in}} \cup \Gamma_{\text{w}}, \tag{4.15c}$$

$$\bar{u}_i^\dagger \bar{u}_j n_j + \bar{u}_j^\dagger \bar{u}_j n_i + \frac{1}{\overline{Re}} \frac{\partial \bar{u}_i^\dagger}{\partial \mathbf{n}} + \bar{u}_p^\dagger n_i = \frac{2w(t)}{\overline{Re}} \frac{\partial \bar{u}_i}{\partial \mathbf{n}} \quad \text{on } \Gamma_{\text{out}} \tag{4.15d}$$

The right hand side source terms of the adjoint equations and boundary conditions depend on the choice of the objective function, while the left hand sides are governed only by the primal steady flow formulation.

4.2.2 Oscillating flow shape sensitivity

For the oscillating flow we wish to control the decay rate and frequency (Luchini and Bottaro, 2014), so the objective function is the complex natural frequency, s, of the thermoviscous acoustic flow (2.27):

$$J_s = s. \tag{4.16}$$

We introduce an adjoint state vector $\mathbf{q}^\dagger = (P^\dagger, \hat{\mathbf{u}}^\dagger, T^\dagger)$ containing the adjoint pressure, velocity, and temperature variables. Taking the inner product of the primal equations and the corresponding adjoint variables, we construct a Lagrangian of the system (Gunzburger, 2002),

$$\mathcal{L} = s - \left\langle \mathbf{q}^\dagger, s\mathrm{A}\hat{\mathbf{q}} + \mathrm{B}\hat{\mathbf{q}} \right\rangle. \tag{4.17}$$

The optimality condition sets any first Lagrangian variation to zero. Variation with respect to the adjoint and primal variables gives the primal and the adjoint state equations, respectively. As discussed in Appendix B.1, the adjoint and the primal states of the thermoviscous acoustic problem are related by $P^\dagger = \hat{P}^*, \mathbf{u}^\dagger = -\hat{\mathbf{u}}^*, T^\dagger = \hat{T}^*$,

subject to the normalization condition:

$$1 = \left\langle \mathbf{u}^\dagger, \hat{\mathbf{u}} \right\rangle + \left(P^\dagger, \gamma_{\text{th}} \hat{P} - \hat{T} \right) + \left(T^\dagger, \frac{\hat{T}}{\gamma_{\text{th}} - 1} - \hat{P} \right) + \\ + \left\{ \mathbf{u}^\dagger, \frac{\partial Z}{\partial s} \hat{\mathbf{u}} \right\} - \left\{ \frac{\partial T^\dagger}{\partial \mathbf{n}}, \frac{(\partial \alpha_w / \partial s)}{(\gamma_{\text{th}} - 1)\tilde{Pe}} \frac{\partial \hat{T}}{\partial \mathbf{n}} \right\}. \tag{4.18}$$

For a shape deformation normal to a boundary $V \equiv (V \cdot \mathbf{n})\,\mathbf{n}$, the oscillating flow eigenvalue sensitivity G_s consists of the surface stress and the thermal terms, $G_s = G_s^{str} + G_s^{th}$ (derived in Appendix B.2). Given that the primal and adjoint states are identical up to the sign of the velocity term, the sensitivity functionals are:

$$G_s^{str} = -2 \frac{\partial \hat{u}_i}{\partial \mathbf{n}} n_j \hat{\sigma}_{ij} - \kappa \hat{u}_i \hat{\sigma}_{ij} n_j + \nabla_j \left(\hat{u}_i \hat{\sigma}_{ij} \right), \tag{4.19a}$$

$$G_s^{th} = 2 \frac{\partial \hat{T}}{\partial \mathbf{n}} \hat{q}_n + \kappa \hat{T} \hat{q}_n - \nabla_j \left(\hat{T} \hat{q}_j \right). \tag{4.19b}$$

where $\hat{q}_i \equiv \left((\gamma_{\text{th}} - 1)\tilde{Pe} \right)^{-1} \nabla_i \hat{T}$ is the boundary heat flux, and $\hat{q}_n = (\hat{q} \cdot \mathbf{n})$ is its normal component. The viscous and the thermal sensitivity functionals have equivalent structure in terms of the $(\hat{\mathbf{u}}, \hat{\sigma}_{ij})$ and $\left(\hat{T}, \hat{q}_i \right)$ pairs.

On the no slip and stress-free boundaries, the viscous sensitivity functional simplifies to

$$G_{s,w}^{str} = -\frac{\partial \hat{u}_i}{\partial n_j} \hat{\sigma}_{ij}, \tag{4.20a}$$

$$G_{s,out}^{str} = \nabla_j \left(\hat{u}_i \hat{\sigma}_{ij} \right), \tag{4.20b}$$

and on the isothermal and adiabatic boundaries, the thermal sensitivity functional simplifies to

$$G_{s,isoth}^{th} = \frac{\partial \hat{T}}{\partial \mathbf{n}} \hat{q}_n, \tag{4.21a}$$

$$G_{s,ad}^{th} = -\nabla_j \left(\hat{T} \hat{q}_j \right). \tag{4.21b}$$

The sensitivity functionals (4.19) are calculated from the discrete solution of the governing equations obtained using the finite element method. The discrete form of the surface normal vector and curvature are provided by the software that generated the domain boudaries (`PySplines`) for each mesh node on the domain surface, and interpolated linearly between the surface nodes.

4.3 Shape optimization in a 2D straight channel

4.3.1 Optimization domain

We start with a flow in a two-dimensional uniform-width channel, defined as

$$\Omega_0 = \left\{(x, y) \in \mathbb{R}^2 \mid [0, 1] \times [0, 0.1]\right\}, \tag{4.22}$$

with inlet and outlet boundaries

$$\Gamma_{in,0} = \left\{(x, y) \in \mathbb{R}^2 \mid x = 0\right\}, \tag{4.23a}$$

$$\Gamma_{out,0} = \left\{(x, y) \in \mathbb{R}^2 \mid x = 1\right\}, \tag{4.23b}$$

and no slip boundaries $\Gamma_{w,0} = \partial\Omega_0 \backslash (\Gamma_{in,0} \bigcup \Gamma_{out,0})$. For the oscillating flow, the stress free boundary is $\Gamma_{free,0} = \Gamma_{in,0} \cup \Gamma_{out,0}$.

The boundary $\Gamma_{w,0}$ is to be optimized by modifying the no slip boundaries, while fixing the inlet and the outlet. If equivalent boundary displacement fields are applied to the top and bottom no slip surfaces then the steady flow and the oscillating flow boundary sensitivities and the shape gradients remain symmetric. Therefore we may consider deformation of only the top boundary.

In this study, we parametrize the boundary with a set of N control points $\left\{a^k \in \mathbb{R}^2 \mid k = 1 \dots N\right\}$ defining the third order rational uniform B-spline curve. This provides a smooth surface of class C^2 for which parametric sensitivities can be calculated (Samareh, 2001). As the positions of the control points are moved in the gradient direction, the domain is updated and the computational mesh is rebuilt. We apply the goal-oriented adjoint-based error control technique (Rognes and Logg, 2013) for the automated adaptive mesh refinement. The goal functional in our case is the target eigenvalue.

We parametrize the top boundary of the initial rectangular domain with 11 control points, $a_i = (i/10, 0.1)\,, i = 0 \dots 10$, spaced uniformly at intervals of 0.1. The first and last points are kept at their initial positions so that the inlet and outlet boundaries are fixed and the channel's length remains equal to 1.

The steady flow is computed in the initially flat channel (4.22) at $\overline{Re} = 0.1$ with a parabolic inflow velocity profile. In the unaltered domain this results in the Poiseuille flow solution, and the corresponding viscous dissipation value J_{vd}^0 is taken as a reference. For the oscillating flow at $\tilde{Re} = 1000$, we choose the smallest non-zero frequency natural mode as the target mode, with $s_0 = -0.555 + 2.81i$. Figure 4.2 shows the real and

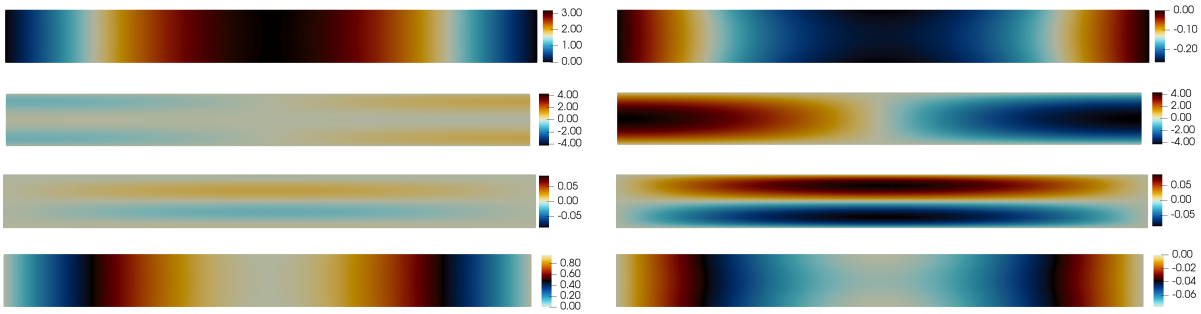

Fig. 4.2 First natural mode of the oscillating flow in a flat channel at $\tilde{Re} = 1000$. From top to bottom: pressure $\hat{P}$, longitudinal $\hat{\mathbf{u}}_x$ and transverse $\hat{\mathbf{u}}_y$ velocity components, and temperature $\hat{T}$ mode shapes; real (left) and imaginary (right) parts.

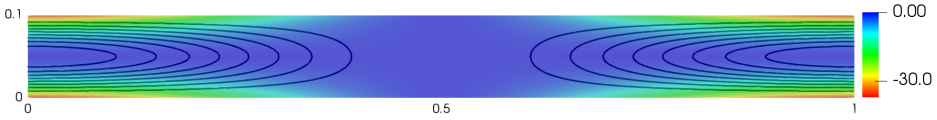

Fig. 4.3 Spatial distribution of the decay rate production σ_Ω in a flat channel. Black lines correspond to the oscillating flow velocity magnitude isolines $\hat{\mathbf{u}} = const$.

imaginary parts of the mode shape, normalized by (4.18). The pressure gradient $\partial_x \hat{P}$ and the longitudinal velocity $\hat{\mathbf{u}}_x$ are highest on the stress-free open end boundaries at $x = 0, x = 1$. As indicated on figure 4.3, the regions with the highest contribution to the decay rate σ_Ω are the no slip wall regions close to the open ends, where the velocity magnitude isolines converge and therefore the transverse velocity gradient is the largest. For the initial channel configuration, $\alpha_p = -0.7$.

The steady flow state in the unperturbed channel is independent of the longitudinal coordinate x so the viscous dissipation shape sensitivity $G_{vd}(\bar{\mathbf{u}}, \bar{\mathbf{u}}^\dagger)$ is constant along the no slip walls (figure 4.4). Here, and later, G_{vd} is normalized by the viscous dissipation value J^0_{vd} in the starting geometry configuration. The shape sensitivity G_{vd} is always negative, so any boundary displacement resulting in contraction of the channel's width leads to growth of viscous dissipation. The complex eigenvalue shape sensitivity $G_s(\hat{P}, \hat{\mathbf{u}}, \hat{T})$ is not uniform; the real part $\mathrm{Re}(G_s)$ is almost zero in the middle part of the boundary and grows towards the channel's open ends where the decay rate production is highest, as shown previously. As for viscous dissipation, any shape deformation directed inwards $(V \cdot \mathbf{n}) < 0$ leads to an increase in the decay rate magnitude.

As indicated on figure 4.4, the decay rate is less sensitive to shape modifications in the middle region of the channel at $0.3 \leq x \leq 0.7$, and has higher sensitivity on the outer region. We expect therefore, that the channel will expand in the middle and

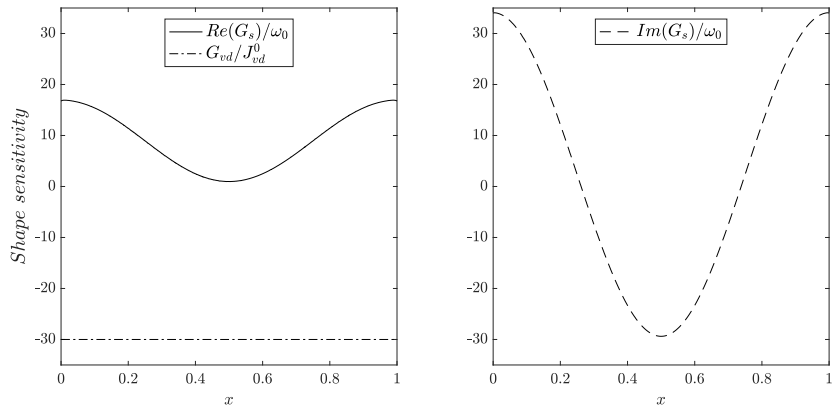

Fig. 4.4 Shape sensitivity distribution along the flat channel top boundary for the decay rate $\mathrm{Re}(G_s)$ (solid line) and frequency $\mathrm{Im}(G_s)$ (dashed line) of the first oscillating mode, and the steady flow viscous dissipation shape sensitivity G_{vd}/J_0 normalized by viscous dissipation inside the channel (dotted line).

shrink around the free boundaries to increase the decay rate while keeping the steady flow viscous dissipation constant. This is also what we expect on physical grounds: the channels will constrict where the acoustic velocity is greater.

4.3.2 Constrained gradient optimization

Our goals are to make the oscillation's decay rate, $-\sigma$, more negative, and decrease (or at least not increase) the steady flow viscous dissipation. There is a trade-off between these goals, so here we set the steady flow dissipation as an inequality constraint and minimize $\mathrm{Re}(s)$.

$$\begin{aligned} \min_{\Omega\subset\mathcal{O}_\Omega} \quad & \mathrm{Re}(s) \\ \text{subject to} \quad & J_{vd} \le J_{vd}^0 \\ \text{and} \quad & \text{state equations } (2.14), (2.27). \end{aligned} \tag{4.24}$$

An alternative approach would be to incorporate the viscous dissipation as a penalty function with an appropriate normalization constant $\beta \ge 0$:

$$\begin{aligned} \min_{\Omega\subset\mathcal{O}_\Omega} \quad & \mathrm{Re}(s) + \beta\left(J_{vd} - J_{vd}^0 + \left|J_{vd} - J_{vd}^0\right|\right) \\ \text{subject to} \quad & \text{state equations } (2.14), (2.27). \end{aligned}$$

We use the method of moving asymptotes (Svanberg, 1987, 2002) as the optimization algorithm for the problem (4.24). This is a widely applied iterative method of structural

optimization (Bendsoe and Sigmund, 2013; Gersborg-Hansen et al., 2005; Perez et al., 2012) that generates strictly convex approximations of the original function. The method conveniently allows us to incorporate state-dependent inequality constraints (viscous dissipation should be less than a certain threshold), and lower and upper bounds for the design variables. These algorithm features make it a perfect choice for our optimization problem.

We use standard internal parameters as discussed in (Svanberg, 1987). The objective and the constraint values and their parametric sensitivities are calculated by:

1. solving the steady steady flow (2.14) and the oscillating eigenvalue (2.27) problems;

2. finding the adjoint steady flow (4.15) and oscillating flow (4.18) states;

3. calculating the boundary sensitivities G_{vd}, G_s using (4.14) and (4.19); and computing the objective and constraint sensitivities with respect to the boundary control points $s'[a_k] = \left\{V^k, G_s\right\}, J'_{vd}[a_k] = \left\{V^k, G_{vd}\right\}$.

We use $\varepsilon_p = \alpha_p + 1$ as a tolerance criteria for the optimization process. At the stage the boundary control points are moved, we also verify that the domain boundaries do not overlap, which essentially adds inequality constraints on the gradient application step.

4.3.3 Optimized 2D channel domain

A nearly optimal configuration is found in 20 iterations, and then fine-tuned during the subsequent 15 iterations of the MMA algorithm. Figure 4.5 shows the objective and constraint values during the optimization, and three different shapes of the channel. The final shape has the optimality coefficient (4.10) of $\alpha_p = -0.98$. The first eigenmode in the optimized channel is $s = -1.31 + 1.68i$. In comparison to the initial solution, the decay rate objective function changes by almost 140%, and the frequency (which is unconstrained) decreases by 40%. The total area almost doubles and the channel's shape loses symmetry around the $x = 0.5$ vertical plane, while remaining symmetric in the horizontal plane. The channel constricts near $x = 0.07$ and $x = 0.99$, and the middle part of the channel expands, as expected.

Figure 4.6 shows the steady flow (top) and the adjoint flow (bottom) velocity magnitude $\bar{u}$ and $\bar{u}^\dagger$ for the optimized channel. The lines correspond to the steady flow streamlines. The no slip boundaries are smooth and the flow remains attached to the

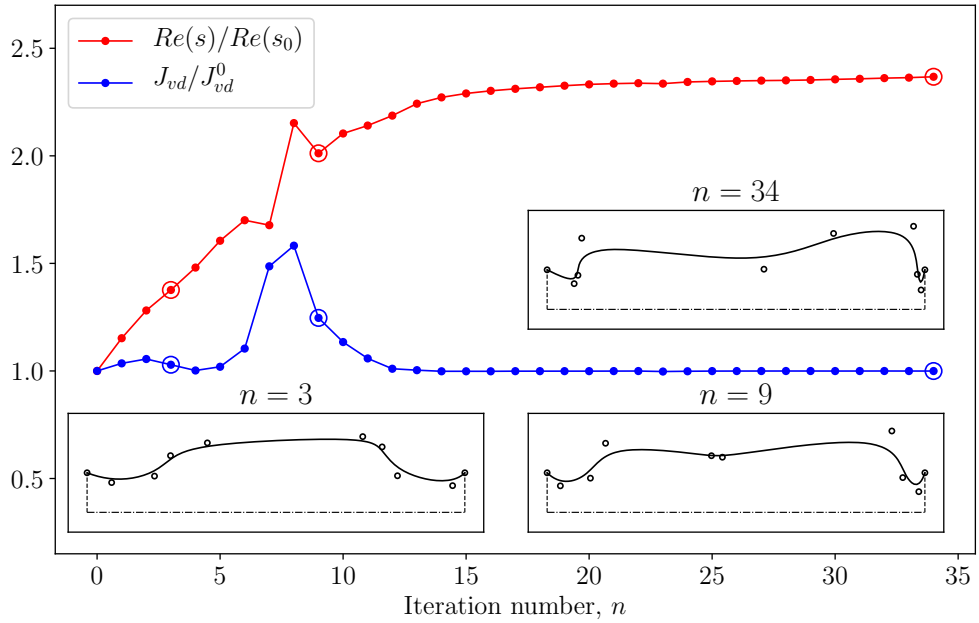

Fig. 4.5 Normalized values of the objective function Re(s) and the constraint (viscous dissipation) during 2D channel shape optimization. Top part of the channels at iterations $n = 3, 9$ and 34 are shown, and the corresponding objective and constraint values are highlighted.

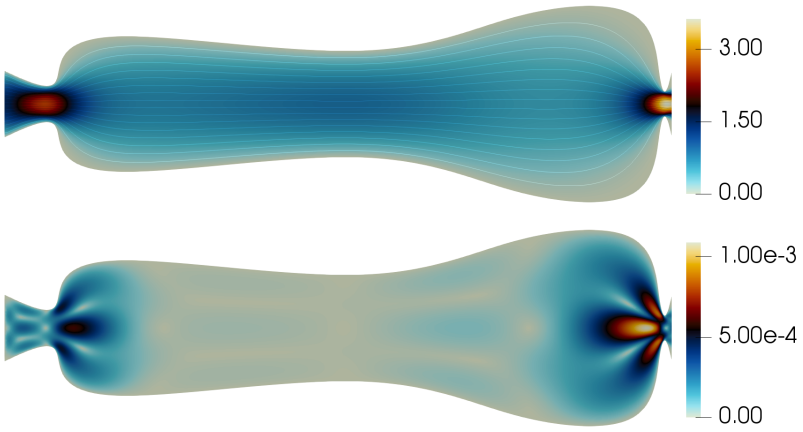

Fig. 4.6 Steady flow in the optimized channel at $\overline{Re} = 0.1$. Top: the steady flow $|\bar{u}|$ velocity magnitude, with the streamlines indicated (solid lines). Bottom: the adjoint steady flow $|\bar{u}^\dagger|$ velocity magnitude.

walls with no recirculation zones. Viscous dissipation in the optimized channel is the same as in the initial channel.

The steady flow velocity amplitude and velocity gradients as well as the adjoint velocity are highest in the constricted areas. This makes the constricted regions much

more sensitive to shape changes than the expanded part, where the adjoint velocity magnitude is almost zero.

The decay rate production is initially located in the corner regions of the uniform width channel. When the boundaries shift, this region shifts inside the channel towards the constrictions, as indicated in figure 4.7. The decay rate production strongly concentrates in the narrow parts of the channel, with the maximum at $x = 0.99$ more than 10000 times higher than the average value. It is almost zero between the constrictions.

Fig. 4.7 Spatial distribution of the decay rate production in the optimized channel (on a logarithmic scale), $\log_{10}(-\sigma_\Omega)$. Black lines correspond to the oscillating flow velocity magnitude isolines $\hat{\mathbf{u}} = const$.

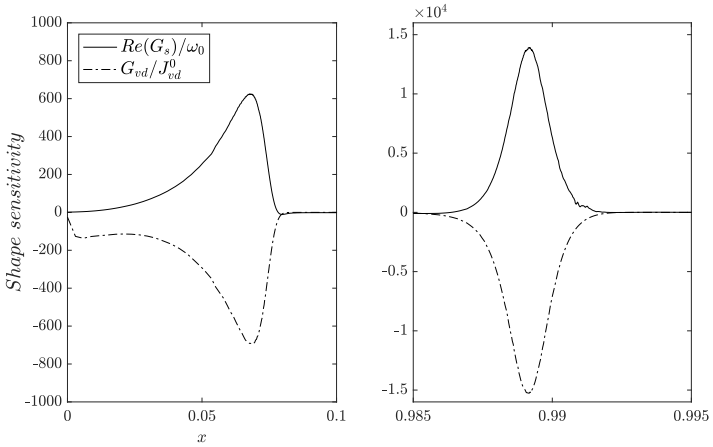

Fig. 4.8 The decay rate shape sensitivity distribution (solid line) of the first oscillating mode in the optimized channel, and the steady flow viscous dissipation sensitivity (dotted line) normalized by viscous dissipation inside the channel.

Figure 4.8 illustrates the viscous dissipation G_{vd}/J^0_{vd} (dash-dotted line) and the decay rate $\mathrm{Re}(G_s)/\omega_0$ (solid line) boundary sensitivities as functions of the longitudinal coordinate along the top boundary in the optimized channel. Both sensitivities reach their extreme values in the constricted areas and are much smaller in the intermediate

region. They are almost equal and opposite to each other, showing that the design is almost optimal. Further improvements can still be made, for instance, by boundary re-parametrization or by introducing additional control points. However, this simple problem has achieved its purpose by showing that the optimization procedure can indeed increase acoustic dissipation while keeping the steady flow dissipation constant.

4.4 Inkjet printhead channel shape optimization

4.4.1 Optimization domain

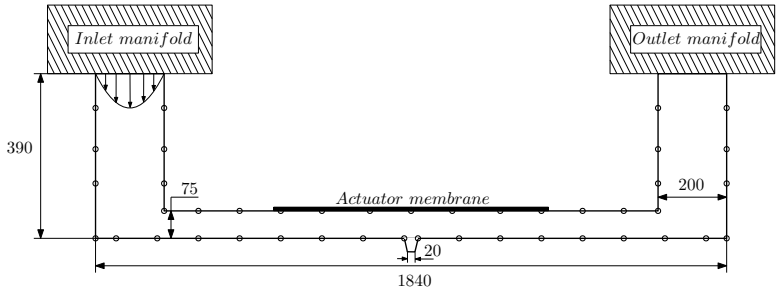

Fig. 4.9 A 2D generic printhead geometry with a piezoelectric actuator. The channel is connected to the ink supply manifolds via the inlet and outlet boundaries. Circles denote the B-spline boundary control points. All sizes are in μm.

Figure 4.9 shows a 2D generic inkjet printhead chamber, which consists of a vertical inlet and outlet, connected to ink manifolds, and a horizontal main channel. The manifolds' cross sections are much larger than the printhead cross section. A 30μm long conical printing nozzle, which has a 20μm outer diameter and a taper of 8°, is located in the middle of the printhead. A flat piezoelectric membrane is located on the top boundary opposite the nozzle. In 3D, the channel has a depth of 60μm into the page. We approximate the channel to be uniform in that direction and examine only 2D deformations, as in §4.3. We aim to increase the decay rate of the oscillating flow while keeping the steady flow viscous dissipation constant.

We parametrize the printhead walls by third order B-splines with the control points indicated on figure 4.9. The inlet and the outlet points are fixed. The nozzle shape cannot change but it can move in both the vertical and horizontal directions. The bottom wall cannot extend below the nozzle tip.

We choose a characteristic length $L = 100\mu$m. The steady flow Reynolds number is $\overline{Re} = 0.066$ and the Reynolds number based on the speed of sound is $\tilde{Re} = 6000$. The steady flow Mach number is $\mu = 10^{-4}$ and the oscillating flow Mach number is

$\epsilon = 10^{-5}$. For the steady flow, the inlet has a fixed parabolic velocity profile, the outlet is an open end with stress-free boundary condition (2.15c), and the walls are no-slip boundaries and the nozzle exit is modelled as a no slip boundary because there is no flow through it. For the acoustic flow, the walls are adiabatic no-slip, and the open boundaries, including the nozzle exit, are stress-free and isothermal. We neglect the surface tension at the nozzle exit.

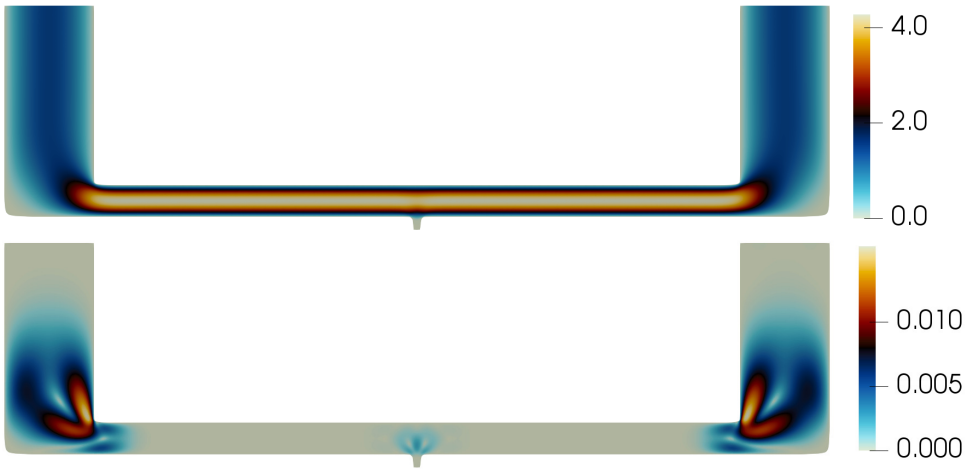

Fig. 4.10 The velocity magnitude $\bar{u}$ (top) and the adjoint velocity magnitude $\bar{u}^\dagger$ (bottom) of the steady flow in the initial printhead channel at $\overline{Re} = 0.066$.

Figure 4.10 shows the steady flow primal $\bar{u}$ and adjoint $\bar{u}^\dagger$ velocity magnitude in the initial geometry. The largest velocity magnitude is in the narrow horizontal channel. The adjoint velocity has highest value near the sharp corners at the channel entrance and the nozzle. These regions have the greatest influence on the steady flow viscous dissipation.

The frequency of the first natural mode is $\mathrm{Im}(s_1/2\pi) = \omega/2\pi = 0.342$ MHz, and the decay rate is $\mathrm{Re}(s_1/2\pi) = \sigma/2\pi = 0.0171$ MHz. Figure 4.11 shows the mode shape, normalized by (4.18). The pressure and the temperature modes are zero on the stress-free boundaries and have antinodes in the middle of the channel. Since the walls are adiabatic, the thermal boundary layer is absent and the pressure and temperature gradients are tangential to the boundaries. The velocity magnitude is highest near the nozzle, as shown in figure 4.11, where the viscous boundary layers overlap. The decay rate production is shown in Fig. 4.12. It is concentrated in the nozzle region of the initial printhead configuration, in the viscous boundary layers along the no slip walls, and around the corners.

The parametric optimality coefficient (4.11) for the initial printhead design is $\alpha_p = 0.017$, which implies that the decay rate and the viscous dissipation gradient

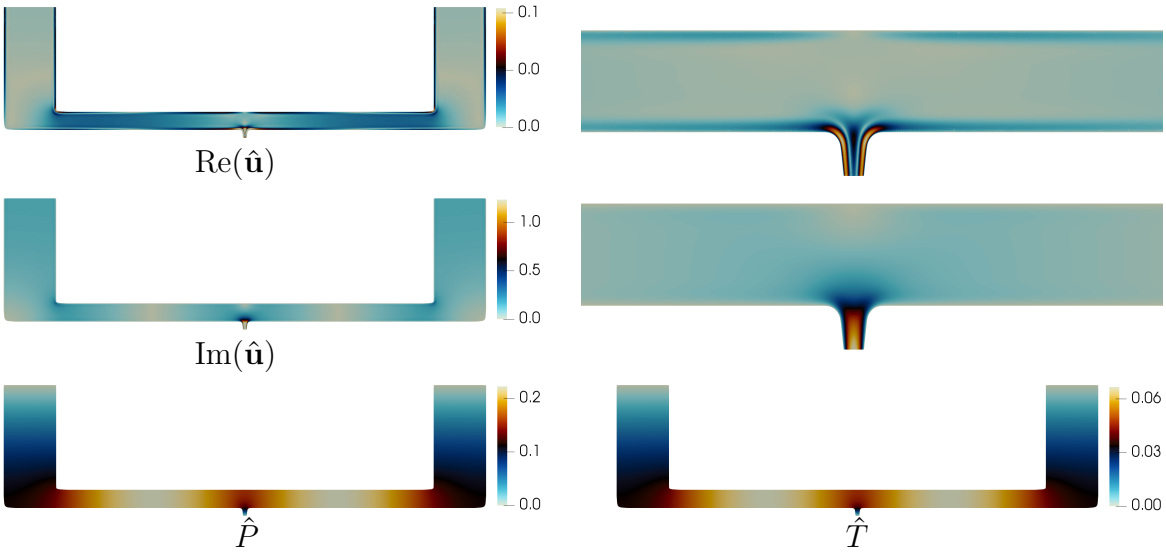

Fig. 4.11 The first natural mode of the oscillating flow in the initial printhead geometry at $\tilde{Re} = 6000$. From top to bottom: the magnitude of the velocity mode real part $\mathrm{Re}(\hat{\mathbf{u}})$ in the entire domain (left) and near the nozzle (right), the velocity mode imaginary part $\mathrm{Im}(\hat{\mathbf{u}})$, and pressure $\hat{P}$ (bottom left) and temperature $\hat{T}$ (bottom right) mode shapes.

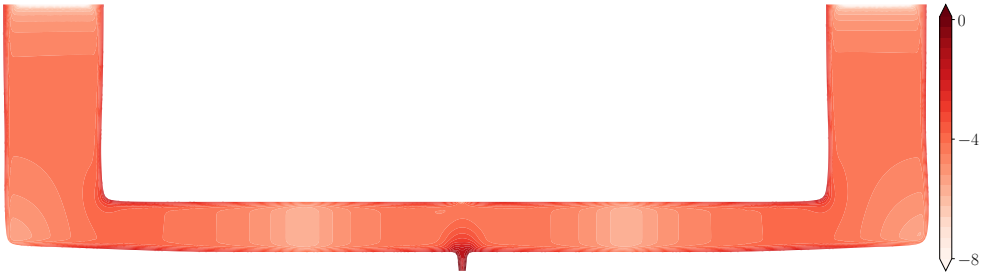

Fig. 4.12 Spatial distribution of the decay rate production in the initial printhead channel (on a logarithmic scale), $\log_{10}(-\sigma_\Omega)$.

vectors are almost orthogonal. Therefore we expect to be able to obtain a noticeable improvement in the objective function.

4.4.2 Optimization

In this section we use the optimization algorithm in section 4.3.2 to update the control points until the relative improvement falls below the tolerance level of $\varepsilon_p \leq 0.1$. The geometry is parameterized by three third-order B-splines, and 53 control points $\left\{a^k \in \mathbb{R}^2 \mid k = 1 \dots 53\right\}$. We impose geometric constraints: the piezoelectric actuator

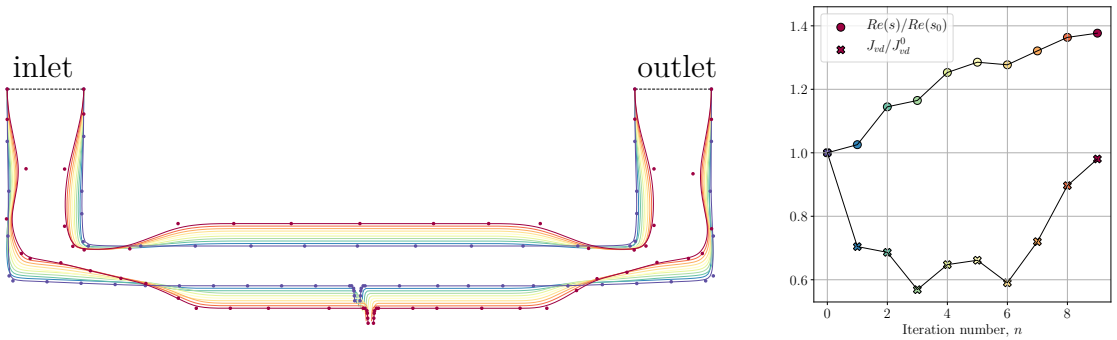

(a) (b)

Fig. 4.13 (a) The initial (violet lines) and the optimized (red lines) printhead geometry, and the B-spline control points. The intermediate geometries are in colour. The inlet and the outlet boundaries (dashed) remain fixed. The piezoelectric membrane and nozzle parts can move up and down but cannot change shape. (b) Normalized values of the objective function $\mathrm{Re}(s)$ and the constraint (viscous dissipation) during 2D printhead microchannel shape optimization.

membrane ($L_{\mathrm{act}} = 800\mu\mathrm{m}$) and the nozzle can move but cannot change shape, and the inlet and outlet boundaries remain fixed, the distance between the bottom channel walls and the tip of the nozzle in the vertical direction cannot be less than that of the initial domain, and the boundaries are C^2 smooth. We account for the geometric constraints and convert the initial 63 controls in $\mathbb{R}^2$ into 96 parameters in $\mathbb{R}$.

The optimized domain is shown in figure 4.13a. The channel constricts near the corners of the top boundary, where the decay rate production had a local maximum. These constrictions increase the steady flow viscous dissipation there, but the central part of the channel expands to compensate. The optimized shape of the channel is not symmetric, and the nozzle shifts slightly towards the outlet. The new frequency of the first natural mode is $\mathrm{Im}(s_1/2\pi) = \omega/2\pi = 0.266$ MHz, and the decay rate increases to $\mathrm{Re}(s_1/2\pi) = \sigma/2\pi = 0.0262$ MHz, which is almost 40% higher than before. The steady flow viscous dissipation is the same as in the initial printhead. The parametric optimality coefficient (4.11) of the optimized shape is $\alpha_p = -0.94$, showing that it is nearly optimal. Figure 4.13b shows the normalized objective and constraint values at intermediate iterations (the colours denote the same steps as in figure 4.13a).

Figure 4.14 shows the spatial distribution of the decay rate production $\log_{10}(-\sigma_\Omega)$ inside the optimized domain. The viscous boundary layers overlap in the narrow parts of the channel, resulting in higher acoustic energy dissipation there. The highest amplitudes of decay rate production are around the nozzle. This shows that changes to the nozzle geometry are particularly influential.

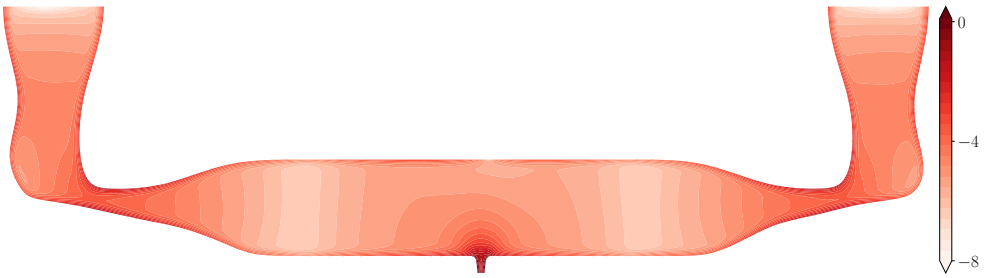

Fig. 4.14 Spatial distribution of the decay rate production in the optimized printhead channel (on a logarithmic scale), $\log_{10}(-\sigma_\Omega)$.

4.5 Concluding remarks

In this chapter we perform constrained gradient-based shape optimization of a microchannel in an inkjet printhead microchannel. We then seek to control two objective functions by changing the shape of the boundaries: viscous dissipation of the incompressible steady mean flow, and the decay rate of the thermoviscous acoustic flow. We obtain expressions for the derivatives of the above objective functions with respect to boundary deformations in Hadamard form by deriving the adjoint equations for both flows.

These equations are general and could be used in many ways. We start by showing how they can be combined with an optimization algorithm in order to increase the viscous and thermal dissipation of oscillations in a channel without changing the viscous dissipation of the steady flow in the channel. This works by constricting the channel where the acoustic velocity is largest and enlarging the channel where the acoustic velocity is smallest. This result is straight-forward and could have been obtained using physical intuition.

We then apply this technique to the same problem in a 2D generic inkjet printhead microchannel. The 2D simulations under-estimate the dissipation because they have two sides, rather than four, but they capture the major shape changes required in both the 2-D and 3-D cases. The printhead manufacturer would like to increase the decay rate of residual oscillations after a drop has been ejected, without changing the pressure drop required to continually flush ink through the head. Starting from a generic design and incorporating constraints such as the sizes of the nozzle and piezo-electric actuator, the algorithm converges to a design with a 40% larger decay rate, but the same pressure drop, which we show to be nearly optimal. The final shape is not straight-forward and would have been difficult to achieve through physical insight or trial and error. It

could be improved further by adapting the parameters that describe the shape, but in this case the improvement would be small.

Chapter 5

Conclusions and future work

5.1 Conclusions

In this thesis the flow inside an inkjet printhead microchannel is studied using the thermoviscous acoustic equations and a reduced order model for the flow in the inkjet nozzle. Adjoint methods are developed to evaluate the sensitivity of various energy objectives with respect to control parameters. For the unsteady simulation, the sensitivity of the total energy of the system with respect to the boundary forcing is obtained. A method to calculate shape sensitivities of the thermoviscous acoustic flow eigenvalues is presented. The gradient information is then used as an input to optimization algorithms to damp the residual reverberations after a droplet is ejected. Successive application of these methods to practical devices will lead to higher temporal resolution and more repeatable droplets.

Chapter 2 concerns the flow models and numerical methods for the unsteady and frequency domain simulations, and solving the eigenvalue problems. The printhead microchannel is split into the non-overlapping channel and nozzle domains, such that the two domains are considered separately and, when analysed numerically, discretized independently. Using the low Mach number asymptotic analysis, the compressible Navier–Stokes equations of the channel flow are separated into equations for a slowly varying incompressible flow and equations for acoustic oscillations with no mean flow. The main requirements are that the steady flow Mach number and oscillating flow Mach number are small, which are often satisfied in microfluidics, so the model in this chapter could be applied to many other applications. The flow in the nozzle domain is given by a reduced order model that accounts for energy conservation and dissipation, and approximates the free surface between the fluid (ink) and the outside gas by a spherical cap with uniform curvature. We discuss the numerical discretization and implement

the flow solvers using the finite element method. We analyse the spectrum and the frequency response of the thermoviscous acoustic flow inside a 2D inkjet printhead microchannel, coupled to the reduced order model nozzle flow that is represented by a nonlinear impedance boundary condition.

Inkjet printhead manufacturers would like to reduce the time between droplet ejections by eliminating residual acoustic reverberations. They currently eliminate these reverberations by deforming the piezo-element as in chapter 3, but find the optimal waveform through trial and error on extensive experimental campaigns. We demonstrate the success of a more systematic approach: adjoint-based optimization of the waveform using numerical simulations. Temporal and spatial waveform shape parameterization is inspired by the limitations of the driving electronics and response of the piezo-electric actuator in practical devices. For a number of test cases, an unconstrained optimization problem is solved to find an optimal waveform. We show that, if this stabilization method is to be used, the minimum time between drops is the sum of the waveform duration and the time taken for an acoustic wave to travel from the nozzle to the manifold boundary and back. Further, it reveals the mechanisms that are exploited. At a minimum, this physical understanding is useful in narrowing down the range of waveforms tested experimentally by trial and error. At best, this technique shows how to use numerical simulations in order to systematically and efficiently find the optimal waveform and the minimum time between drops in inkjet print heads.

In Chapter 4 we derive and demonstrate a new way to optimize the shapes of narrow channels that contain thermoviscous oscillating flows with (or without) steady flow. The efficiency of the inkjet devices depends on the natural frequency and the decay rate of the thermoviscous acoustic oscillations. Manufacturers would like to damp the residual reverberations, without increasing the pressure drop required to drive the steady flow. The discussed 2D optimization process changes the height of the inkjet channel, increasing this dissipation in influential areas. The main novelty is the cheap and accurate calculation of the shape gradients, using adjoint methods, which allows optimization with gradient-based algorithms. This is useful in two complementary ways. Firstly, these algorithms quickly converge to shapes that a human designer, using physical insight and trial and error, would probably not consider. Secondly, the adjoint methods provide physical insight into the mechanisms that influence the objective functions. It can be then used to alter the choice of shape parameters if it becomes apparent that the algorithm is missing a good shape due to a bad choice of shape parameters. The method is general and could be applied to many different applications in microfluidics. Its main requirements are that the steady flow Mach number and

oscillating flow Mach number are small, and that dissipation is dominated by viscous mechanisms.

5.2 Future work

Over the past several years, many open source simulation and automatic differentiation tools have been developed and became available to the research community. Discontinuous Galerkin finite element solver for the compressible Navier–Stokes equations implemented by Houston and Sime (2018) can be considered as replacement for the thermoviscous acoustic solver discussed in chapter 2. Manual derivation, implementation and testing of adjoint models for optimization problems is a great learning tool, and encourages the use of physical knowledge to simplify a problem. In some cases the manual approach might be challenging and not robust. `dolfin-adjoint` (Mitusch et al., 2019) automatically derives adjoint models for problems formulated in FEniCS, including time-dependent PDEs with Dirichlet boundary conditions. In future, algorithmic differentiation tools should be considered to obtain the sensitivity information.

There are three directions for future work: (i) further development and experimental validation of the numerical models taking into account the industry performance and accuracy metrics; (ii) designing new objective functions and respective adjoint methods for specific inkjet system configurations; (iii) development of ad-hoc optimization algorithms, and applying the optimization results in production.

Improved modelling of the printhead microchannel flow

Possible improvements to the models of the channel and nozzle flows are discussed in section 2.7.1. The main step forward, although very challenging, is to implement a droplet formation model for which the adjoint counterpart can be derived. This would allow us to apply the developed control methods to all stages of the inkjet process, not only to the residual reverberations control. It could be possible to utilize the data-driven approach to build an accurate reduced-order droplet model using data assimilation from automated experimental setups (Yu et al., 2021).

Another extension, which is particularly relevant to inkjet printing, is to consider non-Newtonian fluids (McIlroy et al., 2013). Although these are challenging to model, it should be relatively straight-forward to develop adjoints of these models.

Shape optimization

This thesis demonstrates computationally efficient and physically interpretable methods to calculate the shape sensitivity of the acoustic flow eigenvalues and use the gradient information in paramter-based shape optimization. Now that the technique has been proven on a 2D geometry, the desirable next step is to apply it to 3D geometries and with the large number of extra shape parameters that this will entail. For the adjoint methods and optimization algorithms, the extension from 2D to 3D is straightforward. For the shape parametrization, this extension is usually harder. In this case, however, the manufacturable 3D shapes of inkjet print heads are severely constrained because they are etched into silicon wafers. Similar constraints apply to many microfluidic applications. These constraints, which require geometries to be close to 2D, both render the 2D analysis more relevant and make the 3D shape parametrization more simple.

The printhead channel shape optimization (section 4.4) concerns the shape of the channel but not the nozzle shape. We envisage that optimizing the shape of the nozzle in addition to the channel shape could enhance the droplet size controllability and the printing speed. It should be reasonably straightforward to extend the adjoint-based eigenvalue shape sensitivity method to the unsteady problem, and even combine the unsteady waveform optimization with the nozzle shape optimization.

It would be interesting to investigate the existing tolerance criteria of printhead channels manufacturing, and predict receptivity of the acoustic flow to surface roughness using the present sensitivity calculation methods. If this reveals a possibility to control roughness or the thermal conductivity of the channel wall to damp the residual reverberations without affecting the droplet ejection, this would be yet another mechanism to passively improve the inkjet performance. We note, however, that thermal dissipation becomes less influential as the heat capacity ratio decreases towards 1.

Waveform optimization

Waveform parametrization. In section 3.2 we assumed that the electric signal that forces the piezo-electric actuator is translated into a piecewise linear actuator velocity profile with a fixed temporal resolution. Instead, one-dimensional B-splines seem to be a more robust and less constrained choice. The first step would be to develop a model of the piezo actuator's deformation as a function of the applied electric voltage in order to match exactly the actuator control used in industry. Then, a new waveform parametrization can be deduced.

With regards to the spatial parametrization, only uniform actuator deformations have been considered. Deformation profiles corresponding to other piezoelectric actuation modes can be incorporated with little effort. A small research project can be suggested to adapt the existing tools to investigate the efficacy of an array of independent actuators (in contrast to a single one): a technique similar to that used in acoustic ink printing (Hadimioglu et al., 1992).

Waveform optimization for the droplet ejection. The same method could also be used to perform waveform optimization for the droplet ejection, in order to control the droplet volume and momentum. This would require a new differentiable nozzle model (for example, a one-dimensional drop formation model (Driessen and Jeurissen, 2016)) and a new differentiable objective function (a combination of the droplet volume at pinchoff and the residual energy of the system), but the channel model and optimization method would remain the same.

Cross-talk minimization. The waveform optimization method discussed in this study can be applied to minimize cross-talk effects. This can be done by either a one-way or a two-way coupling method. In the one-way coupled case, the droplet ejection in the first (active) channel perturbs the flow in the second (idle) neighboring channel via the external boundary forcing. A residual control actuation pulse in the second channel has to damp those oscillations before the main pulse is applied in the second channel. This does not require direct modelling of multiple channels operating simultaneously. Instead, the flow in the first channel and the external forcing can be calculated first, and used as an input to the waveform optimization problem in the second channel. In the two-way coupled case, the flow in the second channel induces a secondary cross-talk and affects the droplet ejection of the first channel. This would require simultaneous modelling of multiple inkjet channels.

Finally, alternative optimization methods (Riedmiller and Braun, 1993; Rojas-Labanda and Stolpe, 2015) can be explored for both waveform and shape optimization. This includes applying global search in the parameter space prior to performing any local gradient-based optimization.

References

Adams, R. L. and Roy, J. (1986). A one-dimensional numerical model of a drop-on-demand ink jet. *Journal of Applied Mechanics*, 53(1):193–197.

Aguilar, J. G. and Juniper, M. P. (2020). Thermoacoustic stabilization of a longitudinal combustor using adjoint methods. *Physical Review Fluids*, 5:083902.

Alazard, T. (2008). A minicourse on the low mach number limit. *Discrete and Continuous Dynamical Systems-Series S*, 1(3):365–404.

Alnæs, M., Blechta, J., Hake, J., Johansson, A., Kehlet, B., Logg, A., Richardson, C., Ring, J., Rognes, M. E., and Wells, G. N. (2015). The fenics project version 1.5. *Archive of Numerical Software*, 3(100).

Alnæs, M. S., Logg, A., Ølgaard, K. B., Rognes, M. E., and Wells, G. N. (2014). Unified form language: A domain-specific language for weak formulations of partial differential equations. *ACM Trans. Math. Softw.*, 40(2).

Andreev, A. B. and Racheva, M. R. (2007). Superconvergent finite element postprocessing for eigenvalue problems with nonlocal boundary conditions. In *International Conference on Large-Scale Scientific Computing*, pages 645–653. Springer.

Apel, T. and Flaig, T. (2012). Crank–nicolson schemes for optimal control problems with evolution equations. *SIAM Journal on Numerical Analysis*, 50(3):1484–1512.

Badie, R. and Dirk Frits, d. L. (1997). Mechanism of drop constriction in a drop-on-demand inkjet system. *Proceedings of the Royal Society of London. Series A: Mathematical, Physical and Engineering Sciences*, 453(1967):2573–2581.

Bangerth, W., Geiger, M., and Rannacher, R. (2010). Adaptive galerkin finite element methods for the wave equation. *Computational Methods in Applied Mathematics*, 10(1):3–48.

Bängtsson, E., Noreland, D., and Berggren, M. (2003). Shape optimization of an acoustic horn. *Computer methods in applied mechanics and engineering*, 192(11-12):1533–1571.

Basaran, O. A., Gao, H., and Bhat, P. P. (2013). Nonstandard inkjets. *Annual Review of Fluid Mechanics*, 45:85–113.

Batchelor, G. K. (2000). *An Introduction to Fluid Dynamics*. Cambridge Mathematical Library. Cambridge University Press.

Beasley, J. (1977). Model for fluid ejection and refill in an impulse drive jet. *Journal of applied photographic engineering*, 3:78–82.

Beltman, W. (1999a). Viscothermal wave propagation including acousto-elastic interaction, part II: Applications. *Journal of Sound and Vibration*, 227(3):587–609.

Beltman, W. M. (1998). *Viscothermal wave propagation including acousto-elastic interaction*. PhD thesis, University of Twente.

Beltman, W. M. (1999b). Viscothermal wave propagation including acousto-elastic interaction, part I: theory. *Journal of Sound and Vibration*, 227(3):555–586.

Bendsoe, M. P. and Sigmund, O. (2013). *Topology optimization: theory, methods, and applications*. Springer Science & Business Media.

Berggren, M., Bernland, A., and Noreland, D. (2018). Acoustic boundary layers as boundary conditions. *Journal of Computational Physics*, 371:633 – 650.

Beurer, G. and Kretschmer, J. (1997). Function and performance of a shear mode piezo printhead. In *Proc. IS&T's NIP*, volume 13, pages 621–625.

Blauth, S. (2021). cashocs: A computational, adjoint-based shape optimization and optimal control software. *SoftwareX*, 13:100646.

Bogy, D. (1979). Drop formation in a circular liquid jet. *Annual Review of Fluid Mechanics*, 11(1):207–228.

Bogy, D. B. and Talke, F. E. (1984). Experimental and theoretical study of wave propagation phenomena in drop-on-demand ink jet devices. *IBM Journal of research and development*, 28(3):314–321.

Bossart, R., Joly, N., and Bruneau, M. (2003). Hybrid numerical and analytical solutions for acoustic boundary problems in thermo-viscous fluids. *Journal of Sound and Vibration*, 263(1):69–84.

Bradbury, J., Frostig, R., Hawkins, P., Johnson, M. J., Leary, C., Maclaurin, D., and Wanderman-Milne, S. (2018). JAX: composable transformations of Python+NumPy programs.

Brereton, G. J. and Jiang, Y. (2005). Exact solutions for some fully developed laminar pipe flows undergoing arbitrary unsteadiness. *Physics of Fluids*, 17(11):118104.

Brewster, J. (2020). *Shape Optimisation for Hydrodynamic Stability and its Application to Cyclone Separators*. PhD thesis, University of Cambridge.

Brewster, J. and Juniper, M. P. (2020). Shape sensitivity of eigenvalues in hydrodynamic stability, with physical interpretation for the flow around a cylinder. *European Journal of Mechanics-B/Fluids*, 80:80–91.

Brünahl, J. and Grishin, A. M. (2002). Piezoelectric shear mode drop-on-demand inkjet actuator. *Sensors and Actuators A: Physical*, 101(3):371–382.

Carslaw, H. S. and Jaeger, J. C. (1986). *Conduction of Heat in Solids*. Oxford science publications. Clarendon Press.

Chen, A. U. and Basaran, O. A. (2002). A new method for significantly reducing drop radius without reducing nozzle radius in drop-on-demand drop production. *Physics of fluids*, 14(1):L1–L4.

Christensen, R. (2011). Modeling the effects of viscosity and thermal conduction on acoustic propagation in rigid tubes with various cross-sectional shapes. *Acta Acustica united with Acustica*, 97(2):193–201.

Chu, B. T. (1965). On the energy transfer to small disturbances in fluid flow (part I). *Acta Mechanica*, 1(3):215—-234.

Cossu, C. (2014). An introduction to optimal controllecture notes from the flow-nordita summer school on advanced instability methods for complex flows. *Applied Mechanics Reviews*, 66(2).

Crankshaw, M., Rulman, M., Zarezadeh, H., Douaire, M., and Condie, A. (2016). Ink recirculation—xaar tf technology™: A study of the benefits. In *NIP & Digital Fabrication Conference*, number 1, pages 207–211. Society for Imaging Science and Technology.

Culick, F., Heitor, M. V., and Whitelaw, J. H. (2012). *Unsteady combustion*, volume 306. Springer Science & Business Media.

Dalcin, L. D., Paz, R. R., Kler, P. A., and Cosimo, A. (2011). Parallel distributed computing using python. *Advances in Water Resources*, 34(9):1124–1139.

de Jong, J., Jeurissen, R., Borel, H., van den Berg, M., Wijshoff, H., Reinten, H., Versluis, M., Prosperetti, A., and Lohse, D. (2006). Entrapped air bubbles in piezo-driven inkjet printing: Their effect on the droplet velocity. *Physics of Fluids*, 18(12):121511.

De Schepper, H. and Van Keer, R. (1997). On a finite element method for second order elliptic eigenvalue problems with nonlocal direchlet boundary conditions. *Numerical Functional Analysis and Optimization*, 18(3-4):283–295.

Delfour, M. and Zolésio, J. (2011). *Shapes and Geometries*. Society for Industrial and Applied Mathematics, second edition.

Derby, B. (2010). Inkjet printing of functional and structural materials: fluid property requirements, feature stability, and resolution. *Annual Review of Materials Research*, 40:395–414.

Dijksman, J. (1984). Hydrodynamics of small tubular pumps. *Journal of Fluid Mechanics*, 139:173–191.

Dijksman, J. F. (2019). *Design of Piezo Inkjet Print Heads: From Acoustics to Applications*. John Wiley & Sons.

Dokken, J. S., Mitusch, S. K., and Funke, S. W. (2020). Automatic shape derivatives for transient PDEs in FEniCS and Firedrake. *arXiv preprint arXiv:2001.10058*.

Donahue, M. J., Sanchez-Sanchez, A., Inal, S., Qu, J., Owens, R. M., Mecerreyes, D., Malliaras, G. G., and Martin, D. C. (2020). Tailoring pedot properties for applications in bioelectronics. *Materials Science and Engineering: R: Reports*, 140:100546.

Donea, J., Huerta, A., Ponthot, J.-P., and Rodríguez-Ferran, A. (2017). Arbitrary lagrangian–eulerian methods. *Encyclopedia of Computational Mechanics Second Edition*, pages 1–23.

Driessen, T. and Jeurissen, R. (2011). A regularised one-dimensional drop formation and coalescence model using a total variation diminishing (tvd) scheme on a single eulerian grid. *International journal of computational fluid dynamics*, 25(6):333–343.

Driessen, T. and Jeurissen, R. (2016). Drop formation in inkjet printing. *Fundamentals of Inkjet Printing*, pages 93–115.

Eggers, J. and Dupont, T. F. (1994). Drop formation in a one-dimensional approximation of the navier–stokes equation. *Journal of fluid mechanics*, 262:205–221.

Eggers, J. and Villermaux, E. (2008). Physics of liquid jets. *Reports on progress in physics*, 71(3):036601.

Eggl, M. F. and Schmid, P. J. (2020). Shape optimization of stirring rods for mixing binary fluids. *IMA Journal of Applied Mathematics*, 85(5):762–789.

Estep, D. (2004). A short course on duality, adjoint operators, green's functions, and a posteriori error analysis. *Lecture Notes*.

Ezzeldin, M., Van Den Bosch, P., Jokic, A., and Waarsing, R. (2010). Model-free optimization based feedforward control for an inkjet printhead. In *2010 IEEE International Conference on Control Applications*, pages 967–972. IEEE.

Fraters, A., van den Berg, M., de Loore, Y., Reinten, H., Wijshoff, H., Lohse, D., Versluis, M., and Segers, T. (2019). Inkjet nozzle failure by heterogeneous nucleation: Bubble entrainment, cavitation, and diffusive growth. *Physical review applied*, 12(6):064019.

Fraysse, F., Valero, E., and Ponsín, J. (2012). Comparison of mesh adaptation using the adjoint methodology and truncation error estimates. *AIAA journal*, 50(9):1920–1932.

Fumagalli, I., Parolini, N., and Verani, M. (2018). On a free-surface problem with moving contact line: From variational principles to stable numerical approximations. *Journal of Computational Physics*, 355:253 – 284.

Furbank, R. J. and Morris, J. F. (2004). An experimental study of particle effects on drop formation. *Physics of Fluids*, 16(5):1777–1790.

Galusinski, C. and Vigneaux, P. (2008a). On stability condition for bifluid flows with surface tension: Application to microfluidics. *Journal of Computational Physics*, 227(12):6140 – 6164.

Galusinski, C. and Vigneaux, P. (2008b). On stability condition for bifluid flows with surface tension: Application to microfluidics. *Journal of Computational Physics*, 227(12):6140–6164.

Gan, H., Shan, X., Eriksson, T., Lok, B., and Lam, Y. (2009). Reduction of droplet volume by controlling actuating waveforms in inkjet printing for micro-pattern formation. *Journal of micromechanics and microengineering*, 19(5):055010.

Gautschi, G. (2002). Piezoelectric sensors. In *Piezoelectric Sensorics*, pages 73–91. Springer.

Gerbeau, J.-F., Lelièvre, T., and Le Bris, C. (2003). Simulations of mhd flows with moving interfaces. *Journal of Computational Physics*, 184(1):163–191.

Gersborg-Hansen, A., Sigmund, O., and Haber, R. B. (2005). Topology optimization of channel flow problems. *Structural and multidisciplinary optimization*, 30(3):181–192.

Geuzaine, C. and Remacle, J.-F. (2009). Gmsh: A 3-d finite element mesh generator with built-in pre-and post-processing facilities. *International journal for numerical methods in engineering*, 79(11):1309–1331.

Grinfeld, P. (2010). Hadamard's formula inside and out. *Journal of optimization theory and applications*, 146(3):654–690.

Groenendaal, L., Jonas, F., Freitag, D., Pielartzik, H., and Reynolds, J. R. (2000). Poly (3, 4-ethylenedioxythiophene) and its derivatives: past, present, and future. *Advanced materials*, 12(7):481–494.

Gunzburger, M. (2002). *Perspectives in Flow Control and Optimization*. Society for Industrial and Applied Mathematics.

Gunzburger, M. and Manservisi, S. (2000). Analysis and approximation for linear feedback control for tracking the velocity in navier–stokes flows. *Computer methods in applied mechanics and engineering*, 189(3):803–823.

Hadimioglu, B., Elrod, S., Steinmetz, D., Lim, M., Zesch, J., Khuri-Yakub, B., Rawson, E., and Quate, C. (1992). Acoustic ink printing. In *IEEE 1992 Ultrasonics Symposium Proceedings*, pages 929–935. IEEE.

He, M.-w., Sun, L.-l., Hu, K.-y., Zhu, Y.-l., and Chen, H.-n. (2015). Analysis of dod inkjet printhead performance for printable electronics fabrication using dynamic lumped element modeling and swarm intelligence based optimal prediction. *Journal of Central South University*, 22(10):3925–3934.

Hernandez, V., Roman, J. E., and Vidal, V. (2005). SLEPc: A scalable and flexible toolkit for the solution of eigenvalue problems. *ACM Trans. Math. Software*, 31(3):351–362.

Herran, L. (2013). *Jet Instability and Droplet Formation for Bio-Printing Applications*. PhD thesis, Clemson University.

Hinze, M. (2000). *Optimal and instantaneous control of the instationary Navier-Stokes equations*. PhD thesis, Technische Universitat Dresden.

Hirt, C. W. and Nichols, B. D. (1981). Volume of fluid (vof) method for the dynamics of free boundaries. *Journal of computational physics*, 39(1):201–225.

Hoath, S. D., Hsiao, W.-K., Martin, G. D., Jung, S., Butler, S. A., Morrison, N. F., Harlen, O. G., Yang, L. S., Bain, C. D., and Hutchings, I. M. (2015). Oscillations of aqueous pedot: Pss fluid droplets and the properties of complex fluids in drop-on-demand inkjet printing. *Journal of Non-Newtonian Fluid Mechanics*, 223:28–36.

Hoath, S. D. E. (2016). *Fundamentals of Inkjet Printing*. Wiley-VCH Verlag GmbH & Co. KGaA.

Houston, P. and Sime, N. (2018). Automatic symbolic computation for discontinuous galerkin finite element methods. *SIAM Journal on Scientific Computing*, 40(3):C327–C357.

Hsiao, W.-K., Hoath, S. D., Martin, G. D., and Hutchings, I. M. (2011). Jetting, in-nozzle meniscus motion and nozzle-plate flooding in an industrial drop-on-demand print head. In *NIP & Digital Fabrication Conference*, number 1, pages 66–69. Society for Imaging Science and Technology.

Hunter, J. K. (2004). Asymptotic analysis and singular perturbation theory. *Department of Mathematics, University of California at Davis*, pages 1–3.

Jameson, A. and Martinelli, L. (2000). Aerodynamic shape optimization techniques based on control theory. In *Computational Mathematics Driven by Industrial Problems*, pages 151–221. Springer.

Jeurissen, R. J. M. (2009). *Bubbles in inkjet printheads: analytical and numerical models*. PhD thesis, University of Twente.

Jiang, H. and Tan, H. (2018). One dimensional model for droplet ejection process in inkjet devices. *Fluids*, 3(2):28.

Jo, B. W., Lee, A., Ahn, K. H., and Lee, S. J. (2009). Evaluation of jet performance in drop-on-demand (dod) inkjet printing. *Korean Journal of Chemical Engineering*, 26(2):339–348.

Joly, N. (2010). Finite element modeling of thermoviscous acoustics on adapted anisotropic meshes: Implementation of the particle velocity and temperature variation formulation. *Acta acustica united with acustica*, 96(1):102–114.

Jones, E., Oliphant, T., Peterson, P., et al. (2001–2020). SciPy: Open source scientific tools for Python.

Juniper, M. P. (2011). Triggering in the horizontal rijke tube: non-normality, transient growth and bypass transition. *Journal of Fluid Mechanics*, 667:272.

Kampinga, W., Wijnant, Y. H., and de Boer, A. (2010). Performance of several viscothermal acoustic finite elements. *Acta acustica united with Acustica*, 96(1):115–124.

Kampinga, W., Wijnant, Y. H., and de Boer, A. (2011). An efficient finite element model for viscothermal acoustics. *Acta Acustica united with Acustica*, 97(4):618–631.

Kast, S. M. (2016). *Methods for Optimal Output Prediction in Computational Fluid Dynamics.* PhD thesis, University of Michigan.

Kell, G. S. (1970). Isothermal compressibility of liquid water at 1 atm. *Journal of Chemical and Engineering Data*, 15(1):119–122.

Kerswell, R. (2018). Nonlinear nonmodal stability theory. *Annual Review of Fluid Mechanics*, 50:319–345.

Khalate, A. A., Bombois, X., Babuška, R., Wijshoff, H., and Waarsing, R. (2011). Performance improvement of a drop-on-demand inkjet printhead using an optimization-based feedforward control method. *Control Engineering Practice*, 19(8):771–781.

Khalate, A. A., Bombois, X., Ye, S., Babuška, R., and Koekebakker, S. (2012). Minimization of cross-talk in a piezo inkjet printhead based on system identification and feedforward control. *Journal of Micromechanics and Microengineering*, 22(11):115035.

Kiendl, J., Schmidt, R., Wüchner, R., and Bletzinger, K.-U. (2014). Isogeometric shape optimization of shells using semi-analytical sensitivity analysis and sensitivity weighting. *Computer Methods in Applied Mechanics and Engineering*, 274:148–167.

Kierkegaard, A., Boij, S., and Efraimsson, G. (2010). A frequency domain linearized navier–stokes equations approach to acoustic propagation in flow ducts with sharp edges. *The Journal of the Acoustical Society of America*, 127(2):710–719.

Kim, B.-H., Lee, H.-S., Kim, S.-W., Kang, P., and Park, Y.-S. (2014). Hydrodynamic responses of a piezoelectric driven mems inkjet print-head. *Sensors and Actuators A: Physical*, 210:131–140.

Kim, S. H., Kang, H., Kang, K., Lee, S. H., Cho, K. H., and Hwang, J. Y. (2018). Effect of meniscus damping ratio on drop-on-demand electrohydrodynamic jetting. *Applied Sciences*, 8(2):164.

Kirby, R. C. and Logg, A. (2006). A compiler for variational forms. *ACM Trans. Math. Softw.*, 32(3):417–444.

Knol, H. (2017). Knol-edge: Q6. inkjet nozzle plates. https://insights.vecoprecision.com/knol-edge-q6.-inkjet-nozzle-plates. Last accessed on Aug 27, 2020.

Kretschmer, J. and Beurer, G. (1997). Design parameters of a shear mode piezo printhead for a given resolution. In *International conference on digital printing technologies*, pages 626–632. IS & T society for imaging science and technology.

Kungurtsev, P. V. (2020a). firecrest: an optimization tool for acoustic flows. https://github.com/Corwinpro/firecrest.

Kungurtsev, P. V. (2020b). Pysplines: automated generation of uniform rational b-splines and shape properties. https://github.com/Corwinpro/PySplines.

Kungurtsev, P. V. and Juniper, M. P. (2019). Adjoint-based shape optimization of the microchannels in an inkjet printhead. *Journal of Fluid Mechanics*, 871:113–138.

Kungurtsev, P. V. and Juniper, M. P. (2020). Adjoint-based optimization of the actuator velocity profile in an inkjet print head. *Journal of Fluid Mechanics*.

Kwon, K.-S. (2009). Waveform design methods for piezo inkjet dispensers based on measured meniscus motion. *Journal of Microelectromechanical Systems*, 18(5):1118–1125.

Landau, L. D. and Lifschitz, E. (1986). *Fluid mechanics*. Cambridge Mathematical Library. Nauka.

Laue, S. (2019). On the equivalence of forward mode automatic differentiation and symbolic differentiation. *arXiv preprint arXiv:1904.02990*.

Li, H., Liu, J., Li, K., and Liu, Y. (2019). Piezoelectric micro-jet devices: A review. *Sensors and Actuators A: Physical*, page 111552.

Lin, C.-K. (1995). On the incompressible limit of the compressible navier-stokes equations. *Communications in partial differential equations*, 20(3-4):677–707.

Liu, Y. and Derby, B. (2019). Experimental study of the parameters for stable drop-on-demand inkjet performance. *Physics of Fluids*, 31(3):032004.

Luchini, P. and Bottaro, A. (2014). Adjoint equations in stability analysis. *Annual Review of fluid mechanics*, 46.

Manservisi, S. and Scardovelli, R. (2009). A variational approach to the contact angle dynamics of spreading droplets. *Computers & fluids*, 38(2):406–424.

Marinis, T. (2009). The future of microelectromechanical systems (MEMS). *Strain*, 45(3):208–220.

McIlroy, C., Harlen, O., and Morrison, N. (2013). Modelling the jetting of dilute polymer solutions in drop-on-demand inkjet printing. *Journal of Non-Newtonian Fluid Mechanics*, 201:17 – 28.

Meurer, A., Smith, C. P., Paprocki, M., Čertík, O., Kirpichev, S. B., Rocklin, M., Kumar, A., Ivanov, S., Moore, J. K., Singh, S., Rathnayake, T., Vig, S., Granger, B. E., Muller, R. P., Bonazzi, F., Gupta, H., Vats, S., Johansson, F., Pedregosa, F., Curry, M. J., Terrel, A. R., Roučka, v., Saboo, A., Fernando, I., Kulal, S., Cimrman, R., and Scopatz, A. (2017). Sympy: symbolic computing in python. *PeerJ Computer Science*, 3:e103.

Miers, J. C. and Zhou, W. (2017). Droplet formation at megahertz frequency. *AIChE Journal*, 63(6):2367–2377.

Mitusch, S. K., Funke, S. W., and Dokken, J. S. (2019). dolfin-adjoint 2018.1: automated adjoints for FEniCS and Firedrake. *Journal of Open Source Software*, 4(38):1292.

Moser, M. (1980). Damping of structure-borne sound by the viscosity of a layer between 2 plates. *Acustica*, 46(2):210–217.

Müller, B. (1998). Low-Mach-number asymptotics of the Navier–Stokes equations. *Journal of Engineering Mathematics*, 34(1):97–109.

Myers, M. K. (1980). On the acoustic boundary condition in the presence of flow. *Journal of Sound and Vibration*, 71(3):429 – 434.

Nadarajah, S. and Jameson, A. (2000). A comparison of the continuous and discrete adjoint approach to automatic aerodynamic optimization. In *38th Aerospace Sciences Meeting and Exhibit*, page 667.

Ni, F. (2017). *Accounting for complex flow-acoustic interactions in a 3D thermo-acoustic Helmholtz solver*. PhD thesis, Institut National Polytechnique de Toulouse, Toulouse, France.

Nicoud, F., Benoit, L., Sensiau, C., and Poinsot, T. (2007). Acoustic modes in combustors with complex impedances and multidimensional active flames. *AIAA journal*, 45(2):426–441.

Parashkov, R., Becker, E., Riedl, T., Johannes, H.-H., and Kowalsky, W. (2005). Large area electronics using printing methods. *Proceedings of the IEEE*, 93(7):1321–1329.

Perez, R. E., Jansen, P. W., and Martins, J. R. (2012). pyopt: a python-based object-oriented framework for nonlinear constrained optimization. *Structural and Multidisciplinary Optimization*, 45(1):101–118.

Pierce, N. A. and Giles, M. B. (2000). Adjoint recovery of superconvergent functionals from pde approximations. *SIAM review*, 42(2):247–264.

Popinet, S. (2018). Numerical models of surface tension. *Annual Review of Fluid Mechanics*, 50(1):49–75.

Qian, T., Wang, X.-P., and Sheng, P. (2003). Generalized navier boundary condition for the moving contact line. *Communications in Mathematical Sciences*, 1(2):333–341.

Qian, T., Wang, X.-P., and Sheng, P. (2006). A variational approach to moving contact line hydrodynamics. *Journal of Fluid Mechanics*, 564:333–360.

Rayleigh, L. (1879). On the capillary phenomena of jets. *Proc. R. Soc. London*, 29(196-199):71–97.

Rehm, R. G., Baum, H. R., et al. (1978). The equations of motion for thermally driven, buoyant flows. *Journal of Research of the NBS*, 83(3):297–308.

Ren, W. and Weinan, E. (2007). Boundary conditions for the moving contact line problem. *Physics of fluids*, 19(2):022101.

Riedmiller, M. and Braun, H. (1993). A direct adaptive method for faster backpropagation learning: The rprop algorithm. In *IEEE international conference on neural networks*, pages 586–591. IEEE.

Rienstra, S. W. and Hirschberg, A. (2013). An introduction to acoustics. *Eindhoven University of Technology*, 18:19.

Rognes, M. E. and Logg, A. (2013). Automated goal-oriented error control i: Stationary variational problems. *SIAM Journal on Scientific Computing*, 35(3):C173–C193.

Rojas-Labanda, S. and Stolpe, M. (2015). Benchmarking optimization solvers for structural topology optimization. *Structural and Multidisciplinary Optimization*, 52(3):527–547.

Samareh, J. A. (2001). Survey of shape parameterization techniques for high-fidelity multidisciplinary shape optimization. *AIAA journal*, 39(5):877–884.

Schmid, P. J. and Brandt, L. (2014). Analysis of fluid systems: Stability, receptivity, sensitivitylecture notes from the flow-nordita summer school on advanced instability methods for complex flows, stockholm, sweden, 2013. *Applied Mechanics Reviews*, 66(2).

Schmidt, K. and Thöns-Zueva, A. (2019). Impedance boundary conditions for acoustic time harmonic wave propagation in viscous gases. *arXiv preprint arXiv:1905.08585*.

Schmidt, K., Thöns-Zueva, A., and Joly, P. (2014). High-order asymptotic expansion for the acoustics in viscous gases close to rigid walls. *Mathematical Models and Methods in Applied Sciences*, 24(09):1823–1855.

Schmidt, S. and Schulz, V. (2010). Shape derivatives for general objective functions and the incompressible navier-stokes equations. *Control and Cybernetics*, 39(3):677–713.

Schmidt, S., Wadbro, E., and Berggren, M. (2016). Large-scale three-dimensional acoustic horn optimization. *SIAM Journal on Scientific Computing*, 38(6):B917–B940.

Seccombe, D. e. a. (1997). Ink-cooled thermal inkjet printhead.

Shah, M. A., Lee, D.-G., and Hur, S. (2019). Design and characteristic analysis of a mems piezo-driven recirculating inkjet printhead using lumped element modeling. *Micromachines*, 10(11):757.

Shield, T., Bogy, D., and Talke, F. (1987). Drop formation by dod ink-jet nozzles: A comparison of experiment and numerical simulation. *IBM journal of research and development*, 31(1):96–110.

Shin, P., Lee, S., Sung, J., and Kim, J. H. (2011). Operability diagram of drop formation and its response to temperature variation in a piezoelectric inkjet nozzle. *Microelectronics Reliability*, 51(2):437–444.

Shore, H. J. and Harrison, G. M. (2005). The effect of added polymers on the formation of drops ejected from a nozzle. *Physics of Fluids*, 17(3):033104.

Smith, P. J. and Shin, D. H. (2012). *Inkjet-based micromanufacturing*. John Wiley & Sons.

Snoeijer, J. H. and Andreotti, B. (2013). Moving contact lines: scales, regimes, and dynamical transitions. *Annual review of fluid mechanics*, 45.

Snyder, B., Yang, M., Singhal, S., Abed, O., and Sreenivasan, S. (2019). Automated tuning of high-order waveforms for picoliter resolution jetting of rheologically challenging materials. *Precision Engineering*, 56:143–155.

Sokolowski, J. and Zolesio, J.-P. (1992). *Introduction to shape optimization*. Springer.

Sonntag, M., Schmidt, S., and Gauger, N. R. (2016). Shape derivatives for the compressible Navier–Stokes equations in variational form. *Journal of Computational and Applied Mathematics*, 296:334 – 351.

Spears, B. R., Marin, M. A., Chaker, A. N., Lampley, M. W., and Harth, E. (2016). Precise microscale polymeric networks through piezoelectronic inkjet printing. *Acs Biomaterials Science & Engineering*, 2(8):1265–1272.

Stachewicz, U., Dijksman, J. F., Burdinski, D., Yurteri, C. U., and Marijnissen, J. C. (2009). Relaxation times in single event electrospraying controlled by nozzle front surface modification. *Langmuir*, 25(4):2540–2549.

Strevens, A., Condie, A., and Crankshaw, M. (2020). What goes around, comes around: Why Xaar's TF Technology ink recirculation is still the best. https://www.xaar.com/media/2392/xaar-tf-technology-white-paper-eng2.pdf.

Svanberg, K. (1987). The method of moving asymptotes - a new method for structural optimization. *International Journal for Numerical Methods in Engineering*, 24(2):359–373.

Svanberg, K. (2002). A class of globally convergent optimization methods based on conservative convex separable approximations. *SIAM journal on optimization*, 12(2):555–573.

Ta-Tsien, L. (1989). A class of non-local boundary value problems for partial differential equations and its applications in numerical analysis. *Journal of computational and applied mathematics*, 28:49–62.

Tamura, H., Kadota, K., Shirakawa, Y., Tozuka, Y., Shimosaka, A., and Hidaka, J. (2014). Morphology control of amino acid particles in interfacial crystallization using inkjet nozzle. *Advanced Powder Technology*, 25(3):847–852.

Thomas, J. and Roe, P. (1993). Development of non-dissipative numerical schemes for computational aeroacoustics. In *11th Computational Fluid Dynamics Conference*, page 3382.

Thomas, J. W. (2013). *Numerical partial differential equations: finite difference methods*, volume 22. Springer Science & Business Media.

Tijdeman, H. (1975). On the propagation of sound waves in cylindrical tubes. *Journal of Sound and Vibration*, 39(1):1 – 33.

Timoshenko, S. P. and Woinowsky-Krieger, S. (1959). *Theory of plates and shells*. McGraw-hill.

Trefethen, L. N. (1996). *Finite difference and spectral methods for ordinary and partial differential equations*. Cornell University-Department of Computer Science and Center for Applied Mathematics.

van der Bos, A., van der Meulen, M.-J., Driessen, T., van den Berg, M., Reinten, H., Wijshoff, H., Versluis, M., and Lohse, D. (2014). Velocity profile inside piezoacoustic inkjet droplets in flight: comparison between experiment and numerical simulation. *Physical review applied*, 1(1):014004.

van der Meulen, M.-J., Reinten, H., Dijksman, F., Lohse, D., and Versluis, M. (2016). Experimental techniques for retrieving flow information from within inkjet nozzles. *Journal of imaging science and technology*, 60(4):40502–1.

Van Der Meulen, M.-J., Reinten, H., Wijshoff, H., Versluis, M., Lohse, D., and Steen, P. (2020). Nonaxisymmetric effects in drop-on-demand piezoacoustic inkjet printing. *Physical Review Applied*, 13(5):054071.

Voit, W., Jackson, N., Preckel, K., Iqbal, S., Reinhold, I., and Zapka, W. (2011). Evaluation of crosstalk effects in inkjet printing with xaar 1001. In *NIP & Digital Fabrication Conference*, number 1, pages 97–100. Society for Imaging Science and Technology.

Wang, C.-H., Tsai, H.-L., Wu, Y.-C., and Hwang, W.-S. (2016). Investigation of molten metal droplet deposition and solidification for 3d printing techniques. *Journal of Micromechanics and Microengineering*, 26(9):095012.

Wang, D.-P. and Millero, F. J. (1973). Precise representation of the p-v-t properties of water and seawater determined from sound speeds. *Journal of Geophysical Research*, 78(30):7122–7128.

Wang, Z.-P., Abdalla, M., and Turteltaub, S. (2017). Normalization approaches for the descent search direction in isogeometric shape optimization. *Computer-Aided Design*, 82:68–78.

Wassink, G. (2007). *Inkjet printhead performance enhancement by feedforward input design based on two-port modeling*. PhD thesis, Delft University of Technology.

Wijshoff, H. (2004). Free surface flow and acousto-elastic interaction in piezo inkjet. In *Proc. NSTI Nanotechnology Conf. and Trade Show*, volume 2, pages 215–218. Citeseer.

Wijshoff, H. (2010). The dynamics of the piezo inkjet printhead operation. *Physics reports*, 491(4-5):77–177.

Womersley, J. R. (1955). Method for the calculation of velocity, rate of flow and viscous drag in arteries when the pressure gradient is known. *The Journal of physiology*, 127(3):553.

Wu, H.-C., Lin, H.-J., Kuo, Y.-C., and Hwang, W.-S. (2004). Simulation of droplet ejection for a piezoelectric inkjet printing device. *Materials Transactions*, 45(3):893–899.

Xu, Q. and Basaran, O. A. (2007). Computational analysis of drop-on-demand drop formation. *Physics of Fluids*, 19(10):102111.

Yang, A.-S., Yang, J.-C., and Hong, M.-C. (2005). Droplet ejection study of a picojet printhead. *Journal of Micromechanics and Microengineering*, 16(1):180.

Yang, J., Kim, H., Cho, B., and Chung, J. (2014). Modeling of sessile droplet oscillation on electrohydrodynamic jetting nozzle at constant back pressure. *Journal of Mechanical Science and Technology*, 28(7):2815–2823.

Yu, H., Juniper, M. P., and Magri, L. (2021). A data-driven kinematic model of a ducted premixed flame. *Proceedings of the Combustion Institute*, 38(4):6231–6239.

Zahedi, S., Gustavsson, K., and Kreiss, G. (2009). A conservative level set method for contact line dynamics. *Journal of Computational Physics*, 228(17):6361–6375.

Zimmerman, A. G. and Kowalski, J. (2017). Monolithic simulation of convection-coupled phase-change: Verification and reproducibility. In *International Conference on Computational Engineering*, pages 177–197. Springer.

Appendix A

Technical tools

A.1 Testing the gradient consistency using the Taylor test

An optimization program that minimizes (or maximizes) an objective function using the gradient-based approach should verify the calculated gradient vector. This should be done prior to optimization to guarantee optimal convergence of the optimization algorithm. The first type of optimization programs compute the gradient function via the finite-difference approximation. In this case, the gradient is essentially another representation of the objective function, and does not provide any additional information itself. These programs can calculate the gradient value up to machine precision for sufficiently small input perturbation magnitude. The second type of optimization programs compute the gradient function via automated (Bradbury et al., 2018; Dokken et al., 2020; Mitusch et al., 2019) or symbolic differentiation, which are equivalent (Laue, 2019). These programs generate the gradient function as a separate entity, which is not necessarily consistent with the objective function. In this work, we have been discussing gradients calculation using the adjoint approach, which also falls into the second category.

We discuss the Taylor remainder convergence test: a robust approach to verify the correctness of the gradient calculated by the programs of the second type. We define the input parameters $\mathbf{x} \in \mathcal{X}$ and the objective function $F : \mathcal{X} \to \mathbb{R}$. Let $\delta\mathbf{x}$ be a perturbation to $\mathbf{x}$, and ϵ be the magnitude of the perturbation, such that

$$\|F(\mathbf{x} + \epsilon\delta\mathbf{x}) - F(\mathbf{x})\| = \mathcal{O}(\epsilon). \tag{A.1}$$

The exact objective gradient $\nabla F(\mathbf{x})$ together with the appropriate scalar product $(\cdot\ ,\ \cdot)$ computes the variation of the objective with respect to the parameters variation $\Delta_F : \mathcal{X} \times \mathcal{X} \to \mathbb{R}$:

$$\Delta_F(\cdot\ ,\ \cdot) = (\nabla F(\cdot)\ ,\ \cdot)\,.$$

While the exact gradient is usually unknown, the function $\hat{\nabla} F(\mathbf{x})$ provided by the automated differentiation or the adjoint method is used as the gradient approximation. The approximated objective variation is defined as $\hat{\Delta}_F(\cdot\ ,\ \cdot) = \left(\hat{\nabla} F(\cdot)\ ,\ \cdot\right)$.

We introduce the Taylor remainder $\mathbb{T}$, which has to be of order ϵ^2 if the gradient function $\hat{\nabla} F(\mathbf{x})$ is consistent with the objective:

$$\begin{aligned}\mathbb{T}(\mathbf{x}, \delta\mathbf{x}) &\equiv \left\| F(\mathbf{x} + \epsilon\delta\mathbf{x}) - F(\mathbf{x}) - \epsilon\left(\hat{\nabla} F(\mathbf{x})\,, \delta\mathbf{x}\right)\right\| \\ &= \epsilon\left\|(\nabla F(\mathbf{x})\,, \delta\mathbf{x}) - \left(\hat{\nabla} F(\mathbf{x})\,, \delta\mathbf{x}\right)\right\| \\ &= \epsilon\left(\Delta_F(\mathbf{x}, \delta\mathbf{x}) - \hat{\Delta}_F(\mathbf{x}, \delta\mathbf{x})\right) = \mathcal{O}\left(\epsilon^2\right).\end{aligned} \tag{A.2}$$

For sufficiently large ϵ, the Taylor remainder is of order ϵ^2 or higher even if the gradient is inconsistent, due to the higher order terms in the Taylor expansion of the objective function.

We can estimate the convergence order of the Taylor remainder, and prove the consistency of the objective-gradient pair by showing that it is greater than 2. If the convergence order is less than 2, the Taylor remainder $\mathbb{T}$ grows slower than ϵ^2, and therefore the gradient is incorrect (inconsistent with the objective function). Given a vector of input parameters $\mathbf{x}_0$, the algorithm 1 can be used to estimate the order of convergence. The Taylor remainder convergence test evaluates the objective function $N + 1$ times, and the gradient function is evaluated once. The initial perturbation magnitude ϵ can be rather large, but should satisfy (A.1). A heuristic approach is to set $N = 20$, given the algorithm's step reduction strategy.

A preliminary Taylor testing can be performed for an arbitrary feasible input parameter $\mathbf{x}_0$ and a perturbation direction $\delta\mathbf{x}$. If the slope estimated by the Taylor test is 2 or greater, we can safely use the objective and gradients functions in a gradient-based optimazation algorithm. If the optimization algorithm returns an optimal parameter value $\mathbf{x}^*$, a severe Taylor testing can be performed around this value. The optimal parameter value presumes that the gradient norm $\|\nabla F(\mathbf{x}^*)\|$ is nearly zero; therefore the Taylor remainder $\mathbb{T} \approx \epsilon\left\|\left(\hat{\nabla} F(\mathbf{x}^*)\,, \delta\mathbf{x}\right)\right\|$ is of order ϵ^2 only if the exact gradient norm is also nearly zero.

Algorithm 1 Taylor remainder convergence test

procedure TAYLOR TEST($\mathbf{x}_0$, $F(\cdot)$, $\hat{\Delta}_F(\cdot\ ,\ \cdot)$)
  initialize $\delta\mathbf{x}$ :: perturbation vector
  initialize ϵ :: initial perturbation magnitude
  initialize N :: number of evaluations
  initialize r :: empty array of floats of dimension $N \times 2$
  do calculate $F(\mathbf{x}_0)$, $\hat{\Delta}_F(\mathbf{x}_0,\ \cdot)$
  while $N > 0$ **do**
    $r[N][0] \leftarrow \log \epsilon$
    $r[N][1] \leftarrow \log\left(\mathbb{T}(\mathbf{x}_0, \delta\mathbf{x}|\epsilon)/F(\mathbf{x}_0)\right)$
    $\epsilon \leftarrow \epsilon/2$
    $N \leftarrow N - 1$
  end while
  do `slope`, `shift` $\leftarrow$ `linear fit`(r)
  return `slope`
end procedure

A.2 Introduction to `firecrest`

A software tool `firecrest` was developed to formalize the obtained knowledge and automate typical workflows. Currently, this tool concerns only the thermoviscous acoustic flow problems. `firecrest` is a `python` package that uses `PySplines` (Kungurtsev, 2020b) to generate boundaries and surface properties, Gmsh (Geuzaine and Remacle, 2009) for mesh generation, and the FEniCS (Alnæs et al., 2015) finite element solver. `firecrest` is free and open-source; comments and contributions via GitHub are very welcome. We overview the main steps of a numerical problem formulation and solution using `firecrest`.

Defining the computational domain

The first step of the problem formulation is to define a computational domain. The domain initialization approach is motivated by parameter-based shape optimization applications, such that the domain boundaries are defined by collections of parameters, or `control_points`. A simple boundary that consists of multiple line segments can be generated using `LineElement(control_points)`. A more general case is a uniform rational B-spline boundary of degree `degree`: `BSplineElement(control_points, degree)`. The mesh resolution is controlled by setting the size of the mesh elements facets adjacent to the boundary. It is specified by the `elsize` key word of the boundary object; the default value is 0.05.

In this example, a `bspline_boundary` and a `line_boundary` boundaries are defined by two control points lists `line_control_points` and `bspline_control_points`, and compose a simply connected domain `domain`.

```
from firecrest.mesh.boundaryelement import BSplineElement, LineElement
from firecrest.mesh.geometry import SimpleDomain

line_control_points = [[0.5, 0.1], [0.5, -0.2], [0.0, -0.2], [0.0, 0.0]]

bspline_control_points = [
    [0.0, 0.0], [0.1, 0.1], [0.2, -0.1], [0.3, 0.2], [0.4, 0.0], [0.5, 0.1]
]

if __name__ == "__main__":
    bspline_boundary = BSplineElement(bspline_control_points)
    line_boundary = LineElement(line_control_points, el_size=0.1)
    domain = SimpleDomain([bspline_boundary, line_boundary])
```

Figure A.1 shows the resulting domain and the mesh. While the geometry and mesh files are available in the `Mesh/` subdirectory in the script file path, users do not need to interact with these low-level objects directly.

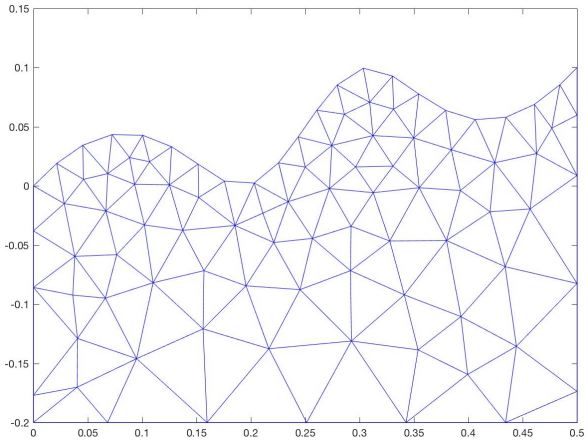

Fig. A.1 An example computational domain and the mesh.

The `LineElement, BSplineElement` classes are based on the `PySplines` machinery, which makes it possible to use the automatically generated surface properties (such as the surface curvature) in the finite element formulation and shape optimization.

Defining the boundary conditions

The `domain` object in the first example knows nothing about the flow problem of interest yet. For each boundary object, boundary conditions can be specified by an argument `bcond` of type dictionary.

For the thermoviscous acoustic flow, there are two groups of boundary conditions: those related to the flow velocity and pressure, and those related to the flow temperature and heat flux. The following code defines a no slip, isothermal boundary `boundary_1` and a stress free, adiabatic boundary `boundary_2`:

```
from firecrest.mesh.boundaryelement import LineElement

control_points_1 = [[0.0, 0.0], [1.0, 0.0], [1.0, 1.0]]
boundary_1 = LineElement(
    control_points_1, bcond={"noslip": True, "isothermal": True}
)
control_points_2 = [[1.0, 1.0], [0.0, 1.0], [0.0, 0.0]]
boundary_2 = LineElement(control_points_2, bcond={"free": True, "adiabatic": True})
```

A boundary with inhomogeneous boundary conditions can be defined in two ways. A fixed value boundary condition can be provided as the `bcond` dictionary element. If a boundary condition value needs to be changed every time it is evaluated (for example, in an unsteady problem), an object that implements the `eval()` evaluation method can be provided. The example below instantiates a boundary with an inhomogeneous temperature boundary condition $T = 1$ using `"temperature": 1.0` in the `bcond`

dictionary, and a periodic velocity boundary condition. The `eval()` method of the `Inflow` object returns a two-dimensional velocity vector.

```
import math
from firecrest.mesh.boundaryelement import LineElement

class Inflow:
    time = 0.0

    def eval(self):
        self.time += 0.01
        return (math.sin(self.time), math.cos(self.time))

control_points = [[0.0, 0.0], [1.0, 0.0]]
boundary = LineElement(
    control_points, bcond={"inflow": Inflow(), "temperature": 1.0}
)
```

The full list of supported acoustic boundary conditions is defined by two attributes of the `firecrest.fem.tv_acoustic_weakform.BaseTVAcousticWeakForm` class: `allowed_stress_bcs` and `allowed_temperature_bcs`.

Defining and solving acoustic flow problems

Three types of the thermoviscous acoustic flow solvers are available: the eigenvalue `EigenvalueTVAcousticSolver` and frequency domain `SpectralTVAcousticSolver` solvers, and the unsteady acoustic flow solver `UnsteadyTVAcousticSolver`. All solvers require the `domain` object as the first argument, and the Reynolds and Prandtl (or Peclet) numbers as keyword arguments. The `EigenvalueTVAcousticSolver` solves the acoustic eigenvalue problem (2.27) and accepts an additional `complex_shift` argument that allows users to specify the search region of the acoustic eigenvalues. The `SpectralTVAcousticSolver` solves the acoustic problem in the frequency domain (2.26), and requires the nondimensional complex-valued `frequency` argument that is the frequency of the time-harmonic acoustic oscillations. The `UnsteadyTVAcousticSolver` solves the time discrete unsteady acoustic problem (2.3.4), and the time step Δt is set by the `dt` argument. The code below demostrates the instantiation of these solvers:

```
from firecrest.api import (
    EigenvalueTVAcousticSolver, SpectralTVAcousticSolver, UnsteadyTVAcousticSolver
)
eigenvalue_solver = EigenvalueTVAcousticSolver(
    domain, complex_shift=-1.0+2.0j, Re=100.0, Pr=10.0
)
spectral_solver = SpectralTVAcousticSolver(
    domain, frequency=10.0j, Re=100.0, Pr=10.0
)
unsteady_solver = UnsteadyTVAcousticSolver(domain, dt=1.0e-3, Re=100.0, Pr=10.0)
```

Solvers implement the `solve` method that returns the solution state `state`. Additionally, the `UnsteadyTVAcousticSolver` implements the `solve_direct` and `solve_adjoint` methods that yield intermediate results of the unsteady simulation. It is possible to choose different time discretization schemes (the default one is Crank–Nicolson).

Use `solver.output_field(state)` to visualize the solution: the resulting `.vtu` files are stored in the `Visualization/` folder. Please refer to the project documentation, and to `firecrest/demos` for more examples.

On the `firecrest` design

The architecture of the `firecrest` is inspired by the components of the finite element method. The low level entities: `Geometry` and `Space` constitute the `BaseFunctionSpace` class that concerns the generation of function spaces using the `dolfin` API. The `TVAcousticFunctionSpace` and `ComplexTVAcousticFunctionSpace` classes inherit from the `BaseFunctionSpace`, and provide the real and complex discrete function spaces for the thermoviscous acoustic problem (as discussed in section 2.3.5). Figure A.2 shows the dependency diagram and the main fields of these objects.

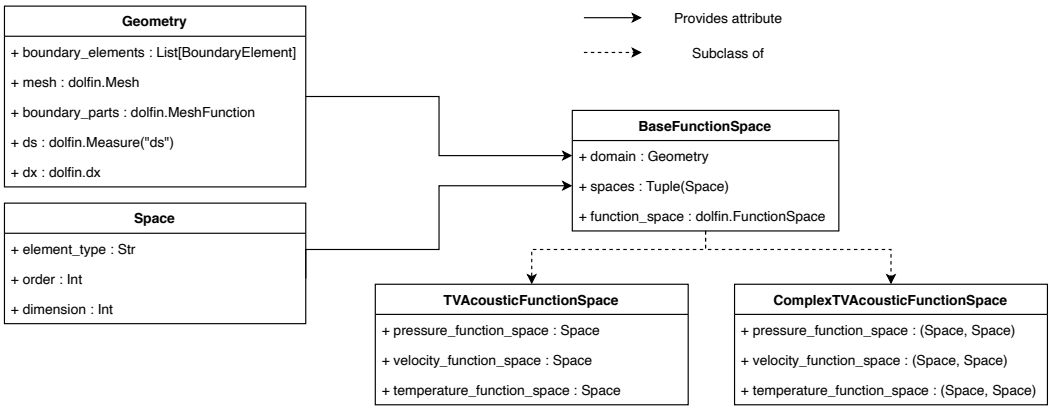

Fig. A.2 The `firecrest` function spaces related objects dependency diagram.

The next functional layer concerns weak forms generation using the function space objects. The acoustic weak form components (2.37) are implemented by the `TVAcousticWeakForm` class (figure A.3). In addition to the necessary volumetric $a(\mathbf{p},\mathbf{q}), b(\mathbf{p},\mathbf{q})$ and surface $b_\Gamma(\mathbf{p},\mathbf{q})$ components, this class also provides methods to calculate some aggregate flow state properties. For example, given the solution state $(\mathbf{u}, P, T)$, the `volume_dissipation` method returns total dissipation $\mathcal{R}_{\text{ac}}$, and `mass_flow_rate` returns the mass flux $\{\mathbf{u}\cdot\mathbf{n}\}$ through a given boundary.

Finally, `firecrest` provides a public API to define and solve acoustic flow problems using the `Solver` objects. Users can access the underlying weak forms from the `.forms` argument of their solvers.

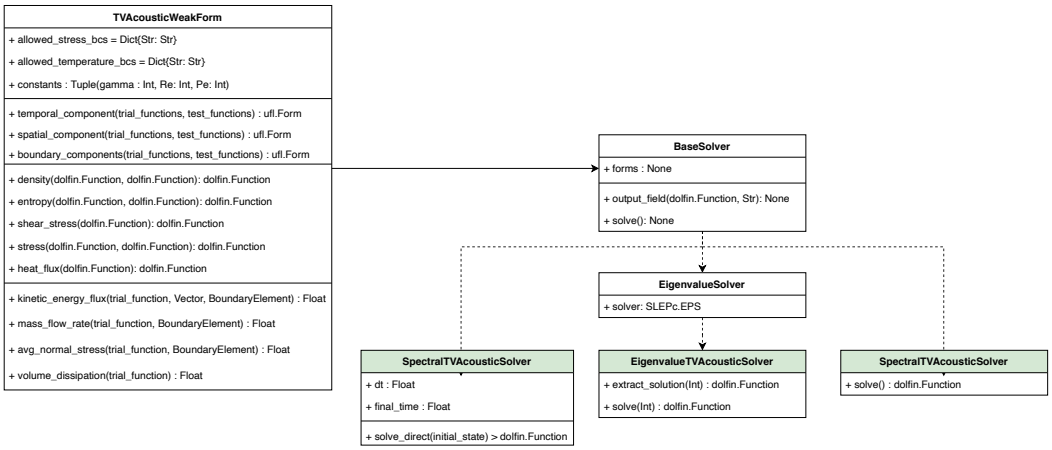

Fig. A.3 The `firecrest` weak forms and solver objects dependency diagram.

We conclude this overview with a simple example of a thermoviscous acoustic eigenvalue problem solved inside a triangular domain. Two sides of the triangle compose a no slip, isothermal boundary `boundary1`, and the third side is an adiabatic, compliant boundary with complex impedance `z = -1.0-2.0j` (`boundary2`). The Reynolds and the Prandtl numbers are specified by the solver arguments `Re` and `Pr`, respectively. We create an instance the eigenvalue solver, and search for one mode that is closest to the target `complex_shift` number. After the eigenproblem is solved, we output the real and imaginary mode components. Finally, we assert that the mass flow rate through the no slip boundary `boundary1` is almost zero.

```
from firecrest.api import LineElement, SimpleDomain, EigenvalueTVAcousticSolver

z = -1.0 - 2.0j
control_points_1 = [[0.0, 0.0], [1.0, 0.0], [1.0, 1.0]]
control_points_2 = [[1.0, 1.0], [0.0, 0.0]]
boundary1 = LineElement(control_points_1, bcond={"noslip": True, "isothermal": True})
boundary2 = LineElement(control_points_2, bcond={"impedance": z, "adiabatic": True})
domain = SimpleDomain((boundary1, boundary2))

solver = EigenvalueTVAcousticSolver(domain, complex_shift=-3.0j, Re=100.0, Pr=1.0)

if __name__ == "__main__":
    (ev, real_mode, imag_mode), *_ = solver.solve(number_of_modes=1)
    solver.output_field(real_mode + imag_mode)
    print(solver.forms.mass_flow_rate(real_mode, boundary1))  # 1.2e-13
```

A.3 Meshes in waveform optimization experiments

In order to verify the accuracy of the numerical computations performed in Chapter 3, simulations results using meshes with different resolution are analysed. The mesh convergence is analysed for the two dimensional straight channel case from section 3.2.2. The total energy $\mathcal{E}(t_f)$ is calculated at $t_f = 2\mu$s with the optimized actuator boundary velocity from figure 3.8. The domain is discretized with an average cell size $h \simeq 0.1$, and this coarse mesh is taken as the initial point (688 cells, 4826 degrees of freedom). The mesh resolution is increased near the nozzle part of the channel, and the actuator boundary. The mesh is uniformly refined several times and the simulation is performed on the refined mesh until the relative difference of $\mathcal{E}(t_f)$ between the subsequent calculations falls below 10^{-3}. Figure A.4 shows the final energy values for different numbers of degrees of freedom (black line). An estimated order of convergence is 2.

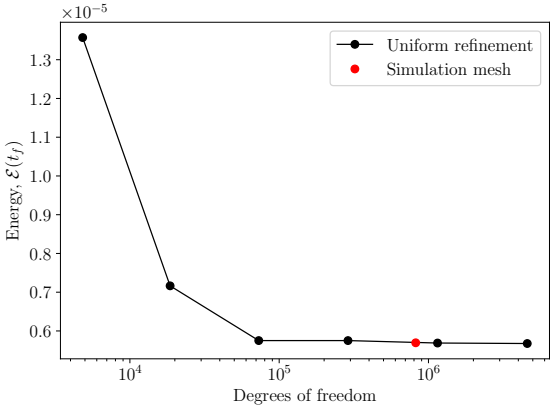

Fig. A.4 Final energy of the controlled flow in a 2D straight channel, $t_f = 2\mu$s (section 3.2.2) for different mesh resolution. A reference mesh with an initial average element size $h = 0.1$ is refined uniformly (black line). Red dot corresponds to the mesh used in the experiments.

For the numerical computations, a sufficiently small characteristic mesh element size is estimated from the convergence data (figure A.4, red marker), and a new mesh is built (figure A.5). The mesh corresponding to the two dimensional long straight print head channel from section 3.2.3 is built using the same mesh resolution.

Using this approach, the characteristic mesh element size is chosen to build the mesh for the U-shaped printhead channel numerical simulations in section 3.2.4. Figure A.6 shows the mesh, which consists of 245000 cells.

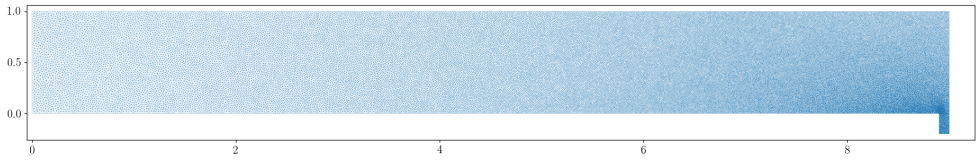

Fig. A.5 A 2D straight channel mesh used in numerical simulations in section 3.2.2.

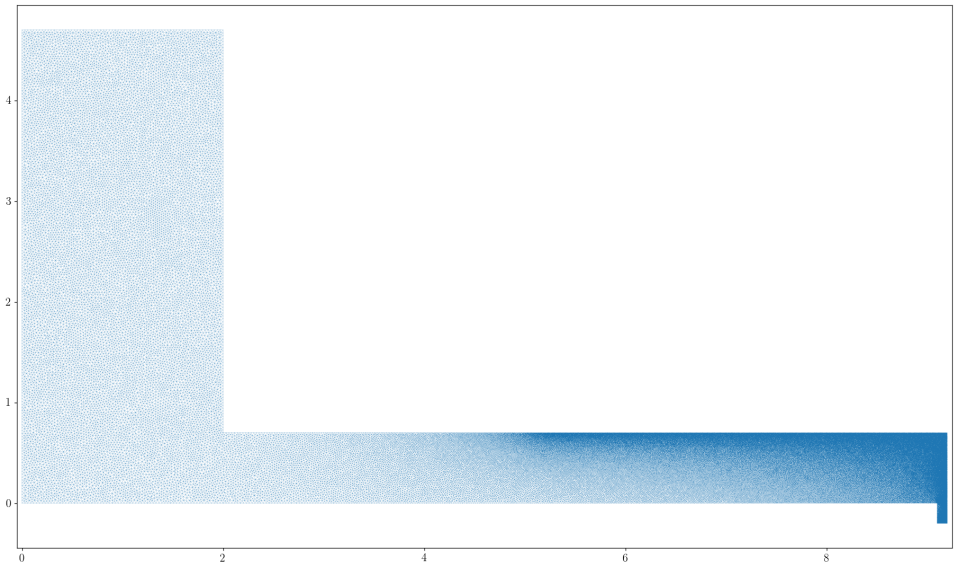

Fig. A.6 A U-shaped printhead channel mesh used in numerical simulations in section 3.2.4.

Future work can consider adjoint-based techniques for mesh adaptation. Kast (2016) discussed a framework for optimal mesh refinement in unsteady problems. Automatic tools such as `AdaptiveLinearVariationalSolver` implemented in FEniCS can also be adapted for transient simulations (see, for example, Zimmerman and Kowalski (2017)).

Appendix B

Shape senstivities

B.1 Adjoint acoustic eigenvalue problem

The thermoviscous acoustic eigenvalue problem (2.27) is written in terms of the acoustic state eigenvector $\hat{\mathbf{q}} \equiv \left(\hat{\mathbf{u}}, \hat{P}, \hat{T}\right)$ and the complex eigenvalue s, $s\mathrm{A}\hat{\mathbf{q}} + \mathrm{B}\hat{\mathbf{q}} = 0$. We generalize the system of primal linearized boundary conditions $\mathcal{N}\hat{\mathbf{q}} = 0$ to the impedance and thermal accomodation conditions (2.32, 2.33)

$$Z(s,x)\hat{u}_i = \left(-\hat{P}\delta_{ij} + \tilde{R}e^{-1}\tau_{ij}\right) n_j, \tag{B.1a}$$

$$\hat{T} = -\,\alpha_w(s,x)\frac{\partial \hat{T}}{\partial \mathbf{n}}. \tag{B.1b}$$

There exists a corresponding adjoint state vector $\mathbf{q}^\dagger = \left(\mathbf{u}^\dagger, P^\dagger, T^\dagger\right)$. A Lagrangian functional of the system (2.27) with a objective function $\mathcal{J}$ is defined as

$$\mathcal{L} = \mathcal{J} - \left\langle \mathbf{q}^\dagger, s\mathrm{A}\hat{\mathbf{q}} + \mathrm{B}\hat{\mathbf{q}} \right\rangle. \tag{B.2}$$

The system's eigenvalue sensitivity can be determined by setting $\mathcal{J} = s$.

The optimality condition yields that the total variation of the Lagrangian with respect to the primal $\hat{\mathbf{q}}, s$, and the adjoint $\mathbf{q}^\dagger$ variables must be zero. The variation with respect to the adjoint variables gives the primal state equations. To determine the adjoint set of equations, we take the variation with respect to the primal variables and integrate the volume term in (B.2) by parts:

$$\frac{\partial \mathcal{L}}{\partial \hat{\mathbf{q}}}\delta\hat{\mathbf{q}} = 0 = \frac{\partial \mathcal{J}}{\partial \hat{\mathbf{q}}}\delta\hat{\mathbf{q}} - \left\langle s^*\mathrm{A}^\dagger\mathbf{q}^\dagger + \mathrm{B}^\dagger\mathbf{q}^\dagger, \delta\hat{\mathbf{q}} \right\rangle - \left\{ \mathcal{N}^\dagger\mathbf{q}^\dagger, \delta\hat{\mathbf{q}} \right\}. \tag{B.3}$$

The volume terms define the adjoint state equations, which in matrix form are:

$$s^* \begin{bmatrix} 1 & 0 & 0 \\ 0 & \gamma_{\text{th}} & -1 \\ 0 & -1 & \frac{1}{\gamma_{\text{th}}-1} \end{bmatrix} \mathbf{q}^\dagger + \begin{bmatrix} -\tilde{Re}^{-1}\nabla_j \hat{\boldsymbol{\tau}}_{ij} & -\nabla_i & 0 \\ -\nabla_i & 0 & 0 \\ 0 & 0 & -\frac{1}{(\gamma_{\text{th}}-1)Pe}\Delta \end{bmatrix} \mathbf{q}^\dagger = 0, \tag{B.4}$$

where $\hat{\boldsymbol{\tau}}_{ij}\mathbf{q}^\dagger = \tau_{ij}^\dagger \equiv \nabla_j u_i^\dagger + \nabla_i u_j^\dagger - 2/3\ \delta_{ij}\text{div}\mathbf{u}^\dagger$ is the adjoint viscous stress tensor. The surface terms determine the adjoint boundary conditions $\mathcal{N}^\dagger\mathbf{q}^\dagger = 0$:

$$Z^*(s,x)u_i^\dagger = \left(P^\dagger\delta_{ij} + \tilde{Re}^{-1}\tau_{ij}^\dagger\right) n_j, \tag{B.5a}$$

$$T^\dagger = -\,\alpha_w(s,x)\frac{\partial T^\dagger}{\partial \mathbf{n}}. \tag{B.5b}$$

Consideration of the primal (2.27) and adjoint (B.4) state equations, and the corresponding boundary conditions (B.1) and (B.5) yields that the adjoint state can be expressed in terms of the primal state variables:

$$\mathbf{q}^\dagger = \left(-\hat{\mathbf{u}}^*, \hat{P}^*, \hat{T}^*\right). \tag{B.6}$$

The variation of the Lagrangian with respect to the eigenvalue δs gives the normalization condition:

$$\frac{\partial \mathcal{L}}{\partial s}\delta s = 0 = \delta s - \left\langle \mathbf{q}^\dagger, A\hat{\mathbf{q}} \right\rangle \delta s - \left\{ \mathbf{q}^\dagger, \frac{\partial \mathcal{N}}{\partial s}\hat{\mathbf{q}} \right\} \delta s. \tag{B.7}$$

Taking into account the adjoint state representation in terms of the primal variables, the normalization condition is:

$$\begin{aligned} 1 = &- \langle \hat{\mathbf{u}}^*, \hat{\mathbf{u}} \rangle + \left\langle \hat{P}^*, \gamma_{\text{th}}\hat{P} - \hat{T} \right\rangle + \left\langle \hat{T}^*, \frac{\hat{T}}{\gamma_{\text{th}}-1} - \hat{P} \right\rangle + \\ &+ \left\{ \hat{\mathbf{u}}^*, \frac{\partial Z}{\partial s}\hat{\mathbf{u}} \right\} - \left\{ \frac{\partial \hat{T}^*}{\partial \mathbf{n}}, \frac{(\partial \alpha_w/\partial s)}{(\gamma_{\text{th}}-1)\tilde{Pe}}\frac{\partial \hat{T}}{\partial \mathbf{n}} \right\}. \end{aligned} \tag{B.8}$$

If the boundaries' impedance and thermal accommodation coefficient are frequency-independent, the surface terms in (B.8) vanish and the normalization condition is given by

$$\left\langle \mathbf{q}^\dagger, \mathrm{A}\hat{\mathbf{q}} \right\rangle = 1. \tag{B.9}$$

B.2 Acoustic flow shape sensitivity

We want to construct the eigenvalue shape sensitivity $G(\hat{\mathbf{q}}, \mathbf{q}^\dagger)$ of the thermoviscous acoustic problem for a given shape displacement field V. We take the variation of the Lagrangian (B.2) with respect to a shape perturbation $\mathcal{L}'[V]$, and, due to the choice of the adjoint state (B.6), only the boundary terms do not vanish. This gives us the shape gradient

$$\begin{aligned}\mathcal{L}'[V] = &- \left\{\mathcal{N}^\dagger \mathbf{q}^\dagger, \hat{\mathbf{q}}'[V]\right\} = \\ &\left\{u_i^\dagger, \left(-\hat{P}'[V]\delta_{ij} + \tilde{Re}^{-1}\hat{\tau}'_{ij}[V]\right) n_j\right\} \\ &- \left\{\left(P^\dagger \delta_{ij} + \tilde{Re}^{-1}\tau_{ij}^\dagger\right) n_j, \hat{u}'_i[V]\right\} \\ &+ \left\{T^\dagger, \frac{1}{(\gamma_{\text{th}}-1)\tilde{Pe}}\frac{\partial \hat{T}'[V]}{\partial n}\right\} - \left\{\frac{\partial T^\dagger}{\partial n}, \frac{1}{(\gamma_{\text{th}}-1)Pe}\hat{T}'[V]\right\}\end{aligned} \tag{B.10}$$

The primal stress tensor is $\hat{\sigma}_{ij} = -\hat{P}\delta_{ij} + \tilde{Re}^{-1}\hat{\tau}_{ij}$ and the adjoint stress tensor is $\sigma_{ij}^\dagger = -P^\dagger\delta_{ij} + \tilde{Re}^{-1}\tau_{ij}^\dagger$. Also, we define the primal $\hat{q}_i = \frac{1}{(\gamma_{\text{th}}-1)Pe}\nabla_i \hat{T}$ and adjoint $q_i^\dagger = \frac{1}{(\gamma_{\text{th}}-1)Pe}\nabla_i T^\dagger$ heat fluxes, and their normal components $\hat{q}_i n_i \equiv \hat{q}_n$, $q_i^\dagger n_i \equiv q_n^\dagger$.

On boundaries, the conditions (B.1) hold, resulting in the compliant and thermal boundary shape derivatives:

$$0 = \mathrm{d}\left(Z\hat{u}_i - \hat{\sigma}_{ij}n_j\right)[V] = \mathrm{d}Z[V]\hat{u}_i + Z\mathrm{d}\hat{u}_i[V] - \mathrm{d}\hat{\sigma}_{ij}[V]n_j - \hat{\sigma}_{ij}\mathrm{d}n_j[V], \tag{B.11a}$$

$$\begin{aligned}0 = \mathrm{d}\left(\hat{T} + \alpha_w\frac{\partial \hat{T}}{\partial n}\right)[V] = &\mathrm{d}\hat{T}[V] + \mathrm{d}\alpha_w[V]\frac{\partial \hat{T}}{\partial n} + \\ &+\alpha_w \mathrm{d}n_j[V]\nabla_j\hat{T} + \alpha_w\frac{\partial \mathrm{d}\hat{T}[V]}{\partial n},\end{aligned} \tag{B.11b}$$

As discussed in section 4.1.1, the total and the local shape derivatives of the Dirichlet and Neumann boundaries, satisfy:

$$\mathrm{d}\hat{u}_i[V] = \hat{u}'_i[V] + (V\cdot\nabla)\hat{u}_i, \tag{B.12a}$$

$$\mathrm{d}\hat{\sigma}_{ij}[V] = \hat{\sigma}'_{ij}[V] + (V\cdot\nabla)\hat{\sigma}_{ij}, \tag{B.12b}$$

$$\mathrm{d}\hat{T}[V] = \hat{T}'[V] + (V\cdot\nabla)\hat{T}, \tag{B.12c}$$

$$\mathrm{d}\left(\nabla_j\hat{T}\right)[V] = \nabla_j\hat{T}'[V] + (V\cdot\nabla)\nabla_j\hat{T} \tag{B.12d}$$

Assuming the boundary properties (impedance and thermal accomodation) to be constant in the displacement direction, the material derivative results in $\mathrm{d}Z[V] = 0, \mathrm{d}\alpha_w[V] = 0$.

The displacement vector field V can be presented as a sum of its normal and tangential components, $V = (V \cdot \mathbf{n})\,\mathbf{n} + \sum_{i=1}^{d-1}(V \cdot \boldsymbol{\tau}_i)\boldsymbol{\tau}_i$, where $\boldsymbol{\tau}_i$ spans the $d-1$ dimensional space tangent to the surface. As shown in (Sokolowski and Zolesio, 1992), a shape derivative vanishes in the tangential direction, since any boundary deformation in the tangential direction does not change the domain boundary. Therefore, for a domain boundary of sufficient smoothness the shape derivatives in the direction of the displacement field are equivalent to the shape derivatives in its normal projection. Therefore V can be replaced with $(V \cdot \mathbf{n})\,\mathbf{n}$ and $(V \cdot \nabla)$ with $(V \cdot \mathbf{n})\,\partial/\partial\mathbf{n}$. By introducing the tangential gradient $\nabla_i^\Gamma = \nabla_i - n_i n_j \nabla_j$, the shape derivative of the boundary normal is (Sonntag et al., 2016)

$$\mathrm{d}n_i[V] = -\nabla_i^\Gamma\,(V \cdot \mathbf{n})\,. \tag{B.13}$$

Combining (B.11 - B.13), the shape derivatives of the compliant boundary condition and the thermal boundary condition result in

$$Z\hat{u}_i'[V] - \hat{\sigma}_{ij}'[V]n_j = -\,Z\,(V \cdot \mathbf{n})\,\frac{\partial \hat{u}_i}{\partial n} + (V \cdot \mathbf{n})\,n_j\frac{\partial \hat{\sigma}_{ij}}{\partial n} - \hat{\sigma}_{ij}\nabla_i^\Gamma\,(V \cdot \mathbf{n})\,, \tag{B.14a}$$

$$\begin{aligned}\hat{T}'[V] + \alpha_w\frac{\partial \hat{T}'[V]}{\partial n} =& -\,(V \cdot \mathbf{n})\,\frac{\partial \hat{T}}{\partial n} \\ &- \alpha_w\,(V \cdot \mathbf{n})\,n_j\frac{\partial \nabla_j \hat{T}}{\partial n} + \alpha_w\nabla_i^\Gamma\,(V \cdot \mathbf{n})\,\nabla_i\hat{T}\end{aligned} \tag{B.14b}$$

Considering the adjoint boundary conditions (B.5) in the primal shape derivative (B.10) and substituting the above expressions, we obtain

$$\mathcal{L}'[V] = \left\{u_i^\dagger, \hat{\sigma}_{ij}'[V]n_j - Z\hat{u}_i'[V]\right\} - \left\{q_n^\dagger, \hat{T}'[V] + \alpha_w\frac{\partial \hat{T}'[V]}{\partial n}\right\} \tag{B.15a}$$

$$= \left\{u_i^\dagger, (V \cdot \mathbf{n})\left(Z\frac{\partial \hat{u}_i}{\partial \mathbf{n}} - n_j\frac{\partial \hat{\sigma}_{ij}}{\partial \mathbf{n}}\right) + \hat{\sigma}_{ij}\nabla_j^\Gamma\,(V \cdot \mathbf{n})\right\} + \tag{B.15b}$$

$$\left\{q_n^\dagger, (V \cdot \mathbf{n})\left(\frac{\partial \hat{T}}{\partial \mathbf{n}} + \alpha_w n_j\frac{\partial \nabla_j \hat{T}}{\partial \mathbf{n}}\right) - \alpha_w\nabla_i^\Gamma\,(V \cdot \mathbf{n})\,\nabla_i\hat{T}\right\}.$$

The shape gradient is represented by stress and thermal contributions. Two terms are still not in Hadamard form, so we apply the surface tangential Green's formula (Delfour and Zolésio, 2011). The relation holds for a smooth vector field A and a scalar

field b:

$$\int_{\partial\Omega}(A,\nabla^{\Gamma})b\;ds=\int_{\partial\Omega}\kappa b(A,n)-b\;\mathrm{div}^{\Gamma}A\;ds. \tag{B.16}$$

Here $\kappa=\mathrm{div}^{\Gamma}n$ describes the surface curvature. With $A_j=-u_i^{\dagger *}\hat{\sigma}_{ij}, b=(V\cdot\mathbf{n})$, the transformation of the stress contribution (the first surface integral in (B.15b)) to Hadamard form is given by

$$u_i^{\dagger *}\hat{\sigma}_{ij}\nabla_j^{\Gamma}\left(V\cdot\mathbf{n}\right)=\kappa\left(V\cdot\mathbf{n}\right)u_i^{\dagger *}\hat{\sigma}_{ij}n_j-\left(V\cdot\mathbf{n}\right)\nabla_j^{\Gamma}(u_i^{\dagger *}\hat{\sigma}_{ij}), \tag{B.17}$$

and using the definition of the tangential gradient, the tangential divergence in (B.17) combines with the following term and we obtain:

$$\nabla_j^{\Gamma}(u_i^{\dagger *}\hat{\sigma}_{ij})+u_i^{\dagger *}n_j\frac{\partial\hat{\sigma}_{ij}}{\partial\mathbf{n}}=\nabla_j(u_i^{\dagger *}\hat{\sigma}_{ij})-\frac{\partial u_i^{\dagger *}}{\partial\mathbf{n}}n_j\hat{\sigma}_{ij}. \tag{B.18}$$

For the thermal contribution (the second surface integral in (B.15b))

$$A_j=\alpha_w\nabla_j\hat{T}\left(\partial T^{\dagger}/\partial n\right)^*$$

so the Hadamard form is:

$$\begin{aligned}
&\alpha_w q_n^{\dagger}\nabla_j\hat{T}\nabla_j^{\Gamma}\left(V\cdot\mathbf{n}\right)=\\
&\quad=\kappa\left(V\cdot\mathbf{n}\right)\alpha_w q_n^{\dagger *}\frac{\partial\hat{T}}{\partial n}-\left(V\cdot\mathbf{n}\right)\nabla_j^{\Gamma}\left(\alpha_w q_n^{\dagger *}\nabla_j\hat{T}\right)\\
&\quad=\left(V\cdot\mathbf{n}\right)\left(\kappa\alpha_w q_n^{\dagger *}\frac{\partial\hat{T}}{\partial\mathbf{n}}-\alpha_w q_n^{\dagger *}\left(\Delta\hat{T}-n_j\frac{\partial\nabla_j\hat{T}}{\partial\mathbf{n}}\right)-\nabla_j^{\Gamma}\left(\alpha_w q_n^{\dagger *}\right)\nabla_j^{\Gamma}\hat{T}\right)
\end{aligned} \tag{B.19}$$

After rearranging the terms in (B.15), the shape derivative in Hadamard form is given by the surface integral of the normal displacement and the sum of the stress and thermal sensitivity functionals, G_s^{str} and G_s^{th}:

$$s'[V]=\mathcal{L}'[V]=\int_{\partial\Omega}\left(V\cdot\mathbf{n}\right)\left(G_s^{str}(\hat{\mathbf{q}},\mathbf{q}^{\dagger})+G_s^{th}(\hat{\mathbf{q}},\mathbf{q}^{\dagger})\right), \tag{B.20}$$

where the functionals are defined as

$$G_s^{str}(\hat{\mathbf{q}},\mathbf{q}^{\dagger})=\frac{\partial\hat{u}_i}{\partial\mathbf{n}}n_j\sigma_{ij}^{\dagger *}+\frac{\partial u_i^{\dagger *}}{\partial\mathbf{n}}n_j\hat{\sigma}_{ij}+\kappa\hat{u}_i\sigma_{ij}^{\dagger *}n_j-\nabla_j\left(u_i^{\dagger *}\hat{\sigma}_{ij}\right), \tag{B.21a}$$

$$G_s^{th}(\hat{\mathbf{q}},\mathbf{q}^{\dagger})=\frac{\partial\hat{T}}{\partial\mathbf{n}}q_n^{\dagger *}+\frac{\partial T^{\dagger *}}{\partial\mathbf{n}}\hat{q}_n+\kappa\hat{T}q_n^{\dagger *}-\nabla_j\left(T^{\dagger *}\hat{q}_j\right). \tag{B.21b}$$

Finally, considering (B.6), the eigenvalue sensitivity functionals can be derived:

$$G_s^{str} = -\left(2\frac{\partial \hat{u}_i}{\partial \mathbf{n}} n_j \hat{\sigma}_{ij} + \kappa \hat{u}_i \hat{\sigma}_{ij} n_j - \nabla_j \left(\hat{u}_i \hat{\sigma}_{ij}\right)\right), \tag{B.22a}$$

$$G_s^{th} = 2\frac{\partial \hat{T}}{\partial \mathbf{n}} \hat{q}_n + \kappa \hat{T} \hat{q}_n - \nabla_j \left(\hat{T} \hat{q}_j\right). \tag{B.22b}$$

Two special cases, the no slip and stress-free boundaries, simplify the viscous sensitivity functional to

$$\begin{aligned} G_{s,w}^{str} &= -\frac{\partial \hat{u}_i}{\partial \mathbf{n}} n_j \hat{\sigma}_{ij}, \\ G_{s,open}^{str} &= \nabla_j \left(\hat{u}_i \hat{\sigma}_{ij}\right), \end{aligned} \tag{B.23}$$

and the thermal sensitivity functional turns into the following expressions on isothermal and adiabatic boundaries:

$$\begin{aligned} G_{s,isoth}^{th} &= \frac{\partial \hat{T}}{\partial \mathbf{n}} \hat{q}_n, \\ G_{s,ad}^{th} &= -\nabla_j \left(\hat{T} \hat{q}_j\right). \end{aligned} \tag{B.24}$$

B.3 Automated mesh adaptation

Mesh refinement (h-adaptation) is one of the approaches to ensure the convergence of a numerical solution. In most cases, it is accuracy of a particular function of the numerical solution that needs to be improved, rather than the global solution error norm. Uniform mesh refinement is a basic approach to reduce numerical error. This approach does not concern any information about the nature of the problem, and therefore generally yields poor convergence of the objective value versus the number of degrees of freedom. Goal-oriented mesh adaptation strategies mark parts of the computational domain that are expected to contribute the most to the output error. Mesh cells are marked and refined according to the estimated local error value. Some algorithms (Joly, 2010) rely on a priori knowledge about sources of the numerical error. These algorithms use the primal solution on a coarse mesh to estimate the contribution of each mesh cell to the error in the objective function. Adjoint-based error control algorithms (Pierce and Giles, 2000) do not make assumptions on how the numerical error in the solution affects the objective value accuracy. Instead, the primal problem solution is combined with the adjoint solution, which incorporates the knowledge about the flow objective. This allows the user to weight the primal solution residuals by their contribution to the objective error, and perform efficient automated mesh adaptation.

For a thermoviscous acoustic flow, the boundary layer thicknesses $\delta_\nu(\omega), \delta_T(\omega)$ (2.20) define the characteristic length scale of the velocity and temperature fields oscillations near the no slip and isothermal boundaries $\nabla \mathbf{u} \sim \delta_\nu^{-1}\mathbf{u}$, $\nabla T \sim \delta_T^{-1}T$. Insufficient mesh resolution in the acoustic boundary layer regions can lead to high numerical error in acoustic dissipation. On the other hand, using high mesh resolution in the whole domain is not only unnecessary, but also results in a computationally infeasible problem. For these reasons, mesh adaptation algorithms have to be applied.

The FEniCS framework implements automated adaptive solvers of linear and nonlinear problems, so the goal-oriented mesh adaptation for the frequency domain acoustic flow (2.26) objective requires one simply to define such an objective. Unfortunately, there are no automated tools for generic eigenvalue problems. We investigate whether it is possible to improve the eigenvalues' convergence using the aforementioned techniques. A thermoviscous acoustic eigenvalue problem inside an L-shaped domain (figure B.1) is considered as an example problem. The bottom and the right boundaries are adiabatic, stress-free boundaries. All other boundaries are no slip, isothermal boundaries. The Reynolds and Prandtl numbers are $Re = 5000$, $Pr = 1$. Two objective functionals are tested: an eigenvalue close to $-0.45 + 3.5\mathrm{i}$ and a higher frequency eigenvalue close to $-0.12 + 12.15\mathrm{i}$. We compare three iterative mesh refinement strategies: uniform, Hessian-based error indicators (Joly, 2010), and adjoint-based error indicators (Kast, 2016; Rognes and Logg, 2013). On each iteration, element-wise error indicators are computed, and cells are sorted in order of decreasing error size. A number of cells that contribute the most to the output error are refined in an isotropic manner. Marking all cells for refinement naturally results in uniform mesh refinement. A new eigenmode and eigenvalue is computed on a finer mesh.

In the Hessian-based approach, Hessian matrices of the velocity and temperature eigenmode components $\mathbf{H}(|\hat{\mathbf{u}}|), \mathbf{H}(\left|\hat{T}\right|)$ are computed for each mesh element. A cell is marked for refinement if the magnitude of any of the Hessian matrix elements exceeds a globally-computed threshold. The velocity and temperature thresholds are computed individually, as the 75th percentile of the absolute values of the respective Hessian matrix elements. Figure B.1a shows the velocity magnitude $|\hat{\mathbf{u}}|$ and the mesh for the first test case ($s = -0.0485 + 3.497\mathrm{i}$) at the fifth refinement iteration (5700 cells). The algorithm refines the mesh along the no slip walls where the velocity magnitude is high, and near the corner $(1.0, 0.3)$. No mesh refinement is applied for $x > 1.3$, where the solution magnitude is small. Figures B.2 and B.3 show the convergence of the real and imaginary parts of the test eigenvalues versus the number of cells (green lines). The algorithm outperforms the uniform mesh refinement (red lines).

In the adjoint-based approach, the error indicators are computed by testing the strong cell and facet residuals against the extrapolated adjoint solution (see Rognes and Logg (2013), Algorithm 2). The strong residuals are derived by hand. Conveniently, the adjoint solution is available from the solution of the primal problem (B.6), subject to the normalization condition (B.8). Figure B.1b shows the velocity magnitude $|\hat{\mathbf{u}}|$ and the mesh for the first test case ($s = -0.049 + 3.497\mathrm{i}$) at the eleventh refinement iteration (6200 cells). Similarly to the previous algorithm, the mesh is refined along the no slip walls and near the corner. The average cell diameter is smaller than that generated by the Hessian-based algorithm. Additionally, the refined cells are located much closer to the boundaries (this also applies to the corner region), while the bulk of the domain is coarser. Figures B.2 and B.3 show the convergence of the real and imaginary parts of the test eigenvalues versus the number of cells (black lines). The adjoint-based algorithm outperforms both the uniform and the Hessian-based mesh refinement strategies.

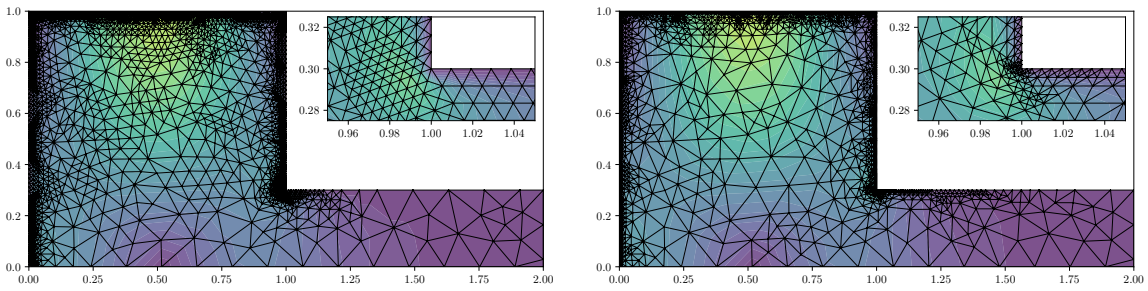

(a) (b)

Fig. B.1 Comparison of the velocity magnitude fields $|\hat{\mathbf{u}}|$ and mesh cells distribution of the (a) Hessian-based algorithm (5700 cells), and (b) the adjoint-based algorithm (6200 cells) for the first test case (approximate eigenvalue is $s = -0.048 + 3.5\mathrm{i}$).

The advantages of using the adjoint-based error control is that it naturally yields a better convergence rate in comparison to other techniques, and does not require any a priori knowledge about the error distribution in the numerical solution.

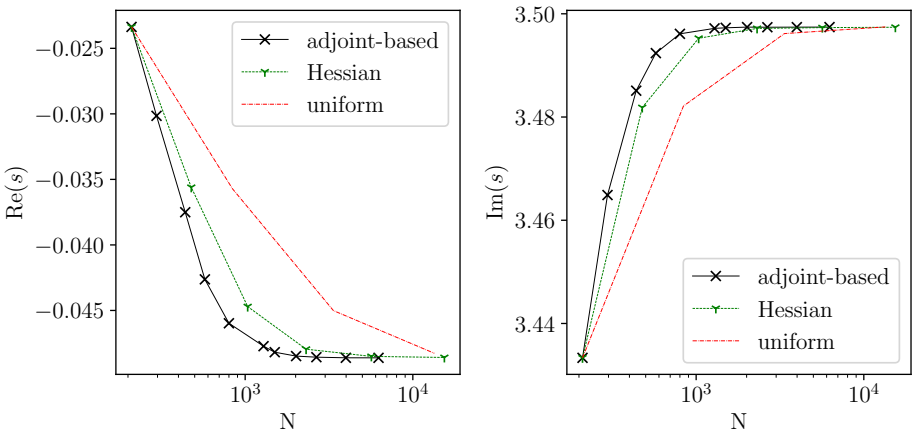

Fig. B.2 The convergence of the real (a) and imaginary (b) eigenvalue components versus the number of cells N for the first test case and different mesh adaptation strategies.

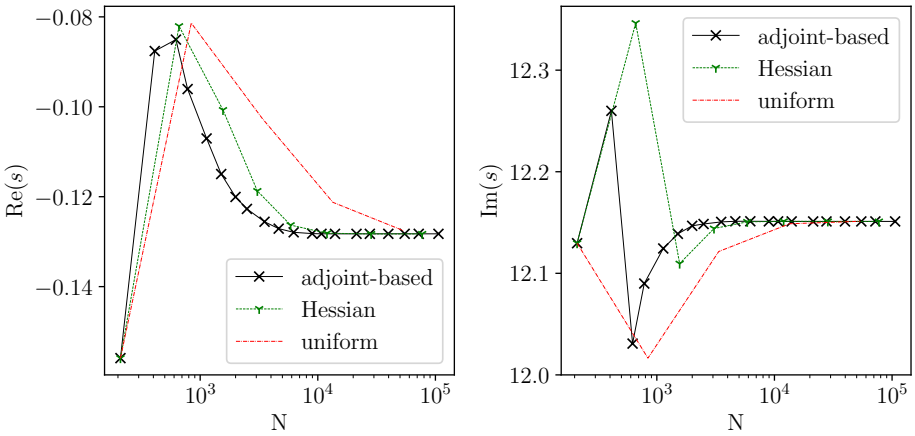

Fig. B.3 The convergence of the real (a) and imaginary (b) eigenvalue components versus the number of cells N for the second test case and different mesh adaptation strategies.

Appendix C

Frequency domain modelling of the inkjet flow

An example acoustic problem is solved in the frequency domain. We measure the mass flux through the shared boundary $\Gamma_{\mathrm{C-N}}$ generated be harmonic oscillations of the printhead actuator for a range of frequencies used in inkjet printing. It is shown that the frequency-dependent impedance boundary condition and the nozzle model boundary condition prescribed on $\Gamma_{\mathrm{C-N}}$ results in almost no mass flux on the free surface for both low and high oscillation frequencies. The actuator motion at $0.1 \leq \omega \leq 1.0$ MHz frequencies maximises the magnitude of the mass transfer $\{\hat{\mathbf{u}}_\omega \cdot \mathbf{n}\}$ through the shared boundary.

C.1 Boundary condition for the frequency domain problem

We derive the boundary conditions for the acoustic frequency domain problem discussed in section 2.3.2. The time-harmonic equation for a given frequency ω is

$$\begin{aligned} &\text{Find } \hat{\mathbf{q}}_\omega(\mathbf{x}) \text{ such that} \\ &\qquad i\omega \mathrm{A}\hat{\mathbf{q}}_\omega + \mathrm{B}\hat{\mathbf{q}}_\omega = 0 \quad \text{in } \Omega. \end{aligned} \tag{C.1}$$

The acoustic stress boundary condition on the surface between the channel and nozzle domains $\Gamma_{\mathrm{C-N}}$ (2.70) is given by a nonlinear system of equations:

$$\sigma_{ij} n_j = -\gamma \hat{\kappa} n_i - h_{\mathrm{CL}} \left(\frac{d}{dt} u_i - \frac{1}{\tilde{Re}} \Delta_\Gamma u_i \right) \quad \text{on } \Gamma_{\mathrm{C-N}}, \tag{C.2a}$$

$$\left(\frac{d \left| \hat{\Omega}_{\mathrm{n}}(\hat{\kappa}) \right|}{d\hat{\kappa}} \right) \frac{d}{dt} \hat{\kappa} = \epsilon \left\{ \mathbf{u} \cdot \mathbf{n} \right\}_{\Gamma_{\mathrm{C-N}}} - \epsilon h_{\mathrm{CL}} \left| \Gamma_{\mathrm{C-N}} \right| \frac{d}{dt} \gamma \hat{\kappa}. \tag{C.2b}$$

We linearize the nozzle state equation (C.2b) around the base state,

$$\hat{\kappa} = \hat{\kappa}^{(0)} + \delta\hat{\kappa}, \quad \left| \Omega_{\mathrm{n}}(\hat{\kappa}) \right| \simeq \left| \Omega_{\mathrm{n}}(\hat{\kappa}^{(0)}) \right|, \quad h_n^{(0)} \equiv h_n(\hat{\kappa}^{(0)}) = h_{\mathrm{CL}} + \frac{\left| \hat{\Omega}_{\mathrm{n}}(\hat{\kappa}^{(0)}) \right|}{\left| \Gamma_{\mathrm{C-N}} \right|}.$$

We perform a Fourier transform $\mathbf{q}(\mathbf{x}, t) \xrightarrow{\mathscr{F}} \hat{\mathbf{q}}_\omega(\mathbf{x})$ for a real-valued frequency $\omega \in \mathbb{R}$ and a complex frequency mode $\hat{\mathbf{q}}$. The time derivative operator is replaced with the complex oscillation frequency of the mode $\frac{\partial}{\partial t} \to i\omega$. The linearized nozzle state equation becomes

$$i\omega \left(\frac{d \left| \hat{\Omega}_{\mathrm{n}}(\hat{\kappa}) \right|}{d\hat{\kappa}} + \epsilon \gamma h_n \left| \Gamma_{\mathrm{C-N}} \right| \right) \Bigg|_{\hat{\kappa}^{(0)}} \delta\hat{\kappa} = \epsilon \left\{ \hat{\mathbf{u}} \cdot \mathbf{n} \right\}_{\Gamma_{\mathrm{C-N}}}.$$

The linearized acoustic stress boundary condition on $\Gamma_{\mathrm{C-N}}$ is an impedance type boundary condition.

$$\begin{aligned} \hat{\sigma}_{ij} n_j =& -\gamma \delta\hat{\kappa} n_i - h_n^{(0)} \left(i\omega - \frac{1}{Re} \Delta_\Gamma \right) \hat{u}_i \\ =& -\frac{1}{i\omega} \frac{\epsilon\gamma}{\left(\frac{d \left| \hat{\Omega}_{\mathrm{n}}(\hat{\kappa}) \right|}{d\hat{\kappa}} + \epsilon\gamma h_n \left| \Gamma_{\mathrm{C-N}} \right| \right) \Big|_{\hat{\kappa}^{(0)}}} \left\{ \hat{\mathbf{u}} \cdot \mathbf{n} \right\}_{\Gamma_{\mathrm{C-N}}} n_i \\ & - i\omega h_n^{(0)} \hat{u}_i + \frac{h_n^{(0)}}{Re} \Delta_\Gamma \hat{u}_i. \end{aligned} \tag{C.3}$$

Given a frequency $\omega : s \equiv i\omega$, a set of boundary conditions on $\partial\Omega_{\mathrm{c}}/\Gamma_{\mathrm{C-N}}$ and the impedance boundary condition (C.3) on $\Gamma_{\mathrm{C-N}}$, we aim to find an acoustic state $\hat{\mathbf{q}}_\omega(\mathbf{x})$ which is a solution to the problem (C.1). In order to simplify the notation, we rewrite

(C.3) in terms of the nonlocal $Z_1(\omega)$ and local $Z_2(\omega)$ impedance variables:

$$\begin{aligned} \hat{\sigma}_{ij} n_j &= Z_1(\omega) \left\{ \hat{\mathbf{u}} \cdot \mathbf{n} \right\}_{\Gamma_{\mathrm{C-N}}} n_i + Z_2(\omega) \hat{u}_i \quad \text{on } \Gamma_{\mathrm{C-N}}, \\ Z_1(\omega) &= -\frac{1}{i\omega} \frac{\epsilon\gamma}{\left(\frac{d\left|\hat{\Omega}_{\mathrm{n}}(\hat{\kappa})\right|}{d\hat{\kappa}} + \epsilon\gamma h_n \left|\Gamma_{\mathrm{C-N}}\right| \right)\Big|_{\hat{\kappa}^{(0)}}}, \\ Z_2(\omega) &= -i\omega h_n^{(0)} + \frac{h_n^{(0)}}{Re} \Delta_\Gamma. \end{aligned} \tag{C.4}$$

We consider two well-posed auxiliary subproblems:

$$\begin{aligned} &\text{Find } \hat{\mathbf{q}}_{\omega,1}(\mathbf{x}) \text{ such that} \\ &\qquad i\omega \mathrm{A} \hat{\mathbf{q}}_{\omega,1} + \mathrm{B} \hat{\mathbf{q}}_{\omega,1} = 0 \quad \text{in } \Omega, \\ &\qquad \hat{\sigma}_{ij,1} n_j = Z_2(\omega) \hat{u}_{i,1} \quad \text{on } \Gamma_{\mathrm{C-N}}, \\ &\qquad \text{original boundary conditions on } \partial\Omega_{\mathrm{c}}/\Gamma_{\mathrm{C-N}}; \end{aligned} \tag{C.5a}$$

$$\begin{aligned} &\text{Find } \hat{\mathbf{q}}_{\omega,2}(\mathbf{x}) \text{ such that} \\ &\qquad i\omega \mathrm{A} \hat{\mathbf{q}}_{\omega,2} + \mathrm{B} \hat{\mathbf{q}}_{\omega,2} = 0 \quad \text{in } \Omega, \\ &\qquad \hat{\sigma}_{ij,2} n_j = 1 \cdot n_i + Z_2(\omega) \hat{u}_{i,2} \quad \text{on } \Gamma_{\mathrm{C-N}}, \\ &\qquad \text{homogeneous boundary conditions on } \partial\Omega_{\mathrm{c}}/\Gamma_{\mathrm{C-N}}. \end{aligned} \tag{C.5b}$$

A standard impedance boundary condition is prescribed on $\Gamma_{\mathrm{C-N}}$ in the first problem (C.5a). An inhomogeneous impedance boundary condition is prescribed on $\Gamma_{\mathrm{C-N}}$ in the second problem (C.5b), where $1 \cdot n_i$ is a unit force in the normal direction.

For an arbitrary constant c, a linear combination of the solutions $\hat{\mathbf{q}}_{\omega,1} + \mathrm{c}\hat{\mathbf{q}}_{\omega,2}$ satisfies the acoustic equations in the volume, and the boundary conditions on $\partial\Omega_{\mathrm{c}}/\Gamma_{\mathrm{C-N}}$. The combined stress vector on $\Gamma_{\mathrm{C-N}}$ equals

$$\begin{aligned} \hat{\sigma}_{ij,1} n_j + \mathrm{c}\hat{\sigma}_{ij,2} &= Z_2(\omega) \hat{u}_{i,1} + \mathrm{c} \left(1 \cdot n_i + Z_2(\omega) \hat{u}_{i,2}\right) \\ &= \mathrm{c} n_i + Z_2(\omega) \left(\hat{u}_{i,1} + \mathrm{c}\hat{u}_{i,2}\right). \end{aligned}$$

We notice that by choosing $\mathrm{c} = \mathrm{c}^\star$ such that $\mathrm{c}^\star = Z_1(\omega) \left\{ (\hat{\mathbf{u}}_1 + \mathrm{c}^\star \hat{\mathbf{u}}_2) \cdot \mathbf{n} \right\}_{\Gamma_{\mathrm{C-N}}}$, the linear combination $\hat{\mathbf{q}}_{\omega,1} + \mathrm{c}^\star \hat{\mathbf{q}}_{\omega,2}$ satisfies not only the acoustic state equations in Ω_{c} and the original boundary conditions on $\partial\Omega_{\mathrm{c}}/\Gamma_{\mathrm{C-N}}$, but also the impedance boundary condition (C.4). This means that the solution $\hat{\mathbf{q}}_\omega$ of the problem of interest with the nonlocal impedance boundary condition can be found as follows:

1. Find the solutions $\hat{\mathbf{q}}_{\omega,1}, \hat{\mathbf{q}}_{\omega,2}$ of the auxiliary problems (C.5a, C.5b).

2. Calculate the value $\mathrm{c}^\star$ given the velocity components $\hat{\mathbf{u}}_1, \hat{\mathbf{u}}_2$ of $\hat{\mathbf{q}}_{\omega,1}$ and $\hat{\mathbf{q}}_{\omega,2}$, respectively.
$$\mathrm{c}^\star = \frac{Z_1(\omega)\left\{\hat{\mathbf{u}}_1 \cdot \mathbf{n}\right\}_{\Gamma_{\mathrm{C-N}}}}{1 - Z_1(\omega)\left\{\hat{\mathbf{u}}_2 \cdot \mathbf{n}\right\}_{\Gamma_{\mathrm{C-N}}}}. \tag{C.6}$$

3. Obtain the problem solution as a linear combination $\hat{\mathbf{q}}_\omega = \hat{\mathbf{q}}_{\omega,1} + \mathrm{c}^\star \hat{\mathbf{q}}_{\omega,2}$.

Since $\mathrm{c}^\star = Z_1(\omega)\left\{\hat{\mathbf{u}} \cdot \mathbf{n}\right\}_{\Gamma_{\mathrm{C-N}}}$ by construction, the mass flux through the shared boundary $\Gamma_{\mathrm{C-N}}$ equals

$$\left\{\hat{\mathbf{u}} \cdot \mathbf{n}\right\}_{\Gamma_{\mathrm{C-N}}} = \frac{\left\{\hat{\mathbf{u}}_1 \cdot \mathbf{n}\right\}_{\Gamma_{\mathrm{C-N}}}}{1 - Z_1(\omega)\left\{\hat{\mathbf{u}}_2 \cdot \mathbf{n}\right\}_{\Gamma_{\mathrm{C-N}}}}. \tag{C.7}$$

A useful feature of the method is that the first impedance coefficient $Z_1(\omega)$ is not involved in the solution of the thermoviscous acoustic problem (C.5). This allows us to compute and store the values of $\left\{\hat{\mathbf{u}}_1 \cdot \mathbf{n}\right\}_{\Gamma_{\mathrm{C-N}}}$, $\left\{\hat{\mathbf{u}}_2 \cdot \mathbf{n}\right\}_{\Gamma_{\mathrm{C-N}}}$, and calculate the mass flux (C.7) for an arbitrary $Z_1(\omega)$ value for free.

C.2 Frequency response of the printhead flow to harmonic excitation

We study the response of the acoustic flow inside the inkjet printhead microchannel (figure 2.7) to harmonic oscillations of the actuator boundary Γ_{act} at different frequencies ω. Mass and energy transfer through the free surface inside the inkjet nozzle is an important metric of a printhead performance. We choose the mass flux $\left\{\hat{\mathbf{u}}_\omega \cdot \mathbf{n}\right\}_{\Gamma_{\mathrm{C-N}}}$ as the response measure of the flow.

The velocity boundary condition $\hat{\mathbf{u}} = 1 \cdot \mathbf{n}$ is prescribed on Γ_{act}. We consider three frequency domain problems (§2.3.2) with different boundary conditions on $\Gamma_{\mathrm{C-N}}$: (i) stress-free, (ii) impedance $Z^{(ii)}$ (2.32), and (iii) reduced order nozzle model (C.4). The frequency-dependent impedance $Z^{(ii)}(\omega)$ of the second problem boundary condition is a local approximation of the reduced order nozzle model boundary condition with $\hat{\kappa}^{(0)} = 0$:

$$Z^{(ii)}(\omega) = -\frac{1}{i\omega} \frac{\epsilon\gamma \left|\Gamma_{\mathrm{C-N}}\right|}{\left(\frac{d\left|\hat{\Omega}_{\mathrm{n}}(\hat{\kappa})\right|}{d\hat{\kappa}} + \epsilon\gamma h_n \left|\Gamma_{\mathrm{C-N}}\right|\right)\Big|_{\hat{\kappa}^{(0)}}} - i\omega h_n^{(0)} - \frac{h_n^{(0)}}{Re}\frac{1}{r_n^2}, \quad \hat{\kappa}^{(0)} = 0.$$

The nondimensional parameters of the experiment are provided in table C.1. The third frequency domain problem with the nozzle model boundary condition is solved using the method discussed in section C.1.

	nondimensional value
Base state of the free surface curvature, $\hat{\kappa}^{(0)}$	$0, 0.5$
Mach number, ϵ	10^{-5}
Reynolds number, Re,	$1.6 \cdot 10^{-5}$
Prandtl number, Pr	10
surface tension, γ,	1

Table C.1 Nondimensional parameters of the experiments of the inkjet microchannel flow response to harmonic excitation.

We vary the oscillation frequency from $\omega = 0.25$ kHz to $\omega = 40$ MHz. Figure C.1 shows the nondimensional absolute value and the phase of the mass flux through the shared boundary $\{\hat{\mathbf{u}}_\omega \cdot \mathbf{n}\}_{\Gamma_{\mathrm{C-N}}}$ as a function of the actuator oscillation frequency. The solid red line corresponds to the first problem with the stress-free boundary condition $\hat{\sigma}_{ij} n_j = 0$ on $\Gamma_{\mathrm{C-N}}$. The solid blue line corresponds to the second problem with the impedance boundary condition $\hat{\sigma}_{ij} n_j = Z^{(ii)}(\omega)\hat{u}_i$ on $\Gamma_{\mathrm{C-N}}$. The dashed and dash-dotted blue lines corresponds to the third problem with the nozzle model boundary condition, $\hat{\kappa}^{(0)} = 0$ and $\hat{\kappa}^{(0)} = 0.5$, respectively. The solid, dashed and dash-dotted green lines show phases of the complex-value boundary mass flux for the second problem, the third problems with $\hat{\kappa}^{(0)} = 0$, and the third problem with $\hat{\kappa}^{(0)} = 0.5$, respectively.

The mass flux through the shared boundary $\Gamma_{\mathrm{C-N}}$ with the stress-free boundary condition is almost uniform for frequencies below 1 MHz and rapidly decreases for higher frequencies $\omega/(2\pi) \geq 1$ MHz, because of the natural inductance-type impedance of the nozzle part of the channel. The maximum magnitude of the mass flux through the stress-free boundary is reached at $\omega = 0.1$ MHz. The magnitude and phase of the mass fluxes through $\Gamma_{\mathrm{C-N}}$ with the impedance boundary condition (the second problem) and the nozzle model boundary condition with $\hat{\kappa}^{(0)} = 0$ (the third problem) are almost identical. We conclude that it is possible to use the local approximation impedance boundary condition instead of the reduced order nozzle model to calculate the mass flux through the $\Gamma_{\mathrm{C-N}}$ boundary generated by the harmonic oscillations of the actuator. For the lower part of the frequency range $\omega/(2\pi) \leq 0.1$ MHz, the capacitance term dominates, and the boundary acts as a no slip surface. For higher frequencies $\omega/(2\pi) \geq 1$ MHz, the inductance term damps the acoustic oscillations, and reduces

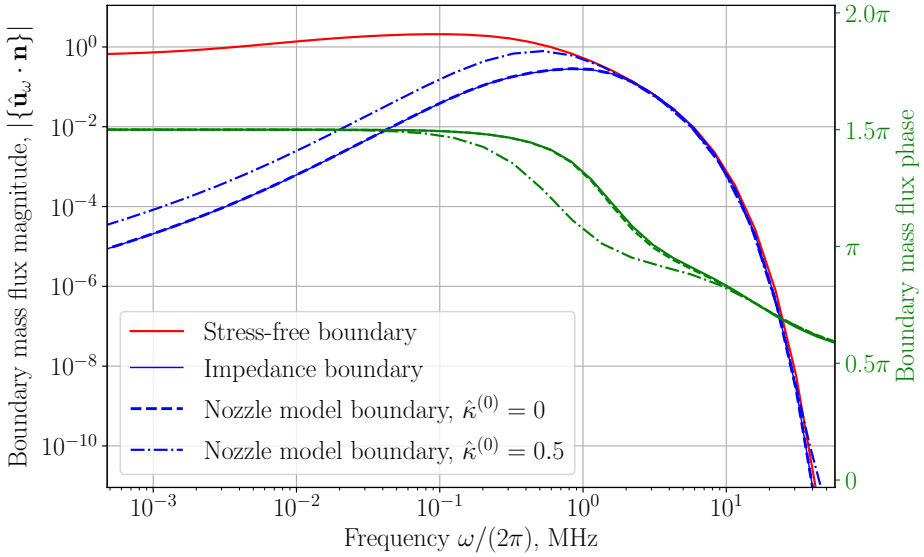

Fig. C.1 Magnitude and phase of the mass fluxes through the shared boundary $\Gamma_{\mathrm{C-N}}$ for different boundary conditions and different oscillation frequencies.

the mass flux through $\Gamma_{\mathrm{C-N}}$. The maximum magnitude of the mass flux through the nozzle model boundary, $\hat{\kappa}^{(0)} = 0$, is reached at $\omega = 0.8$ MHz.

For a fixed frequency, the capacitance of the nozzle model boundary condition is bounded from above (2.83) and has the maximum value at $\hat{\kappa}^{(0)} = 0$. A non-zero base state curvature $\hat{\kappa}^{(0)} = 0.5$ results in lower magnitude of the capacitance term $\left| \frac{\epsilon\gamma|\Gamma_{\mathrm{C-N}}|}{\left(\frac{d|\hat{\Omega}_{\mathrm{n}}(\hat{\kappa})|}{d\hat{\kappa}} + \epsilon\gamma h_n |\Gamma_{\mathrm{C-N}}|\right)\Big|_{\hat{\kappa}^{(0)}}} \right|$, and the mass flux $\{\hat{\mathbf{u}}_\omega \cdot \mathbf{n}\}_{\Gamma_{\mathrm{C-N}}}$ approaches the stress-free case. The maximum magnitude of the mass flux through the nozzle model boundary, $\hat{\kappa}^{(0)} = 0.5$, is reached at $\omega = 0.4$ MHz.